Dynamics of Globular Proteins in Crowded Electrolyte Solutions

Studied by Neutron Scattering

Dissertation

der Mathematisch-Naturwissenschaftlichen Fakultät

der Eberhard Karls Universität Tübingen

zur Erlangung des Grades eines

Doktors der Naturwissenschaften

(Dr. rer. nat.)

vorgelegt von

Marcus Hennig

aus Mittweida

Tübingen

2011

Tag der mündlichen Qualifikation: 15.07.2011

Dekan: Prof. Dr. Wolfgang Rosenstiel
1. Berichterstatter: Prof. Dr. Frank Schreiber
2. Berichterstatter: Prof. Dr. Helmut Schober
3. Berichterstatter: Prof. Dr. Judith Peters

This Ph.D. thesis is dedicated to my wife Dan, and my children Mia and Justin.

Preamble

The research for this thesis was carried out within the Ph.D. studentship grant scheme of the *Institut Laue-Langevin*, Grenoble, France, jointly with the *University of Tübingen*, Germany. At the Institut Laue-Langevin Dr. Tilo SEYDEL supervised the project and provided assistance to design, prepare and conduct the Experiments.

List of Papers

This thesis based on the following papers, which will be referred to in the text by their Latin letters.

A **Protein Diffusion in Crowded Electrolyte Solutions**
F. Roosen-Runge, M. Hennig, T. Seydel, F. Zhang, M.W.A. Skoda, S. Zorn, R.M.J. Jacobs, M. Maccarini, P. Fouquet, and F. Schreiber
Biochimica et Biophysica Acta **1804** (2010) 68-75

B **Protein Self-Diffusion in Crowded Solutions**
F. Roosen-Runge, M. Hennig, F. Zhang, R.M.J. Jacobs, M. Sztucki, H. Schober, T. Seydel, and F. Schreiber
Proceedings of the National Academy of Sciences (USA) **108** (2011) 29:11815-11820

C **Dynamics of Highly Concentrated Protein Solutions around the Denaturing Transition**
M. Hennig, F. Roosen-Runge, F. Zhang, S. Zorn, M.W.A. Skoda, R.M.J. Jacobs, T. Seydel, and F. Schreiber
In preparation for Physical Review Letters

D **Salt-Induced Local Crowding of Proteins**
M. Hennig, F. Roosen-Runge, F. Zhang, P. Falus, S. Zorn, M.W.A. Skoda, R.M.J. Jacobs, H. Schober, T. Seydel, and F. Schreiber
In preparation for Soft Matter

Contents

Kapitel 1

Deutsche Zusammenfassung

Inhalt

1.1 Motivation

Betrachtet man das Innere einer Zelle auf der Nanometerskala, so offenbart sich eine immense Vielfalt aus Molekülen unterschiedlicher Form und Größe, die sich auf engsten Raum in einer wässrigen Lösung drängeln. Unter ihnen spielen Proteine eine herausragende Rolle, da sie für die Zelle und den damit verbundenen Organismus lebenswichtige biologische Funktionen erfüllen. Proteine sind bemerkenswerte kleine molekulare Maschinen, die sich aus einem Repertoire von 20 Aminosäuren zusammensetzen [114, 26].

In einer wässrigen Umgebung faltet sich ein Protein in eine charakteristische dreidimensionale Struktur, die durch die Sequenz der Aminosäuren bestimmt wird. Diese sogenannte native Struktur zeichnet sich dadurch aus, dass sich hydrophobe Aminosäuren im inneren des Proteins befinden. Umgekehrt sind die hydrophilen Aminosäuren auf der dem Wasser zugewandten Oberfläche lokalisiert [31, 26, 66].

Proteine werden als weiche Materie betrachtet und weisen eine interne Dynamik auf unterschiedlichen Längen- und Zeitskalen auf. Dazu zählen unter anderem die Fluktuation der Atome, die Reorientierung von Seitenketten und die Bewegung kompletter Proteindomänen [20]. Diese Art von interner Bewegung kann man mittels einer totalen mittleren Bewegungsamplitude quantifizieren. Erhöht man die Temperatur hinreichend, dann entfaltet sich das Protein in eine “Random Coil” einhergehend mit dem Verlust der biologischen Funktion [123, 47].

Die Funktion als Kriterium nehmend, kann man zwei Klassen von Proteinen unterscheiden: Proteine, die in der Zellmembran eingebaut sind und solche, die in der intra- und extrazellulären Umgebung frei vorkommen. In dieser Arbeit konzentrieren wie uns auf die zuletzt genannte Kategorie. Diese sind häufig globuläre Proteine, die zahlreiche für den Organismus essentielle Aufgaben ausführen. Dazu zählt etwa: der Transport kleiner Moleküle, die Transmission von Signalen, um biologische Prozesse zu regulieren, und die Katalyse organischer Reaktionen. Als Beispiel führen wir Serum Albumin auf. Dieses kann mitunter kleine Moleküle wie Fettsäuren oder Arzneimittel im Blutstrom transportieren [29].

Die Wichtigkeit der Transportprozesse motiviert die Frage: Wie bewegen sich Moleküle innerhalb und außerhalb der Zelle und wie wird diese Bewegung insbesondere durch das Vorhandensein von Molekülen und Ionen in der Zelle beeinflusst?

Proteine existieren in einer "Welt der kleinen Reynolds - Zahlen", mit anderen Worten in einer Umgebung, in welcher das Verhältnis zwischen Trägheit und Viskosität sehr klein ist. Proteine bewegen und reorientieren sich daher thermisch durch eine enorme Anzahl an Kollisionen mit den sie umgebenen Wassermolekülen [133, 118]. Diese sogenannte Translations- beziehungsweise Rotationsdiffusion führt zu einer mittleren quadratischen Verschiebung der Anfangsposition und Winkelabweichung der Orientierung des Proteins abhängig von der verstrichenen Zeit, der Viskosität des Lösungsmittels und der Größe und Form des Proteins [164].

In einem vereinfachten Bild dargestellt, operiert die Zelle durch die Bewegung von Proteinen in einer hochkonzentrierten wässrigen Lösung [49]. Wir können daher annehmen, dass sich die Funktion von Proteinen nur verstehen lässt, wenn man deren Dynamik – sowohl interne Moden als auch Rotations – und Translationsdiffusion – und Interaktion mit Ionen, Wassermolekülen und Proteinen einbezieht [11]. Es ist daher das Ziel dieser Arbeit, die Dynamik und Struktur einer Lösung von Proteinen unter biologisch relevanten Bedingungen zu untersuchen. Um dieses Ziel zu erreichen, modellieren wir die intrazelluläre Umgebung durch ein vereinfachtes *in vitro* System, welches durch Umgebungsparameter wie den Protein-Volumenanteil, die ionische Stärke der Lösung und die Temperatur kontrolliert wird. Dabei soll der zu untersuchende Temperaturbereich auch den Denaturierungsübergang umfassen.

Konkret wollen wir in dieser Arbeit die folgenden Punkte behandeln:
Erstens wollen wir die Mobilität eines globulären Proteins in Abhängigkeit von der Proteinkonzentration untersuchen. Ergänzend, wollen wir die Gleichgewichtstruktur der Lösung studieren. Das Ziel ist es, die folgenden zwei Fragen zu beantworten: Wie konzentriert muss eine Proteinlösung sein, damit die "räumliche Beengtheit" der Moleküle das Diffusionsverhalten signifikant beeinflusst? Ist es unter Zuhilfenahme etablierter Kolloidmodelle möglich, die zu messende Diffusionskonstante vorherzusagen?
Zweitens wollen wir die Dynamik eines Proteins in der Umgebung des temperaturinduzierten Denaturierungsüberganges studieren und gegebenfalls neue analytische Verfahren zur Bestimmung der internen diffusiven Moden entwickeln.

Drittens ist ein wichtiges Charakteristikum der natürlichen Umgebung das Vorhandensein von Ionen. Wir wollen daher untersuchen, wie die ionischen Stärke und die Valenz der Ionen die Dynamik eines Proteins in Lösung beeinflusst.

1.2 Experimentelle Ergebnisse

In diesem Abschnitt fassen wir die wichtigsten Ergebnisse der Publikationen A bis D zusammen. Diese sind im Stile von wissenschaftlichen Veröffentlichungen in den Kapiteln 7, 8, 9 und 10 dieser Dissertation eingearbeitet. Infolge dieser Form der Darstellung ist es unvermeidlich, dass sich bestimmte Teile der Veröffentlichungen mit Teilen anderer Abschnitte inhaltlich überschneiden. Wir fassen die wesentlichen Resultate jeder Veröffentlichung zusammen und stellen diese kohärent in den Kontext dieser Arbeit.

1.2.1 Publikation A. Protein Diffusion in hochkonzentrierten elektrolytischen Lösungen

In Publikation A (siehe Kap. 7) untersuchen wir den messbaren Diffusionskoeffizienten des globulären Proteins Bovine Serum Albumin (BSA) in hochkonzentrierter wässriger Lösung als Funktion der Protein- und Natriumchloridkonzentration mit Hilfe von Neutronenrückstreuung und Spin-Echo-Spektroskopie. Ferner analysieren wir die Gleichgewichtsstruktur der Lösung mittels Röntgen-Kleinwinkelstreuung (RKWS).

Das Ziel dieser Studie ist, Auskunft darüber zu geben, wie konzentriert eine Proteinlösung sein muss, damit die "räumliche Beengtheit" der Moleküle das Diffusionsverhalten signifikant beeinflusst.

Mittels RKWS finden wir eine qualitative Änderung von einem unkorrelierten zu einen stark korrelierten System mit zunehmender Raumfüllung. Durch eine genauere Analyse finden wir heraus, dass unterhalb von einem Raumfüllungsgrad von ungefähr 10 % die "räumliche Beengtheit" der Moleküle vorrangig durch nicht abgeschirmte Ladungen hervorgerufen wird. Im Gegensatz dazu dominieren oberhalb von ungefähr 10 % Verdrängungseffekte.

Konträr zu den statischen Daten zeigen die dynamischen Daten keinen ausgezeichneten Raumfüllungsgrad, oberhalb dessen Verdrängungseffekte signifikant hervorträten.

Stattdessen beobachten wir ein stetiges Abfallen des gemessenen Diffusionskoeffizienten mit steigender Proteinkonzentration. Desweitern führt die Zugabe von Salz zu keiner signifikanten Änderung des Diffusionskoeffizienten, obzwar die durch das Salz hervorgerufene Ladungsabschirmung eine deutliche Änderung der intermolekularen Interaktion bewirkt. Vorwegnehmend weisen wir darauf hin, dass Publikation B (siehe Kap. 8) eine Erklärung für die zuletzt genannte Beobachtung gibt. In dieser Studie zeigen wir, dass sich die Diffusion von globulären Proteinen mittels Kolloidmodellen beschreiben lässt. Die theoretischen Selbstdiffusionskoeffizienten von kolloidalen ungeladenen und geladenen harten Kugeln sind im Kurzzeitgrenzwert sehr

ähnlich. Die gemessene Genauigkeit erlaubt keine Unterscheidung. Zusätzlich ist der Einfluss der Ladung im Kolloidmodell sehr gering. Infolgedessen haben Abschirmungseffekte keinen signifikanten Einfluss. Auch wenn die Bildung einer Gegenionenschicht auf der Oberfläche des Moleküls den hydrodynamischen Radius ändert, so ist dieser Effekt innerhalb der Messgenauigkeit nicht nachweisbar. Schlussendlich ist die durch das Salz induzierte Viskositätsänderung für die untersuchten Salzkonzentrationen von 0 bis 300 mM vernachlässigbar.

1.2.2 Publikation B. Protein Selbstdiffusion in hochkonzentrierten Lösungen

Perez et al. [125] haben gezeigt, dass die mit Neutronenspektroskopie bestimmte Diffusionskonstante grösser ist als die Translationsdiffusion aufgrund eines nicht unerheblichen Anteils der Rotationsdiffusion des Moleküls. An Veröffentlichung A anknüpfend konzipieren wir deshalb einen analytischen Rahmen, um aus der gemessenen Diffusionskonstanten den Translationsanteil zu bestimmen. Dies ermöglicht einen Vergleich mit theoretischen Modellen. Folglich ist die der Veröffentlichung B (siehe Kap. 8) zugrundeliegende Motivation, die Verwendbarkeit von Diffusionsmodellen der Kolloidphysik für globuläre Proteine zu untersuchen. Unter Verwendung von Neutronenrückstreuung messen wir die Selbstdiffusion im Kurzzeitgrenzwert für Raumfüllungsgrade von $7\,\% \leq \varphi \leq 30\,\%$ und vergleichen die berechnete Translationsdiffusion mit Kurzzeit-Diffusionsmodellen der Kolloidphysik. Mittels RKWS bestimmen wir die Form des Proteins mit einem Ellipsoid Modell. In der Studie zeigen wir, dass sich im gesamten Raumfüllungsbereich die experimentelle Translationsdiffusion mit folgender Gleichung beschreiben lässt:

$$D_t(\varphi) \approx D_t(0)\, f\left[\varphi \left(\frac{R_h}{R}\right)^3\right]. \tag{1.1}$$

Darin ist die normalisierte Diffusionskonstante f ununterscheidbar von einem Modell für geladene oder ungeladene harte Kugeln innerhalb des Messfehlers. R ist der Radius einer Kugel mit gleichem Volumen wie das Protein, R_h ist der hydrodynamische Radius, errechnet aus dem mit RKWS bestimmten Ellipsoiden und $D_t(0)$ ist der Diffusionskoeffizient bei unendlicher Verdünnung. Zusammenfassend haben wir damit demonstriert, dass sich die Translationsdiffusion von Proteinen mittels effektiver harter Kugeln unabhängig von der Ladung sehr akkurat beschreiben lässt. Die Studie zeigt, dass abgesehen von Volumenverdrängungseffekten hydrodynamische Wechselwirkungen maßgeblich die "räumliche Beengtheit" beeinflussen. Diese Erkenntnis bestätigt auf fundamentale Weise Simulationsresultate von Ando and Skolnick [7] im Kurzzeitgrenzwert.

1.2.3 Publikation C. Dynamik hochkonzentrierter Protein Lösungen nahe des Denaturierungsübergangs

Vermittels Computersimulationen haben Kudlay et al. [91] gezeigt, dass eine hohe Polymerkonzentrationen einen Einfluss auf den temperaturinduzierten Random Coil zu Helix Übergang des Polymeres hat. Die Erkenntnis, dass sich die Proteinstabilität und Faltungsrate mit steigender Packungsrate vergrößert, hat Mittal [111] mit Hilfe von Simulationen der Langevin-Dynamik demonstrieren können.

Zur Validierung dieser Aussagen ist es deshalb auf der experimentellen Seite von Bedeutung, Faltung und insbesondere den inversen Prozess der Denaturierung im Falle hochkonzentrierter Proteinlösung zu quantifizieren.

Publikation C (siehe Kap. 9) ist eine aus quasi-elastischer und elastischer Neutronenrückstreuung kombinierte Studie, welche sowohl die globale als auch die interne Dynamik von Bovine Serum Albumin in hochkonzentrierten Lösungen in der Nähe des Denaturierungsüberganges analysiert. Unter Verwendung von elastischer Neutronenrückstreuung, bestimmen wir die totale mittlere quadratische Bewegungsamplitude $\langle u^2 \rangle$ für das Temperaturintervall $280\,K < T < 370\,K$. Im quasi-elastischen Bereich messen wir die entsprechenden Diffusionskoeffizienten. Einher mit den Daten entwickeln wir eine neuartige Analysestrategie, die es erlaubt, quantitativ den Denaturierungsprozess zu beschreiben.

Wir untersuchen die Temperaturabhängigkeit von $\langle u^2 \rangle$ und quantifizieren dabei den zugrundeliegenden Denaturierungs- und Cross-Linking Prozess.

Inspiriert durch das Zimm-Bragg Modell [187] und die Tatsache, dass die Sekundärstruktur von Bovine Serum Albumin von α-Helices dominiert wird (siehe Abschn. 5.1.1), beschreiben wir die Temperaturabhängigkeit der totalen mittleren quadratischen Bewegungsamplitude folgendermaßen:

$$\langle u^2 \rangle = a\,T + b - \Delta u^2\,\Theta\left(\frac{T - T_0}{\Delta T}\right). \tag{1.2}$$

Darin sind a, b, Δu^2, T_0 und ΔT Fitparameter, die den Denaturierungs- und Cross-Linking Prozess beschreiben. Θ ist eine verwischte Stufenfunktion der Form:

$$\Theta(x) = \frac{1}{1 + e^{-x}}\ , \tag{1.3}$$

welche die Besetzungsanteile der denaturierten und cross-verlinkten Proteine widerspiegelt. Unter Zuhilfenahme des quasi-elastisch messbaren Diffusionskoeffizienten D kann man die mittlere quadratische Amplitude der internen Bewegungsmoden $\langle u^2_{\text{int}} \rangle$ durch Separieren der Schwerpunktsdiffusion folgendermaßen bestimmen:

$$\langle u^2_{\text{int}} \rangle = \langle u^2 \rangle - (2\,\pi)^{-3/2}\,6\,D\,\tau. \tag{1.4}$$

Darin ist τ die zeitliche Auflösung des Spektrometers. In der Studie zeigen wir, dass die Temperaturabhängigkeit von $\langle u^2_{\text{int}} \rangle$ ein nichtstetige Änderung aufweist. Wir spekulieren, dass die Ursache dafür eine Änderung der Flexibilität der diffusiven Moden

der molekularen Untereinheiten des Proteins ist. Es wichtig festzustellen, dass sich die von uns entwickelte analytische Methode auch auf andere Systeme mit sowohl interner als auch Schwerpunktsdynamik anwenden lässt. Das gilt insbesondere für konventionelle Polymere in Lösungen.

1.2.4 Publikation D. Ladungsinduzierte dynamische Dichteinhomogenitäten in Proteinlösungen

In Publikation A (siehe Kap. 7) haben wir unter anderem gezeigt, dass die Veränderung der ionischen Stärke einer BSA-Lösung mittels eines monovalenten Salzes keinen oder nur einen marginalen Effekt auf die Diffusion der BSA-Moleküle hat. Multivalente Salze wie YCl_3 unterscheiden sich zum Beispiel von NaCl dadurch, dass sie nicht nur die ionische Stärke der Lösung modifizieren sondern auch die Ladung der Proteine ändern können. In diesem Zusammenhang haben Zhang et al. [185] gezeigt, dass Yttrium-Ionen eine Ladungsumkehr eines anfänglich negativ geladenen Proteins durch Ionenbindung auf der Oberfläche des Proteins hervorrufen können. Mittels Kleinwinkel-Röntgenstreuung haben sie gezeigt, dass wenn die Salzkonzentration sich einem durch die Proteinkonzentration bestimmten Wert c^* nähert, die Anziehungskräfte zunehmend das Verhalten der Lösung dominieren und in der unmittelbaren Umgebung von c^* zur Bildung von sichtbaren Aggregaten führen. Desweitern konnten sie zeigen, dass bei c^* die Ladung vernachlässigbar klein ist.

Demzufolge ermöglicht die spezifische Bindung von Y^{3+} auf der Proteinoberfläche ein Durchstimmen der Oberflächenladung und damit eine Einflussnahme auf das Zusammenspiel anziehender und abstoßender intermolekularer Wechselwirkungen.

In Publikation D kombinieren wir Neutronen Spin-Echo-Spektroskopie mit Kleinwinkel-Röntgenstreuung, um zum einen die Kurzzeit-Selbstdiffusion von BSA und zum anderen die isotherme Kompressibilität der BSA-Lösung bei verschiedenen YCl_3-Konzentrationen zu studieren. Dabei erhöhen wir die YCl_3 Konzentration bis nahe unter die kritische Konzentration c^*.

Mittels der gemessenen isothermen Kompressibilität beobachten wir, dass die Erhöhung der YCl_3 Konzentration das Gleichgewicht zwischen Abstoßung und Anziehung zu Gunsten des letzteren verschiebt. Gleichzeitig beobachten wir eine signifikante Reduktion des Kurzeit-Selbstdiffusionskoeffizienten. Wir deuten dies wie folgt: Durch die zunehmende Dominanz der Attraktion nimmt die Anzahl der Proteine in der unmittelbaren Umgebung eines Proteins zu und hindert dessen Diffusion durch hydrodynamische Wechselwirkung.

Wir nehmen an, dass der attraktive Teil des Wechselwirkungspotenzials die Bildung von Proteinclustern in der Lösung begünstigt, während der repulsive Teil die Lebensdauer der Cluster reguliert [27, 99]. Nähern wir uns der kritischen Salzkonzentration, so schwächen wir zunehmend die Repulsion, und die Lebenszeit der Cluster wächst. Aufgrund der hohen Ladung von BSA spekulieren wir, dass die Lebenszeit unterhalb von c^* kleiner als die instrumentelle Zeitauflösung (1ns) ist. Kommen wir der kritischen Salzkonzentration c^* sehr nahe (die Netto-Oberflächenladung der Proteine ist ungefähr Null), dann divergiert die Lebenszeit, und es bilden sich stati-

sche Cluster. Dies ist in Übereinstimmung mit der Beobachtung, dass knapp über c^* die Proteinlösung sehr trübe wird und makroskopische Aggregate sichtbar werden.

Aufgrund der kurzen Lebenszeit relativ zur instrumentellen Zeitauflösung kann man die Proteine als unabhängige Monomere betrachten, die sich nur für sehr kurze Zeiten zu sogenannten "transient clusters" zusammenschließen. Liu et al. [99] weisen darauf hin, dass man "transient clusters" eher als dynamische lokale Dichteinhomogenitäten deuteten sollte, anstatt den Begriff Cluster zu verwenden.

Um diese Inhomogenitäten zu quantifizieren, verallgemeinern wir das Model effektiver harter Kugeln, welches wir in Publikation B (siehe Kap. 8) eingeführt haben, folgendermaßen:

$$d_s\left(c_s, \varphi\right) = d_0\, f_{\mathrm{HS}}\left[\left(\frac{R_h}{R}\right)^3 \varphi_{\mathrm{local}}\left(c_s\right)\right], \tag{1.5}$$

Darin ist f_{HS} der theoretische reduzierte Kurzeit-Selbstdiffusionscoeffizient für harte Sphären [115, 162], d_0 ist der Diffusionskoeffizient im Grenzwert stark verdünnter Lösungen, R ist der Radius einer Kugel mit gleichen Volumen wie das Protein, R_h ist der hydrodynamische Radius von BSA. Ist kein YCl_3 in der Lösung, dann begünstigt die hohe Ladung der Proteine durch Repulsion eine homogene Verteilung der Proteine. In diesem Fall ist der Volumenanteil der Proteine φ, folglich $\varphi_{\mathrm{local}}(0) = \varphi$. Mit steigender Salzkonzentration wird die Dichteverteilung inhomogener und im Mittel sehen die Teilchen eine effektive lokale Dichte

$$\varphi_{\mathrm{local}}\left(c_s\right) = \xi\left(c_s\right)\, \varphi. \tag{1.6}$$

Darin haben wir den lokalen Anhäufungsfaktor $\xi\left(c_s\right)$ eingeführt. Wir stellen fest, dass bei der höchsten Salzkonzentration der nächste Nachbarabstand, der dem lokalen φ entspricht, um 20% relativ zum Fall ohne Salz abgenommen hat. Dies unterstützt unsere Hypothese, dass wir lokale dynamische Inhomogenitäten beobachten, statt dicht gepackte Cluster.

1.3 Schlussfolgerung

In den folgenden drei Paragraphen werden wir aus den Ergebnissen der Publikationen A bis D unter den Gesichtspunkten, wie sich die räumliche Beengtheit, die Temperatur und das Vorhandensein von mono- wie auch multivalenten Salzen auf die Dynamik von Proteinen und die Struktur der Lösung auswirkt, Schlussfolgerungen ziehen. Ergänzend werden wir, sowohl auf Grundlage unserer Ergebnisse als auch auf Erkenntnissen aus Neuveröffentlichungen anderer Autoren, Forschungsperspektiven vorschlagen.

Räumliche Beengtheit Wir haben nachgewiesen, dass man die Volumenanteilabhängigkeit der Kurzzeitselbstdiffusion eines globulären Proteins mit Hilfe von Vorhersagen für kolloidale harte Kugeln mit sehr hoher Genauigkeit modellieren kann. Dies ist ein Indiz für den wesentlichen Einfluss der hydrodynamischen Wech-

selwirkungen im Falle hochkonzentrierter Proteinlösungen. Bei der Modellierung der Proteinform haben wir eine experimentell verifizierter Ellipsoid verwendet. Wir schlussfolgern daher, dass man allgemeine Eigenschaften der Proteindiffusion mittels existierender kolloidaler harter Kugelmodelle verstehen kann, sofern man die Anisotropie der Proteine durch geeignete Modellierung beachtet. Der Erfolg dieser einfachen Abbildung komplexer Proteine auf effektive harte Kugeln ist vielversprechend für weitere Untersuchungen. Davon ausgehend, dass globuläre Proteine gemeinsame physikalische Mobilitätseigenschaften teilen, ist es zunächst wichtig, die Anwendbarkeit des Modells effektiver harter Kugeln auf andere globuläre Proteine neben BSA zu testen. Ein nächster wichtiger Schritt ist, die intra- und extrazelluläre Umgebung realistischer zu simulieren. In diesem Kontext haben Ando and Skolnick [7] mittels Computersimulation in einer neulich veröffentlichten Publikation gezeigt, dass die Größe und Form der "crowding agents" eine wichtige Rolle bei der Diffusion spielt. Dies inspiriert, den Einfluss der Form und Größe, sowie des Volumenanteils von "crowding agents" auf das Diffusionsverhalten eines globulären Proteins systematisch zu untersuchen.

Denaturierungsübergang Wir haben die totale mittlere quadratische Bewegungsamplitude $\langle u^2 \rangle$ und die Kurzzeitselbstdiffusion eines globulären Proteins in einer hochkonzentrierten Lösung in der Nähe des Denaturierungsüberganges studiert. Unterhalb und oberhalb beobachten wir eine monotone Zunahme von $\langle u^2 \rangle$ mit steigender Temperatur. Im Denaturierungsbereich jedoch fällt $\langle u^2 \rangle$ sehr deutlich ab. Wir haben diese Beobachtung als einen Übergang von einer flüssigen Proteinlösung zu einem gel-ähnlichen Zustand, in welchem die Proteine ein quervernetztes Netzwerk bilden, interpretiert. Um diese Zustandsänderung zu quantifizieren und zu verstehen, haben wir ein neuartiges analytisches Model entwickelt. Die Kurzzeitselbstdiffusion des Proteins wird signifikant durch die Strukturänderung des Proteins und die Ausbildung von Querverbindung zwischen den Proteinen verlangsamt. Diese Verlangsamung erklärt den Abfall von $\langle u^2 \rangle$ im Denaturierungsintervall.

In einer neueren Publikation haben Stagg et al. [155] gezeigt, dass in einer Umgebung mit "räumlicher Beengtheit" eine kompakte Proteinform begünstigt wird. Experimentell haben sie gezeigt, dass dies die Denaturierungstemperatur eines globulären Proteins signifikant verändern kann. Dieser experimenteller Befund wirft die Frage auf, inwieweit die räumliche Beengtheit die mit der Proteinentfaltung verbundene Entropieänderung modifiziert. Um dies systematisch zu studieren, können wir unsere Analysis dahingehend erweitern, dass man ein Model ähnlich wie das α-Helix-zu-"random-coil"-Übergangsmodel von Zimm and Bragg: [187] einbezieht.

Salzeffekte Wir haben beobachtet, dass die Zugabe von monovalenten Salzen wie NaCl keine oder nur eine marginale Änderung der Kurzzeitselbstdiffusion eines Proteins in Lösung hervorruft. NaCl schirmt die Ladung ab und schwächt damit die Reichweite der Coulomb-Abstoßung zwischen den Proteinen. Wir schlussfolgern, dass die Kurzzeitselbstdiffusion nur sehr schwach durch Ladungsabschirmungen be-

einflusst wird. Im Gegensatz dazu haben höher geladene Ionen wie Y^{3+} einen dramatischen Effekt auf die Kurzzeitselbstdiffusion eines Proteins. Y^{3+}-Ionen können auf der Oberfläche eines negativen geladenen Proteins spezifische Bindungsstellen besetzen und damit die Ladung modifizieren. Gleichzeitig führt dies zu einer Änderung des Zusammenspieles von repulsiven und attraktiven Kräften. Erhöht man die Y^{3+}-Ionen Konzentration bis knapp unterhalb einer kritischen Konzentration c^*, dominieren zunehmend attraktive Wechselwirkung zwischen den Proteinen in Lösung. Unterhalb von c^* bilden sich kurzlebige lokale Dichteinhomogenitäten in der Proteinlösung und führen zu einer Reduktion der Kurzzeitselbstdiffusion aufgrund der Verdichtung unmittelbarer nächster Nachbarproteine. In der unmittelbaren Umgebung von c^* ist die Netto-Oberflächenladung vernachlässigbar und man beobachtet eine abrupte Bildung langlebiger sichtbarer Aggregate. Wir schlussfolgern, dass Ionen, die eine Ladungsumkehr des Proteins induzieren können, das Zusammenspiel von Attraktion und Repulsion zu Gunsten der Attraktion verschieben und damit die Bildung von lokalen Dichteinhomogenitäten in der Proteinlösung begünstigen. Diese Inhomogenitäten verlangsamen die Kurzzeitselbstdiffusion der Proteine. Dies ist ein bemerkenswerter Mechanismus von hochgeladenen Ionen um intra- und interzelluläre Transportprozesse zu kontrollieren aber auch zu stören. Es stellt sich damit die Frage, ob es andere insbesondere biologisch relevante organische Ionen gibt, die einen ähnlichen Effekt bewirken.

Chapter 2

Abstract

Proteins are molecular machines crucial for the function of living cells. Some proteins occur in the cell membrane, whilst others, in particular globular proteins, occur freely in the extra- and intracellular environment. These globular proteins carry out their biological function in an environment filled with both other molecules of a multitude of shapes and sizes and ions. Such a highly concentrated solution is termed "crowded". Macromolecular crowding plays an important role for processes involving volume-change such as thermal unfolding and those including particularly protein diffusion as a limiting or driving factor.

In the present thesis we investigate the dynamics and structural properties of a crowded aqueous solution of a model globular protein, namely *bovine serum albumin*, depending on several environmental parameters such as the protein volume fraction, the ionic strength of the solution, and the temperature including in particular the denaturing transition. The motivation is to understand proteins under biologically relevant conditions by, *inter alia* utilizing knowledge and methods established in soft matter macromolecular research.

To this end, we employ cold neutron high-resolution backscattering spectroscopy to record quasi-elastic and elastic signals. Using this technique we retrieve the short-time self-diffusion coefficient and the total mean-squared displacement of the protein in solution. Moreover, we determine the short-time self-diffusion from relaxation rates using cold neutron spin-echo spectroscopy. Complementary, we investigate the suspension structure and the shape of the proteins in solution using small-angle X-ray scattering.

We find that the short-time self-diffusion strongly decreases with increasing protein volume fraction. Furthermore, we show that the short-time self-diffusion can be accurately modeled with effective colloid hard-spheres, underlining the importance of hydrodynamic interactions under the condition of crowding. For the presence of salt ions in solution we observe two effects: The addition of a monovalent salt has little or no effect on the short-time self-diffusion. By contrast, the addition of a multivalent salt can induce a charge inversion of the protein. We observe that if the salt concentration is in the vicinity to the critical point, where the net surface charge of the protein is zero, the suspension structure contains local inhomogeneities, causing a reduction of the short-time self-diffusion. Studying the temperature behaviour below and above the denaturing, we observe that the total mean-squared displacement increases monotonically with temperature, but at the denaturing transition it decreases strongly. This observation can be rationalized and quantitatively modeled as a transition from a liquid protein solution to a gel-like state.

Chapter 3

Introduction

The interior of a cell of an organism is filled with molecules of a multitude of shapes and sizes. In this heterogeneous mixture of molecules, proteins play a prominent role by carrying out functions crucial for the living of the cell. Proteins are remarkable molecular machines engineered in a unique way from a sequence of small building blocks selected from a repertoire of 20 amino acids [114, 26]. All these amino acids have different chemical and physical properties. Some of these amino acids are hydrophilic and interact strongly with water and ions, while others are hydrophobic.

Placed in an aqueous environment a proteins will fold into a shape – the so-called native structure – that will bury the hydrophobic amino acids in the interior and expose the hydrophilic amino acids on the surface to the water [31, 26, 66]. Conversely, when the temperature is sufficiently elevated, the protein will unfold into a random coil, combined with a loss of its biological function [123, 47]. The structure of a protein is soft and, therefore, proteins show a rich spectrum of internal dynamics, ranging from stochastic fluctuations of atoms, diffusive motions of side chains to the movements of complete subdomains [20]. Considering the biological function of proteins, one can distinguish two main categories: Proteins that can be found in the cell membrane and proteins that occur freely in the extra- and intracellular environment. In this thesis we will focus on the latter category, which are frequently globular proteins performing biological functions such as the transport of small biomolecules, the transmission of messages to regulate biological processes, and the catalyzation of organic reactions. Transporting smaller molecules such as drugs or fatty acids in the blood stream, *Serum albumin* is an example of a globular protein [29]. In this context, two important questions arise: How do proteins move inside and outside of the cell and how does the presence of other molecules and ions affect this motion? Proteins exist in a world of low Reynolds numbers, in other words in an environment where the ratio of inertia to viscosity is small [133]. Therefore, both the motion and the reorientation of a protein are realized by thermal motion caused by an enormous number of collisions with the surrounding solvent molecules [133, 118]. In spite of its random nature, this so-called translational and rotational diffusion lead to net displacement of the protein's position and the orientation, depending on the elapsed time, the viscosity of the solvent, the size and shape of the molecule, the temperature and the interaction with surrounding molecules [164].

In a simplified picture, living cells operate through the motion of proteins

embedded in a crowded aqueous solution of various macromolecules and salts [49]. It can be assumed that protein function cannot be understood without taking into account the mobility of the proteins – comprising both internal dynamics as well as translational and rotational diffusion – in their charged watery matrix [11]. Therefore, in this work we aim to study both the structure and the dynamics of a solution of proteins mimicking the crowded intracellular environment by a simplified *in vitro* system controlled by several environmental parameters such as the protein volume fraction, the ionic strength of the solution, and the temperature including in particular the denaturing transition. The motivation for this work arises from the pursuit to understand proteins under biologically relevant conditions.

A unique tool to investigate the dynamics of proteins in aqueous solution is neutron spectroscopy [15]. Whilst most other spectroscopic techniques, such as dynamic light scattering, are restricted to mesoscopic length scales, neutrons probe motion as a function of length scale from interatomic to mesoscopic distances in the sample, on time scales from sub-picoseconds to approximately 200 nanoseconds. An important aspect for the study of proteins in aqueous solution is the pronounced sensitivity for hydrogen atoms. Coincidentally, hydrogen is a frequent element in proteins and nearly equally distributed in the protein volume. Complementarily, we will employ X-ray scattering to investigate the shape of the proteins in solution and study the equilibrium structure of the solution of proteins under different environmental parameters. This will allow us to characterize the nature of the interaction between the proteins.

Guided by the central motive to understand the dynamics of proteins under biologically relevant conditions we formulate three main goals for this project.
Firstly, we will study the dependence of the protein mobility on the protein volume fraction under the condition of crowding. To mimic the volume-occupied environment in the cytoplasm, we investigate volume fractions of up to 30 %. We try to answer two questions: How concentrated does a protein solution have to be for crowding to impact the protein diffusion behavior? Furthermore, we will investigate if established colloid models can be used to describe the diffusion of proteins.
Secondly, proteins operate in the cell in a narrow temperature range defining the limits of the existence of live. We will therefore study temperature-induced denaturations.
Thirdly, characteristic to the native environment of proteins is the aqueous solvent containing salt ions. We assume that ions are important for the proteins to carry out the biological function. We therefore will investigate the effect of the ionic strength and particular the valence of the salt on the dynamic and the structure of a solutions of proteins.

The present thesis is organized into the following chapters: Chapter 4 introduces the essential principles and concepts of dynamic and static scattering to

understand the experimental data. Furthermore, the theoretical aspects relevant to understand the random motion of a protein in a crowded environment are reviewed and the corresponding measurable scattering functions are developed. Chapter 5 provides the reader with the experimental methods involved in this project. The sample description and preparation is presented, followed by a review of the employed instruments. The chapter finalizes with explaining the data analysis and introducing novel conceptual frameworks developed along the project. Chapter 6 briefly discusses the key results of four papers, which are incorporated in the subsequent four publication-style chapters. Chapter 7 addresses the central question at which concentration crowding starts to influence the static and in particular also the dynamic behaviour. To this end, we investigate the diffusion of the model globular protein *Bovine Serum Albumin* (BSA) in aqueous solution as a function of the protein concentration as well as NaCl salt concentration by employing cold neutron backscattering and spin-echo. Complementary small-angle X-ray scattering data were used to study spatial correlation between the proteins. Chapter 8 studies the self-diffusion of BSA in crowded aqueous solutions on nanosecond time and nanometer length scales employing cold neutron backscattering. In this study we provide experimental evidence that the obtained diffusion can be described by effective colloid spheres. Chapter 9 investigates the dynamics of highly concentrated aqueous protein solutions of *bovine serum albumin* around the denaturing transition employing both quasi-elastic and fixed-window neutron spectroscopy. We model the transition from a liquid protein solution to gel-like state and thereby quantify the underlying physics. Chapter 10 discusses the dynamics and structure of solutions of BSA near the transition from a homogeneous to a cluster-dominated phase using small-angle X-ray scattering and neutron spin-echo spectroscopy. By analyzing the short-time self-diffusion of the protein, we introduce an observable quantifying the charge-induced inhomogeneities due to the cluster formation. The thesis closes with a summary and a conclusion in Chapter 11. Moreover we present an outlook for future work.

Chapter 4

Fundamentals

Contents

For the understanding of both dynamic and static scattering of a system consisting of proteins suspended in a solvent, we will introduce and develop the essential theoretical concepts in this chapter. Due to the major role of time-correlation

functions as the investigated quantities in this thesis, we will commence this chapter by elucidating their mathematical concept (Sec. 4.1). Since most experimental work was carried out using neutron scattering, we will subsequently describe in-depth how a neutron beam is scattered at a sample system in Sec. 4.2. Thereby, we derive measurable correlation functions that shed light on the underlying microscopic dynamical properties of the sample. In Sec. 4.3 we will briefly explain the special case of static scattering, which provides information about the equilibrium structure of the investigated matter.

The remaining sections will focus on physical concepts that are relevant to understand both the equilibrium structure of a solution of proteins and the translational as well as rotational diffusion of a protein in a crowded environment. Sec. 4.4 covers direct and hydrodynamic intermolecular interactions. While direct interactions determine the equilibrium structure, hydrodynamic interactions will play an important role for molecular crowding effects on the nanosecond time scale as we will show in paper B (see Chap. 8). In Sec. 4.5 we turn our intention to the translational diffusion of proteins. In particular, we introduce the Smoluchowski equation that describes the diffusion of proteins in a concentrated solution, thereby taking both direct and hydrodynamic interactions into account. Furthermore, we will briefly review short-time diffusion coefficients since the short-time scale is accessible by the main experimental techniques used for this thesis, neutron backscattering and spin-echo spectroscopy. Finally, in Sec. 4.6 we discuss random reorientations of a protein in solution which are essential for an analytical framework, we will introduce in Sec. 5.5.1 to separate translational and rotational diffusion to the measured apparent diffusion.

4.1 Time-Correlation Functions

In this section we will in a nutshell explain the mathematical idea of time-correlation functions, which is indispensable to comprehend the dynamic correlation functions introduced in the subsequent sections. For a more expounded description of time-correlation functions we refer to the textbook by Dhont [40]. Serving as a template for the time-correlation functions encountered throughout this thesis, we will introduce a general form of a time-correlation function. This class of functions can be conceived as measure of the dependence of two stochastic processes. We consider two N-dimensional continuous stochastic processes $\mathbf{X}(t)$ and $\mathbf{Y}(s)$ with time parameters t and s, respectively. Assuming that the stochastic processes $\mathbf{X}(t)$ and $\mathbf{Y}(s)$ have the joint probability density distribution $P(\mathbf{X}, t, \mathbf{Y}, s)$ and given two functions f and g, we define a general time-correlation function:

$$C_{f,g}(t,s) := \langle f[\mathbf{X}(t)]\ g[\mathbf{Y}(s)]\rangle = \int\int P(\mathbf{X},t,\mathbf{Y},s)\ f(\mathbf{X})\, g(\mathbf{Y})\, \mathrm{d}^N\mathbf{X}\, \mathrm{d}^N\mathbf{Y} \quad (4.1)$$

If $\mathbf{X}(t)$ and $\mathbf{Y}(s)$ are uncorrelated, tantamount to

$$P(\mathbf{X}, t, \mathbf{Y}, s) = P(\mathbf{X}, t)\, P(\mathbf{Y}, s), \tag{4.2}$$

the time-correlation function Eq. 4.1 then decomposes into the product

$$C_{f,g}\,(t, s) = \langle f\,[\mathbf{X}(t)]\rangle\ \langle g\,[\mathbf{Y}\,(s)]\rangle\,. \tag{4.3}$$

Exemplary, as we will see in Sec. 4.5 the trajectory of two molecules in solutions can be described by two continuous stochastic processes, $\mathbf{X}(t)$ and $\mathbf{Y}(s)$, due to the numerous irregular collisions with the surrounding solvent molecules. When the two molecules have a non-negligible surface charge, they interact and at each time step their succeeding positions depend on the position history of the other molecule. This can be considered as a memory effect. Therefore, their trajectories are correlated. Only if $t \gg s$, $\mathbf{X}(t)$ and $\mathbf{Y}(s)$ are nearly uncorrelated, because due to the random kicks the memory of past events is gradually erased.

4.1.1 Classical System

We consider an N-dimensional stochastic process $\mathbf{X}(t)$, representative for the configuration vector of a classical system, the corresponding probability density of P is governed by the equation

$$\partial_t P(\mathbf{X}, t) = \hat{\mathcal{O}}\, P(\mathbf{X}, t), \tag{4.4}$$

therein, $\hat{\mathcal{O}}$ is an arbitrary operator acting on P. In order to facilitate the readability, we colorize the operator and the operand on which the operation is performed in blue. To calculate the Green's function of Eq. 4.4, P has to fulfill the initial condition

$$P(\mathbf{X}, s) = \delta(\mathbf{X} - \mathbf{Y}). \tag{4.5}$$

Using the operator exponential the Green's function of Eq. 4.4 is

$$P(\mathbf{X}, t \mid \mathbf{Y}, s) = \exp\left[(t - s)\,\hat{\mathcal{O}}\right]\ \delta(\mathbf{X} - \mathbf{Y}). \tag{4.6}$$

Given that the distribution of initial states is given by $P(\mathbf{Y})$, the joint distribution can be expressed as

$$P(\mathbf{X}, t, \mathbf{Y}, s) = P(\mathbf{X}, t \mid \mathbf{Y}, s)\, P(\mathbf{Y}). \tag{4.7}$$

With this the time-correlation function Eq. 4.1 reads:

$$C_{f,g}(t, s) = \int\int P(\mathbf{X}, t \mid \mathbf{Y}, s)\, P(\mathbf{Y})\, f(\mathbf{X})\, g(\mathbf{Y})\, \mathrm{d}^N\mathbf{X}\, \mathrm{d}^N\mathbf{Y}. \tag{4.8}$$

By integrating over $\mathbf{Y}$ the time-correlation function simplifies to

$$C_{f,g}(t, s) = \int f(\mathbf{X})\, \exp\left[(t - s)\,\hat{\mathcal{O}}\right]\ \{g(\mathbf{X})\, P\,(\mathbf{X})\}\ \mathrm{d}^N\mathbf{X}. \tag{4.9}$$

In general it is a cumbersome task to calculate time-correlation functions since each term of the operator exponential must be evaluated. However, if $t \approx s$ short-time expansions can be calculated considering only the first two terms of the operator exponential.

4.1.2 Quantum Mechanical System

The mathematical formulation of the time-correlation function in the framework of quantum mechanics is less intuitive. We will formulate a general time-correlation function, which differs from Eq. 4.4 due to the use of time-dependent operators in the Heisenberg picture [34]. To characterize the canonical ensemble of a general N-particle quantum mechanical system, firstly, we have to solve the eigenproblem

$$\hat{H} \; |n\rangle = E_n \; |n\rangle \,, \tag{4.10}$$

thereby obtaining the eigenvectors $|n\rangle$ and the associated energy eigenvalues E_n to the system Hamiltonian $\hat{H}$. Secondly, we have to calculate the statistical weight in the canonical ensemble with temperature

$$\begin{aligned} P_n &= \frac{1}{Z} \exp\left(-\beta \, E_n\right), \\ Z &= \sum_n \exp\left(-\beta \, E_n\right) \end{aligned} \tag{4.11}$$

therein, $\beta = k_B \, T$ with k_B being the Boltzmann constant and T the temperature. With this a general quantum mechanical time-correlation function is

$$C_{f,g}\left(t, s\right) := \left\langle f\left[\hat{\mathbf{X}}(t)\right] \; g\left[\hat{\mathbf{X}}(s)\right] \right\rangle = \sum_n P_n \left\langle n \left| \, f\left[\hat{\mathbf{X}}(t)\right] \; g\left[\hat{\mathbf{X}}(s)\right] \right| n \right\rangle \tag{4.12}$$

therein, $\mathbf{X}(t)$ is the $3N$-dimensional time-dependent operator corresponding to the configurational vector of the system. The following product gives the time-dependence of the operator

$$\hat{\mathbf{X}}(t) = \hat{T}(t) \cdot \hat{\mathbf{X}} \cdot \hat{T}(t)^{\dagger}, \tag{4.13}$$

in which, $\hat{T}(t) = \exp(\mathrm{i} \, t \, \hat{H}/\hbar)$ and $\hat{T}(t)^{\dagger} = \exp(-\mathrm{i} \, t \, \hat{H}/\hbar)$ are the time-evolution operator and its adjoint operator, respectively.

4.2 Dynamic Neutron Scattering

4.2.1 Neutron Radiation

When the neutron was discovered in 1932 by the physicist Sir James Chadwick [30], who was awarded the Nobel Prize only three years later, nobody could anticipate the technologic advance this discovery would bring to the investigation of the dynamics and structure of condensed matter only a few decades later. Even though first

experiments using radium-beryllium sources could demonstrate the scattering ability of neutrons the intensity was too weak as to allow any practical experiments. With the development of reactor sources delivering sufficiently high fluxes the field of neutron scattering commenced to flourish [177]. Today, a modern research reactor such as the high-flux reactor of the *Institut Laue-Langevin* can provide a continuous neutron flux of $1.5{\cdot}10^{15}$ neutrons per second per cm^2 with a thermal power of 53 MW. Using moderators neutrons with kinetic energies ranging from 10^{-7} to 10^{-1}eV can be generated. Depending on the temperature T of the moderator, the flux velocity density distribution $\phi(v)$ of those moderated neutrons is sufficiently well described by a Maxwellian function

$$\phi(v) \propto v^3 \exp\left(-\frac{m\,v^2}{2\,k_B\,T}\right) \tag{4.14}$$

with k_B being the Boltzmann constant and m the mass of the neutron. Among those, the so-called thermal neutrons are the most suitable to investigate condensed matter because their kinetic energy $E = m\,v^2/2$ is comparable to the energy of the quantum states of condensed matter (several milli-electron volts).

Therefore, the energy exchange between thermal neutrons and matter by excitation and annihilation of quantum states is detectable. Neutrons, consisting of one up- and two down-quarks, hence, carrying a neutral charge, are insensitive to the presence of charges in matter. Consequently, when penetrating into matter their trajectory is not perturbed until they are scattered in the vicinity of the nucleus caused by a short-range interaction. Due to their magnetic dipole moment neutrons interact with unpaired electrons in the atom. Moreover, a free neutron has an average lifetime of 885.6 s before it decays into a proton, an electron and an antineutrino (compare Table 4.1).

The above properties render them the perfect scattering probe particle for a non-invasive and non-destructive investigation of structural, dynamical and magnetic properties. In the next section we will show how in a neutron scattering experiment, dynamical and structural information can be extracted from the spatial and energetic distribution of the scattered neutron beam. To this end, we will shortly summarize how neutrons are treated within the framework of quantum mechanics. Neutrons are imagined to be contained in a large box with volume V whose wavefunction is described by the free particle Hamiltonian

$$\hat{H}_0 = \frac{\hat{P}}{2\,m}, \tag{4.15}$$

therein $\hat{P}$ is the momentum operator. Note, in the following we will use the Bra-ket notation introduced by Dirac [41]. Solving the corresponding eigenproblem of the Hamiltonian Eq. 4.15 using periodic boundary conditions yields the wavefunction $|\mathbf{k}\rangle$. Moreover, we have to consider that neutrons are spin-1/2 particles. Consequently, we obtain the full quantum mechanical state of the neutron by a direct

Properties of the Neutron	
mass (m)	$1.674927 \cdot 10^{-27}\,\mathrm{kg}$
spin-parity (J^π)	$1/2^+$
electric charge (q)	0
spin (s)	1/2
magnetic dipole moment	$-1.9130427\,\mu_N$
$n \to p^+ + e^- + \bar{\nu}_e$	$\approx 100\%$
mean lifetime	885.6 s
half-life	613.9 s

Table 4.1: Basic properties of the neutron [180, 84]. Note, the unit of the magnetic dipole moment is the nuclear magneton defined by $\mu_N = e\,\hbar/(2\,m_p)$, in which e is the elementary charge, $\hbar$ the reduced Planck constant and m_p the proton mass.

product of two kets:

$$|\mathbf{k}, s, s_z\rangle = |\mathbf{k}\rangle\ |s, s_z\rangle \tag{4.16}$$

therein, the first ket has the spatial wavefunction

$$\psi_{\mathbf{k}}(\mathbf{x}) := \langle \mathbf{x} \mid \mathbf{k}\rangle = \frac{1}{\sqrt{V}}\,\exp\left(\mathrm{i}\,\mathbf{k}\,\mathbf{x}\right), \tag{4.17}$$

and is characterized by the discrete wavevector

$$\mathbf{k} \in \frac{2\,\pi}{L}\,\mathbb{Z}^3. \tag{4.18}$$

The second ket $|s, s_z\rangle$ characterizes the spin orientation, in which $s = 1/2$ is the angular momentum quantum and s_z is the magnetic quantum number, which only have the values $\pm 1/2$. The eigenvalues corresponding to $|\mathbf{k}, s, s_z\rangle$ are given by the energy dispersion relation

$$E_{\mathbf{k}} = \frac{\hbar^2\,\mathbf{k}^2}{2\,m}. \tag{4.19}$$

4.2.2 Dynamic Scattering

Emanating from a simple classical and intuitive picture of dynamic scattering, we will derive a measurable quantity, namely the partial differential cross-section, which is related to the probe-specific intermediate scattering function – a correlation function reflecting the average dynamics of the atoms of the probe. A more comprehensive analysis can be found e.g. in the textbooks by Squires [151] and Lovesey [101].

4.2.2.1 Partial Differential Cross-Section

Fig. 4.1 illustrates the principle of dynamic neutron scattering. A neutron characterized by its wavevector $\mathbf{k}$ (left red arrow) impinges on a sample of matter (yellow cuboid in the middle). When interacting with the nuclei it excites or annihilates energy states. As a result the neutron is scattered at an angle $2\,\theta$. Thereby, it changes its wavevector from $\mathbf{k}$ to $\mathbf{k}'$ and therefore experiences both a momentum and an energy transfer, $\mathbf{q} = \mathbf{k} - \mathbf{k}'$ (purple vector) and $\hbar\,\omega = \hbar^2\,\left(\mathbf{k}^2 - \mathbf{k}'^2\right)/(2\,m)$, respectively. The semitransparent yellow spherical shell denotes the position of all neutron wavevectors with the same energy $E' = \hbar^2\,\mathbf{k}'^2/(2\,m)$. In an experiment one measures the partial differential cross-section $\partial^2\sigma/(\partial\mathbf{\Omega}\,\partial E')$, which counts the number of neutrons per second that scatter into the solid angle $d\mathbf{\Omega}$ with final energy between E' and $E' + dE'$ (corresponding to the small green cuboidal element the green arrow is pointing to) divided by the flux Φ of incident neutrons.

In the following we will in detail explain the scattering process. The basic idea is to describe the scattering event with time-dependent perturbation theory and to use Fermi's golden rule to derive the partial differential cross-section. When a neutron interacts with matter the interaction Hamiltonian is

$$\hat{H}' = \hat{H} + \hat{H}_0 + \hat{V}. \tag{4.20}$$

Therein, $\hat{H}_0$ is the free particle Hamiltonian of the neutron Eq. 4.15 and $\hat{H}$ is the matter Hamiltonian. The interaction between the bound nuclei of the matter and the neutron, denoted by $\hat{V}$, causes a perturbation. $\hat{V}$ is approximated by a sum of Fermi pseudo-potentials, reading

$$\hat{V} = \sum_{j=1}^{N} \frac{2\,\pi\,\hbar^2}{m}\,\hat{b}_j\,\delta\left(\mathbf{x} - \mathbf{R}_j\right), \tag{4.21}$$

in which $\mathbf{R}_j$ is the position of the j^{th} bound nucleus, and $\mathbf{x}$ the position of the neutron. The scattering length operator $\hat{b}_j$ [148], depending on both the neutron and the nucleus spin, denoted by their corresponding quantum mechanical operators $\hat{\mathbf{s}}$ and $\hat{\mathbf{I}}_j$, respectively, reads:

$$\hat{b}_j = b_{\text{coh}}^{(j)} + \frac{2\,b_{\text{inc}}^{(j)}}{\sqrt{I_j\;(I_j+1)}}\,\hat{\mathbf{s}}\cdot\hat{\mathbf{I}}_j, \tag{4.22}$$

therein, $b_{\text{coh}}^{(j)}$ is the bound coherent and $b_{\text{inc}}^{(j)}$ the bound incoherent scattering length of the j^{th} nucleus with spin I_j. Denoting the spin states of the neutron and the nuclei by a single quantum number σ, the complete state of the neutron and the matter is described by the ket

$$|\mathbf{k},\lambda,\sigma\rangle = |\mathbf{k}\rangle\;|\lambda\rangle\;|\sigma\rangle\,. \tag{4.23}$$

Therein, $\mathbf{k}$ is the wavevector of the neutron and λ labels the quantum states of

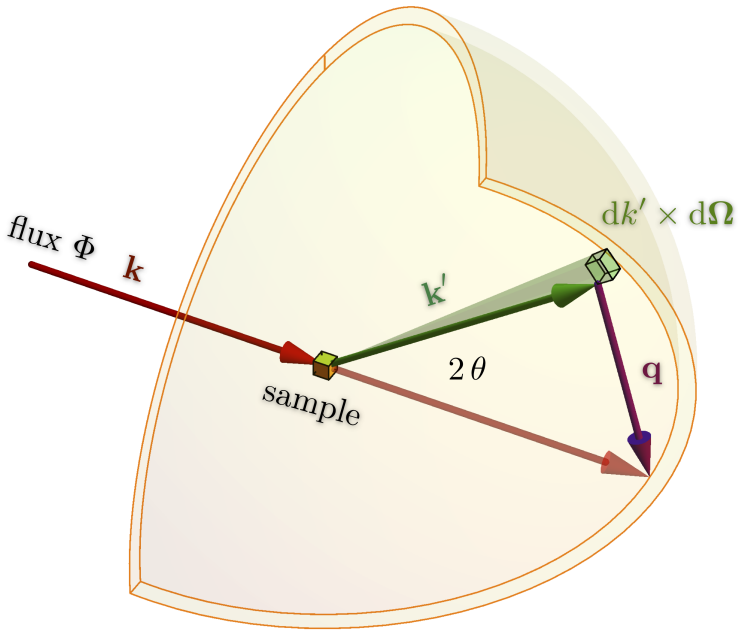

Figure 4.1: Principle of dynamic neutron scattering. A neutron characterized by its wavevector $\mathbf{k}$ (left red arrow) impinges on a sample (yellow cuboid in the middle) and, hence, excites or annihilates energy states of the sample. As a result the neutron is scattered at an angle $2\,\theta$ and alters its wavevector to $\mathbf{k}'$ (green arrow). Thereby, it experiences both a momentum and an energy transfer, which is $\mathbf{q} = \mathbf{k} - \mathbf{k}'$ (purple vector) and $\hbar\,\omega = \hbar^2 \left(\mathbf{k}^2 - \mathbf{k}'^2\right)/(2\,m)$, respectively. The semitransparent yellow spherical shell denotes the position of all neutron wavevectors with the same energy $E' = \hbar^2\,\mathbf{k}'^2/(2\,m)$. In a scattering experiment the measured quantity is the partial differential cross-section $\partial^2\sigma/(\partial\mathbf{\Omega}\,\partial E')(\mathbf{q},\omega)$, which is the number of neutrons per second that scatter into the small solid angle $d\mathbf{\Omega}$ with final energy between E' and $E' + dE'$ (corresponding to the small green cuboidal element where the green arrow points to) divided by the flux Φ of incident neutrons.

the matter corresponding to the energy eigenvalue E_λ. When interacting with the nuclei of the matter, the wavefunction of the neutron changes its initial propagation direction from $\mathbf{k}$ to $\mathbf{k}'$. Thereby, the neutron experiences the momentum transfer,

$$\mathbf{q} = \mathbf{k} - \mathbf{k}' \tag{4.24}$$

and the energy change

$$\hbar\,\omega = E - E' = \frac{\hbar^2}{2\,m}\left(\mathbf{k}^2 - \mathbf{k}'^2\right). \tag{4.25}$$

Responding to this energy change, the matter alters its quantum state from $|\lambda\rangle$ to $|\lambda'\rangle$. Energy conservation requires that $E_{\lambda'} - E_\lambda = \hbar\,\omega$. We will briefly outline how to obtain the partial differential cross-section. Using Fermi's golden rule one can show [101] that the partial differential cross-section of those neutrons causing a transition from the quantum state labeled by (λ, σ) to (λ', σ') is

$$\left(\frac{\partial^2\sigma}{\partial\Omega\partial E'}\right)_{(\lambda,\sigma)}^{(\lambda',\sigma')} = \frac{k'}{k}\left(\frac{m}{2\,\pi\,\hbar^2}\right)\left|\left\langle \mathbf{k}', \lambda', \sigma' \middle| \hat{V} \middle| \mathbf{k}, \lambda, \sigma \right\rangle\right|^2 \delta\left(\hbar\,\omega + E_\lambda - E'_\lambda\right), \tag{4.26}$$

in which the Dirac-delta function $\delta\left(\hbar\,\omega + E_\lambda - E'_\lambda\right)$ enforces energy conservation. In a real experiment, however, we have neither information about the initial quantum state (λ, σ) of the matter nor are we able to determine its final quantum state (λ', σ'), which renders Eq. 4.26 not measurable. The knowledge about macroscopic quantities such as the temperature gives us knowledge about the statistical weight $P_{(\lambda,\sigma)} = P_\lambda\,P_\sigma$ of the state (λ, σ). When matter contained in a sample holder is illuminated by a neutron beam we can assume to observe a canonical ensemble since the illuminated volume is comparable to the dimensions of the holder. By averaging over all initial and summation over all final states we obtain

$$\frac{\partial^2\sigma}{\partial\mathbf{\Omega}\,\partial E'} = \sum_{\lambda,\lambda'}\sum_{\sigma,\sigma'} P_\lambda\,P_\sigma\,\left(\frac{\partial^2\sigma}{\partial\Omega\partial E'}\right)_{\lambda\to\lambda'}, \tag{4.27}$$

and with Eq.4.21 we finally arrive at

$$\frac{\partial^2\sigma}{\partial\mathbf{\Omega}\,\partial E'} = \frac{k'}{k}\,\frac{N}{2\,\pi\,\hbar}\int_{-\infty}^{\infty}\tilde{I}(\mathbf{q}, t)\exp(-\mathrm{i}\,\omega\,t)\,\mathrm{d}t \tag{4.28}$$

in which

$$\tilde{I}(\mathbf{q}, t) = \frac{1}{N}\sum_{i,j}\left\langle \hat{b}_i^\dagger\,\hat{b}_j\,\exp\left[-\mathrm{i}\,\mathbf{q}\,\hat{\mathbf{R}}_j(0)\right]\,\exp\left[\mathrm{i}\,\mathbf{q}\,\hat{\mathbf{R}}_i(t)\right]\right\rangle \tag{4.29}$$

is the intermediate scattering function. It is important to note that $\hat{\mathbf{R}}_j(t)$ is the time-dependent quantum mechanical position operator calculated as follows:

$$\hat{\mathbf{R}}_j(t) = \hat{T}(t)\,\hat{\mathbf{R}}_j\,\hat{T}(t)^\dagger, \tag{4.30}$$

Neutron scattering cross-sections

Element	σ_{coh}	σ_{inc}	σ_{scatt}	σ_{abs}
C	5.551	0.001	5.551	0.0035
H	1.7583	80.27	82.03	0.3326
D	5.592	2.05	7.64	0.000519
O	4.232	0.0008	4.232	0.00019
N	11.01	0.5	11.51	1.9
S	1.0186	0.007	1.026	0.53
Al	1.495	0.0082	1.503	0.231
V	0.0184	5.08	5.1	5.08

Table 4.2: Neutron scattering cross-sections of elements [1] frequently encountered in organic matter in units of barn= 10^{-24} cm^2. Aluminum is presented due to its important role as material for sample holders. Note, that the absorption cross-section σ_{abs} holds only for thermal neutrons with velocity 2200 m/s.

with $\hat{T}(t) = \exp(\mathrm{i}\, t\, \hat{H}/\hbar)$ being the time-evolution operator of the matter hamiltonian $\hat{H}$. In the subsequent section we will describe how to decompose Eq. 4.29 into a coherent and incoherent scattering contribution.

4.2.2.2 Coherent and Incoherent Scattering

The angular brackets in Eq. 4.29 denote the statistical average over all energy eigenvalues of the matter as well as the neutron and nuclear spins. In most types of material we can expect that the nuclear spins are randomly distributed and therefore are uncorrelated. However, when a neutron is scattered at a nucleus the coupling between the neutron and the nuclear spin becomes crucial, as revealed by the spin-dependent scattering length operator Eq. 4.22. As a result, we can decompose the intermediate scattering Eq. 4.29, in a similar manner as the operator 4.22, into an incoherent and coherent contribution:

$$\tilde{I}(\mathbf{q}, t) = \tilde{I}_{\text{inc}}(\mathbf{q}, t) + \tilde{I}_{\text{coh}}(\mathbf{q}, t) \tag{4.31}$$

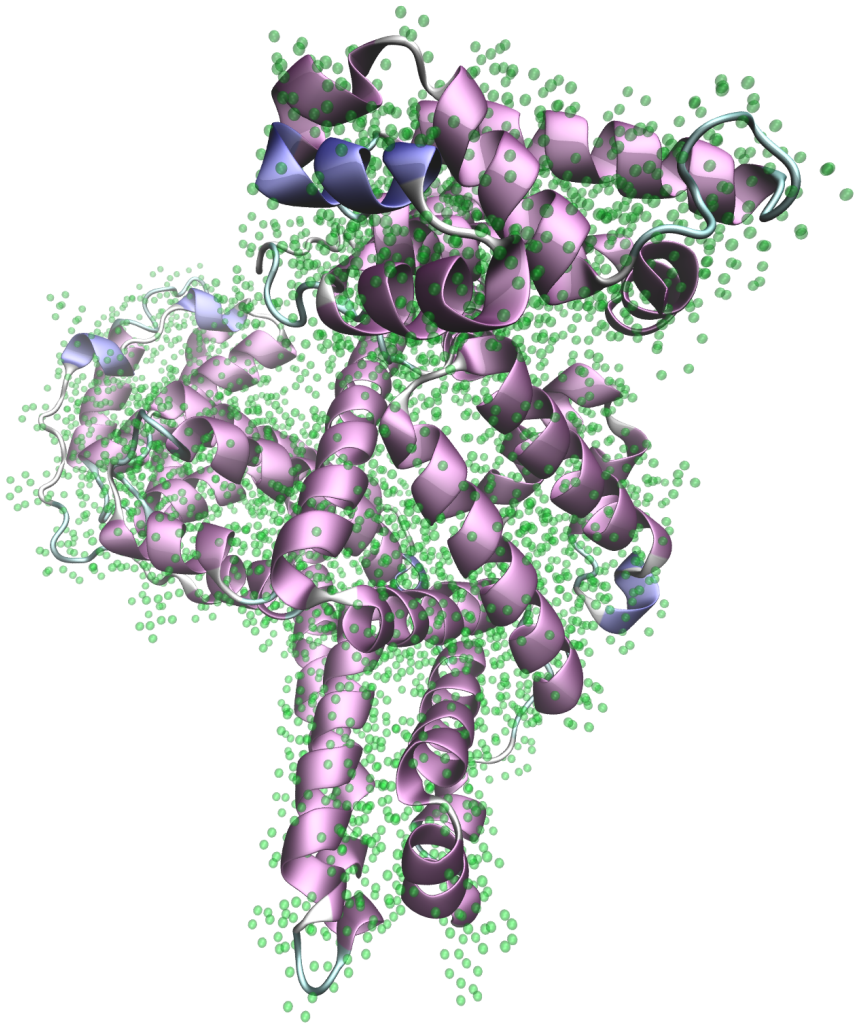

Figure 4.2: Distribution of hydrogen atoms (green semi-transparent spheres) in the homology model of *bovine serum albumin* [175] (cartoon plot of its secondary structure). Like most proteins *bovine serum albumin* has a high fraction of hydrogen atoms, which can be assumed to be equally distributed within the molecular volume. The illustration was rendered with VMD [77].

with the incoherent and coherent intermediate scattering function

$$\tilde{I}_{\mathrm{inc}}(\mathbf{q},t) = \frac{1}{N}\sum_{j=1}^{N}\frac{\sigma_{j,\mathrm{inc}}}{4\pi}\left\langle \exp\left[-\mathrm{i}\,\mathbf{q}\,\hat{\mathbf{R}}_j(0)\right]\exp\left[\mathrm{i}\,\mathbf{q}\,\hat{\mathbf{R}}_j(t)\right]\right\rangle \tag{4.32}$$

$$\tilde{I}_{\mathrm{coh}}(\mathbf{q},t) = \frac{1}{N}\sum_{i,j=1}^{N}\frac{\sqrt{\sigma_{i,\mathrm{coh}}\,\sigma_{j,\mathrm{coh}}}}{4\,\pi}\left\langle \exp\left[-\mathrm{i}\,\mathbf{q}\,\hat{\mathbf{R}}_i(0)\right]\exp\left[\mathrm{i}\,\mathbf{q}\,\hat{\mathbf{R}}_j(t)\right]\right\rangle . \tag{4.33}$$

Evidently, the incoherent part depends only on the correlation of the positions of the *same* nucleus at different times. By contrast the coherent counterpart depends on the spatial correlation of *different* nuclei at different times. Consequently, aside from dynamical effects, the coherent scattering additionally sheds light on structural information. In comparison, the incoherent part predominantly reveals the average dynamics of the nuclei. The strength of the contribution to the coherent and incoherent intermediate scattering function of a single nucleus is given by its incoherent and coherent cross-section, respectively:

$$\begin{aligned}\frac{\sigma_{\mathrm{inc}}}{4\,\pi} &= \left\langle \hat{b}^\dagger\,\hat{b}\right\rangle - \left\langle \hat{b}\right\rangle^\dagger\left\langle \hat{b}\right\rangle = b_{\mathrm{inc}}^2 \\ \frac{\sigma_{\mathrm{coh}}}{4\,\pi} &= \left\langle \hat{b}\right\rangle^\dagger\left\langle \hat{b}\right\rangle = b_{\mathrm{coh}}^2 .\end{aligned} \tag{4.34}$$

Note that for better readability we skipped the index j. Moreover, if there are several isotopes denoted by the index ξ with relative abundance c_ξ in the scattering system, we have to replace $\left\langle \hat{b}\right\rangle$ and $\left\langle \hat{b}^\dagger\,\hat{b}\right\rangle$ in the above expressions by

$$\left\langle \hat{b}\right\rangle = \sum_\xi c_\xi\left\langle \hat{b}_\xi\right\rangle \tag{4.35}$$

$$\left\langle \hat{b}^\dagger\,\hat{b}\right\rangle = \sum_\xi c_\xi\left\langle \hat{b}_\xi^\dagger\,\hat{b}_\xi\right\rangle . \tag{4.36}$$

One can conceive coherent scattering as the scattering of the same system if all scattering lengths were identical. Incoherent scattering occurs due to both isotopes and the fluctuation of scattering lengths caused by the degeneracy of neutron and nuclear spin eigenstates. Table 4.2 shows the coherent and incoherent scattering cross-section for elements frequently encountered in organic molecules. The most prominent member is hydrogen with a large incoherent cross-section exceeding all other elements. Consequently, it is reasonable to partition the sum in Eq. 4.32 into contributions from the same element

$$\tilde{I}_{\mathrm{inc}}(\mathbf{q},t) = \sum_{\alpha=1}^{n} f_\alpha\,\frac{\sigma_{\alpha,\mathrm{inc}}}{4\pi}\,\frac{1}{N_\alpha}\sum_{j_\alpha=1}^{N_\alpha}\left\langle \exp\left[-\mathrm{i}\,\mathbf{q}\,\hat{\mathbf{R}}_{j_\alpha}(0)\right]\exp\left[\mathrm{i}\,\mathbf{q}\,\hat{\mathbf{R}}_{j_\alpha}(t)\right]\right\rangle \tag{4.37}$$

therein $f_\alpha = N_\alpha/N$ is the fraction of the element of kind α. Proteins have a high fraction of hydrogen atoms and it can be assumed that they are equally distributed

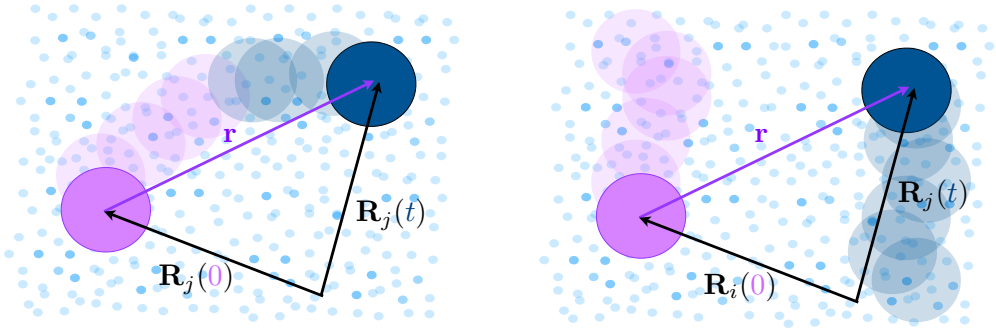

Figure 4.3: Physical interpretation of the classical van-Hove correlation functions. The purple and blue colors correspond to time $t = 0$ and $t > 0$, respectively. The left-hand image shows the *same* particle (the j^{th} particle) at time $t = 0$ and time $t > 0$, at position $\mathbf{R}_j(0)$ and $\mathbf{R}_j(t)$, respectively. Snap shoots of its trajectory are indicated by transparent circles. The summand of the time-dependent self-correlation function in Eq. 4.42 corresponds to the probability that the j^{th} particle has traveled a distance $\mathbf{r}$ within the time t. The right-hand image shows the trajectories of *different* particles. Particle i is at position $\mathbf{R}_i(0)$ at time $t = 0$. At time $t > 0$ particle j is at $\mathbf{R}_j(t)$. The summand of the time-dependent pair-correlation function in Eq. 4.41 corresponds to the probability that the i^{th} particle (purple circle) is at any position, which is separated by the vector $\mathbf{r}$ from the position at which at time $t > 0$ the j^{th} particle (blue circle) can be found.

within the molecular volume as it is illustrated for the homology model of *bovine serum albumin* [175] in Fig. 4.2. Therefore, we can approximate the incoherent intermediate scattering function of a protein by the part stemming from the hydrogen atoms:

$$\tilde{I}_{\text{inc}}(\mathbf{q}, t) \approx f_H \, \frac{\sigma_{H,\text{inc}}}{4\pi} \, \frac{1}{N} \sum_{j=1}^{N} \left\langle \exp\left[-\mathrm{i}\,\mathbf{q}\,\hat{\mathbf{R}}_j(0)\right] \, \exp\left[\mathrm{i}\,\mathbf{q}\,\hat{\mathbf{R}}_j(t)\right] \right\rangle \tag{4.38}$$

in which the Heisenberg operators $\hat{\mathbf{R}}_j(0)$ and $\hat{\mathbf{R}}_j(t)$ correspond to the position of the jth hydrogen atom at time 0 and t, respectively.

4.2.3 Dynamic Correlation Functions

In his seminal paper van Hove [166] introduced an elegant formalism that relates the measured cross-section of a neutron scattering experiment with two time-space correlation functions of the scattering system, which are the time-dependent pair-correlation function,

$$\mathcal{G}(\mathbf{r}, t) = \frac{1}{N} \sum_{i,j=1}^{N} \int \left\langle \delta\left(\mathbf{r}' - \hat{\mathbf{R}}_i(0)\right) \, \delta\left(\mathbf{r}' + \mathbf{r} - \hat{\mathbf{R}}_j(t)\right) \right\rangle \mathrm{d}^3\mathbf{r}' \tag{4.39}$$

and the time-dependent self-correlation function

$$\mathcal{G}_s(\mathbf{r},t) = \frac{1}{N}\sum_{j=1}^{N}\int \left\langle \delta\left(\mathbf{r}' - \hat{\mathbf{R}}_j(0)\right)\, \delta\left(\mathbf{r}' + \mathbf{r} - \hat{\mathbf{R}}_j(t)\right)\right\rangle \mathrm{d}^3\mathbf{r}', \tag{4.40}$$

therein, the angular brackets denote the ensemble average and $\hat{\mathbf{R}}_j(t)$ is the time-dependent Heisenberg operator of the position of the j particle at time t (see Sec. 4.1). The calculations are quite general and refer to any system, gas, solid or fluid. For most systems, the quantum mechanical calculations are not feasible, and therefore $\mathcal{G}$ and $\mathcal{G}_s$ are frequently approximated from their classical forms,

$$\mathcal{G}^{\mathrm{cl}}(\mathbf{r},t) = \frac{1}{N}\sum_{i,j=1}^{N}\left\langle \delta\left(\mathbf{r} - \mathbf{R}_j(t) + \mathbf{R}_i(0)\right)\right\rangle, \tag{4.41}$$

$$\mathcal{G}_s^{\mathrm{cl}}(\mathbf{r},t) = \frac{1}{N}\sum_{j=1}^{N}\left\langle \delta\left(\mathbf{r} - \mathbf{R}_j(t) + \mathbf{R}_j(0)\right)\right\rangle. \tag{4.42}$$

Fig. 4.3 illustrates the physical interpretation of the classical van-Hove correlation functions Eqs. 4.41 and 4.42 exemplified by a system of particles in solution. For clarity only two particles are shown. The left-hand image displays the *same* particle (the j^{th} particle) at time $t = 0$ and at time $t > 0$. Both positions are separated by a vector $\mathbf{r}$ due to the motion of the particles. The summand of the time-dependent self-correlation function in Eq. 4.42 corresponds to the probability that the j^{th} particle has traveled a distance $\mathbf{r}$ within the time t. *Conversely*, the right-hand image shows an almost identical situation as the left-hand figure but for *different* particles (the i^{th} and the j^{th} particle). The summand of the time-dependent pair-correlation function in Eq. 4.41 corresponds to the probability that the i^{th} particle is at any position at time $t = 0$, which is separated by the vector $\mathbf{r}$ from the position at which at time $t > 0$ the j^{th} particle is found. Linked to the van Hove correlation function by a spatial Fourier transform are the coherent and incoherent intermediate scattering functions

$$\mathcal{I}_{\mathrm{coh}}(\mathbf{q},t) = \int \mathcal{G}(\mathbf{r},t)\, \exp\left(\mathrm{i}\,\mathbf{q}\,\mathbf{r}\right)\, \mathrm{d}^3\mathbf{r} \tag{4.43}$$

$$\mathcal{I}_{\mathrm{inc}}(\mathbf{q},t) = \int \mathcal{G}_s(\mathbf{r},t)\, \exp\left(\mathrm{i}\,\mathbf{q}\,\mathbf{r}\right)\, \mathrm{d}^3\mathbf{r}. \tag{4.44}$$

Note, for reasons of readability the index α will refers to both 'inc' or 'coh' in the following part of this section. Applying another Fourier transform in the time domain, the coherent and incoherent scattering function

$$\mathcal{S}_\alpha(\mathbf{q},\omega) = \frac{1}{2\,\pi}\int \mathcal{I}_\alpha(\mathbf{q},t)\, e^{-\mathrm{i}\,\omega\,t}\, \mathrm{d}t \tag{4.45}$$

Properties of correlation functions

$\int \mathcal{G}_s(\mathbf{r},t)\,\mathrm{d}^3\mathbf{r} = 1$	$\int \mathcal{G}(\mathbf{r},t)\,\mathrm{d}^3\mathbf{r} = N$
$\mathcal{G}_s(\mathbf{r},0) = \delta(\mathbf{r})$	$G(\mathbf{r},0) = \delta(\mathbf{r}) + g(\mathbf{r})$
$\int \mathcal{S}_{\mathrm{inc}}(\mathbf{q},\omega)\,d\omega = 1$	$\int S_{\mathrm{coh}}(\mathbf{q},\omega)\,\mathrm{d}\omega = S(\mathbf{q})$

$$\mathcal{S}_\alpha(\mathbf{q},\omega) = \tfrac{1}{2\pi}\int \mathcal{I}_\alpha(\mathbf{q},t)\,e^{-\mathrm{i}\,\omega\,t}\,\mathrm{d}t$$

$$\mathcal{S}_\alpha(\mathbf{q},\omega) = \exp(\hbar\,\omega\,\beta)\;\mathcal{S}_\alpha(-\mathbf{q},-\omega)$$

Table 4.3: Important properties of correlation functions. Note, that $g(\mathbf{r})$ is the pair correlation function. Note, that $S(\mathbf{q})$ is the structure factor Eq. 4.60, which we will describe in the next section of static scattering. For reasons of readability the index α will refers to both 'inc' or 'coh'.

is obtained. Finally, for a system consisting of identical nuclei, the functions S_{coh} and $\mathcal{S}_{\mathrm{inc}}$ are closely related to the coherent and incoherent cross-section by

$$\frac{\partial^2\sigma}{\partial\mathbf{\Omega}\,\partial E'} = \left(\frac{\partial^2\sigma}{\partial\mathbf{\Omega}\,\partial E'}\right)_{\mathrm{inc}} + \left(\frac{\partial^2\sigma}{\partial\mathbf{\Omega}\,\partial E'}\right)_{\mathrm{coh}} \tag{4.46}$$

with

$$\left(\frac{\partial^2\sigma}{\partial\mathbf{\Omega}\,\partial E'}\right)_{\alpha} = \frac{k'}{k}\,\frac{N\,\sigma_\alpha}{4\,\pi\,\hbar}\,\mathcal{S}_\alpha(\mathbf{q},\omega). \tag{4.47}$$

Table 4.3 summarizes the key properties of the correlation function mentioned in this section. Among these the most astonishing relation is $S(\mathbf{q},\omega)_\alpha = \exp(\hbar\,\omega\,\beta)\;\mathcal{S}_\alpha(-\mathbf{q},-\omega)$, also known as the principle of detailed balance. It is a purely quantum mechanical effect that is crucial for very low temperature. In essence it states an asymmetry of energy gain and loss of the neutrons caused by the Boltzmann factor of the energy states of the scattering system [151].

4.2.4 Incoherent Scattering Function of a Molecule

In this section we will elucidate how the incoherent scattering function $\mathcal{I}_{\mathrm{inc}}(q,t)$ Eq. 4.44 of a macromolecule such as a protein can be separated into a product of contributions from different molecular dynamical modes, encompassing atomic vibrations, internal diffusive modes and global translational as well as rotational diffusion. Such a decomposition of $\mathcal{I}_{\mathrm{inc}}(q,t)$ is achievable for samples with hierarchically ordered dynamics, or in other words for samples with dynamical modes

separable on the time scale.

Within a molecule the time-dependence of the position vector of a nucleus $\mathbf{R}(t)$ stems from a multitude of different molecular dynamical modes. The position vector of the scattering nucleus can be decomposed into its equilibrium position and a displacement due to atomic vibrations:

$$\mathbf{R}(t) = \mathbf{r}(t) + \mathbf{u}(t). \tag{4.48}$$

The equilibrium position is time-dependent caused by the motion of the entire molecule. In a solution the molecule has additionally a translational and rotational component, that we will describe later in more detail. This allows to separate $\mathbf{R}$ further into

$$\mathbf{R}(t) = \mathbf{r}_T(t) + \mathbf{r}_R(t) + \mathbf{u}(t) \tag{4.49}$$

in which $\mathbf{r}_T(t)$ and $\mathbf{r}_R(t)$ are the rotational and translational component, respectively. Geometrically, one can conceptualize the motion of the position of a single nucleus as a point moving in a sphere shell – whose thickness is determined by the vibrational mean-squared displacement – with a center translating in all space. Calculating the intermediate scattering function (Eqs. 4.40 and 4.44)

$$\mathcal{I}_{\text{inc}}(\mathbf{q}, t) = \frac{1}{N} \sum_{j=1}^{N} \left\langle \exp\left[-\mathrm{i}\,\mathbf{q}\,\hat{\mathbf{R}}_j(0)\right] \exp\left[\mathrm{i}\,\mathbf{q}\,\hat{\mathbf{R}}_j(t)\right] \right\rangle \tag{4.50}$$

is in most cases not feasible, when all motions are taken into account. Similar to the separation of the nucleus position vector into different contributions, we can decompose the intermediate scattering function into factors accounting for different kinds of motion (for a detailed analysis see e.g. [13]):

$$\mathcal{I}_{\text{inc}}(\mathbf{q}, t) = \mathcal{I}^T_{\text{inc}}(\mathbf{q}, t) \cdot \mathcal{I}^R_{\text{inc}}(\mathbf{q}, t) \cdot \mathcal{I}^V_{\text{inc}}(\mathbf{q}, t), \tag{4.51}$$

thereby, we assume that intramolecular vibrations are independent of rotational and translational modes. Furthermore, the decomposition is only valid if the coupling between translation, the rotation and the reorientations are negligible. Using the convolution theorem the corresponding scattering function is

$$\mathcal{S}_{\text{inc}}(\mathbf{q}, \omega) = \mathcal{S}^T_{\text{inc}}(\mathbf{q}, \omega) \otimes \mathcal{S}^R_{\text{inc}}(\mathbf{q}, \omega) \otimes \mathcal{S}^V_{\text{inc}}(\mathbf{q}, \omega). \tag{4.52}$$

The scattering function related to the vibrational modes of the molecule can be decomposed into an elastic and a inelastic part [13]

$$\mathcal{S}^V_{\text{inc}}(\mathbf{q}, \omega) = \exp\left[-\frac{1}{3}\left\langle u^2 \right\rangle q^2\right] \left\{\delta(\omega) + \mathcal{S}^V_{\text{inel}}(\mathbf{q}, \omega)\right\}, \tag{4.53}$$

therein, $\left\langle u^2 \right\rangle$ is the average mean-squared displacement of the scattering nuclei. In Sec. 4.5 we will study $\mathcal{S}^T_{\text{inc}}(\mathbf{q}, \omega)$ and $\mathcal{S}^R_{\text{inc}}(\mathbf{q}, \omega)$ in more detail.

4.3 Static X-Ray Scattering

4.3.1 X-Rays

Structural information of matter on molecular length scales became for the first time visible with the discovery of highly energetic electromagnetic radiation by the physicist Röntgen [136] in 1895. Since he was not exactly sure what kind of radiation he had discovered, Röntgen called this new radiation X-rays, thereby making use of the connotation that X is the symbol for an unknown quantity. The famous radiographic image of Röntgen's wife's hand exemplifies the power of X-rays to penetrate biological matter and to serve as a tool to investigate structural properties. Their wavelength and energy render them a perfect probe to investigate atomic and molecular structure. In 1901 Röntgen was the first recipient of the Nobel Prize in Physics.

4.3.2 Static Scattering

In this subsection we summarize the essential concept of static scattering using X-ray photons. A comprehensive introduction to this topic is e.g. given in the textbook by Als-Nielsen and McMorrow [6]. We note that for static neutron scattering the framework is very similar and the only parameter to be changed is the scattering length density.

In contrast to neutrons, the X-ray photons are scattered at the electron "cloud" of the atoms. As X-rays are electromagnetic waves they induce an oscillation of the electrons, which causes the emission of an electromagnetic wave at identical wavelength. In a simplistic picture the interaction with the electron "cloud" is described by a single scattering length $f = N_e\, r_0$, therein N_e is the number of electrons in the "cloud" and the Thomson radius $r_0 = 1.82 \cdot 10^{-13}\,\mathrm{cm}$. When a monochromatic X-ray beam with wavevector $\mathbf{k}$ is scattered at a sample the amplitude of the scatted wave with wavevector $\mathbf{k}'$ is

$$A(\mathbf{q}) = \int \rho(\mathbf{r}) \, \exp\left(\mathrm{i}\,\mathbf{q}\,\mathbf{r}\right) \, \mathrm{d}^3\mathbf{r}, \tag{4.54}$$

therein, ρ is the scattering length density of the illuminated sample and $\mathbf{q} = \mathbf{k} - \mathbf{k}'$ the momentum transfer vector. In case of a monodisperse system of N particles, whose center of mass positions are denoted by $\mathbf{R}_i$, the total scattering length density can be decomposed into a sum of non-overlapping densities

$$\rho(\mathbf{r}) = \sum_{j=1}^{N} \rho_{\mathrm{V}}\left(\mathbf{r} - \mathbf{R}_j\right), \tag{4.55}$$

therein, ρ_{V} is the scattering length density of a single particle with volume V. Using

this summation the scattering amplitude turns into a the following sum:

$$A(\mathbf{q}) = \sum_{j=1}^{N} \exp\left(\mathrm{i}\,\mathbf{q}\,\mathbf{R}_j\right) \int \exp(\mathrm{i}\,\mathbf{q}\,\mathbf{r})\,\rho\left(\mathbf{r}\right)\,\mathrm{d}^3\mathbf{r}. \tag{4.56}$$

Instead of measuring $A(\mathbf{q})$ in an experiment, we gauge the ensemble averaged intensity, which coincides with the differential cross-section,

$$\frac{\mathrm{d}\sigma(\mathbf{q})}{\mathrm{d}\mathbf{\Omega}} = \left\langle A(\mathbf{q})\,A(\mathbf{q})^*\right\rangle. \tag{4.57}$$

Fig.4.4 illustrates the scattering length density ρ_V, which can be conceived to be the smeared out form of the particle shape. Outside of the particle volume V the density rapidly decays to zero, whilst within V the density fluctuates about the average scattering length density $\bar{\rho_\mathrm{V}}$. With this in mind and assuming that the density fluctuation in V is negligible, we can approximate

$$\rho_\mathrm{V}(\mathbf{r}) \approx \bar{\rho_\mathrm{V}}\,\chi_\mathrm{V}(\mathbf{r}), \tag{4.58}$$

where χ_V is the shape function of the particle with volume V. With this approximation, we finally obtain the scattering intensity

$$\frac{\mathrm{d}\sigma(\mathbf{q})}{\mathrm{d}\mathbf{\Omega}} = N\,V^2\,\bar{\rho_\mathrm{V}}^2\,S(\mathbf{q})\,P(\mathbf{q}). \tag{4.59}$$

with the structure factor described by the equilibrium structure of the system

$$S(\mathbf{q}) = \left\langle \frac{1}{N} \sum_{j,k=1}^{N} \exp\left[i\,\mathbf{q}\,\left(\mathbf{R}_j - \mathbf{R}_k\right)\right] \right\rangle, \tag{4.60}$$

and the form factor

$$P(\mathbf{q}) = \left| \frac{1}{V} \int_V \exp\left(\mathrm{i}\,\mathbf{q}\,\mathbf{r}\right)\,\mathrm{d}^3\mathbf{r} \right|^2, \tag{4.61}$$

which is the Fourier transform of the particle shape. In highly diluted systems, the structure factor is nearly unity and we only observe the form factor when measuring the scattering intensity. Conversely, in non-diluted systems, where interactions are present, the scattering intensity is strongly modulated by the structure factor S. For an isotropic system we observe that the form and structure factor only depend on the magnitude of $\mathbf{q}$

$$\begin{aligned} P(q) &= \langle P(\mathbf{q})\rangle_\Omega \\ S(q) &= \langle S(\mathbf{q})\rangle_\Omega, \end{aligned} \tag{4.62}$$

where the angular brackets denote the averaging over all orientations of $\mathbf{q}$ assuming that they are equally distributed, which happens to be the case in dilute suspension where interactions of the suspended particles can be neglected.

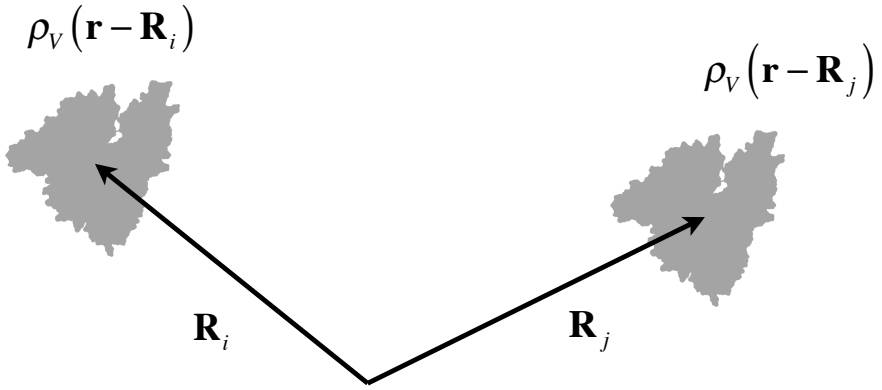

Figure 4.4: Two particles with center of mass positions $\mathbf{R}_i$ and $\mathbf{R}_j$. Each particle has a scattering length density ρ_{V}, which can be conceived to be a smeared out form of the particle shape. Outside the particle volume V the density rapidly decays to zero and within V it fluctuates about the average scattering length density $\bar{\rho_{\mathrm{V}}}$. If this fluctuation is negligible we can approximate $\rho_{\mathrm{V}}(\mathbf{r}) \approx \bar{\rho_{\mathrm{V}}}\,\chi_{\mathrm{V}}(\mathbf{r})$ as displayed in the figure by the two gray solid shapes.

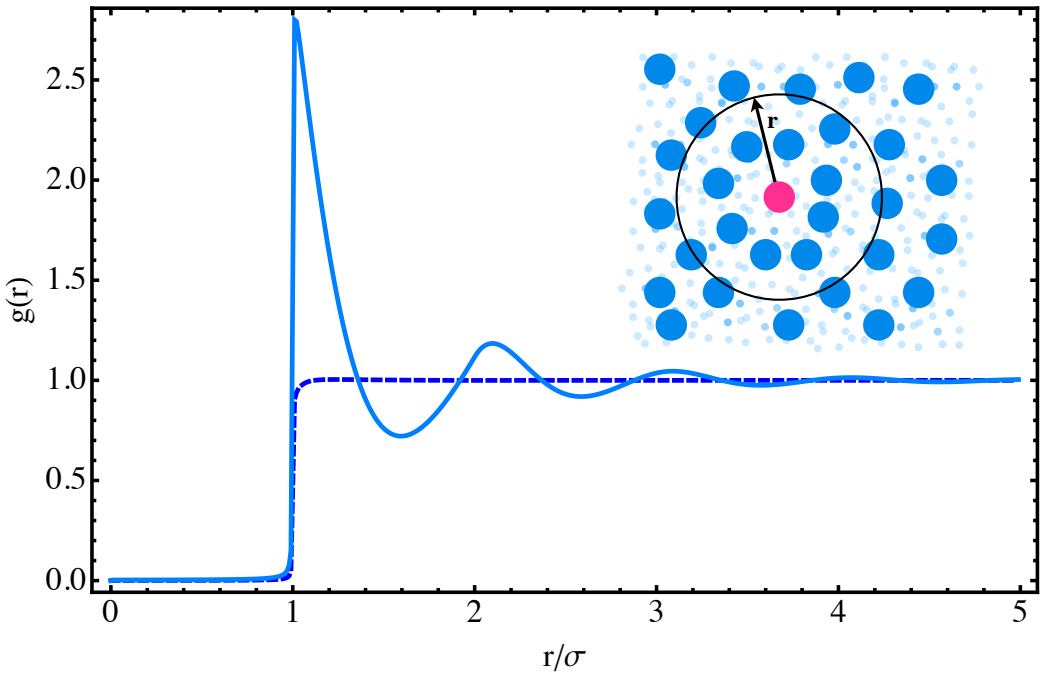

Figure 4.5: Pair correlation function $g(r)$ for a system of charged spheres ($Z = 11$) with diameter $\sigma = 70\,\text{Å}$ in a liquid with relative dielectric constant $\varepsilon_r = 78$ at temperature $T = 298\,\text{K}$. The blue solid line shows $g(r)$ of spheres at high volume fraction ($\varphi = 0.4$) and low ionic strength ($I = 10\,\text{mM}$). In contrast the light blue dashed line shows the same spheres at low volume fraction ($\varphi = 0.004$) and very high ionic strength ($I = 10^3\,\text{mM}$). The pair correlation function $g(r)$ was calculated from the analytical structure factor of macro-ions obtained by Hayter and Penfold [71].

4.3.3 Static Correlation Function

Similar to the dynamic structure factor the static structure factor S can be expressed in terms of the static pair-correlation function:

$$S(q) = 1 + 4\,\pi\,n_p \int_0^\infty [g(r) - 1]\,\frac{\sin(q\,r)}{q\,r}\,r^2\,\mathrm{d}r \tag{4.63}$$

therein, the pair-correlation $g(r)$ function describes the spatial arrangement set by the interparticle interactions. For particles of diameter σ with a hardcore, the pair-correlation function can be approximated from the Ornstein-Zernicke relation equation with the mean-spherical closure relation [95]. This method allows to relate the interaction of two particles $u(r)$ with the pair-correlation function $g(r)$ using a linear integral equation. The Ornstein-Zernicke equation reads

$$h(r) = c(r) + \rho \int c\left(\|\mathbf{r} - \mathbf{r}'\|\right)\,h(r')\,\mathrm{d}^3\mathbf{r}', \tag{4.64}$$

where, $h(r) = g(r) - 1$. With the mean-spherical approximation

$$\begin{aligned} h(r) &= -1, \quad r < \sigma \\ c(r) &\approx -\beta\, u(r), \quad r > \sigma \end{aligned} \tag{4.65}$$

the pair correlation function can be calculated for $r > \sigma$.

4.4 Intermolecular Interactions

In this section we want to describe the main types of molecular interactions relevant for this study. These are intermolecular interactions. Intramolecular interactions, which are much stronger, could not be resolved with the spectroscopic techniques we used for this study. For a more comprehensive review of intermolecular interactions we refer to the textbooks by Dhont [40], Kleman and Lavrentovich [89] and Nägele [116]. In solution macromolecules feel two types of intermolecular interactions, namely, long-range hydrodynamic and medium-range direct interactions. In the *first* part, we will elaborate on hydrodynamic interactions, which only occur in macromolecular solutions and originate from the solvent flow field. In the *second* part, we want to focus on the direct interactions, which crucially determine the equilibrium structure of the molecules in solution.

4.4.1 Hydrodynamic Interactions

Molecules moving in a solvent generate both a flow and a pressure field, $\mathbf{u}$ and p, respectively. The motion of other particles feeling this field is influenced by a force

$$\mathbf{F} = \oint_{\partial\Omega} \{p(\mathbf{r}) - \eta\, \boldsymbol{\tau}[\mathbf{v}(\mathbf{r})]\}\ \mathbf{n}\, \mathrm{d}S(\mathbf{r}), \tag{4.66}$$

where η is the dynamical viscosity coefficient and $\mathbf{n}$ is the normal vector of the macromolecular surface $\partial\Omega$ pointing towards the fluid. The flow field velocity acts via the shear stress tensor $\boldsymbol{\tau}$ on the particle, reading

$$\boldsymbol{\tau} = \nabla\, \mathbf{v}^{\top} + \left(\nabla\, \mathbf{v}^{\top}\right)^{\top}. \tag{4.67}$$

with $\top$ denoting the transposition. In the following we will derive how hydrodynamic forces are described in terms of the velocity and position of all particles. To this end, we will consider a system of spherical particles emerged in a fluid. In the world of macromolecules viscous forces dominate [133] the motion, which allow us to describe the hydrodynamic interaction using the so-called creeping flow equations

$$\begin{aligned} \nabla\, p(\mathbf{r}) - \eta\, \nabla^2\, \mathbf{v}(\mathbf{r}) &= \mathbf{f}(\mathbf{r}) \\ \nabla \cdot \mathbf{v}(\mathbf{r}) &= 0 \end{aligned} \tag{4.68}$$

in which η is the sheer viscosity, $\mathbf{v}$ the flow field velocity, $\mathbf{f}$ and external force field, and p the pressure of the fluid. Using Green's method the general solution is

$$\begin{aligned} \mathbf{v}(\mathbf{r}) &= \int \mathbf{T}\left(\mathbf{r}-\mathbf{r}'\right)\ \mathbf{f}\left(\mathbf{r}'\right)\ \mathrm{d}^3\mathbf{r}' \\ p(\mathbf{r}) &= \int \mathbf{g}\left(\mathbf{r}-\mathbf{r}'\right)\ \mathbf{f}\left(\mathbf{r}'\right)\ \mathrm{d}^3\mathbf{r}' \end{aligned} \tag{4.69}$$

therein

$$\begin{aligned} \mathbf{T}(\mathbf{r}) &= \frac{1}{8\,\pi\,\eta\,r}\left(\mathbf{1}_3+\frac{\mathbf{r}\,\mathbf{r}^\top}{r^2}\right) \\ \mathbf{g}(\mathbf{r}) &= \frac{1}{4\,\pi\,r^3}\,\mathbf{r} \end{aligned} \tag{4.70}$$

Suppose we have N spheres of radius a with surface $\partial\Omega$ emerged in the suspension. When the external force $\mathbf{F}_j$ is applied to the sphere labeled by j, it induces a flow field that can be calculated from Eq. 4.69.

$$\mathbf{v}(\mathbf{r}) = \frac{1}{4\,\pi\,a^2}\sum_{j=1}^{N}\oint_{\partial\Omega_j}\mathbf{T}(\mathbf{r}-\boldsymbol{\xi})\,\mathbf{F}_j\,\mathrm{d}S(\boldsymbol{\xi}). \tag{4.71}$$

If we assume sticky boundary conditions, the fluid at the surface has the same velocity as the corresponding surface element. This allows to relate the velocities of the spheres to the external forces that the spheres exerted on the fluid. The average velocity on the surface on sphere i is

$$\begin{aligned} \mathbf{v}_i &= \frac{1}{4\,\pi\,a^2}\oint_{\partial\Omega_i}\mathbf{v}(\boldsymbol{\xi}')\,\mathrm{d}S(\boldsymbol{\xi}') \\ &= \frac{1}{6\,\pi\,\eta\,a}\,\mathbf{F}_i+\frac{1}{(4\,\pi\,a^2)^2}\sum_{j\neq i}^{N}\oint_{\partial\Omega_i}\oint_{\partial\Omega_j}\mathbf{T}(\boldsymbol{\xi}'-\boldsymbol{\xi})\,\mathrm{d}S(\boldsymbol{\xi}')\,\mathrm{d}S(\boldsymbol{\xi})\,\mathbf{F}_j. \end{aligned} \tag{4.72}$$

According to Newton's law, the hydrodynamic force that the fluid exerts on the j^{th} particle is $\mathbf{F}_h^{(j)} = -\mathbf{F}_j$. Hence, the hydrodynamics force is an N-body force $\mathbf{F}_h^N$, which depends on the position and velocities of all particles, denoted by $\mathbf{r}^N$ and $\mathbf{v}^N$, respectively.

$$\mathbf{F}_h^N = -\boldsymbol{\Upsilon}\left(\mathbf{r}^N\right)\ \mathbf{v}^N, \tag{4.73}$$

in which $\boldsymbol{\Upsilon}^{-1}$ is the mobility tensor describing the dynamic response of the spheres due to the hydrodynamic forces applied.

Fig. 4.6 illustrates the hydrodynamic forces experienced by three spheres moving in a solvent. Due to their motion they induce a pressure (not shown) and flow field (gray stream lines) that causes hydrodynamic forces acting on the spheres. As Eq. 4.73 implies the hydrodynamic force is related to the velocity and positions of all spheres, but not necessarily points in the same direction as the velocity.

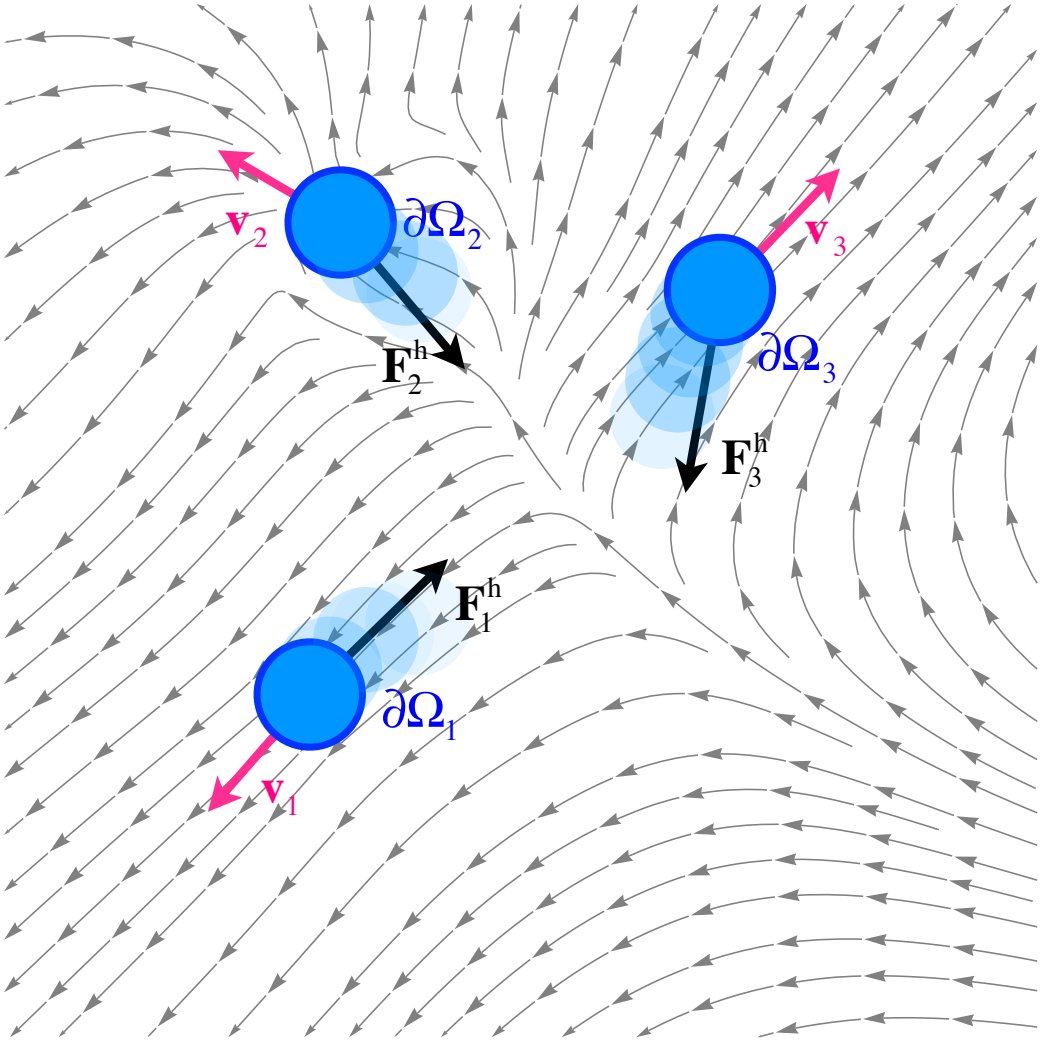

Figure 4.6: Spheres moving in a solvent induce a pressure and flow field that lead to hydrodynamic forces acting on the spheres. The flow field $\mathbf{v}$ calculated with Eq. 4.71 is visualized by its stream lines (gray arrow lines). At the surface $\partial\Omega_j$ of the sphere j the average velocity of the flow field is equal to the sphere's velocity due to the sticky boundary conditions. The hydrodynamic force is related to the velocity and positions of all spheres by $\mathbf{F}_h^N = -\boldsymbol{\Upsilon}\left(\mathbf{r}^N\right)\,\mathbf{v}^N$.

4.4.2 Direct Interactions

Aside from the solvent mediated interactions described in the previous section, macromolecules directly interact due to their surface charge distribution and their excluded volume. Fig. 4.7 displays the typical direction interaction potential $u(r)$ of spherical charged macromolecules of diameter σ. A long-range repulsive and short-range attractive force characterize the potential. For clarity the hard-core interaction is not displayed but reflected by the choice of the axis limits. For $r < \sigma$ the potential is infinity due to the fact that two molecules cannot be closer than the sum of their radii.

Hard-Sphere Interaction In a simplistic picture macromolecules can be considered as hard spheres of diameter σ. To account for the fact that they do not interpenetrate, their hard-core interactions are approximated by the hard sphere potential

$$u_{\mathrm{hs}}(r) = \begin{cases} +\infty & r \leq \sigma \\ 0 & r > \sigma \end{cases}, \tag{4.74}$$

therein r is the center to center distance of the macromolecules. Hard sphere interaction allows to define the excluded volume fraction φ, which for proteins can be determined from their concentration via $\varphi = v\, c_p$, where the specific volume is for most proteins $v = 0.74\,\mathrm{cm}^3/\mathrm{g}$ (more details in Sec.5.1.1).

Screened Coulomb Interaction Due to the dissociation of solvent exposed hydrogen atoms of surface groups or the adsorption of micro-ions [159, 144], macromolecules assume in general a very complex charging pattern. Only considering the monopole interaction described solely by an effective charge Z, we can describe the repulsive interaction of macromolecules by colloidal charged hard spheres: Charged hard spheres of diameter $\sigma = 2\,a$ immersed at volume fraction φ in a continuous electrolyte solvent with dielectric constant ε and ionic strength I interact by a Yukawa repulsion [17]

$$\beta\, u_{\mathrm{el}}(r) = Z^2\, \lambda_B\, Y^2\, \frac{\exp\left(-\kappa\, r\right)}{r} \tag{4.75}$$

where $\beta = (k_B\, T)^{-1}$, $\lambda_B = \beta\, e^2 / (4\,\pi\,\varepsilon)$ is the Bjerrum length and κ is the screening constant given in terms of the ionic strength

$$\kappa = \left(8\,\pi\, e^2\, I\, \beta\right)^{1/2}. \tag{4.76}$$

The effect of screening and the size of the particles on the interaction strength is characterized by

$$Y = \cosh\left(\kappa\, a\right) + U\ \left[\kappa\, a\ \cosh\left(\kappa\, a\right) - \sinh\left(\kappa\, a\right)\right] \tag{4.77}$$

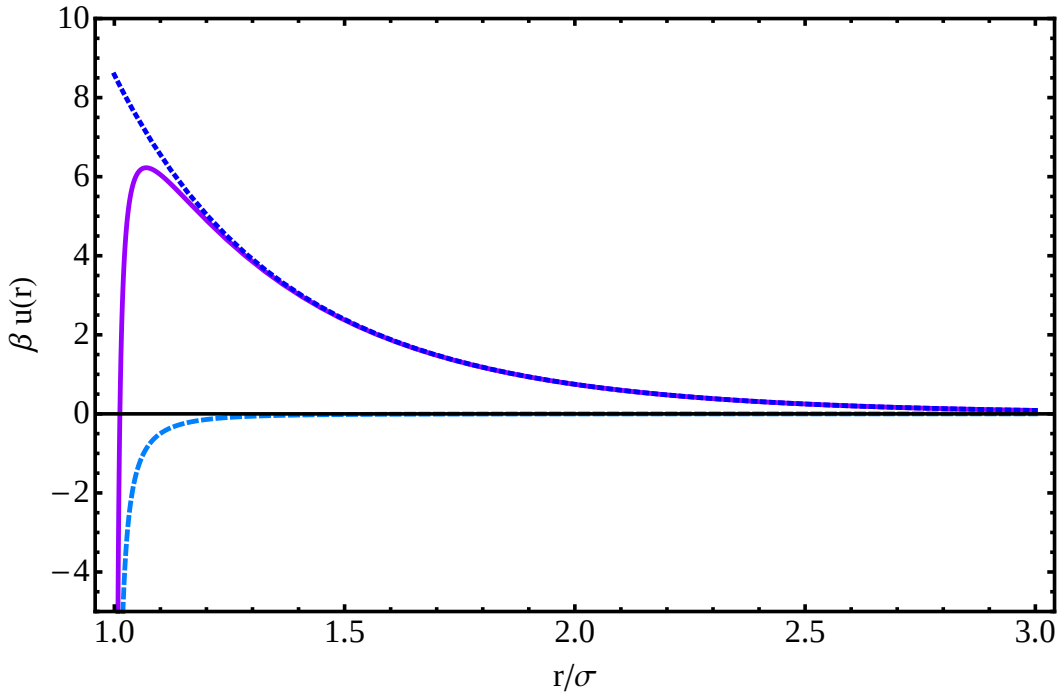

Figure 4.7: Interaction potential u between two charged hard spheres with diameter σ at a center-center distance r (purple solid line). V consists of an hard-sphere potential u_{hs}, an attractive van-der-Waals potential u_{vdW} (light blue dashed line) and a repulsive Yukawa potential u_{el} (dark blue dashed line).

with

$$\begin{aligned} U &= \frac{x}{(\kappa\, a)^3} - \frac{\gamma}{\kappa\, a} \\ z &= \frac{3\,\varphi}{1-\varphi} \\ \gamma &= \frac{\Gamma\, a + z}{1 + \Gamma\, a + z}. \end{aligned} \tag{4.78}$$

The general screening parameter Γ satisfies the nonlinear relation

$$\Gamma^2 = \kappa^2 + \frac{q^2}{(1 + \Gamma\, a + z)^2}, \tag{4.79}$$

therein the screening due to the presence of the macromolecule is

$$\begin{aligned} q^2 &= 4\,\pi\,\lambda_B\,\rho\,Z^2, \\ \rho &= \frac{\varphi}{4/3\,\pi\,a^3}. \end{aligned} \tag{4.80}$$

Note that for a dilute suspension the Derjaguin-Landau-Verwey-Overbeek [169] repulsive potential is obtained:

$$Y_0 := \lim_{\varphi \to 0} Y = \frac{1}{1 + \kappa\, a}\, \exp\left(\kappa\, a\right). \tag{4.81}$$

In the non-dilute case the presence of surrounding macromolecules decreases the screening ability of the solvent-ions around two interacting macromolecules and thereby produces a stronger effective repulsion between them; it can be shown that $Y_\varphi > Y_0$.

van-der-Waals Interaction A comprehensive introduction to van-der-Waals interactions is given in the review by Nir [119] and in the textbook by Kleman and Lavrentovich [89]. Van-der-Waals interaction is a generic term summarizing the interaction of two neutral molecules from three contributions: These are Keesom interaction (dipole-dipole), Debye interaction (induced-dipole dipole) and London interactions (induced-dipole induced-dipole). All these interactions have in common to be attractive and vary with the 6^{th} power of the molecular distance. For two neutral molecules of arbitrary shape described by the volumes V_1 and V_2 the energy of the van-der-Waals attraction is given by

$$u_{\text{vdW}} = -\frac{A_{\text{H}}}{\pi} \int_{V_1} \int_{V_2} \frac{\mathrm{d}^3\mathbf{r}_1\, \mathrm{d}^3\mathbf{r}_2}{\|\mathbf{r}_1 - \mathbf{r}_2\|^6}\ , \tag{4.82}$$

in which A_{H} is the Hamaker constant [68, 119]. In publication B (see Chap. 8) we will give experimental evidence that a globular protein can be described as an effective sphere. This simple picture of a protein motivates to simplify the shape

dependent interaction described by Eq. 4.82 by using identical spheres. For the case of two identical spherical molecules of diameter σ separated by a center-center distance r Hamaker [68] calculated:

$$u_{\mathrm{vdW}}(r) = -\frac{A_{\mathrm{H}}}{12}\left[\frac{\sigma^2}{r^2-\sigma^2} + \frac{\sigma^2}{r^2} + 2\,\log\left(1-\frac{\sigma^2}{r^2}\right)\right]. \tag{4.83}$$

For proteins in water at temperature T, the so-called Hamaker constant A_{H} was estimated by Nir [119] to be in the range $3-5\,k_B\,T$. When the molecule is highly charged the van-der-Waals attraction might be masked by the static repulsion.

Total Potential The equilibrium structure of a macromolecular solution is determined by the pair-wise additive total potential

$$U\left(\mathbf{r}^N\right) = \sum_{i<j}^{N} u\left(|\mathbf{r}_i - \mathbf{r}_j|\right) \tag{4.84}$$

where $\mathbf{r}^N$ denotes the N-particle configuration vector. The pair potential u is composed of the hard-core, repulsive and attractive interaction

$$u(r) = u_{\mathrm{hs}}(r) + u_{\mathrm{vdW}}(r) + u_{\mathrm{el}}(r) \tag{4.85}$$

In case of highly charged macromolecules in solution the interaction is dominated by the hard-core and the repulsive Coulomb part, leading to a charge-stabilized solution. Adding salt can screen and alter the surface charge. This can cause a change of the balance of repulsive and attractive forces and eventually give rise to a complex equilibrium behavior such as the formation of clusters [157, 98].

Potential of Mean Force In an N-particle system the total force is not directly measurable, however we can calculate the average force $\mathbf{F}$ between two particles over all configurations of the remaining $N-2$ particles. The mean force on particle 1 if we hold particle 2 fixed is

$$\mathbf{F}(r_{12}) = \frac{\int\left(-\nabla_1 U\right)\exp\left(-\beta\,U\right)\,\mathrm{d}^3\mathbf{r}_3\ldots\mathrm{d}^3\mathbf{r}_N}{\int\exp\left(-\beta\,U\right)\,\mathrm{d}^3\mathbf{r}_3\ldots\mathrm{d}^3\mathbf{r}_N} = \left\langle-\nabla_1\,U\left(\mathbf{r}^N\right)\right\rangle_{1,2}. \tag{4.86}$$

Therein, ∇_1 is the derivative with respect to the position vector $\mathbf{r}_1$ and the angular brackets denote the canonical average over all particles expect particle 1 and 2. There exists a remarkable link to the pair-correlation g(r) function which we introduced in Eq. 4.63. One can show that [116]

$$-\nabla_1\,w\left(r_{12}\right) = \mathbf{F}(r_{12}), \tag{4.87}$$

with

$$w(r) = -k_B\,T\,\log[g(r)] \tag{4.88}$$

being the so-called potential of mean force.

4.5 Translational Diffusion

If compared to the microscopic world of molecules, inertia plays a rather negligible role than in the macroscopic world. By contrast, frictional forces govern the motion of molecules through the solvent. Collision with the much smaller surrounding solvent molecules, which are in random thermal motion, causes an irregular trajectory. By examining the random motion of pollen grains Brown [24] sparked the interest in developing mathematical models able to describe such kind of random movements.

Many years later Fick [55] introduced his law of diffusion

$$\frac{\partial \rho}{\partial t} = D \frac{\partial^2 \rho}{\partial x^2}, \tag{4.89}$$

thereby, introducing the diffusion coefficient D, which measures how rapidly a particle explores isotropically its surrounding. Later, Einstein found the link between the diffusion coefficient of non-interacting particles performing the so-called "Brownian molecular motion" with the viscosity and the size of the suspended particles [48],

$$D = \frac{k_B T}{6 \pi \eta R}, \tag{4.90}$$

therein, R is the radius of the suspended particles, T the temperature and η the viscosity of the solvent. Moreover, Einstein showed that the diffusion of non-interacting particles could be well described by Fick's law, which was originally developed by Fick to describe relaxation of concentration gradients.

4.5.1 Diffusion Coefficient of Proteins

The first mathematical concepts to describe random motions were developed for spherical particles suspended in a fluid. However, when studying the "Brownian Motion" of proteins it is crucial to take their non-sphericity into account. To model the shape of a protein, one uses in general ellipsoidal spheroids or more frequently an ellipsoid of revolution in order to take the anisotropy into account. Perrin [128, 90] generalized the Stokes-Einstein relation Eq. 4.90 for the case of ellipsoids with semi-principal axes $(a, 0, 0)$, $(0, b, 0)$ and $(0, 0, c)$. Due to the anisotropy the diffusion coefficient is not a scalar anymore, but a diagonal 2^{nd}-order tensor

$$\mathbf{D} = k_B T \operatorname{diag}\left(\frac{1}{f_a}, \frac{1}{f_b}, \frac{1}{f_c}\right), \tag{4.91}$$

therein, the friction coefficients about the semi-principal axes are

$$f_\gamma = \frac{16 \pi \eta}{S + \gamma^2 P_\gamma} \tag{4.92}$$

where S and P_γ are the following elliptic integrals

$$P_\gamma = \int_0^\infty \frac{\mathrm{d}s}{(\gamma^2+s)\sqrt{(a^2+s)(b^2+s)(c^2+s)}} \tag{4.93}$$

$$S = \int_0^\infty \frac{\mathrm{d}s}{\sqrt{(a^2+s)(b^2+s)(c^2+s)}}. \tag{4.94}$$

Using ellipsoidal spheroids to describe the form of proteins is clearly a strong simplification. If the solution structure of the protein is known, one can use more complicated models. Hubbard and Douglas [76] introduced a simple method to estimate the translational diffusion coefficient of an arbitrarily shaped Brownian particle. The translational diffusion coefficient takes the form

$$D = \frac{k_B\,T}{6\,\pi\,\eta\,C_V}, \tag{4.95}$$

therein, C_V is mathematically similar to the electrostatic capacitance of the particle with shape V, for a sphere of radius R the relation is simply $C_V = R$. For the atomic-level structure of proteins, de la Torre et al. [38] elaborated a bead model that can estimate the diffusion coefficient. For this end they developed the public-domain HYDROPRO computer program [38].

4.5.2 Free Diffusion

Einstein showed that the diffusion of non-interacting particles in a viscose medium can be well described by Fick's law. The time evolution of the configurational probability density function is

$$\frac{\partial}{\partial t}\,P\left(\mathbf{r},t \mid \mathbf{r}_0,t_0\right) = D\,\nabla^2\,P\left(\mathbf{r},t \mid \mathbf{r}_0,t_0\right), \tag{4.96}$$

with the initial condition that at time $t = t_0$ the diffusing particle is at position $\mathbf{r}_0$:

$$P\left(\mathbf{r},t_0 \mid \mathbf{r}_0,t_0\right) = \delta\left(\mathbf{r}-\mathbf{r}_0\right). \tag{4.97}$$

One refers to the solution as Green's function ψ, reading

$$P\left(\mathbf{r},t \mid \mathbf{r}_0,t_0\right) = \psi\left(\mathbf{r}-\mathbf{r}_0,t-t_0\right) \tag{4.98}$$

$$\psi\left(\mathbf{r},t\right) = \frac{1}{\left(4\,\pi\,D\,t\right)^{3/2}}\,\exp\left(-\frac{\mathbf{r}^2}{4\,D\,t}\right), \tag{4.99}$$

describing the probability to find a particle at position $\mathbf{r}$ at time t when it was at position $\mathbf{r}_0$ at time t_0. The mean-squared displacement, measuring how the particle explores its surroundings over time t is

$$W(t) = \left\langle\left(\mathbf{r}-\mathbf{r}_0\right)^2\right\rangle = 6\,D\,t. \tag{4.100}$$

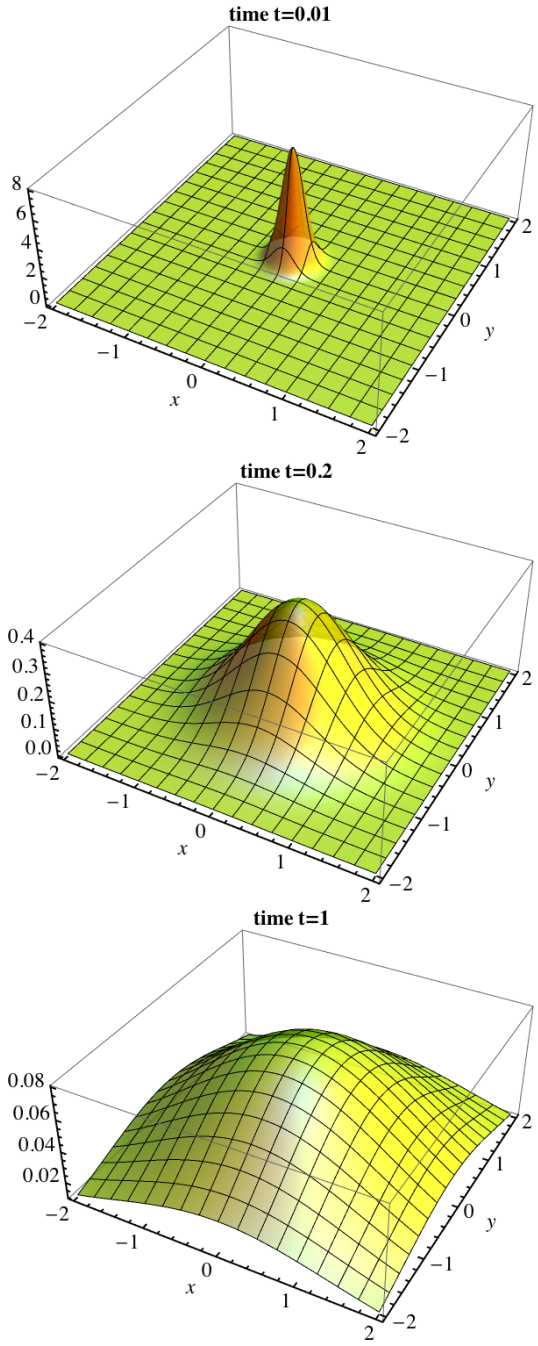

Figure 4.8: Time evolution of the probability density $P(\mathbf{r}, t \mid \mathbf{0}, 0)$ to find a particle at position $\mathbf{r} = (x, y)$ at a certain time t when it was initially at the origin at time 0. For small times $P(\mathbf{r}, t \mid \mathbf{0}, 0)$ resembles a delta function. With progressing time $P(\mathbf{r}, t \mid \mathbf{0}, 0)$ is spreading isotropically out in space while being centered at the origin.

Fig. 4.8 displays the time evolution of the two-dimensional version of Green's function for the case that the particle was initially at the origin. As the linear dependence of the mean-squared displacement Eq. 4.100 on time t implies, the probability density function is spreading out with progressing time. The speed of this isotropic explorations of space is measured by the diffusion coefficient D. By plugging Eq. 4.99 into Eq. 4.42 and employing the general relation for classical correlations Eq. 4.8, we obtain:

$$\begin{aligned} \mathcal{G}_s^{\mathrm{cl}}(\mathbf{r},t) &= \int\int \delta\left(\mathbf{r}-\mathbf{x}+\mathbf{x}_0\right)\, P\left(\mathbf{x},t \mid \mathbf{x}_0,0\right)\, P(\mathbf{x}_0,0)\,\mathrm{d}^3\mathbf{x}_0\,\mathrm{d}^3\mathbf{x} && (4.101)\\ &= \int\int \delta\left(\mathbf{r}-\mathbf{x}+\mathbf{x}_0\right)\, \psi\left(\mathbf{x}-\mathbf{x}_0,t\right)\, P(\mathbf{x}_0,0)\,\mathrm{d}^3\mathbf{x}_0\,\mathrm{d}^3\mathbf{x} && (4.102)\\ &= \psi\left(\mathbf{r},t\right) \int P(\mathbf{x}-\mathbf{r},0)\,\mathrm{d}^3\mathbf{x}\\ &= \psi\left(\mathbf{r},t\right). \end{aligned}$$

Note, without loss of generality, we set $t_0 = 0$. It turns out that the time dependent self -correlation function of the free diffusing particle is equal to the Green's functions of the free-diffusion equation

$$\mathcal{G}_s(\mathbf{r},t) = \frac{1}{(4\,\pi\,D\,t)^{3/2}}\,\exp\left(-\frac{\mathbf{r}^2}{4\,D\,t}\right). \tag{4.103}$$

Consequently, according to Eq. 4.44 the incoherent intermediate scattering function is

$$\begin{aligned} \mathcal{I}_{\mathrm{inc}}^{\mathrm{T}}(q,t) &= \int \mathcal{G}_s(\mathbf{r},t)\,\exp\left(\mathrm{i}\,\mathbf{q}\,\mathbf{r}\right)\,\mathrm{d}^3\mathbf{r} && (4.104)\\ &= \exp\left(-D\,q^2\,|t|\right). \end{aligned}$$

Using Eq. 4.45 the corresponding incoherent scattering function becomes a Lorentzian function

$$\mathcal{S}_{\mathrm{inc}}^{\mathrm{T}}(q,t) = \frac{1}{\pi}\,\frac{D\,q^2}{\omega^2+\left(D\,q^2\right)^2}. \tag{4.105}$$

4.5.3 Diffusion of Interacting Particles

Smoluchowski Equation Smoluchowski [150] generalized Fick's law for diffusion to a system of N interacting particles. In contrast to free diffusion, the suspended particles feel the presence of the surrounding molecules mediated by both hydrodynamic interactions and direct interactions (for details see Secs. 4.4.1 and 4.4.2). The diffusive motion is then described in terms of an N-particle density distribution function P, whose time evolution is governed by the Smoluchowski equation:

$$\frac{\partial}{\partial t}\,P\left(\mathbf{r}^N,t \mid \mathbf{r}_0^N,t_0\right) = \hat{\mathcal{S}}\,P\left(\mathbf{r}^N,t \mid \mathbf{r}_0^N,t_0\right), \tag{4.106}$$

in which the operator in the right-hand equation is the so-called Smoluchowski operator which operates on a function $\psi\left(\mathbf{r}^N\right)$ as follows:

$$\hat{\mathcal{S}}\,\psi\left(\mathbf{r}^N\right) = \nabla^\top\,\left[\mathbf{D}\left(\mathbf{r}^N\right)\,\left\{\beta\,\psi\left(\mathbf{r}^N\right)\,\left[\nabla\,U\left(\mathbf{r}^N\right)\right] + \nabla\,\psi\left(\mathbf{r}^N\right)\right\}\right], \tag{4.107}$$

therein, $\beta = (k_B\,T)^{-1}$ with T being the temperature and $\nabla = \partial/\partial\mathbf{r}^N$ the Nabla operator in column vector representation. The solvent mediated hydrodynamic interactions between the particles are determined by the microscopic diffusion tensor $\mathbf{D}$, which is related to the mobility tensor Eq. 4.73 by

$$\mathbf{D}\left(\mathbf{r}^N\right) = \left\{\beta\,\boldsymbol{\Upsilon}\left(\mathbf{r}^N\right)\right\}^{-1}. \tag{4.108}$$

Particle-particle direct interactions are described by $U\left(\mathbf{r}^N\right)$, which can be calculated from Eq. 4.84. Finally, the configuration vector $\mathbf{r}^N = (\mathbf{r}_1, ..., \mathbf{r}_N)$ bundles all N particle position vectors. Given that at time t_0 the configurational probability of the diffusing particles is

$$P\left(\mathbf{r}^N, t_0 \mid \mathbf{r}_0^N, t_0\right) = f\left(\mathbf{r}^N\right). \tag{4.109}$$

where f is an arbitrary density distribution, the time evolution of the Smoluchowski equation will restore the equilibrium distribution of the particles' configuration in space for infinite times,

$$P_\infty\left(\mathbf{r}^N\right) := \lim_{t\to\infty} P\left(\mathbf{r}^N, t \mid \mathbf{r}_0^N, t_0\right) = \frac{1}{Z}\,\exp\left[-\beta\,U\left(\mathbf{r}^N\right)\right] \tag{4.110}$$

in which the normalization factor Z is the corresponding partition function Z. Using the steps in Sec. 4.1 it is possible to find an ensemble average using the Boltzmann distribution and the Smoluchowski operator for both the incoherent and the coherent intermediate scattering function,

$$\mathcal{I}_{\mathrm{inc}}^{\mathrm{T}}(\mathbf{q}, t) = \tag{4.111}$$
$$\frac{1}{N}\sum_{j=1}^{N}\int \exp\left(-\mathrm{i}\,\mathbf{q}\,\mathbf{r}_j\right)\,\left\{\exp\left(t\,\hat{\mathcal{S}}^\dagger\right)\,\exp\left(\mathrm{i}\,\mathbf{q}\,\mathbf{r}_j\right)\right\}\,P_\infty\left(\mathbf{r}^N\right)\,\mathrm{d}\mathbf{r}^N,$$

and

$$\mathcal{I}_{\mathrm{coh}}^{\mathrm{T}}(\mathbf{q}, t) = \tag{4.112}$$
$$\frac{1}{N}\sum_{i,j=1}^{N}\int \exp\left(-\mathrm{i}\,\mathbf{q}\,\mathbf{r}_i\right)\,\left\{\exp\left(t\,\hat{\mathcal{S}}^\dagger\right)\,\exp\left(\mathrm{i}\,\mathbf{q}\,\mathbf{r}_j\right)\right\}\,P_\infty\left(\mathbf{r}^N\right)\,\mathrm{d}\mathbf{r}^N,$$

respectively. Therein, $\hat{\mathcal{S}}^\dagger$ is the adjoint operator to $\hat{\mathcal{S}}$, which operates on an arbitrary function $\psi\left(\mathbf{r}^N\right)$ as follows

$$\hat{\mathcal{S}}^\dagger\,\psi\left(\mathbf{r}^N\right) = \left\{\nabla + \beta\,\nabla\,U\left(\mathbf{r}^N\right)\right\}^\top\,\left[\mathbf{D}\left(\mathbf{r}^N\right)\,\nabla\,\psi\left(\mathbf{r}^N\right)\right] \tag{4.113}$$

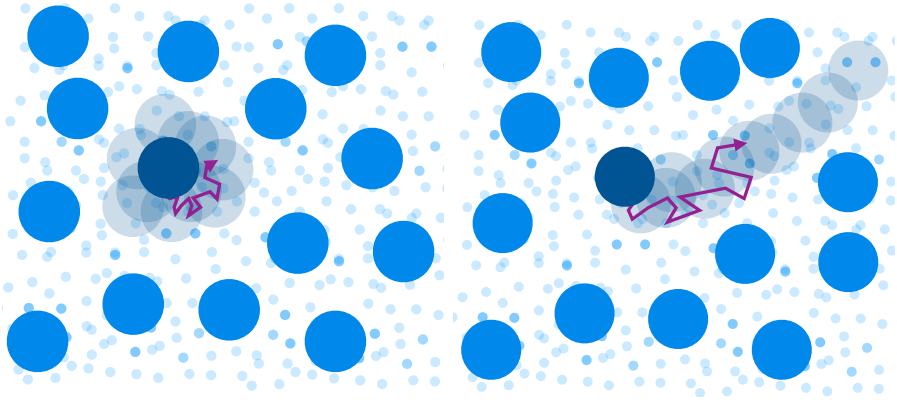

Figure 4.9: Left-hand image: The physical picture of short-time self-diffusion is that the tracer-particle (dark blue circle) diffuses inside the cage of its surrounding particles (light-blue circles). The diffusion trajectory of the tracer-particle is indicated by the transparent dark blue circles. The free-diffusion coefficient of the tracer given by the Stokes-Einstein relation 4.90 is slowed down mainly due to the hydrodynamic interactions with other particles. Right-hand image: long-time self-diffusion refers to the case when the tracer-particle (dark blue circle) breaks through the cage of surrounding particles (light-blue circles) and during its travel path (indicated by the transparent dark circles) it collides with others. Hence, apart from the hydrodynamic interactions, the direct interactions further slow down the particles free-diffusion coefficient.

However, canceling the operator would result in an infinite series and for most systems it is not feasible to obtain an explicit analytical expression.

Short-Time Self-Diffusion Inspired by the simple exponential form of the incoherent intermediate scattering function Eq. 4.105 of a free diffusing particle, one can define in a similar fashion the self-diffusion coefficient $\mathbf{D}_s$ linked to the incoherent intermediate scattering function by

$$\mathcal{I}_{\text{inc}}^{\text{T}}(\mathbf{q},t) = \exp\left\{-\mathbf{q}^{\top}\,\mathbf{D_s}(\mathbf{q},t)\,\mathbf{q}\,|t|\right\}, \tag{4.114}$$

Consequently, $\mathbf{D}_s$ in general depends on both time t and scattering vector $\mathbf{q}$ and can be conceived as a measure of the average single particle mobility under the influence of intermolecular interactions. For very short times t the incoherent intermediate scattering function Eq. 4.112 can be expanded as

$$\mathcal{I}_{\text{inc}}^{\text{T}}(\mathbf{q},t) = 1 - t\,\mathbf{q}^{\top}\,\mathbf{D}_s^s\,\mathbf{q} + \mathcal{O}\left(t^2\right) \tag{4.115}$$

with

$$\mathbf{D}_s^s = \frac{1}{N}\sum_{j=1}^{N}\int \mathbf{D}_{j,j}(\mathbf{r}^N)\,P_{\infty}(\mathbf{r}^N)\,\mathrm{d}\mathbf{r}^N. \tag{4.116}$$

denoting the short-time self-diffusion tensor. For a system of N identical particles $\mathbf{D}_s^s$ reduces to

$$\mathbf{D}_s^s = \int \mathbf{D}_{1,1}(\mathbf{r}^N)\, P_\infty(\mathbf{r}^N)\, \mathrm{d}\mathbf{r}^N. \tag{4.117}$$

If we measure the scattering cross-section of molecules in solution, we cannot determine the diffusion tensor since we measure the average over all possible orientations of the molecules. To account for this we average the intermediate scattering function over all directions of $\mathbf{q}$, which for small times results in

$$\mathcal{I}_{\mathrm{inc}}^{\mathrm{T}}(q,t) = 1 - t\,q^2\,\frac{1}{3}\,\mathrm{tr}(\mathbf{D}_s^s) + \mathcal{O}\left(t^2\right), \tag{4.118}$$

thereby, we obtain the scalar short-time self-diffusion coefficient

$$D_s^s = \frac{1}{3}\,\mathrm{tr}\left(\mathbf{D}_s^s\right), \tag{4.119}$$

where tr denotes the trace of a tensor. Consequently, for a system of interacting particles the scattering function in the short-time limit reads

$$\mathcal{S}_{\mathrm{inc}}^{\mathrm{T}}(\mathbf{q},\omega) = \frac{1}{\pi}\,\frac{D_s^s\,q^2}{\omega^2 + \left(D_s^s\,q^2\right)^2}. \tag{4.120}$$

Fig. 4.9 illustrates the self-diffusion coefficient, thereby focusing on the limiting cases for short-time self-diffusion and long-time self-diffusion (for detailed description see e.g. Ref.[40]). For very short times t the molecules diffuse a short distance of the order of their own size influenced only by the quasi-instantaneous hydrodynamic interactions. Direct interactions play a less important role, since the potential does not change on the corresponding length scale. Thus, short-time self-diffusion can be understood intuitively as relatively free diffusion on a length scale limited by the direct interactions, while the hydrodynamic interactions act via a change of the effective solvent viscosity. In contrast, in the long-time limit the particle breaks through the cage of surrounding particles and collides with others. Hence, apart from the hydrodynamic interactions, the direct interactions further slow down the particle free-diffusion coefficient.

Short-Time Collective-Diffusion Unlike self-diffusion, collective diffusion relates to the motion of many Brownian particles simultaneously and describes in the small q limit the relaxation of the macroscopic density according to Fick's law [55]. Therefore, it is measured in a coherent experiment like dynamic light scattering or neutron spin echo spectroscopy. The time and q dependent collective diffusion coefficient $\mathbf{D}_c$ can be expressed by means of the coherent intermediate scattering function as follows

$$\mathcal{I}_{\mathrm{coh}}^{\mathrm{T}}(\mathbf{q},t) =: S(\mathbf{q})\,\exp\left\{-\mathbf{q}^\top\,\mathbf{D}_c(\mathbf{q},t)\,\mathbf{q}\,|t|\right\} \tag{4.121}$$

The importance of direct interactions are reflected in the appearance of the static structure factor $S(\mathbf{q})$. For very small times t the operator exponential in Eq. 4.113 can be approximated by a Taylor expansion up to second order in time and the coherent intermediate scattering simplifies to

$$\mathcal{I}^{\mathrm{T}}_{\mathrm{coh}}(\mathbf{q},t) = S(\mathbf{q}) - t\,\mathbf{q}^{\top}\,\mathbf{D}^{s}_{c}(\mathbf{q})\,\mathbf{q} + \mathcal{O}\left(t^{2}\right), \tag{4.122}$$

thereby defining the short-time collective-diffusion tensor,

$$\mathbf{D}^{s}_{c}(\mathbf{q}) = \frac{1}{N}\sum_{i,j=1}^{N}\int \exp\left[\mathrm{i}\,\mathbf{q}\,(\mathbf{r}_i - \mathbf{r}_j)\right]\,\mathbf{D}_{i,j}\left(\mathbf{r}^N\right)\,P_{\infty}\left(\mathbf{r}^N\right)\,\mathrm{d}\mathbf{r}^N. \tag{4.123}$$

For large wavevectors $\mathbf{q}$ the collective diffusion coefficient converges to the self-diffusion coefficient since all contributions in the above sum with $i \neq j$ cancel out due to the rapid oscillation of the exponential [100, 44, 170].

4.6 Rotational Diffusion

Even though the structure of a solution-suspended protein is flexible due to atomic vibrations and spatially constrained motions of its sub-units and side chains, a protein has a very well defined average structure that is determined by the minimum of its free energy landscape. This motivates the physical picture to regard a protein in solution as a rigid body that besides translational diffusion of its center-of-mass performs random re-orientation due to kicks by the surrounding solvent molecules. In this section we will introduce the rotational version of Fick's law that governs the time evolution of the probability density distribution of the protein's orientation vector $\mathbf{u}$.

4.6.1 Free Rotational Diffusion

Similar to the Fick's law Eq. 4.96, the time evolution of the probability P to find the orientation vector

$$\mathbf{u} = \begin{pmatrix}\cos(\varphi)\,\sin(\theta)\\ \sin(\varphi)\,\sin(\theta)\\ \cos(\theta)\end{pmatrix}, \tag{4.124}$$

pointing into the direction $\mathbf{\Omega} = (\theta,\,\varphi)$ can be described by a diffusion equation:

$$\begin{aligned}\frac{\partial}{\partial t}\,P\left(\mathbf{\Omega},t \mid \mathbf{\Omega}_0,t_0\right) &= D_r\,\nabla^2_{\mathbf{u}}\,P\left(\mathbf{\Omega},t \mid \mathbf{\Omega}_0,t_0\right) \qquad (4.125)\\ \nabla^2_{\mathbf{u}} &= \frac{1}{\sin(\theta)^2}\left[\sin(\theta)\frac{\partial}{\partial\theta}\left(\sin(\theta)\,\frac{\partial}{\partial\theta}\right) + \frac{\partial^2}{\partial\varphi^2}\right] = -\hat{\mathbf{L}}^2,\end{aligned}$$

with the initial condition

$$P\left(\mathbf{\Omega},t_0 \mid \mathbf{\Omega}_0,t_0\right) = \frac{1}{4\,\pi\,\sin(\theta)}\,\delta\left(\mathbf{\Omega} - \mathbf{\Omega}_0\right) \tag{4.126}$$

where D_r is the rotational diffusion coefficient and $\hat{\mathbf{L}}^2$ the angular momentum operator. Similar to the Stokes-Einstein relation Eq. 4.90 the free rotational diffusion coefficient for a suspended sphere with radius R in a liquid of viscosity η at temperature T is given by the Stokes-Einstein Debye law:

$$D_r = \frac{k_B\,T}{8\,\pi\,\eta\,R}. \tag{4.127}$$

Using the spherical harmonics $Y_{l,m}$, which are the eigenfunctions of $\hat{\mathbf{L}}^2$, the Green's function to this initial value problem is

$$P\left(\mathbf{\Omega}, t_0 \mid \mathbf{\Omega}_0, t_0\right) = \sum_{l=0}^{\infty} \exp\left[-l\,(l+1)\,D_r\;(t-t_0)\right] \sum_{m=-l}^{l} Y_{l,m}\left(\Omega_0\right)^{\dagger}\,Y_{l,m}\left(\Omega\right). \tag{4.128}$$

Further, employing the addition theorem

$$P_l(\mathbf{u}\,\mathbf{u}_0) = \frac{4\,\pi}{2\,l+1} \sum_{m=-l}^{l} Y_{l,m}\left(\Omega_0\right)^{\dagger}\,Y_{l,m}\left(\Omega\right) \tag{4.129}$$

where P_l is the l^{th} Legendre polynomial and the two unit vectors $\mathbf{u}$ and $\mathbf{u}_0$ vectors having orientations $\mathbf{\Omega}$ and $\mathbf{\Omega}_0$, receptively, we finally obtain

$$P\left(\mathbf{\Omega}, t \mid \mathbf{\Omega}_0, t_0\right) = \frac{1}{4\,\pi} \sum_{l=0}^{\infty} \exp\left[-l\,(l+1)\,D_r\;(t-t_0)\right]\,(2\,l+1)\,P_l\left(\mathbf{u}^{\top}\,\mathbf{u}_0\right). \tag{4.130}$$

Fig. 4.10 illustrates the time-dependent probability Eq. 4.130. The time direction of the time progression is indicated by the black horizontal arrow. Initially, the orientation points upwards in z- direction (red arrows). With progressing time the probability to find the protein pointing in the direction $\mathbf{\Omega} = (\theta, \varphi)$ is smearing out about the initial orientation and, finally, for infinite times the probability density converges into a uniform density distribution,

$$\lim_{t\to\infty} P\left(\mathbf{\Omega}, t \mid \mathbf{\Omega}_0, t_0\right) = \frac{1}{4\,\pi}, \tag{4.131}$$

indicating that all orientations have equal probability (4^{th} spherical plot from the left in Fig. 4.10).

4.6.2 Diffusion of a Rigid Protein

In this section we will develop the intermediate scattering function of a single rigid protein performing both translational and rotational diffusion. In order to achieve that, we assume that both kinds of diffusive motion are uncoupled. Pointing into the solid angle $\mathbf{\Omega} = (\theta, \varphi)$ the orientation vector $\mathbf{u}(\mathbf{\Omega})$ represents the protein orientation. A physical representation for $\mathbf{u}$ might be the orientation of a static electric or magnetic dipole. We remind, that only hydrogen atoms of the protein significantly

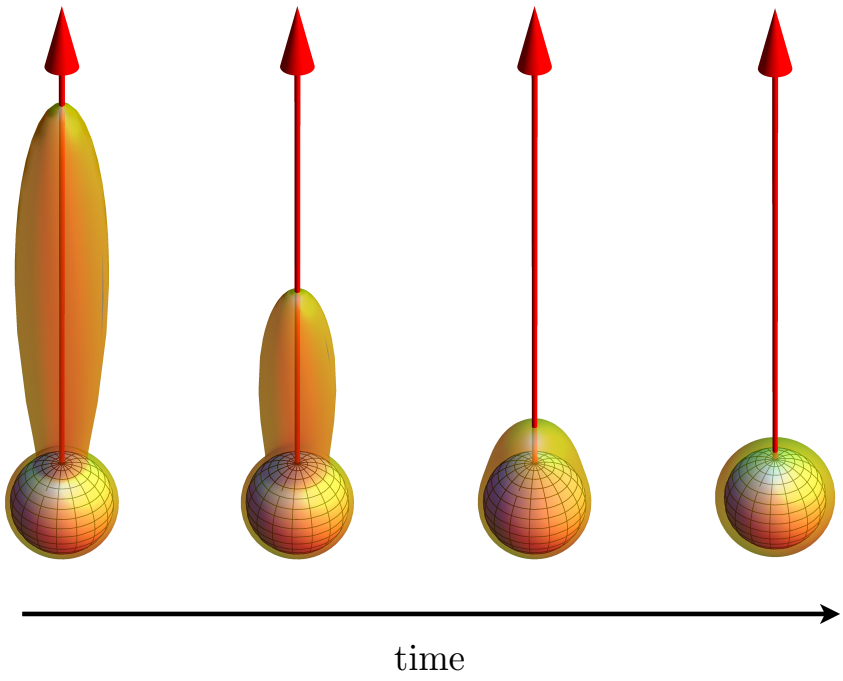

Figure 4.10: Time evolution of the probability density $P(\mathbf{\Omega}, t \mid \mathbf{\Omega}_0, t_0)$ Eq. 4.130 (transparent yellow hull) of the orientation $\mathbf{\Omega} = (\theta, \varphi)$ of a rigid protein. For better illustration, the probability density is superimposed on a unit sphere (wireframe in the interior of the hull). In other words: a spherical plot with radius $r(\mathbf{\Omega}) = 1 + P(\mathbf{\Omega}, t \mid \mathbf{\Omega}_0, t_0)$ is displayed. The initial orientation and the time progression are indicated by the red and the black arrows, respectively.

contribute to the incoherent scattering signal. Consequently, we calculate the incoherent intermediate scattering function only taking the position of the hydrogen atoms $\mathbf{R}_j$ into account. Using the orientation vector $\mathbf{u}$ the time-dependent position of the j^{th} hydrogen atom can be decomposed into

$$\mathbf{R}_j(t) = \mathbf{R}(t) + \mathbf{r}_j\left[\mathbf{\Omega}(t)\right] \tag{4.132}$$

therein, $\mathbf{R}$ is the position of the center-of-mass. The relative position $\mathbf{r}_j$ of the j^{th} hydrogen atom can be expressed in terms the orientation vector $\mathbf{u}$ having unit length as follows

$$\mathbf{r}_j[\mathbf{\Omega}(t)] = r_j\,\mathbf{u}\left[\mathbf{\Omega}(t) + \mathbf{\Omega}_j\right], \tag{4.133}$$

in which $\mathbf{\Omega}_j$ is the relative solid angle of the j^{th} hydrogen position to the orientation vector $\mathbf{u}$. Assuming independence of rotational and translational motion, the incoherent intermediate scattering function of a single protein factorizes into

$$\mathcal{I}_{\text{inc}}(\mathbf{q},t) = \mathcal{I}^T_{\text{inc}}(\mathbf{q},t)\,\mathcal{I}^R_{\text{inc}}(\mathbf{q},t), \tag{4.134}$$

in which

$$\mathcal{I}^T_{\text{inc}}(\mathbf{q},t) = \langle \exp\left[\mathrm{i}\,\mathbf{q}\,\left\{\mathbf{R}(t) - \mathbf{R}(0)\right\}\right]\rangle \tag{4.135}$$

is the tranlational contribution and

$$\mathcal{I}^R_{\text{inc}}(\mathbf{q},t) = \left\langle \frac{1}{N}\sum_{j=1}^{N} \exp\left[\mathrm{i}\,\mathbf{q}\,\left\{\mathbf{r}_j\left(\mathbf{\Omega}(t)\right) - \mathbf{r}_j\left(\mathbf{\Omega}(0)\right)\right\}\right] \right\rangle \tag{4.136}$$

the rotational contribution to the scattering function. According to Eq. 4.105 the translational part is $\mathcal{I}^T_{\text{inc}}(\mathbf{q},t) = \exp\left(-D_t\,Q^2\,|t|\right)$. For reasons of lucidity, we first calculate the summand of the rotational intermediate scattering function. Note, for readability we skip the index j

$$\langle \exp\left[\mathrm{i}\,\mathbf{q}\,\left\{\mathbf{r}\left(\mathbf{\Omega}(t)\right) - \mathbf{r}\left(\mathbf{\Omega}(0)\right)\right\}\right]\rangle = \tag{4.137}$$
$$\int\int \exp\left[\mathrm{i}\,\mathbf{q}\,\left\{\mathbf{r}\left(\mathbf{\Omega}\right) - \mathbf{r}\left(\mathbf{\Omega}_0\right)\right\}\right]\,P\left(\mathbf{\Omega},t\mid\mathbf{\Omega}_0\right)\,P\left(\mathbf{\Omega}_0\right)\,\mathrm{d}\mathbf{\Omega}\,\mathrm{d}\mathbf{\Omega}_0$$

Using the Green's function of the rotational diffusion equation Eq. 4.128 and the Boltzmann density distribution for the initial values $P\left(\mathbf{\Omega}_0\right) = 1/4\,\pi$ we obtain

$$= \frac{1}{4\,\pi}\sum_{l,m}\exp\left[-l\,(l+1)\,D_r\,t\right]\left|\int \exp\left[\mathrm{i}\,\mathbf{q}\,\mathbf{r}(\Omega)\right]\,Y_{l,m}(\mathbf{\Omega})\,\mathrm{d}\mathbf{\Omega}\right|^2. \tag{4.138}$$

In order to calculate the integral we make use of the following two lemmas

$$\int \exp\left(\mathrm{i}\,\mathbf{X}\,\mathbf{Y}\right)\,Y_{l,m}\left(\mathbf{\Omega}_\mathbf{X}\right)\,\mathrm{d}\mathbf{\Omega}_\mathbf{X} = 4\,\pi\,\mathrm{i}^l\,j_l(X\,Y)\,Y_{l,m}\left(\mathbf{\Omega}_\mathbf{Y}\right) \tag{4.139}$$

and

$$4\,\pi \sum_{m=-l}^{l} |Y_{l,m}(\mathbf{\Omega})| = 2\,l + 1. \tag{4.140}$$

We finally obtain the incoherent intermediate scattering function of a rigid protein,

$$\mathcal{I}^{\mathrm{R}}_{\mathrm{inc}}(q,t) = \sum_{l=0}^{\infty} B_l(q)\, \exp\left[-l\,(l+1)\,D_r\,|t|\right], \tag{4.141}$$

and by applying Fourier transform (see Table 4.3) the incoherent scattering function is obtained

$$\mathcal{S}^{\mathrm{R}}_{\mathrm{inc}}(q,t) = \sum_{l=0}^{\infty} B_l(q)\, \mathcal{L}\left[\omega, l\,(l+1)\,D_r\right], \tag{4.142}$$

in which $\mathcal{L}(\omega,\gamma) = \pi^{-1}\,\gamma/\left(\gamma^2+\omega^2\right)$ is a Lorentzian function and the coefficient

$$B_l(q) = (2\,l+1)\,\frac{1}{N}\sum_{j=1}^{N} j_l^2\,(q\,r_j) \tag{4.143}$$

describes the distribution of the hydrogen atoms within the protein. For convenience, we approximate the discrete sum by an integral using the radial distribution function of the hydrogen atoms in the protein $\rho_H(r)$ and obtain

$$B_l(q) = (2\,l+1)\int \rho_H(r)\, j_l^2(q\,r)\,\mathrm{d}r. \tag{4.144}$$

4.6.3 Rotational Diffusion Coefficient of a Protein

Modeling a rigid protein as an ellipsoidal spheroid, the orientation averaged rotational diffusion coefficient is according to Perrin [128, 90]:

$$D_r = \frac{k_B\,T}{3}\left(\frac{1}{C_a}+\frac{1}{C_b}+\frac{1}{C_c}\right). \tag{4.145}$$

Using the factors P_γ for $\gamma = a,b,c$ as described in Eq. 4.93 the rotational friction coefficients about the semi-principal axes $(a,0,0)$, $(0,b,0)$ and $(0,0,c)$ are

$$\begin{aligned} C_a &= \frac{16\,\pi}{3}\,\eta\,\frac{b^2+c^2}{b^2\,P_b + c^2\,P_c} \\ C_b &= \frac{16\,\pi}{3}\,\eta\,\frac{a^2+c^2}{a^2\,P_a + c^2\,P_c} \\ C_c &= \frac{16\,\pi}{3}\,\eta\,\frac{a^2+b^2}{a^2\,P_a + b^2\,P_b}. \end{aligned} \tag{4.146}$$

4.6.4 Coupling of Translational and Rotational Diffusion

For this study we assumed the decoupling of translational and rotational diffusion. We note that the employed experimental techniques in this study have not sufficient accuracy to resolve this coupling. However, for a more accurate picture the diffusion of a rigid protein in future studies, it is important to include the coupling of rotational and translation diffusion. This coupling is taken into account by the generalized Smoluchowski equation, which for N interacting spheres is

$$\frac{\partial}{\partial t} P = \frac{\partial}{\partial \mathbf{X}} \cdot \mathbf{D} \cdot \left[\frac{\partial P}{\partial \mathbf{X}} + \beta \frac{\partial u}{\partial \mathbf{X}} P \right], \tag{4.147}$$

therein, the location of the spheres are denoted by $\mathbf{X}_T = (\mathbf{R}_1, ...\mathbf{R}_N)$, and their orientation is described by $\mathbf{X}_R = (\mathbf{u}_1, ..., \mathbf{u}_N)$. The total configuration is summarized using the $6\,N$-dimensional vector $\mathbf{X} = (\mathbf{X}_T, \mathbf{X}_R)$. Hydrodynamic interactions are described by the $6\,N \times 6\,N$-diffusion tensor $D(\mathbf{X})$. The potential $u(\mathbf{X})$ includes interactions between particles depending on both orientation and position. The rotational part of the gradient operator is

$$\frac{\partial}{\partial \mathbf{X}_R} = \left(\frac{\partial}{\partial \mathbf{u}_1}, ..., \frac{\partial}{\partial \mathbf{u}_N} \right) \tag{4.148}$$

with

$$\frac{\partial}{\partial \mathbf{u}} = \mathbf{e}_\theta \frac{\partial}{\partial \theta} + \mathbf{e}_\varphi \frac{1}{\sin(\varphi)} \frac{\partial}{\partial \varphi}. \tag{4.149}$$

For a more detailed discussion of coupling of rotational and translational diffusion we refer to the publications of the following authors: Felderhof and Jones [53] studied the orientational relaxation of a colloidal suspension of spheres based on the generalized Smoluchowski equation. Jones [83] used the generalized Smoluchowski equation to describe the relaxation of position and orientation in a suspension of interacting spherical particles.

Chapter 5

Materials & Methods

Contents

In this chapter we review the materials and methods essential for the experiments conducted within the framework of this thesis. Sec. 5.1 provides an overview of the used materials. We describe the chemicals used for the sample preparation and summarize their properties, which are relevant for this thesis. Additionally, we will briefly comment on the sample cell and its material composition. Following the experimental procedures, we will then in-detail explain the sample preparation protocol for the investigated protein solutions in Sec. 5.2. A comprehensive overview of the employed instruments is contained in Sec. 5.3. Finally, Sec. 5.4 and Sec. 5.5 will present the treatment and analysis of the measured data, respectively. In particular, we will introduce two novel analytic frameworks in Subsec. 5.5.1 and Subsec. 5.5.2, which we have developed along this thesis.

Amino acid composition of Bovine Serum Albumin

Leucine	65	Proline	28
Lysine	60	Arginine	26
Glutamic acid	59	Tyrosine	21
Alanine	48	Glutamine	20
Aspartic acid	40	Glycine	17
Valine	38	Histidine	17
Cysteine	35	Isoleucine	15
Threonine	34	Asparagine	14
Serine	32	Methionine	5
Phenylalanine	30	Tryptophan	3

Table 5.1: Amino acid composition of *bovine serum albumin*, which has the chemical formula $C_{3071}H_{6038}N_{816}O_{1533}S_{40}$. The primary structure was obtained from [35].

5.1 Materials

5.1.1 Bovine Serum Albumin

Biological Role

Bovine Serum Albumin (BSA and HSA, respectively) widely serve as model proteins in biochemistry and biophysical studies due to their low cost, high abundance and stability. We briefly review the importance of serum albumin in biology. In the circulatory system with a usual blood concentration of 50 mg/ml, serum albumin controls the colloid osmotic blood pressure [29]. Serum albumin has a high capacity to bind water, Ca^{2+}, Na^{+}, K^{+}, fatty acids, hormones, bilirubin and drugs. In the plasma, it generally binds about 80 % of all zinc and thereby acts as a major transporter of zinc. Furthermore, serum albumin plays the role of a weak acid and participates in acid-base balance to stabilize the pH value of the blood [56]. In the following subsections we describe only those properties that are relevant for this study. For an exhaustive review about albumin we refer to [29].

Structure and Shape

BSA is composed of 607 amino acids (see Table 5.1), closely packed into a heart-shaped form [97]. To the author's knowledge there is no crystallographic structure of BSA available. However, Weggler et al. [175] constructed a homology model of BSA based on the known crystal structure of HSA. Fig. 5.1 shows a superposition of the secondary and atomistic structure of this homology model for BSA. A small number

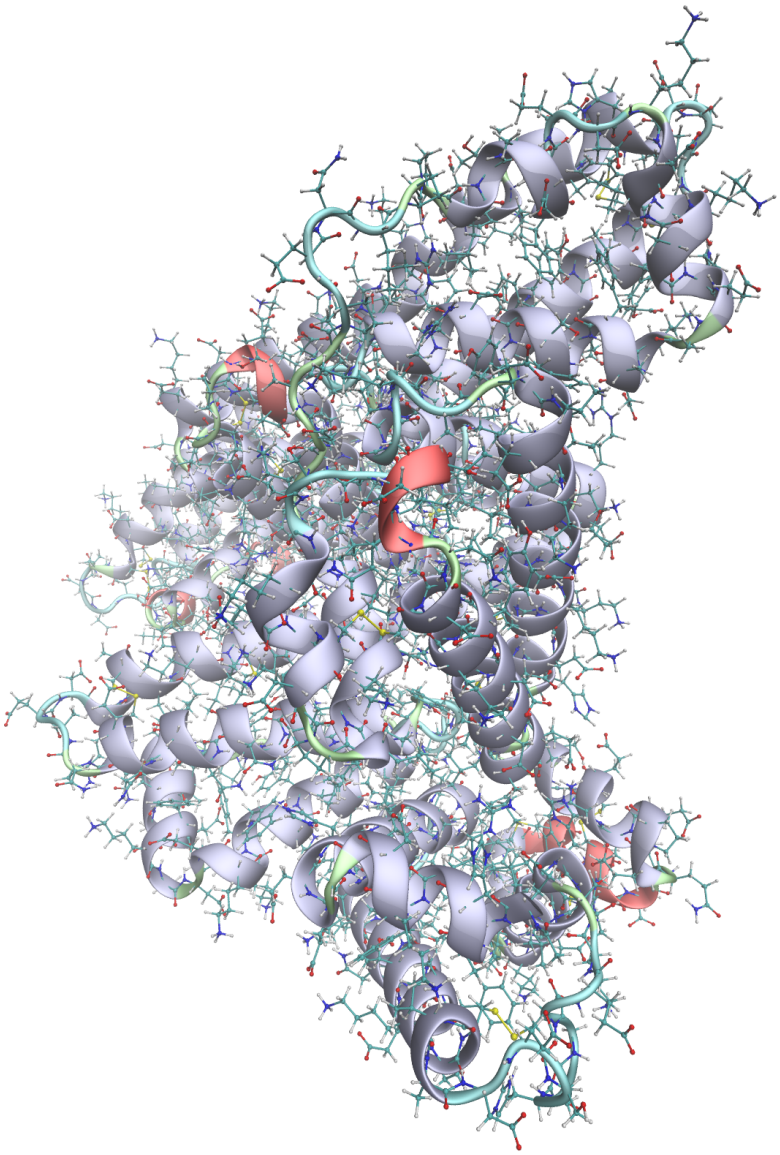

Figure 5.1: Homology model of *bovine serum albumin* in solution calculated at pH 7 [175]. Superimposed to the atomistic structure with atomic bonds indicated by sticks is a cartoon drawing of the secondary structure. The secondary structure is color coded as follows: α-helix (ice blue), 3_{10}-helix (red), turn (cyan), coil (lime). The illustration was rendered using VMD [77].

of polypeptides occur in 3_{10}-helices (red), turns (cyan) and coils (lime color) whilst α-helices (ice blue) dominate the secondary structure. Remarkably, there are no β-sheets. From small-angle X-ray scattering measurements on BSA aqueous (D_2O) solutions Roosen-Runge et al. [137] derived that an oblate ellipsoidal with polar semi-axis $a = (1.8 \pm 0.05)\,\mathrm{nm}$ and equatorial semi-axis $b = (4.6 \pm 0.15)\,\mathrm{nm}$ describes the shape of a BSA molecule in solution.

Hydration Shell and Volume Fraction

When dissolved in water a protein, such as BSA, changes its structure and a shell of hydrogen-bonded water molecules forms around the molecular surface [104]. Since the hydration shell sticks to the protein and, thereby, changes its hydrodynamic properties, an accurate knowledge of its size is essential for the investigation of the dynamic behavior. A crucial parameter for the comparison of colloidal diffusion models with measured diffusion coefficients is the protein volume fraction φ. In the following we outline how to compute φ for a given protein concentration c. A more comprehensive analysis is explained in Appendix A.3. In the sample preparation process we dissolved BSA with mass m in D_2O with volume V to obtain the protein concentration $c = m/V$. With it the volume fraction of BSA reads

$$\varphi = \frac{c\left(\vartheta + \frac{\eta}{\rho_{D_2O}}\right)}{1 + c \cdot \vartheta}, \tag{5.1}$$

therein $\vartheta = 0.735\,\mathrm{ml/g}$ is the apparent specific volume for the native structure of BSA in solution [96] and $\eta = 0.4$ g D_2O/g BSA is the hydration level, taken as the average of published values [92, 44, 135]. The temperature dependence of the density of heavy water ρ_{D_2O} can be found in [70].

Surface Charge

At neutral pH BSA is soluble in D_2O at very high volume fractions of up to 30 % due to the surface charge, which prevents aggregation. We observed that our samples at neutral pH do not display any precipitate even after several months of storage. At pH 7 the surface charge is $Z = -11$ [21] and consequently, due to the strong charge stabilization, we can assume that the BSA solution consists mainly of monomers [78]. Tanford et al. [159] investigated the dissociation of H^+ from BSA. They concluded that the surface charge of BSA is primarily due to bound H^+-ions and those that dissociated from the proteins surface, but also influenced by bound salt ions. Zhang et al. [184] have shown that Y^{3+} is strongly bound to the protein surface and can cause charge inversion. For NaCl, Scatchard et al. [144] showed that Cl^- is bound to the protein surface, whereas Na^+ is not.

Coefficients for Viscosity Formula

Solvent	C [Pa·s]	a [K^{-2}]	b [K^{-3}]	c [K^{-4}]	γ	T_0 [K]
D_2O	8.86	$2.80 \cdot 10^{-3}$	$-1.63 \cdot 10^{-5}$	$2.91 \cdot 10^{-8}$	1.55	231.83
H_2O	8.02	$3.47 \cdot 10^{-3}$	$-1.74 \cdot 10^{-5}$	$2.77 \cdot 10^{-8}$	1.53	225.33

Table 5.2: Parameters for the empirical formula Eq. 5.2 describing the viscosity of water in dependence of the temperature.

5.1.2 Water

In this section, we focus only on the physical parameters of water, which are relevant for this study. For thermal neutrons the scattering cross-section of hydrogen is much larger than the cross-section of deuterium (compare with Table 4.2). Therefore, instead of using H_2O as solvent, D_2O is used to increase the scattering contrast between solvent and solute. On the diffusive time scale, water acts as a featureless matrix and its impact on the motion of the proteins is described by a viscosity constant, which determines the strength of hydrodynamic interactions. The temperature dependence of the viscosity of water was determined by Cho et al. [32] in form of an empirical formula

$$\eta_0(T) = C\,(\Delta T + a\,\Delta T^2 + b\,\Delta T^3 + c\,\Delta T^4)^{-\gamma}, \tag{5.2}$$

with $\Delta T = T - T_0$. The corresponding empirical parameters for D_2O and H_2O are listed in Table 5.2. In the presence of salts the viscosity changes with the salt concentration c_s for $c_s < 0.5M$ according to the Jones-Dole Formula:

$$\eta\,(c_s, T) = \eta_0(T)\;(1 + A\,\sqrt{c_s} + B\,c_s)\,, \tag{5.3}$$

therein the parameters A and B can be found for different ions in a comprehensive review from Jenkins and Marcus [81]. On the energy and q range of the spectrometers IN10 and IN16 the dynamic structure factor $S(q,\omega)$ of D_2O has a pronounced coherent component (compare Table 4.2) and is nearly flat on the energy axis due to the fast translational diffusion of D_2O molecules comparable to H_2O [160]. $S(q,\omega)$ can be approximated by a background $B(q)$ peaked at $q \approx 1.9\,\text{Å}^{-1}$ [16].

5.1.3 Resolution Calibration Sample

Vanadium is a strong elastic incoherent scatterer (Table 4.2) and serves as a standard to determine both the resolution function and the efficiency of the detectors of a neutron backscattering instrument. Furthermore, the peak of the vanadium line is used as the zero-position for the energy channels. In the following we explain how

Composition of Aluminum Alloy

Si	Fe	Cu	Mn	Mg	Cr	Zn	Ti	Al
$0.3 - 0.6$	$0.1 - 0.3$	0.1	0.1	$0.35 - 0.6$	0.05	0.15	0.1	$98 - 98.75$

Table 5.3: Aluminum alloy composition of sample cells in mass %. The alloy have a linear attenuation coefficient for thermal neutrons of $\Sigma = 0.011\,\mathrm{mm}^{-1}$ due to scattering and absorption. For comparison 100 mg/ml and 500 mg/ml aqueous (D_2O) BSA solution have a linear attenuation coefficient $0.11\,\mathrm{mm}^{-1}$ and $0.22\,\mathrm{mm}^{-1}$, respectively.

those two important instrumental quantities can be determined from the scattering function of a vanadium standard. The theoretical incoherent scattering function of vanadium in the μeV energy regime is:

$$\mathcal{S}^{\mathrm{V}}_{\mathrm{inc}}(q,\omega) = \exp\left[-\left\langle u^2\right\rangle_T q^2\right]\,\delta(\omega) \tag{5.4}$$

where $\left\langle u^2\right\rangle_T$ is the temperature dependent mean-squared displacement, which for $T = 296\,\mathrm{K}$ is $\left\langle u^2\right\rangle_T = (6.7 \pm 0.6)\cdot 10^{-3}\,\mathrm{\AA}^2$ [85]. Hence, for the q-range of typical backscattering spectrometers, $0.2\,\mathrm{\AA}^{-1} \leq q \leq 2\,\mathrm{\AA}^{-1}$ (IN10 and IN16), we can assume that the Debye-Waller exponent in Eq. 5.4 is negligible at ambient temperatures. Consequently, the vanadium signal can be approximated by a delta function with a q-independent peak intensity. The corresponding measured partial differential cross-section is

$$\frac{\partial^2\sigma}{\partial\mathbf{\Omega}\partial E'}(\mathbf{q},\omega) \approx \frac{\|\mathbf{k}+\mathbf{q}\|}{\|\mathbf{k}\|}\frac{N_{\mathrm{V}}\,\sigma^{\mathrm{V}}_{\mathrm{inc}}}{4\,\pi\,\hbar}\,\delta(\omega). \tag{5.5}$$

in which N_{V} is the number of vanadium nuclei with incoherent scattering cross-section $\sigma^{\mathrm{V}}_{\mathrm{inc}}$ in the scattering volume by the neutron beam. $\mathbf{k}$ is the wavevector of the incoming neutron.

5.1.4 Sample Cell

For the neutron scattering experiments we filled the protein solutions into cylindric thin-walled aluminum containers (Fig. 5.2a) with an outer diameter 23 mm and gap width 0.23 mm. The gap of 0.23 mm between the cylinder walls is chosen such that neutrons for a 500 mg/ml aqueous (D_2O) BSA solution, our highest protein concentration, are scattered with a probability of approximately 9.9 %. Consequently, we reduce multiple scattering effects, because the probability for scattering twice is for less concentrated sample less than 1 %. Fig. 5.2b exemplifies that aluminum is

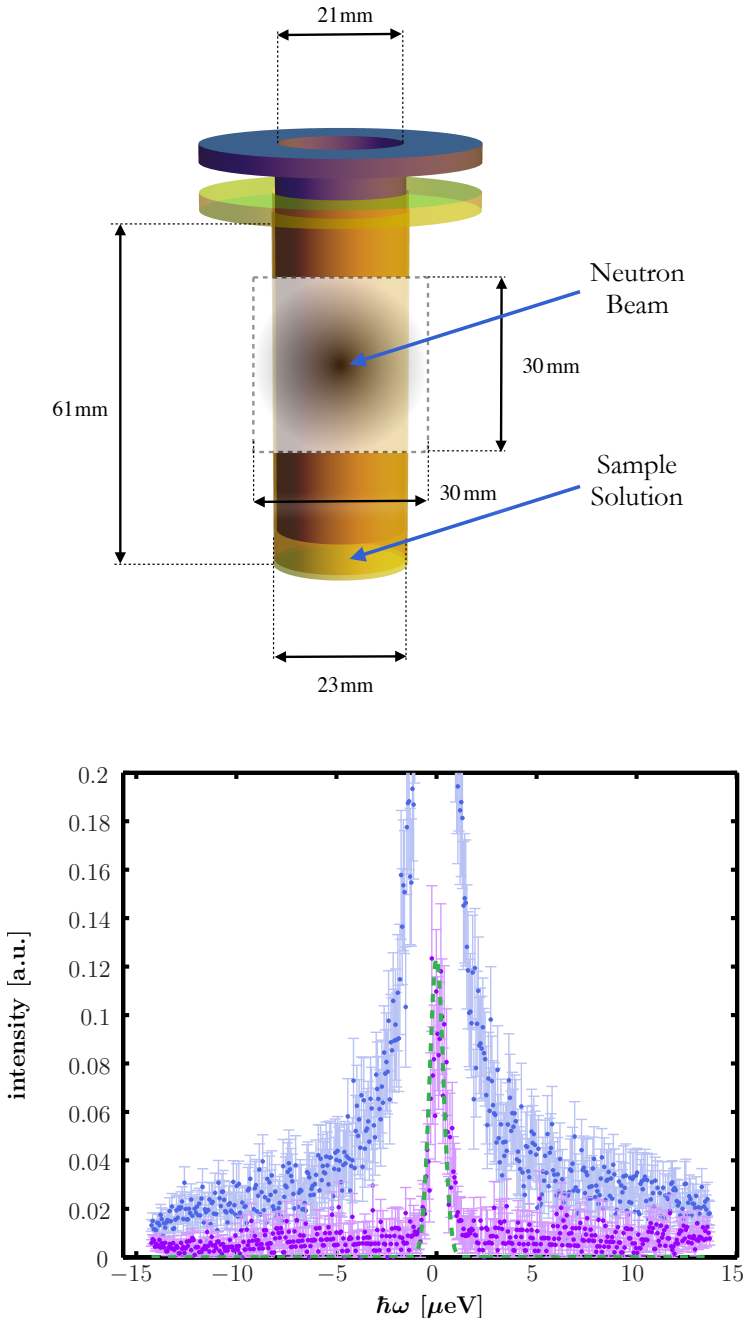

Figure 5.2: Upper image: Aluminum sample holder consisting of an inner (gray) cylinder and outer (transparent yellow) cylinder. Approximately 2 ml of the sample solution is filled into the outer cylinder and thereafter the inner cylinder is mounted such that the sample is squeezed between the inner and outer wall of the cylinders. A cross-section of the neutron beam for IN10/IN16 is approximately $3 \times 3\,\mathrm{cm}^2$ (square with dashed boundary line), hence the sample cell must be positioned in the beam such that most of the sample solution is illuminated. Lower image: Quasi-elastic spectrum for $q = 0.81\,\text{Å}^{-1}$ recorded at IN16 of the empty cylinder (purple circles) compared to the sample spectrum of a BSA 177 mg/ml aqueous (D_2O) solution with 0.118 M YCl_3 at 280 K (light blue circles). The green dashed line denotes a gaussian model of the resolution function scaled to the empty cylinder spectrum. Note that the intensity of the sample spectrum is scaled to unity.

Eppendorf Pipette precision

volume [μl]	volume increment [μl]	systematic error [%]	error [%]
200 μl pipette			
50	0.2	± 1	≤ 0.3
100		± 0.9	≤ 0.3
200		± 0.6	≤ 0.2
1000 μl pipette			
100	1	± 3	≤ 0.3
500		± 1	≤ 0.2
1000		± 0.6	≤ 0.2

Table 5.4: Volume error of the two different pipettes from *Eppendorf* used for the sample preparation.

a weak elastic coherent scatterer (compare Table 4.2) within the quasi-elastic energy range. Since the Debye-Waller factor is nearly unity in the temperature range $280 - 380\,\mathrm{K}$ and for the typical momentum transfer values accessible by IN10 and IN16 [88], it is sufficient to measure the background only for a single temperature.

5.2 Sample Preparation

For all measurements we purchased BSA powder with a purity of 99 % and anhydrous YCl_3 powder with a purity of 99.99 % from the *Sigma-Aldrich®* company (product codes: A3059 and 451363, respectively) and stored it in a cold room at temperature slightly less than 8°C. D_2O with a purity of 99 % was kindly provided by the *Institut Laue-Langevin*. Several days prior to the experiment we prepared the samples as follows:

- Using an analytic balance with a precision of $\pm 0.1\,\mathrm{mg}$ we weighted the mass m of BSA powder and filled it in 4 ml glass vials by using a metal spatula.
- For samples without salt we added the volume V of pure D_2O using 1000 μl pipette from *Eppendorf*. The manufacturer declares a volume precision as stated in Table 5.4. For the samples with salt we prepared a stock solution

with the highest salt concentration of the sample batch. We then added pure D_2O and stock solution to the BSA such that the required salt solution was achieved. When small volume quantities were needed we used additionally a $200\,\mu l$ pipette.

- ☐ We closed the glass vials with lids and sealed them additionally with paraffin strips wrapped tightly around the lid.

- ☐ For several hours we homogenized the sample solutions with a laboratory shaker until the BSA was completely dissolved.

- ☐ We dispensed approximately 1.3 ml of the sample solution into the aluminum cylinder using the $1000\,\mu l$ pipette. The filling procedure must be done very slowly and carefully to prevent air bubbles. If there were any air bubbles, we aspirated them with the pipette. When the filling was done, we slowly mounted the inner into the outer cylinder, such that the solution was homogeneously distributed between the container walls. Finally we sealed the sample cell against vacuum with indium wire and screwed the inner and outer cylinder together with aluminum screws.

Mounted on a sample stick with temperature control the aluminum sample holder was then put in the cryostat of the respective neutron spectrometer.

5.3 Instruments

In this section we briefly explain how cold neutrons are generated and delivered to the instruments. Then, we will shed light on the principles of both cold neutron backscattering and spin-echo spectrometry, since both techniques, particularly the first one, were mainly used for studying the diffusive dynamics of proteins in solutions. In the final part of this section, we will additionally explain the setup of a X-ray small-angle scattering instrument which we used for complementary measurements. For a comprehensive description of the synchrotron-based production of X-rays we refer to the textbook by Als-Nielsen and McMorrow [6].

Reactor-based nuclear fission using for instance enriched uranium and accelerator-based spallation using a metal target such as uranium, tungsten, lead or mercury, serve as main sources to provide a high-flux neutron beam. The Institut Laue-Langevin, where we conducted the majority of our experiments, employs the first mentioned technique to produce a continuous high-flux neutron beam. As fuel element serves an enriched uranium core with a content of 93% of the ^{235}U isotope. Initially, the fission-generated neutrons have energies of a few MeVs. However, the energy transfers in matter are in the μeV – meV energy regime. Consequently, using a D_2O moderator the highly energetic neutrons are thermalized and the average thermal flux is $\Phi_0 = 1.5{\cdot}10^{15}$ neutrons per second. The neutron velocity distribution

is approximately governed by a Maxwellian density function,

$$\Phi(v) = \Phi_0 \frac{1}{2} \left(\frac{m}{k_B T} \right) v^3 \exp\left(-\frac{m v^2}{2 k_B T} \right). \tag{5.6}$$

Therein, m is the mass of a single neutron and v its velocity. For the investigation of translational as well as rotational diffusion of the BSA in the sample solution, we used cold neutrons having a narrow energy distribution around $E_0 = 2.08\,\mathrm{meV}$. Shifting the energy of the thermalized reactor-neutrons to even lower temperatures produces these cold neutrons. Therefore a second moderator, consisting of 2.5 l of liquid deuterium at a temperature of 25 K is used. The liquid deuterium is confined in an aluminum sphere immersed in the D_2O of the first moderator near the uranium core. Subsequently, the cold neutrons are delivered to the instrument by zigzagging through the neutron guide by means of total external reflections on nickel-titanium multilayers.

5.3.1 Cold-Neutron Backscattering Spectrometer

Maier-Leibnitz and Springer [103] discussed for the first time the feasibility and possible usefulness of a neutron spectroscopy for cold neutrons and thereby initiating the development of the neutron backscattering technique [5, 58, 60].

By operating in the so-called “inverse spectroscopy" mode, backscattering spectrometers achieve particularly high energy resolutions. This kind of spectrometer only detects neutrons within a very narrow energy range around a precise value. Different energy transfers by the sample can be detected by varying the energy of the initial neutrons around this value using a Doppler monochromator.

The achievable energy range of a couple of μeV and the high energy (in the order of μeV) resolution renders cold neutron backscattering instruments suitable for the investigation of the diffusive motion of proteins in solution [141]. For the experiments we will present in Chap. 7 till 9 we used the IN10 and IN16 backscattering spectrometer at the Institut Laue-Langevin (Grenoble, France) with the setup shown in Table 5.5.

Before we will illustratively follow the trajectory of a neutron through a backscattering spectrometer, we will briefly review the essential theory important for the understanding of monochromators and analyzers, the most important components in a backscattering spectrometer. To this end, we will begin with a description of Bragg reflection, then explain the principle of a Doppler monochromator and finally elucidate the operation mode of neutron detector.

Bragg Reflection at Monochromator & Analyzer

For a comprehensive review of the concepts used in the following theoretical section we refer to the textbook about solid state physics by Ashcroft and Mermin [10]. In order to explain the intensity peaks of X-rays elastically scattered from a perfect crystal lattice, W. L. Bragg [173] derived the subsequent law

Neutron Backscattering Spectrometers

Instrument	IN10	IN16
Detector	7 ^{3}He counters 1 monitor	20 ^{3}He counters 1 monitor
Monochromator	Si(111)	Si(111)
Analyzer	Si(111)	Si(111)
Beam size at sample [cm^2]	3.5×3.5	3×4
Flux at sample [n cm^{-2} s^{-1}]	$\approx 2 \cdot 10^4$	$\approx 5 \cdot 10^4$
Incident energy [meV]	2.08	2.08
Energy resolution δE [μeV]	0.9	0.9
Energy transfer range E [μeV]	$-10 \ldots 10$	$-15 \ldots 15$
Elastic q-range [Å^{-1}]	$0.50 \ldots 1.96$	$0.24 \ldots 1.85$
Accessible time scale τ [ns]	$0.41 \ldots 4.56$	$0.28 \ldots 4.60$
Accessible length scale l [nm]	$0.32 \ldots 1.26$	$0.34 \ldots 2.62$

Table 5.5: Configuration of the cold neutron backscattering spectrometers IN10 and IN16 at the Institut Laue-Langevin (Grenoble, France) as used for the experiments reported in this thesis. For a comprehensive overview of the possible setups of both instruments we refer to Refs. [59] and [79]. Note, for both instruments the resolution function can be adequately modeled by a Gaussian line shape with a full width at half maximum of δE. We calculate the accessible time and length scales of the instruments as follows: $2\pi\hbar/E_{\max} \leq \tau \leq 2\pi\hbar/\delta E$ and $2\pi\hbar/q_{\max} \leq l \leq 2\pi\hbar/q_{\min}$, receptively. In paper A and paper B (see Chaps. 7 and 8) we use IN10 and IN16 to investigate the short-time self-diffusion coefficient of the globular protein BSA by analyzing the q-dependence of the line width of the scattering signal. In paper C (see Chap. 9) we employ the elastic fixed window mode of IN10 to study the temperature-induced denaturation of BSA.

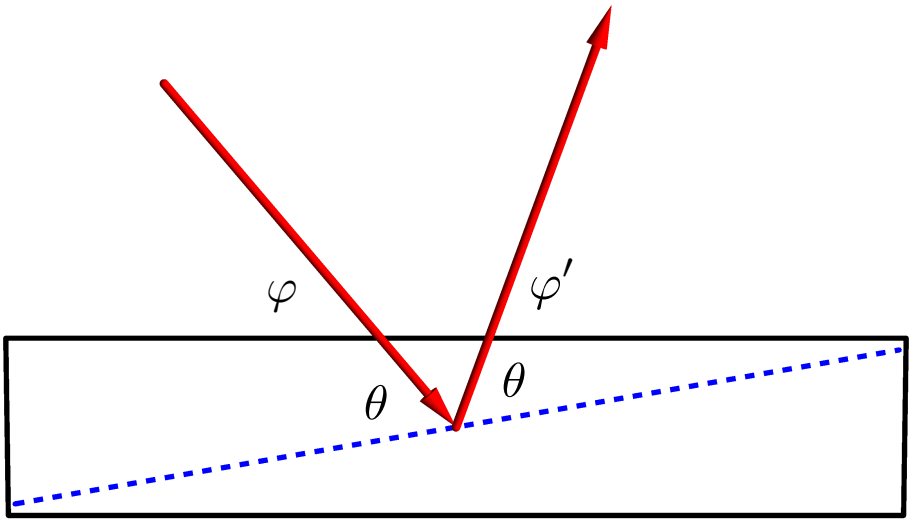

Figure 5.3: Reflection of a neutron beam (red arrows) from a Bragg plane (blue dashed line) at an angle θ. For reasons of generality the Bragg plane is not parallel to the surface of the crystal slap (black rectangle). The incident angle of the neutron beam and the angle of the reflected neutron beam, are φ and φ', respectively. Note, that for the crystal of the analyzers and the monochromator of a backscattering spectrometer the Bragg plane of the reflection is parallel to the surface of the crystal slap.

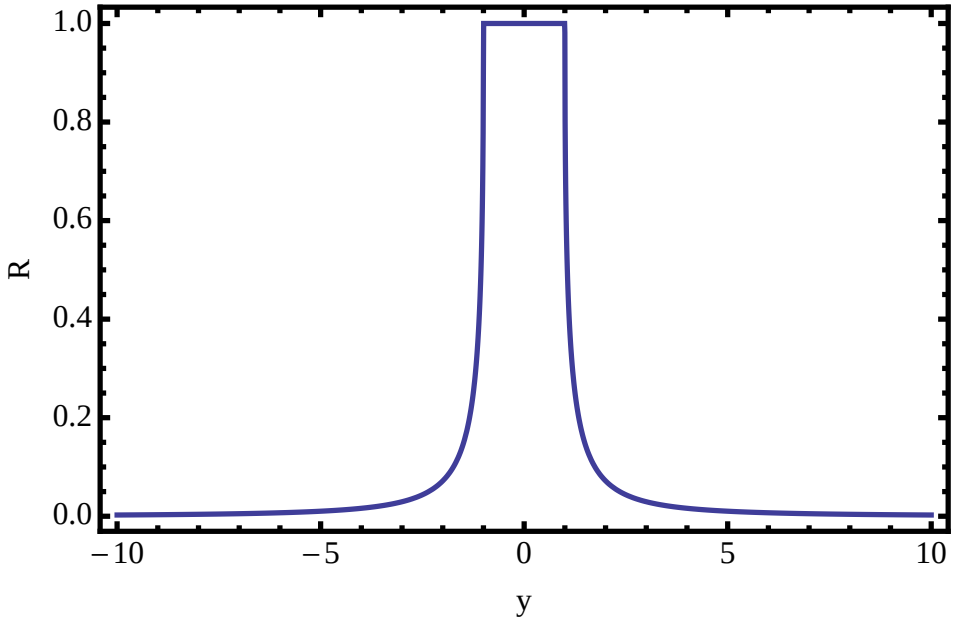

Figure 5.4: Reflection curve $R(y)$ of a perfect crystal calculated with Eq. 5.10. The dimensionless variable y is defined by Eq. 5.11. Within the interval $|y| < 1$ the reflectivity curve has a plateau.

$$\|\mathbf{G_h}\|\ \lambda = 4\,\pi\ \sin\left(\theta_{\text{Bragg}}\right), \tag{5.7}$$

in which λ is the wavelength of the incident X-rays, θ_{Bragg} the reflection angle and $\mathbf{G_h}$ the reciprocal lattice vector perpendicular to the lattice plane, denoted by the Miller indices $\mathbf{h} = (h_1, h_2, h_3)$, on which the X-rays are scattered. The later known as Bragg's law applies equally to the scattering intensity of neutrons.

In reality the wavelength λ and the incident angle θ of a neutron beam are not well defined and therefore their uncertainties are characterized by a wavelength error $\Delta\lambda$ and angular deviation $\Delta\theta$, respectively. Based on Bragg's law the basic idea of backscattering is to select the mean incident angle θ such that the wavelength error of the reflected beam is minimized. Applying 2^{nd}-order error propagation on Eq. 5.7 the relative width of the reflected wavelength band $\Delta\lambda$ reads

$$\frac{\Delta\lambda}{\lambda} = \frac{\Delta G_{\mathbf{h}}}{G_{\mathbf{h}}} + \Delta\theta\,|\cot(\theta)| + \frac{1}{2}\,\Delta\theta^2 + \frac{\Delta G_{\mathbf{h}}}{G_{\mathbf{h}}}\left[\frac{\Delta G_{\mathbf{h}}}{G_{\mathbf{h}}} + \Delta\theta\,|\cot(\theta)|\right], \tag{5.8}$$

with $G_{\mathbf{h}} = \|\mathbf{G_h}\|$. In order to facilitate the readability, we colorize the 1^{st}-order term of the error in blue. Consequently, selecting $\theta = 90°$ the wavelength error is in 1^{st}-order independent of the beam divergence and simplifies to

$$\frac{\Delta\lambda}{\lambda} = \frac{\Delta G_{\mathbf{h}}}{G_{\mathbf{h}}} + \frac{1}{2}\,\Delta\theta^2 + \frac{\Delta G_{\mathbf{h}}^2}{G_{\mathbf{h}}^2}. \tag{5.9}$$

In the following we will rewrite the parameter $\Delta G_{\mathbf{h}}/G_{\mathbf{h}}$ in terms of properties of the perfect crystal. Darwin [36] showed that even for a perfect crystal $\Delta G_{\mathbf{h}}/G_{\mathbf{h}}$ has a finite value caused by primary extinction. For a perfect crystal with negligible absorption, the reflectivity is [183]

$$R(y) = \begin{cases} 1 & \text{if } |y| < 1 \\ \left(|y| - \sqrt{y^2 - 1}\right)^2 & \text{if } |y| \geq 1 \end{cases}, \tag{5.10}$$

in which the variable y is given by

$$y = \frac{(1-b)\,\psi(\mathbf{0}) + E\,\alpha\,b}{2\sqrt{|b|}\;|\psi(\mathbf{G_h})|}. \tag{5.11}$$

For the case of neutrons the parameters in the above expression are

$$\psi(\mathbf{G_h}) = \frac{h}{m} N_c\, F(\mathbf{G_h}) \tag{5.12}$$

$$E = \frac{\hbar^2 k^2}{2m} \tag{5.13}$$

$$b = \frac{\cos(\varphi)}{\cos(\varphi')}, \tag{5.14}$$

in which $F(\mathbf{G_h})$ is the structure factor of the unit cell, reading

$$F(\mathbf{G_h}) = b_c \exp\left[-\frac{(u_0\,|\mathbf{G_h}|)^2}{2}\right] \sum_{\mathbf{r}\in V} \exp(2\,\pi\,\mathrm{i}\,\mathbf{G_h}\,\mathbf{r}), \tag{5.15}$$

N_c is the number density of unit cells, u_0 is the root-mean-squared displacement of the atom perpendicular to the Bragg planes, and E is the energy of the neutrons (compare Eq. 4.19). For reasons of clarity, the angles φ and φ' are illustrated in Fig. 5.3. The parameter α in the case of variation of the wavevector $\mathbf{k}$ of the neutron is according to [183]

$$\alpha = 4\,\frac{k - k_{\mathrm{Bragg}}}{k_{\mathrm{Bragg}}} \tag{5.16}$$

in which $k = \|\mathbf{k}\|$ and k_{Bragg} is obtained from Bragg's law $G_{\mathbf{h}} = 2\,k_{\mathrm{Bragg}}\sin(\theta_B)$. With this we finally obtain for the width of the plateau, which is shown in Fig. 5.4, of the reflection curve Eq. 5.10:

$$\Delta y = \frac{\Delta G_{\mathbf{h}}}{G_{\mathbf{h}}} = \frac{16\,\pi\,N_c\,|F(\mathbf{G_h})|}{G_{\mathbf{h}}^2}. \tag{5.17}$$

$\Delta G_{\mathbf{h}}/G_{\mathbf{h}}$ is often called the "radial" mosaic distribution caused by primary extinction in analogy to the mosaic spread of imperfect crystals. For the energy error

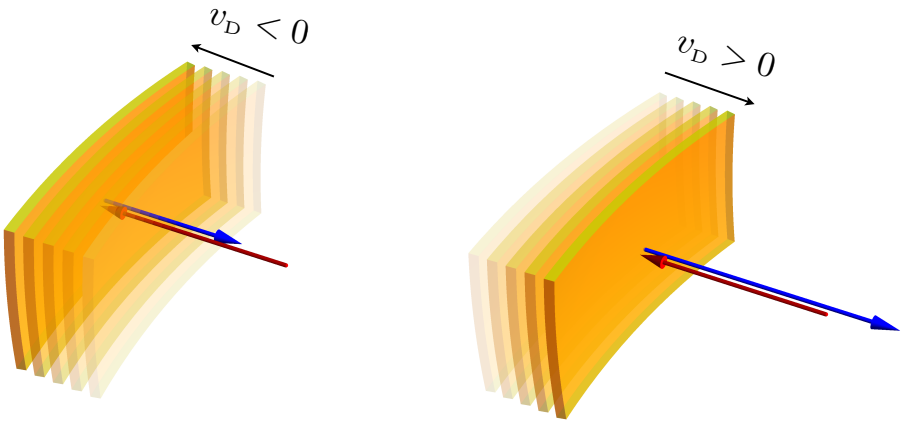

Figure 5.5: The principle of a Doppler monochromator: An incident neutron beam (red arrow) is backscattered (blue arrow) on a moving single crystal slap (yellow spherical element). Note the path of the Doppler monochromator is illustrated by the superposition of time shots. The transparency level of the illustrated crystal slap is higher if the time shots are further into the past. Left image: The monochromator velocity is parallel to the direction of the incoming beam (red arrow) hence the energy of the reflected neutrons (blue arrow) is decreased. Right image: The monochromator velocity is antiparallel to the direction of the incident beam (red arrow) therefore the energy of the reflected neutrons (blue arrow) is increased. Note the energy of the neutrons corresponds to the length of the arrows.

$\Delta E = 2\,E\,\Delta\lambda/\lambda$ we obtain using Eq. 5.9 in the case of backscattering [59]

$$\Delta E = \frac{\hbar^2}{m}\,4\,\pi\,N_c\,|F\,(\mathbf{G_h})| + \frac{\hbar^2\,G_{\mathbf{h}}^2}{8\,m}\,\Delta\theta^2 + \frac{64\,\hbar^2\,\pi^2\,N_c^2\,|F\,(\mathbf{G_h})|^2}{m\,G^2} \tag{5.18}$$

Consequently, in the backscattering geometry the energy resolution depends only on two crystal parameters. The IN10 and IN16 spectrometers employ Si(111) single crystals for the monochromator and analyzers (see Table 5.5). For both instruments the angular beam divergence is approximately $\Delta\theta = 3°$. Using the above formulas with constants from Ref. [149] related to Si(111) the energy error is $\Delta E = (0.076 + 0.145)\,\mu$eV. This value significantly underestimates the real energy resolution of IN10 and IN16 of approximately $0.9\,\mu$eV (see Table 5.5). We attribute this difference to the following missing contributions to ΔE: Firstly, the beam has a cross-section of $4 \times 4\,\mathrm{cm}^2$, which effectively increases $\Delta\theta$ and, secondly, the Si(111) crystals are not perfect crystal since they are spherically bent (compare Fig. 5.7) and therefore have a mosaic spread, which additionally increases $\Delta G_{\mathbf{h}}/G_{\mathbf{h}}$.

Doppler Monochromator

Next, we describe how to vary the energy of the neutron with a moving monochromator crystal. For a detailed analysis of the Bragg reflection of neutrons from a moving crystal we refer to the publication by Hennig et al. [72] and references therein. The energy of neutrons E' reflected from a Bragg plane with reciprocal lattice vector $\mathbf{G_h}$ of a moving crystal is

$$E' = E + \hbar\,\mathbf{G_h}\cdot\mathbf{v}_\mathrm{D} \tag{5.19}$$

in which E is the energy of the incident neutrons and $\mathbf{v}_\mathrm{D}$ is the velocity of the moving crystal. Fig. 5.5 illustrates the reflection of neutrons from a moving crystal for the case of backscattering. The energy of the reflected neutrons is increased or decreased depending wether the direction of the incident neutrons is antiparallel or parallel, respectively. The energy E' of neutrons reflected from a crystal with the Bragg plane moving parallel or antiparallel to the beam direction simplifies to

$$\begin{aligned} E' &= E + \hbar\,v_\mathrm{D}\,\frac{2\,\pi}{\lambda} + 2\,m\,v_\mathrm{D}^2 && (5.20)\\ &\approx E + \hbar\,v_\mathrm{D}\,\frac{2\,\pi}{\lambda}, && (5.21)\end{aligned}$$

in which λ is the wavelength of the incident neutrons. At IN10 and IN16 the Doppler monochromator velocity has a sine profile, with maximal velocities of $1.57\,\mathrm{m/s}$ (IN10) and $2.3\,\mathrm{m/s}$ (IN16), respectively, corresponding to maximum energy changes of the incident neutrons of $\pm 10\,\mu\mathrm{eV}$ and $\pm 15\,\mu\mathrm{eV}$.

^{3}He-Detector

At the backscattering instruments IN10 and IN16, the detection of cold and thermal neutrons is realized by ^{3}He detectors. Fig. 5.6 illustrates schematically the design and the principle of such a detector. A neutron passes through an aluminum entrance window (yellow transparent disk) and enters a cylindrical ionization chamber filled with ^{3}He. The cylinder is shielded with cadmium to prevent the count of neutrons not entering the aluminum window (gray transparent cylinder). Between the cylinder cathode and the anode (red line) there is a strong electric field. When a neutron enters through the aluminum window, it is absorbed by a ^{3}He molecule causing the following nuclear reaction,

$$^3_2\mathrm{He} + \mathrm{n}(2.08\,\mathrm{meV}) \longrightarrow\ ^3_1\mathrm{H}^-(191\,\mathrm{keV}) + \mathrm{p}(573\,\mathrm{keV}), \tag{5.22}$$

thereby, the tritium ion and the proton are emitted in opposite directions since the energy of the neutron is comparably small. The emitted proton is heavily ionizing and travels through the chamber thereby leaving a trail of ion pairs along its trajectory, making the gas conductive. This conduction is amplified by a cascading effect due to the strong electric field. This causes an impulse, which is detected by the acquisition electronics.

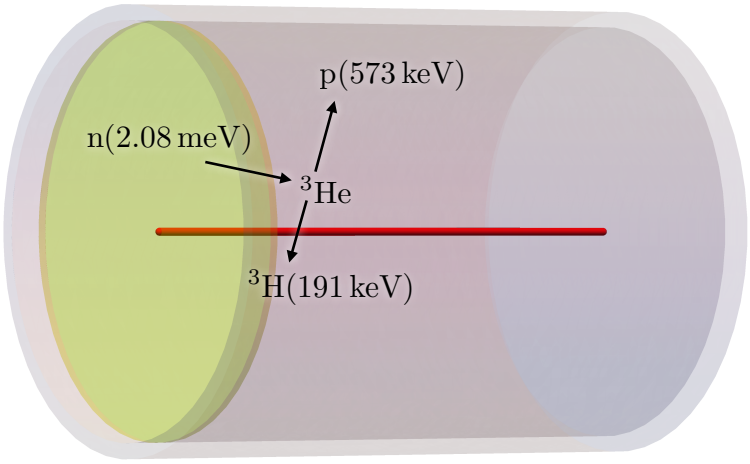

Figure 5.6: Schematic of a ^{3}He-detector using the example of IN10.

Principle

Fig 5.7 illustrates the path of a neutron through a backscattering spectrometer in three steps. For clarity the essential parts of the instrument at each step are highlighted in red, whilst the other parts are semi-transparently depicted.

- Fig. 5.7a: Cold neutrons (represented by the wavevector [red arrows]) with an energy typically spread around $E_0 = 2.08\,\text{meV}$ are Bragg reflected at a mosaic crystal, mounted on a rotating disk (red flat cylinder) – the so-called phase space transformation chopper (PST). The basic idea of the PST is to reshape the energy and angular distribution of the neutron beam such that the reflected beam has a very narrow energy distribution about E_0 and broad angular divergence. A detailed description and analysis is given in Ref. [72]. When the neutrons hit the horizontally oscillating Doppler monochromator (red rectangle, the trajectory of the movement is indicated by transparent rectangles), they are back reflected and their average energy E_0 is shifted in correspondence with the Doppler velocity.

- Fig. 5.7b: By exciting or annihilating energy states of the sample system (red cuboid in the middle) the neutron's wavevector $\mathbf{k}$ changes to $\mathbf{k}'$. Thereby the

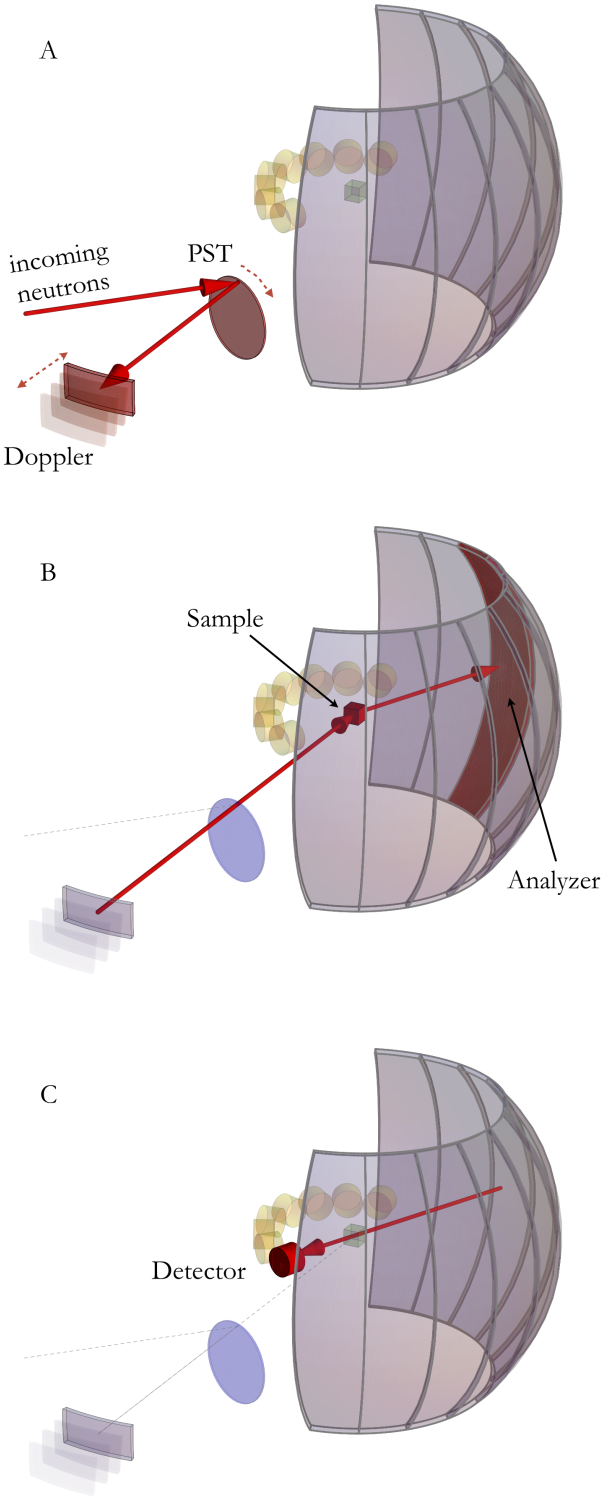

Figure 5.7: Principle of a backscattering spectrometer.5.7a: Incoming neutrons are Bragg reflected by rotating disk (PST). A Doppler monochromator alters the velocity of the perpendicularly impinging neutrons. 5.7b Neutrons are inelastically scattered by the sample. 5.7c: Neutrons fulfilling the Bragg condition at the analyzer are back-reflected towards the detector.

neutrons lose or gain energy,

$$\hbar\omega = \frac{\hbar^2}{2\,m}\left(\mathbf{k}^2 - \mathbf{k}'^2\right) \tag{5.23}$$

and synchronously experience a momentum change of $\mathbf{q} = \mathbf{k} - \mathbf{k}'$. For a more detailed description of the scattering process we refer to Sec. 4.2.

- Fig. 5.7c: At the analyzer crystal (red curved spherical element) only those neutrons fulfilling the Bragg condition are back-reflected towards the cylindric detector tubes (yellow cylinders). On their way, the reflected neutrons penetrate the sample again. Assuming that the scattering probability is less than 10 %, only 1 % of all neutrons are scattered a second time. Consequently, 90 % of the analyzed neutrons reach the detector unscattered where it is counted.

Using the energy information prior to the scattering event from the Doppler speed, the neutron count is stored in the corresponding energy channel. Knowing the number neutrons per second at a given scattering angle and the energy change the partial differential cross-section Eq. 4.47 can be calculated.

5.3.2 Spin-Echo Spectrometer

The idea of a high resolution neutron spectrometer employing the neutron spin precession – called spin-echo spectrometer – was first conceived by Mezei [108]. In the following we will explain the basic principle of such a spectrometer. An exhaustive and detailed description can be found in the textbook by Mezei et al. [110].

For the experiments reported in paper A and paper D (see Chaps. 7 and 10) we employed the IN11 and the IN15 at the Institute Laue-Langevin (Grenoble, France) by using the configuration presented in Table 5.6.

The basic idea is to use the neutron spin as an "internal clock" running at a speed depending on the magnetic field to probe the intermediate scattering function Eq. 4.31. Hence, this method allows to measure the Fourier transform of the scattering function, which for instance can be determined by neutron backscattering spectroscopy (compare the previous subsection 5.3.1). Fig. 5.8 displays both the path (two gray arrows in the middle) and the corresponding spin (red arrows) of a neutron traveling through a spin-echo spectrometer. We start describing the neutron path and the essential instrumental components starting from the right- to the left-hand side of the figure.

- A neutron beam with a wavelength distribution $P_{\Delta\lambda}(\lambda - \lambda_0)$ centered at λ_0 and having typically$\Delta\lambda/\lambda_0 \approx 15\,\%$ (see Table 5.6), is polarized by a polarizer often consisting of a mirror magnetized along the propagation direction (schematically represented by a gray disk). The neutrons leave the polarizer with a spin parallel to the guide field. Hence, the neutrons transverse the guide field without any spin precessing, emblematized by a "internal clock" turned off.

Neutron Spin-Echo Spectrometers

Instrument	IN11	IN15
Detector	32×32 pixels ^{3}He delay line multidetector	32×32 pixels multidetector 1 bar ^{3}He and 0.3 bar CF_4
Polarizer	FeAg supermirrors	V cavity, 1 m long FeCo-Si supermirrors on Si substrate
Analyzer	CoTi supermirrors	FeCo supermirrors
Beam diameter at sample [mm]	45	40
Incident beam divergence [mrad]	15	< 17
Incident wavelengths λ_0 [Å]	8.5, 10	8, 10, 16
Monochromatization $\Delta\lambda/\lambda_0$	$(15 \ldots 22)\,\%$	15 %
Elastic q-range [Å^{-1}]	$0.04 \ldots 0.2$	$0.023 \ldots 0.23$
Fourier time range τ [ns]	$0.02 \ldots 47$	$0.35 \ldots 207$
Accessible length scale l [nm]	$3.14 \ldots 15.7$	$2.73 \ldots 27.3$
Accessible energy scale E [μeV]	$-207 \ldots 207$	$-12 \ldots 12$
Accessible energy resolution δE [μeV]	0.1	0.02

Table 5.6: Setup of the neutron spin-echo spectrometers IN11 and IN15 at the Institut Laue-Langevin (Grenoble, France) for the experiments reported in paper A and paper D (see Chaps. 7 and 10). Other setups and a review of the characteristics of both spectrometers can be found in Refs. [79, 52, 145]. We calculate the accessible energy and length scales of the instruments as follows: $\delta E = 2\,\pi\,\hbar/\tau_{\max} \leq |E| \leq 2\,\pi\,\hbar/\tau_{\min}$ and $2\,\pi\,\hbar/q_{\max} \leq l \leq 2\,\pi\,\hbar/q_{\min}$, respectively.

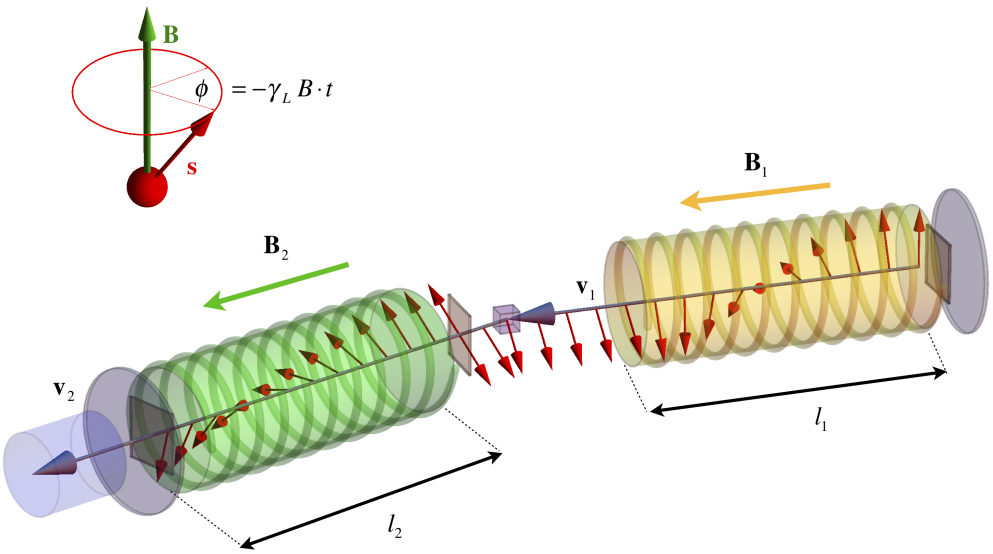

Figure 5.8: Principle of a spin-echo spectrometer. We describe the path of a neutron beam from the right- to the left-hand side. A beam of unpolarized neutrons with velocity vector $\mathbf{v}_1$ passes through a polarizer (left-hand gray transparent disk). Thereafter, the neutron spin is parallel to the magnetic guide field (pointing along the optical axis, [gray arrow in the middle of the two cylindric solenoids]). When the neutrons pass a $\pi/2$-flipper (orange rectangular plate), the "internal clock" of the neutrons is switched on by flipping the spin such that it is orthogonal to the magnetic field $\mathbf{B}_1$ of the first solenoid (yellow cylinder with coils). Within the solenoid the magnetic field is homogeneous and points along the optical axis. While transversing the field the neutron spin (red arrows) is precessing about the field lines. After scattered from the sample (purple cuboid) the neutron velocity is $\mathbf{v}_2$ and the neutron spin is inverted by a π-flipper (orange rectangular plate). Then, the scattered neutron beam enters a second solenoid (green cylinder with coils) with a homogeneous magnetic field $\mathbf{B}_2$. Consequently, its spin (red arrow) continuously precessing about the field lines. Next, the neutrons spin is flipped parallel to the guide-field by an another $\pi/2$-flipper (orange rectangular plate) and transverse through the analyzer (right-hand gray transparent disk) and finally, the beams intensity is measured by a detector (blue cylinder).

- After a short distance the neutrons hit a $\pi/2$-flipper, a very thin plat with two orthogonal coil windings (flat orange rectangle), causing a flip of the spin such that the spins turned to be orthogonal to the homogeneous field $\mathbf{B}_1$ of the first solenoid (yellow cylinder with concentric coil). Now the "internal clock" is switched on and while traveling along the field with a velocity $\mathbf{v}_1$ the spin processes about the field lines with a Larmor frequency $\omega_1 = -\gamma_L B_1$. Therein, $\gamma_L = 2/\hbar\,\gamma_n$ is the neutron's gyromagnetic ratio with γ_n being the magnetic dipole moment (see Table 4.1). The upper inset shows a spin $\mathbf{s}$ (red arrow) of a neutron precessing about magnetic field vector $\mathbf{B}$ (green arrow), after time t the spin is precessed by an angle $\phi = -\gamma_L B\,t$. The precession angle after transversing the first solenoid of length l_1 at speed v_1 is

$$\phi = -\gamma_L B_1 l_1 / v_1. \tag{5.24}$$

- When a neutrons scatters at the sample (purple cuboid) it experience a momentum and the energy transfer,

$$\begin{aligned} \hbar\,\mathbf{q} &= m\,(\mathbf{v}_1 - \mathbf{v}_2) \\ \hbar\,\omega &= \frac{m}{2}\left(\mathbf{v}_1^2 - \mathbf{v}_2^2\right), \end{aligned} \tag{5.25}$$

  respectively. Since scattering is a statistical process, the scattering changes the divergence and the energy distribution of the neutron beam. For a fixed $\mathbf{q}$, the energy change $\hbar\,\omega$ has probability density distribution P, which can be expressed by the dynamic structure factor of the sample

$$P(\mathbf{q},\omega) = \frac{S(\mathbf{q},\omega)}{\int S(\mathbf{q},\omega)\,d\omega} \tag{5.26}$$

  Thereafter, the neutrons impinge on a π-flipper (flat orange rectangle), as result the spin angle ϕ is transformed into $-\phi$.

- A precession about the homogeneous magnetic field $\mathbf{B}_2$ in the second solenoid (green cylinder with concentric coil) will change the total precession angle to

$$\phi = \gamma_L \left(\frac{B_1 l_1}{v_1} - \frac{B_2 l_2}{v_2}\right) \tag{5.27}$$

  The energy changes $\hbar\,\omega$ relevant for the study of diffusion processes as carried out in this thesis are small compared to the average kinetic energy of the neutrons. Therefore, restricting ourselves to small energy transfers and adjusting the magnetic fields such that $B_1 l_1 = B_2 l_2$, the precession angle ϕ can be approximated at v_1 up to first order in $\hbar\,\omega$ by

$$\phi \approx \gamma_L \frac{m^2 B_1 l_1}{8\,\pi^3\,\hbar^2}\,\lambda^3\,\omega. \tag{5.28}$$

- Finally, the neutrons are $\pi/2$-flipped (orange flat plat) and after passing by a second polarizer (gray disk) a detector (blue cylinder) measures the intensity of the x-component of the polarization vector of the neutron beam:

$$P_x = \langle \cos(\phi) \rangle = \int_0^\infty \int_{-\infty}^\infty P_{\Delta\lambda}\left(\lambda - \lambda_0\right)\, P(\mathbf{q}, \omega)\, \cos(\phi)\, \mathrm{d}\omega\, \mathrm{d}\lambda \tag{5.29}$$

Consequently, using Eq. 5.26 and restricting to small energy changes the measured quantity turns out to be the normalized intermediate scattering function convoluted with the wavelength distribution function,

$$P_x = P_{\Delta\lambda}\left(\lambda - \lambda_0\right) \otimes \frac{\mathrm{Re}\left[\mathcal{I}(\mathbf{q}, \tau)\right]}{\mathcal{I}(\mathbf{q}, 0)}. \tag{5.30}$$

Therein, we have introduced the Fourier-time

$$\tau = \gamma_L \, \frac{m^2 \, B_1 \, l_1}{8 \, \pi^3 \, \hbar^2} \, \lambda^3. \tag{5.31}$$

The convolution with the wavelength distribution function causes a smearing out of the Fourier-time and the $\mathbf{q}$-values, which for small energy transfers are approximated by

$$\mathbf{q} = \frac{4\,\pi}{\lambda} \left(\frac{\mathbf{v}_1}{v_1} - \frac{\mathbf{v_2}}{v_2} \right). \tag{5.32}$$

In case of $\hbar\omega \ll k_B\, T$ the detailed balance factor is unity and, hence, $\mathcal{S}(\mathbf{q}, \omega)$ is an even function of ω. Therefore, the real part in Eq. 5.30 can be skipped (compare Table 4.3 and last part of Sec. 4.2.3).

5.3.3 SAXS Instrument

Complementary to the neutron spectroscopy experiments, we employed small-angle X-ray scattering (SAXS) to study the structure of the solution of proteins. In Table 5.7 we show the setup of the ID02 beamline at the European Synchrotron Radiation Facility (Grenoble, France) and the beamline 6.2 of the Synchrotron Radiation Source at Daresbury Laboratory (Warrington, UK), used to for the experiments reported in paper A and paper D (see Chaps. 7 and 10). With the used instruments, we access q-values in the range of $0.002 \ldots 0.5\,\text{Å}^{-1}$ (see Table 5.7) corresponding to inter- and intra-molecular length scales, such that it can access not only the shape of the molecule but also its equilibrium structure (for details see section 4.3). Therefore small-angle scattering is a crucial technique to investigate macromolecules near physiological conditions. Here, we briefly explain the concept of a small-angle-scattering instrument being aware of that the technical implementation is very complex. A detailed review of SAXS can be found in Ref. [23]. Fig. 5.9 displays the pathway of a X-ray beam through a small-angle scattering instrument. The divergence of a highly monochromatized X-ray beam from a synchrotron source with wavevector $\mathbf{k}$ (red arrow) is reduced by a collimator (purple cylinder). There-

Small-Angle X-Ray Instruments

Instrument	Beamline ID02	Beamline 6.2
Detector	2018×2048 pixels CCD $10 \times 10\,\mathrm{cm}^2$	RAPID2 technology 20 cm radius
Spatial detector resolution [μm]	80	–
Sample Detector distance [m]	2	3.3
Beam size at sample [mm^2] (horizontal $\times$ vertical)	0.4×0.2	1.3×0.3 –
Incident beam divergence [μrad^2]	20×40	–
Monochromatization $\Delta\lambda/\lambda$	$2 \cdot 10^{-4}$ ($\lambda = 12.5\,\mathrm{keV}$)	$\approx 2 \cdot 10^{-4}$
Incident Energy [keV]	16.062	15
Incident Wavelength [Å]	0.77	0.827
Elastic q-range [Å^{-1}]	$0.002 \ldots 0.5$	$0.013 \ldots 0.45$
Accessible length scale l [nm]	$1.3 \ldots 314$	$1.4 \ldots 48$

Table 5.7: Configuration of the SAXS instruments at which the SAXS data for this thesis was recorded. The SAXS measurements reported in paper A were carried out on the beamline 6.2 of the Synchrotron Radiation Source at Daresbury Laboratory, (Warrington, UK). For the SAXS data in shown paper D we employed the ID02 beamline at the European Synchrotron Radiation Facility (Grenoble, France).

after, the X-ray beam hits the sample (green cuboid) where it is scattered. The scattered X-ray photons propagating with a wavevector $\mathbf{k}'$ (red arrow) are impinging on a CCD detector in a vacuum chamber (yellow transparent tube), which then detects the scattering amplitude $I(\mathbf{q})$ depending on $\mathbf{q} = \mathbf{k} - \mathbf{k}'$.

5.4 Data Treatment

In this section we describe the treatment of neutron backscattering and SAXS data. We note that the data treatment of the backscattering data can be analogously applied to the spin-echo data. However, one minor modification has to be considered. Instead of using vanadium to determine both the detector efficiency and the resolution function, graphite powder is used.

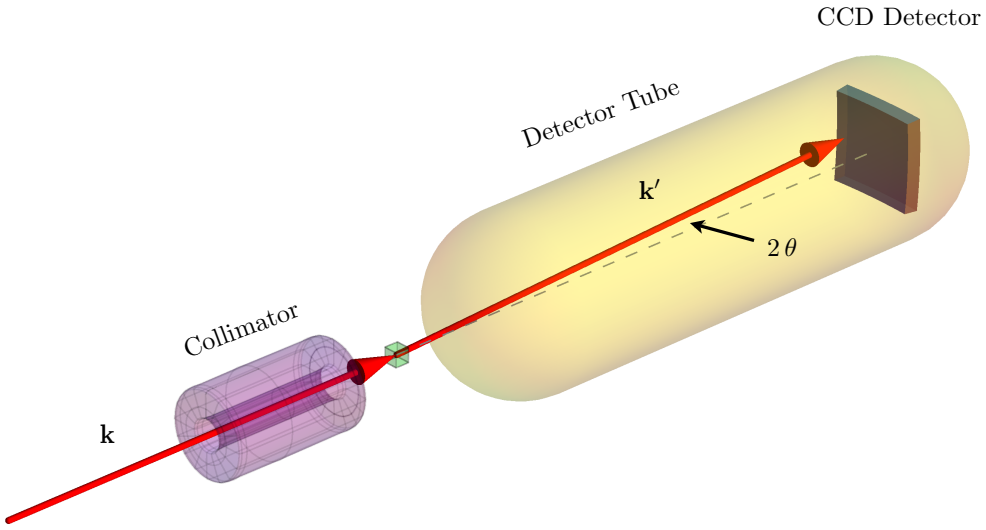

Figure 5.9: Principle of a small-angle scattering instrument.

5.4.1 Neutron Backscattering

This section elucidates how to extract the incoherent scattering function $S_{\text{inc}}(\mathbf{q},\omega)$ of a protein in solution from the intensity signal calculated from the monitor normalized neutron counts recorded at the detectors of a neutron backscattering spectrometer. For the data treatment of the backscattering data, we developed MATLAB [2] scripts in accordance with the procedure outlined in this section. The measured intensity $I(\mathbf{q},\omega)$ of a sample with a theoretical partial differential cross-section $\partial^2\sigma/\partial\mathbf{\Omega}\partial E'$ (for details see Sec. 4.2.2.1) can be decomposed into

$$I(\mathbf{q},\omega) := \mathcal{D}(\mathbf{q})\,\mathcal{R}_{\Delta\omega}(\omega) \otimes \frac{\partial^2\sigma}{\partial\mathbf{\Omega}\partial E'}(\mathbf{q},\omega) + B(\mathbf{q}), \tag{5.33}$$

where $\mathcal{R}_{\Delta\omega}(\omega)$ indicates the resolution of the instrument, $D(\mathbf{q})$ is the detector efficiency, and $B(\mathbf{q})$ denotes a flat background. For the backscattering data of this study, we determined the differential cross-section of a sample consisting of a protein solution confined in an aluminum cylinder, denoted by I_{PWC}. The subindex in the previous symbol will be explained later. Therefore, besides the scattering from the protein, both the cylinder and the solvent contribute to the measured scattering intensity. In order to remove these contributions, the subsequent samples must be measured additionally

- ☐ Vanadium foil similar to the sample geometry in the sample cylinder: I_{VC}
- ☐ Empty cylinder: I_{C}

- D_2O in the sample cylinder I_{WC}

For clarity we use the acronyms V, C, W and P to denote vanadium, the aluminum cylinder, water and the protein, respectively. Hence, the subindex of the symbol I_{PWC} indicates each contribution, namely from the protein (P), the water molecules (W) and the aluminum cylinder (C), to the measured scattering signal. Consequently, we have to retrieve the protein signal by elimination those unwanted contributions. Moreover, we remove the instrumental background and the influence of the detector efficiency from the signal.

To begin with, we determine the detector efficiency $D(\mathbf{q})$ and the instrumental resolution function $\mathcal{R}_{\Delta\omega}(\omega)$ using the vanadium signal (the reasons are explained in Sec. 5.1.3). For this end, we subtract the empty cylinder background I_{C} by using the corresponding Paalman-Pings coefficients α and β accounting for self-shielding effects (Appendix A.1):

$$I_{\mathrm{V}}(\mathbf{q},\omega) = \alpha_{\mathrm{VC}}(\mathbf{q})\, I_{\mathrm{VC}}(\mathbf{q},\omega) - \beta_{\mathrm{VC}}(\mathbf{q})\, I_{\mathrm{C}}(\mathbf{q},\omega) \tag{5.34}$$

In the absence of an instrumental background, the detector efficiency could be easily retrieved by

$$D(\mathbf{q}) = \int I_{\mathrm{V}}(\mathbf{q},\omega)\, d\omega. \tag{5.35}$$

However, the background would significantly shift the detector efficiency due to the integration. In its place, we fit the vanadium data with the following model function:

$$I_{\mathrm{V}}^{\mathrm{model}}(\mathbf{q},\omega) = A_1(\mathbf{q})\, R_{\Delta\omega}(\omega) + A_2(\mathbf{q}), \tag{5.36}$$

therein, the coefficients A_1 and A_2 account for the detector efficiency and the background, respectively. For the spectrometers IN10 and IN16, the resolution function $\mathcal{R}_{\Delta\omega}$ can be accurately modeled by a single Gaussian function

$$R_{\Delta\omega}(\omega) = \frac{1}{\sqrt{2\,\pi}\,\Delta\omega(\mathbf{q})} \exp\left[-\frac{\omega^2}{2\,\Delta\omega(\mathbf{q})^2}\right]. \tag{5.37}$$

From the fit we obtain the instrumental parameters, which are crucial for the further data analysis:

$$\begin{aligned} D(\mathbf{q}) &\approx A_1(\mathbf{q}), \\ B(\mathbf{q}) &\approx A_2(\mathbf{q}), \\ \mathcal{R}_{\Delta\omega}(\omega) &\approx R_{\Delta\omega}(\omega). \end{aligned} \tag{5.38}$$

Next, we normalize the water and protein solution spectra with the detector efficiency and synchronously subtract the empty cylinder background

$$\begin{aligned} I_{\mathrm{W}}(\mathbf{q},\omega) &= \frac{1}{D(\mathbf{q})}\left[\alpha_{\mathrm{WC}}(\mathbf{q})\, I_{\mathrm{WC}}(\mathbf{q},\omega) - \beta_{\mathrm{WC}}(\mathbf{q})\, I_{\mathrm{C}}(\mathbf{q},\omega)\right] \\ I_{\mathrm{PW}}(\mathbf{q},\omega) &= \frac{1}{D(\mathbf{q})}\left[\alpha_{\mathrm{PWC}}(\mathbf{q})\, I_{\mathrm{PWC}}(\mathbf{q},\omega) - \beta_{\mathrm{PWC}}(\mathbf{q})\, I_{\mathrm{C}}(\mathbf{q},\omega).\right] \end{aligned} \tag{5.39}$$

Finally, we subtract the water background by taking the volume fraction of the hydrated proteins ϕ Eq. 5.1 into account:

$$I(\mathbf{q},\omega) := I_{\mathrm{P}}(\mathbf{q},\omega) = I_{\mathrm{PW}}(\mathbf{q},\omega) - (1-\phi)\, I_{\mathrm{W}}(\mathbf{q},\omega). \tag{5.40}$$

For backscattering experiments the kinematic factor in Eq. 4.47

$$\frac{k'}{k} = \sqrt{\frac{1}{1+\hbar\omega/E_0}} \approx 1 \tag{5.41}$$

can be neglected, since the energy of incoming neutrons is around $E_0 \gg \hbar\omega$. Furthermore, the scattering is dominated by the incoherent contribution of the hydrogen atoms of the protein. Therefore, we obtain

$$I(\mathbf{q},\omega) \propto \mathcal{R}_{\Delta\omega}(\omega) \otimes \mathcal{S}_{\mathrm{inc}}(\mathbf{q},\omega), \tag{5.42}$$

in which $\mathcal{S}_{\mathrm{inc}}(\mathbf{q},\omega)$ is the incoherent dynamic structure factor of the protein's hydrogen atoms. Since the hydrogen atoms are nearly equally distributed over the protein volume (compare Fig. 4.2), $\mathcal{S}_{\mathrm{inc}}(\mathbf{q},\omega)$ reflects the dynamics of the whole protein.

5.4.2 Small-Angle X-Ray Scattering

In this section we shed light on how to recover the differential scattering cross-section Eq. 4.59 of a dissolved protein from the SAXS raw data recorded at the CCD detector in Fig. 5.9. Each pixel of the CCD detector measures the counts of the scattered photons from the sample per second. Due to the technical setup of the SAXS instrument the pixel data have to be preprocessed. The preprocessing occurs online immediately after the beam exposure of the sample and includes the following steps:

- Dark image subtraction to eliminate the background due to photons not originating from the X-ray beam
- Distortion correction due to spatial orientation of the detector
- Flat field correction using a flat field image that describes the sensitivity of each pixel of the CCD
- Average using a curve integral along a circle with constant q

As result we obtain the number of photons per second, which is

$$I(q)_{\text{exp}} = I_0\, A\, d\, T\, \Delta\Omega\, e\, d\, \frac{d\Sigma(q)}{d\Omega}, \tag{5.43}$$

therein, I_0 is the incident beam intensity, A the sample exposure area (beam size), d is the sample thickness, T is sample transmission, e the detector efficiency and $\Delta\Omega$ is the detector view angle. The scattering cross-section per unit volume is

$$\frac{d\Sigma(q)}{d\Omega} = \frac{N}{V}\frac{d\sigma(q)}{d\Omega}, \tag{5.44}$$

which is also known as the absolute intensity in units of cm^{-1} and is related via the particle density to the differential cross-section $d\sigma(q)/d\Omega$. To eliminate the instrument parameters in Eq. 5.43 we use a water calibration sample [120] since theoretical value for the corresponding differential cross-section is known to be

$$\left(\frac{d\Sigma(q)}{d\Omega}\right)_{\text{W}} = \rho_{\text{W}}^2\, k_B\, T\, \chi_T \tag{5.45}$$

in which χ_T is temperature-dependent isothermal compressibility and ρ_{W} the scattering-length density of water. Consequently, the product of the instrumental parameters is

$$I_0\, A\, d\, T\, \Delta\Omega\, e\, d = \frac{I_{\text{W}}(q)}{\rho_{\text{W}}^2\, k_B\, T\, \chi_T}, \tag{5.46}$$

therein $I_{\text{W}}(q)$ is the preprocessed intensity of a water sample. We use Eq. 5.46 to normalize a measured intensity and thereby obtain the absolute intensity. To calculate the differential cross-section of a protein in solution the following absolute intensities are to be determined:

- ☐ empty glass capillary in which the sample is contained during the measurement, $(d\Sigma(q)/d\Omega)_{\text{C}}$
- ☐ water background at the same temperature as protein solution, $(d\Sigma(q)/d\Omega)_{\text{WC}}$
- ☐ protein solution, $(d\Sigma(q)/d\Omega)_{\text{PWC}}$

Note, we use a similar acronyms convention as in Sec. 5.4.1. Consequently, C, W and P denote the empty capillary, water and the protein, respectively. Similar to the data treatment in Sec. 5.4.1 apart from the Paalman-Pings coefficients, we first subtract the empty capillary intensity from the other samples and then retrieve the protein absolute intensity by subtracting the volume-fraction scaled water signal from the protein solution signal:

$$\left(\frac{d\Sigma(q)}{d\Omega}\right)_{\text{P}} = \left(\frac{d\Sigma(q)}{d\Omega}\right)_{\text{PW}} - (1-\varphi)\left(\frac{d\Sigma(q)}{d\Omega}\right)_{\text{W}} \tag{5.47}$$

Using Eq. 5.44 the differential cross-section of the protein can be calculated.

5.5 Data Analysis

Following up the previous section, we will expound the data analysis used in this study. Part of the analysis, particularly for quasi-elastic spectra, is well established in the literature [46, 39, 125, 86, 140]. The other part was collaboratively elaborated by the author of this thesis and his co-workers. Inspired by Perez et al. [125] we develop in Sec. 5.5.1 an analytic framework to separate the translational diffusion coefficient from the measurable diffusion at a finite volume fraction. Moreover, in Sec. 5.5.2 we present a framework that allows to measure the mean-squared displacement of the internal motion of a protein in solution from a fixed elastic window scan.

5.5.1 Quasi-Elastic Neutron Backscattering

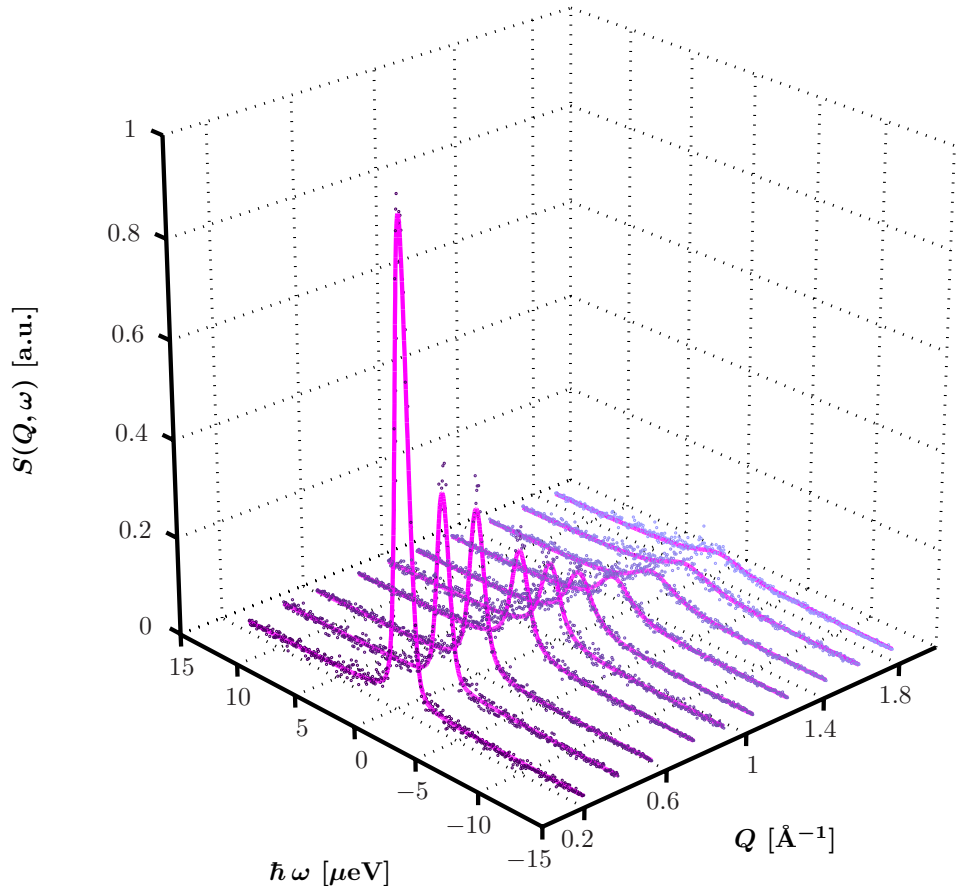

Figure 5.10: Quasi-elastic neutron backscattering spectra of a 500 mg/ml *bovine serum albumin* aqueous (D_2O) solution at a temperature of 300 K (purple circles). The data were recorded at the IN16 spectrometer at the ILL in Grenoble. The solid pink line is a fit of the model function Eq. 5.55 to the data.

In Sec. 5.4.1 we have explained how to calculate the spectrum of a protein solution by using the spectra from background and calibration measurements. We remind that the resolution function of the instrument was not reduced from the calculated spectra and, consequently, has to be considered in the following data analysis. Furthermore, we point out that the reduced data from a neutron backscattering measurement as described in Sec. 5.4.1 is proportional to the incoherent scattering function of the hydrogen atoms of the protein.

In this section we elucidate how to fit the neutron scattering spectrum of a protein in solution. Emanating from a theoretical model on the quasi-elastic energy range, we will derive a fit function that can be employed to extract important dynamical parameters such as the self-diffusion coefficient of the protein.

Here, we shortly shed light on which principles we construct a theoretical model that sufficiently captures the dynamics of a protein. In Sec. 4.2.4 we explained the basic idea how to describe the different motions of a protein in terms of the product of intermediate scattering functions. The dynamic modes of a protein are hierarchically ordered on their time scales. One can approximately categorize the dynamics into three main contributions:

- **Atomic Vibrations**
  The atoms of the protein vibrate about a well defined equilibrium position. Using a harmonic approximation one can prove that the scattering function related to the vibrational modes of the molecule can be decomposed into an elastic and inelastic part [13]

$$\mathcal{S}^{\mathrm{V}}_{\mathrm{inc}}(\mathbf{q},\omega) = \exp\left[-\frac{1}{3}\left\langle u^2_{\mathrm{vib}}\right\rangle q^2\right]\left\{\delta(\omega) + S^{\mathrm{V}}_{\mathrm{inel}}(\mathbf{q},\omega)\right\}. \tag{5.48}$$

  Therein, $\langle u^2\rangle$ is the average mean-squared displacement of the atoms. The inelastic component $S^{V}_{\mathrm{inel}}(\mathbf{q},\omega)$ has pronounced peaks at distinct energies in the meV-regime, which can be neglected on the quasi-elastic energy scale.

- **Internal Motion**
  A diversity of amplitudes and correlation times renders the characterization of internal motion an intricate task. At room temperature, the diffusive motion of side chains predominantly contributes to the internal motion. These solvent exposed side chains (displayed in Fig. 5.11) perform spatially confined reorientational diffusive motions. Furthermore, subdomain movements with amplitudes on the Angstrom length scale and nanoseconds time scale give rise to a wide range of spatial constrained diffusive modes. The incoherent scattering function is approximated by

$$\mathcal{S}^{\mathrm{I}}_{\mathrm{inc}}(q,\omega) = A(q)\,\delta(\omega) + [1 - A(q)]\,\mathcal{L}_{\beta}(\omega,\Gamma) \tag{5.49}$$

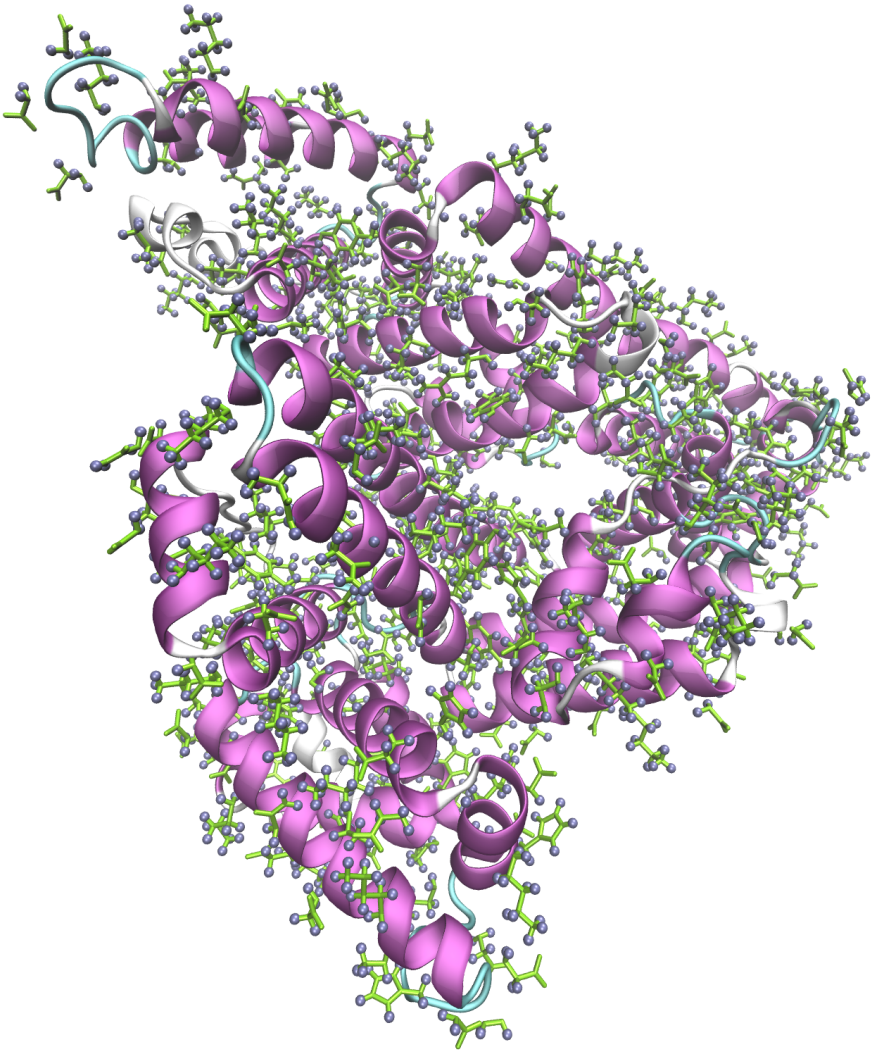

Figure 5.11: Hydrogen atoms (blue spheres) of the solvent-exposed side chains (green) of the homology model of *bovine serum albumin* (secondary structure is shown in different colors [purple, white, blue and cyan]) [175] . These solvent side chains perform spatially confined reorientational diffusive motions and therefore significantly contribute to the quasi-elastic scattering signal. The illustration was generated by using VMD [77].

in which the Kohlrausch-Williams-Watts function [178]

$$\mathcal{L}_\beta(\omega,\Gamma) = \int_{-\infty}^{\infty} \frac{dt}{2\,\pi} e^{-\mathrm{i}\,\omega\,t}\, \exp\left(-|t\,\Gamma|^\beta\right), \tag{5.50}$$

can describe a broad range of correlation times with a single phenomenological parameter $0 \leq \beta \leq 1$. $A(q)$ is the elastic incoherent structure factor, which is related to the average accessible space of internal diffusive scatterers, such as side chains or molecular subunits [14]. Γ and β are assumed to be nearly constant for $q < 2$ Å^{-2} [171, 86]. In this thesis we chose $\beta = 1$ since the accuracy of the measured data does not allow to distinguish between different β.

- **Global Diffusion**
  Combining the scattering function of translational and rotational diffusion (Eq. 4.105 and Eq. 4.142), denoted by $\mathcal{S}^{\mathrm{T}}_{\mathrm{inc}}(q,\omega)$ and $\mathcal{S}^{\mathrm{R}}_{\mathrm{inc}}(q,\omega)$, respectively, yields

$$\mathcal{S}^{\mathrm{TR}}_{\mathrm{inc}}(q,\omega) = \mathcal{S}^{\mathrm{T}}_{\mathrm{inc}}(q,\omega) \otimes \mathcal{S}^{\mathrm{R}}_{\mathrm{inc}}(q,\omega). \tag{5.51}$$

  Perez et al. [125] showed that on the quasi-elastic energy scale the center of mass diffusion and the rotational diffusion can be approximated by a single Lorentzian function

$$\mathcal{S}^{\mathrm{TR}}_{\mathrm{inc}}(q,\omega) \approx \mathcal{L}(\omega,\gamma), \tag{5.52}$$

  with a width $\gamma = D\,q^2$, thereby defining the apparent diffusion coefficient.

Assuming independence of these modes, the total scattering function is the convolution product

$$\mathcal{S}_{\mathrm{inc}}(q,\omega) = \mathcal{S}^{\mathrm{V}}_{\mathrm{inc}}(q,\omega) \otimes \mathcal{S}^{\mathrm{I}}_{\mathrm{inc}}(q,\omega) \otimes \mathcal{S}^{\mathrm{TR}}_{\mathrm{inc}}(q,\omega), \tag{5.53}$$

in which $\otimes$ denotes a convolution with respect to ω. Consequently, we describe the incoherent scattering function of the hydrogen atoms with the general model [46, 39, 125, 86, 140]:

$$\mathcal{S}_{\mathrm{inc}}(q,\omega) = \exp\left[-\frac{1}{3}\left\langle u^2_{\mathrm{vib}}\right\rangle q^2\right] \mathcal{L}(\omega,\gamma) \otimes \left\{A(q)\,\delta(\omega) + [1-A(q)]\,\mathcal{L}_\beta(\omega,\Gamma)\right\}. \tag{5.54}$$

Finally, taking the convolution with the instrumental resolution function into account, the fit model except for a scaling parameter reads

$$I_{\mathrm{model}}(q,\omega) \propto \mathcal{R}_{\Delta\omega}(\omega) \otimes \mathcal{S}_{\mathrm{inc}}(q,\omega). \tag{5.55}$$

Note, if the resolution function consists of one or more Gaussians the convolution can be made explicit by using Voigt functions [8, 167, 146]. Fig. 5.10 exemplifies the fit procedure with a sample data set. For each q-value of the spectra the model function Eq. 5.55 (pink solid line) was fitted to the energy spectrum (dark purple circles).

Apparent Diffusion

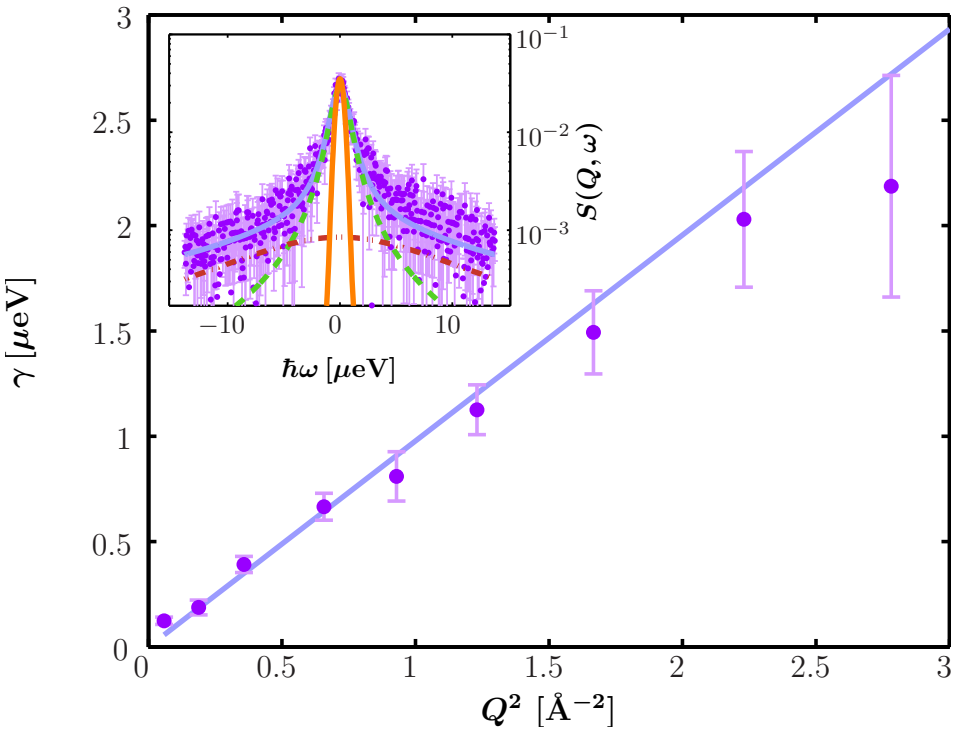

Figure 5.12: Inset: Example backscattering spectrum $S(Q,\omega)$ (symbols) recorded at IN16 for BSA in D_2O ($c = 500\,\mathrm{mg/ml}$, $\varphi = 28.5\,\%$, T = 300 K, individual detector at $q = 0.81\text{Å}^{-1}$). The magenta solid line is the fit of the model from Eq. (5.55). The two Lorentzians in Eq. (8.3) are indicated by the dashed and dash-dotted lines. The orange solid line denotes the resolution function. Main figure: Fitted γ (symbols) versus q^2 for the full q-range of the example data. The fit of $\gamma = D\,q^2$ (blue line) is consistent with simple diffusive behavior. For statistical reasons the fit range is restricted to $q^2 < 1.5\,\text{Å}^{-2}$.

In the short-time limit translational self-diffusion of a protein in a concentrated solution is described by a scattering function functionally equivalent to Eq. 4.105 aside from the interpretation of the diffusion coefficient. We will prove in the following section that this even holds for the inclusion of rotational diffusion to the scattering function. In this section we elucidate how to determine the apparent diffusion coefficient D, which we introduced in the previous section. D is simply an observable originating from the fit parameters γ for different q-values of the model Eq. 5.55 and characterizes the translational and rotational diffusion of the entire protein. Fig. 5.12 shows the widths γ of an example sample. For $q^2 < 1.5\,\text{Å}^{-2}$, a clear relationship $\gamma = D\,q^2$ is observed, defining the apparent diffusion coefficient D. For $q^2 > 1.5\,\text{Å}^{-2}$ the scattering signal from the proteins becomes weaker and considerably broadened with respect to the accessible energy range. Since these two factors can cause fitting artifacts, we neglected these data points for the fitting of

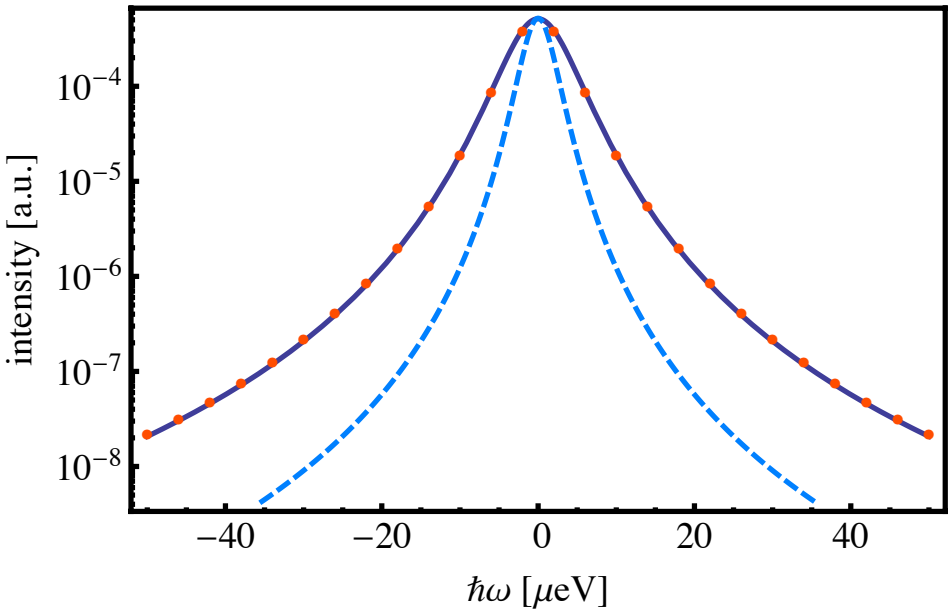

Figure 5.13: Incoherent scattering function $\mathcal{S}^{\mathrm{TR}}_{\mathrm{inc}}(q,\omega)$ of a diffusing hypothetical particle of radius $r = 36\,\text{Å}$ at $q = 1\,\text{Å}^{-1}$ (orange circles). The translational and rotational diffusion coefficients are $D_t = 6\,\text{Å}^2/\text{ns}$ and $D_r = 3.1 \cdot 10^{-3}\,\text{ns}^{-1}$, respectively. These values reflect the respective parameters of *bovine serum albumin* at room temperature in water. The dark blue solid line is a Lorentz function fitted to $\mathcal{S}^{\mathrm{TR}}_{\mathrm{inc}}(q,\omega)$. The light blue dashed line is the incoherent scattering function $\mathcal{S}^{\mathrm{T}}_{\mathrm{inc}}(q,\omega)$ without taking the rotational diffusion into account. Note, that $\mathcal{S}^{\mathrm{T}}_{\mathrm{inc}}$ was scaled to the same peak position as $\mathcal{S}^{\mathrm{TR}}_{\mathrm{inc}}$.

the diffusion coefficient, although the q^2 relationship seems conserved.

Extraction of Translational Diffusion Coefficients

Perez et al. [125] revealed that because of a non-negligible contribution of the rotational diffusion, the apparent diffusion coefficient is in general larger than the translational diffusion coefficient. Therefore, in this section we develop an analytic framework to extract the translational diffusion coefficient from the apparent diffusion. This permits a comparison of the translational diffusion behaviour with theoretical models. Fig. 5.13 illustrates the theoretical incoherent scattering function $\mathcal{S}^{\mathrm{TR}}_{\mathrm{inc}}$ of a hypothetical molecule emerged in a solvent for parameters that coincide with a *bovine serum albumin* molecules in water at room temperature (orange circles). Additionally the scattering function $\mathcal{S}^{\mathrm{T}}_{\mathrm{inc}}$ (calculated from Eq. 4.105) of the same molecule *only* performing translational diffusion is depicted. Evidently, the line broadening of $\mathcal{S}^{\mathrm{TR}}_{\mathrm{inc}}$ is larger than that of $\mathcal{S}^{\mathrm{T}}_{\mathrm{inc}}$ illustrating that the rotational contribution is significant. The scattering function $\mathcal{S}^{\mathrm{TR}}_{\mathrm{inc}}(q,\omega)$ is the convolution of

Eq. 4.105 and Eq. 4.142 and, consequently, reads

$$\mathcal{S}_{\text{inc}}^{\text{TR}}(q,\omega) = \sum_{l=0}^{\infty} B_l\,(q)\,\mathcal{L}\,(\omega,\Gamma_l)\,, \tag{5.56}$$

where

$$\Gamma_l = l\,(l+1)\,D_r + q^2\,D_t \tag{5.57}$$

with D_t and D_r being the translational and the rotational diffusion coefficient, respectively. We remind that the rotational dynamic structure factors for a molecule are entirely determined by the density distribution of the position of the molecule's hydrogen atoms ρ_{H} (compare Sec. 4.6.2):

$$B_l(q) = (2\,l+1)\int \rho_{\text{H}}(r)\,j_l^2(q\,r)\mathrm{d}r. \tag{5.58}$$

A comparison of $\mathcal{S}_{\text{inc}}^{\text{TR}}$ with the scattering function solely stemming from the translational diffusion (dashed light blue line), shows that the rotational contribution is not negligible. Perez et al. [125] observed that $\mathcal{S}_{\text{inc}}^{\text{TR}}$ can be sufficiently accurately approximated by a single Lorentzian function (solid dark blue line). Remarkably, the line broadening of this Lorentzian reveals the same $D\,q^2$ behavior, which is the hallmark for free translational diffusion (see Eq. 4.105). In this section, we will analyze this observation in detail and derive a relation defining the apparent diffusion coefficient D in terms of D_r or D_t. Fitting a single Lorentzian line shape, with the line broadening parameter Γ and the amplitude α, to the scattering function $\mathcal{S}_{\text{inc}}^{\text{TR}}$ is mathematically equivalent to the minimization of the $\mathbb{L}^2$-distance between these two functions:

$$\min_{\alpha,\Gamma}\left\{\int\left[\mathcal{S}_{\text{inc}}^{\text{TR}}(q,\omega) - \alpha\,\mathcal{L}(\omega,\Gamma)\right]^2\mathrm{d}\omega\right\}. \tag{5.59}$$

Solving the above equation yields two coupled nonlinear equations determining the parameters α and Γ:

$$\alpha = 2\,\Gamma\sum_{l=0}^{\infty}\frac{B_l}{\Gamma_l+\Gamma} \tag{5.60}$$

$$0 = \sum_{l=0}^{\infty}\frac{B_l}{\Gamma_l+\Gamma}\left(\frac{1}{\Gamma_l+\Gamma} - \frac{1}{2\,\Gamma}\right). \tag{5.61}$$

For better readability, we skip the explicit q-dependence of Γ, α and B_l. In the limiting case $q \to 0$ Eq. 5.61 and Eq. 5.60 are explicitly solvable yielding $\Gamma/q^2 = D_t$ and $\alpha = 1$. This motivates to introduce the general (q-dependent) apparent diffusion coefficient D by plugging $\Gamma = D\,q^2$ into Eq. 5.61:

$$\sum_{l=0}^{\infty}\frac{B_l}{\Gamma_l + D\,q^2}\left(\frac{1}{\Gamma_l + D\,q^2} - \frac{1}{2\,D\,q^2}\right) = 0. \tag{5.62}$$

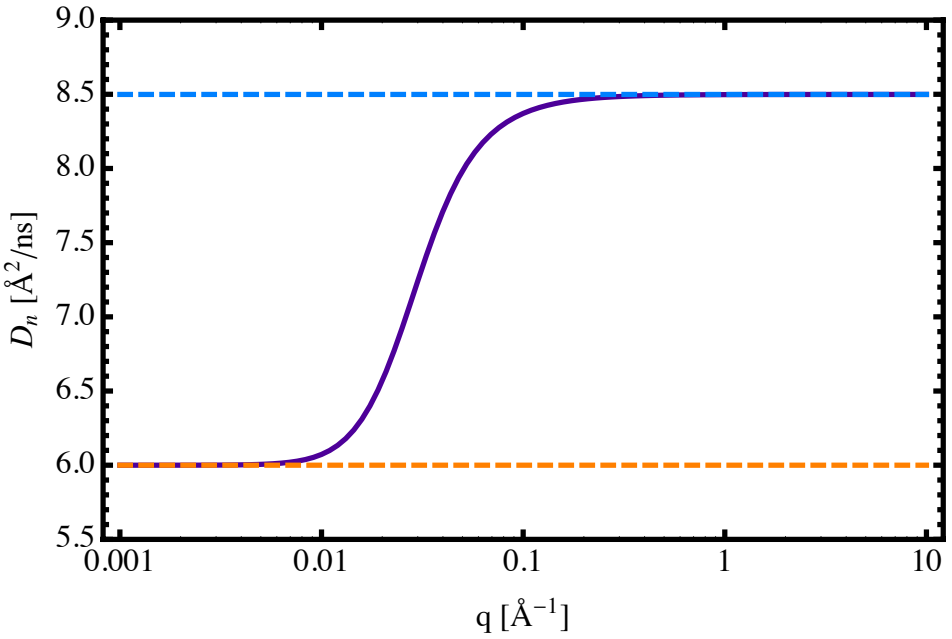

Figure 5.14: General apparent diffusion coefficient $D^{(n)}(q, D_t, D_r)$ of a hypothetical diffusing particle of radius $r = 36$ Å(orange circles). The translational and rotational diffusion coefficient are $D_t = 6\,\text{Å}^2/\text{ns}$ and $D_r = 3.1 \cdot 10^{-3}\,\text{ns}^{-1}$, respectively. For the calculation we truncated the sum in Eq. 5.63 at $n = 550$, since convergence was sufficient.

As next step, we introduce a sequence converging to D. For this end, we approximate Eq. 5.61 by truncating the infinite sum. Moreover, using Eq. 5.57 and replacing D by $D^{(n)}$, we finally obtain:

$$\sum_{l=0}^{n} B_l(q) \frac{l\,(l+1)\,D_r + q^2\,\left(D_t - D^{(n)}\right)}{\left[l\,(l+1)\,D_r + q^2\,\left(D_t + D^{(n)}\right)\right]^2} = 0. \tag{5.63}$$

Thereby, we implicitly define a sequence of functions $D^{(n)}\,(q, D_t, D_r)$ converging to the general apparent diffusion coefficient for $n \to \infty$. Fig. 5.14 shows $D^{(n)}\,(q, D_t, D_r)$ for a particle with the same parameters as in Fig. 5.13. We observe that $D^{(n)}\,(q, D_t, D_r)$ starts at D_t for $q = 0$ (dashed orange line) and converges rapidly to a constant value (dashed light blue line). Therefore, with the double limit of the sequence

$$D\,(D_t, D_r) = \lim_{q\to\infty}\left[\lim_{n\to\infty} D^{(n)}\,(q, D_t, D_r)\right], \tag{5.64}$$

we eliminate the influence of q and define the apparent diffusion coefficient D. With heuristic arguments we can finally turn the double into a single limit. Considering that if we chose $q = l/(2\,R)$ with $R = \sup\{r, \rho(r) \neq 0\}$, $B_l(q)$ in Eq. 5.63 strongly decays for large l, we rewrite Eq. 5.64:

$$D = \lim_{n\to\infty} D^{(n)}\left(\frac{n}{2\,R}, D_t, D_r\right). \tag{5.65}$$

This equation equally allows to calculate D_t in dependence of D and D_r, enabling us to extract the translational diffusion coefficient from the measured apparent diffusion.

5.5.2 Fixed Elastic Window Neutron Backscattering

In this section we develop an analytic framework for the calculation and decomposition of the total mean squared-displacement $\langle u^2 \rangle$ of a protein in solution determined with fixed elastic window neutron backscattering. The presented new analysis scheme is based on quasi-elastic concepts we have explained in the previous section. With fixed elastic window neutron backscattering, one measures the incoherent scattering function at $\omega = 0$ within the instrumental resolution function. The so-called elastic intensity of proteins in solution is

$$\mathcal{S}\,(q, |\omega| < \Delta\omega) := \mathcal{R}_{\Delta\omega}(\omega) \otimes \mathcal{S}_{\mathrm{inc}}(q,\omega)|_{\omega=0} = \int \mathcal{R}_{\Delta\omega}(\omega)\,\mathcal{S}_{\mathrm{inc}}(q,\omega)\,\mathrm{d}\omega. \tag{5.66}$$

Anticipating the result from the derivation subsequent to this section, the total mean-squared displacement $\langle u^2 \rangle$ is retrieved from the elastic intensity by fitting $-3\,\log\left[S\,(q, |\omega| < \Delta\omega)\right]$ with the following polynomial:

$$P\,(q) = b + \langle u^2 \rangle\, q^2 + c\,q^4. \tag{5.67}$$

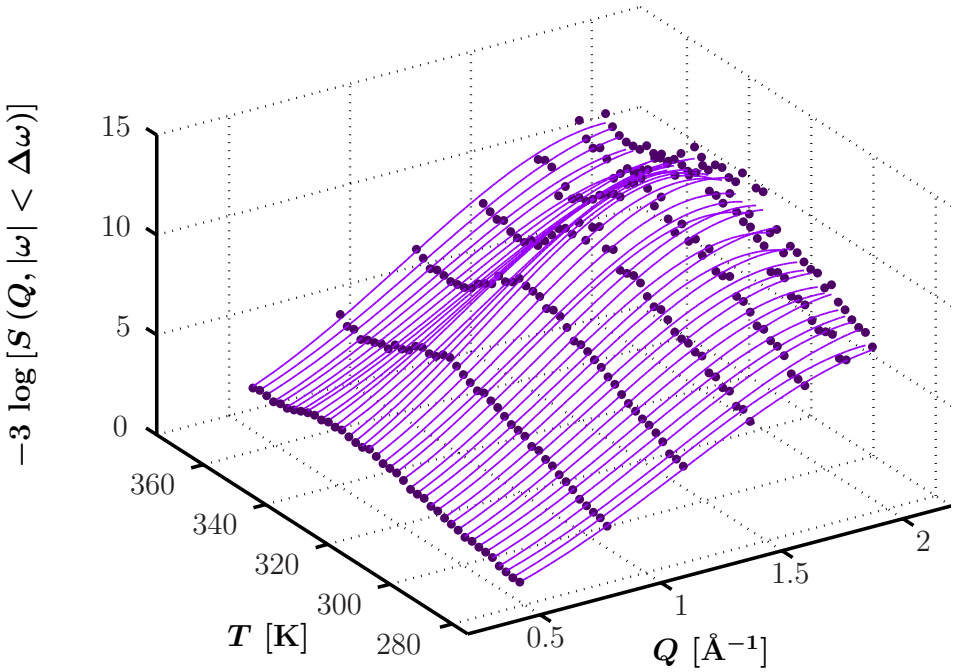

Figure 5.15: Raw data (dark purple solid circles) for the elastic intensity $S\left(q,|\omega|<\Delta\omega\right)$ of a 500 mg/ml BSA aqueous (D_2O) solution upon heating from 280 to 370 K with $7.4\cdot10^{-2}$ K/min. The data were recorded at IN10. Fits of the polynomial Eq. 5.67 to the data at fixed temperatures are superimposed as purple solid lines.

Therein, b accounts for both the background and the arbitrary scaling of the experimental elastic line, c originates from higher spatial correlations as described in detail in the next section. In Fig. 5.15 we display raw data for $-3\,\log\left[S\left(Q,|\omega|<\Delta\omega\right)\right]$ of a 500 mg/ml BSA aqueous (D_2O) solution upon heating from 280 to 370 K with $7.4\cdot10^{-2}$ K/min. At each temperature we fit the polynomial Eq. 5.67 to determine the total mean-squared displacement.

Analysis of the Elastic Intensity

In the following, we derive a formula describing the elastic line intensity in terms of vibrational, global and internal diffusive modes for small q values. To start with, we solve the integral Eq. 5.66 by using the model function Eq. 5.54 and assume a Gaussian resolution function of the instrument (which is valid for the spectrometers IN10 and IN16) of the form

$$\mathcal{R}_{\Delta\omega}(\omega)=\exp\left(-\frac{\omega^2}{2\Delta\omega^2}\right), \tag{5.68}$$

thereby, for reasons of readability we skip any scaling parameter. With this the integral Eq. 5.66 yields

$$\begin{aligned}S\left(q,|\omega|<\Delta\omega\right)=\exp\left(-\frac{1}{3}\left\langle u_{\mathrm{vib}}^2\right\rangle\,q^2\right)\cdot\Big\{&A(q)\,F_1\left(\frac{\gamma}{\Delta\omega},0\right)\\&+\left[1-A(q)\right]\,F_\beta\left(\frac{\gamma}{\Delta\omega},\frac{\Gamma}{\Delta\omega}\right)\Big\},\end{aligned} \tag{5.69}$$

where F_β is the integral expression

$$F_\beta(x,y)=\sqrt{\frac{2}{\pi}}\,\exp\left(\frac{x^2}{2}\right)\int_0^\infty\exp\left[-\frac{1}{2}\left(\xi+x\right)^2-\left|y\,\xi\right|^\beta\right]\,\mathrm{d}\xi\;. \tag{5.70}$$

Mean-Squared Displacement First we introduce the following apparent quantity

$$\left\langle u^2\right\rangle:=-3\,\lim_{q\to0}\left\{\frac{\log\left[S\left(q,|\omega|<\Delta\omega\right)\right]}{q^2}\right\}. \tag{5.71}$$

and term it total mean-squared displacement. In the following we will attach a physical meaning to it and will prove that it merits its name.

General Mean-Squared Displacement In order to analyze $\left\langle u^2\right\rangle$, we define the general (q-dependent) total mean-squared displacement $\left\langle u^2\right\rangle_q$ by

$$\exp\left[-\frac{q^2}{3}\,\left\langle u^2\right\rangle_q\right]:=S\left(q,|\omega|<\Delta\omega\right). \tag{5.72}$$

Note that the explicit q-dependence is denoted by a subindex q to distinguish it from $\langle u^2 \rangle$. Using Eq. 5.72 and Eq. 5.69, we obtain

$$\langle u^2 \rangle_q = \langle u^2_{\text{vib}} \rangle - \frac{3}{q^2} \log \xi(q), \tag{5.73}$$

in which

$$\xi(q) = A(q)\, F_1 \left(\frac{\gamma}{\Delta\omega}, 0 \right) + [1 - A(q)]\; F_\beta \left(\frac{\gamma}{\Delta\omega}, \frac{\Gamma}{\Delta\omega} \right). \tag{5.74}$$

We approximate Eq. 5.73 up to 3$^{\text{rd}}$ order using a Taylor polynomial at $q = 0$:

$$\langle u^2 \rangle_q = \sum_{n=0}^{3} \frac{a_n}{n!}\, q^n + \mathcal{O}(q^4), \tag{5.75}$$

therein, $\mathcal{O}(q^4)$ is the remainder of the series and the coefficients are defined by

$$a_n = \lim_{q \to 0} \frac{\mathrm{d}^n}{\mathrm{d}q^n} \langle u^2 \rangle_q \ . \tag{5.76}$$

n^{th}-Derivative of Incoherent Elastic Structure Factor In order to calculate the Taylor coefficients a_n, we have to first determine the n^{th}-derivative of the incoherent elastic structure factor. To start with, we introduce a general form of the incoherent elastic structure factor, which according to Bée [14] reads

$$B(\mathbf{q}) = \frac{1}{N} \sum_{j=1}^{N} \left| \langle e^{\mathrm{i}\, \mathbf{q}\, \mathbf{r}_j} \rangle \right|^2. \tag{5.77}$$

Therein, $\mathbf{r}_j = (x_j, y_j, z_j)^T$ might be the position vector of the j^{th} scatterer in one of the solvent exposed side chains of the protein (see Fig. 5.11). We recall that a protein in solution has no preferential orientation vector due the random collisions with the surrounding solvent molecules. We assume that the orientations of the molecules are nearly equally distributed. Therefore, we have to average the general elastic incoherent structure factor $A(q)$ over all possible orientations yielding

$$A_0(q) = \frac{1}{4\,\pi} \int_0^{2\,\pi} \int_0^{\pi} B(\mathbf{q}) \sin\theta \, \mathrm{d}\theta \, \mathrm{d}\varphi. \tag{5.78}$$

in which $\mathbf{q} = q\, [\cos(\varphi)\, \sin(\theta), \sin(\varphi)\, \sin(\theta), \cos(\theta)]^T$. For reasons of generality we additionally consider the pseudo-elastic incoherent structure factor [86, 140], based on the following conception: Correlation times much longer than the instrumental time window correspond to a very narrow signal in ω, which is indistinguishable from the elastic peak in the quasi-elastic signal. Therefore, a fraction p of scatterers is considered as immobile, the remaining fraction $1 - p$ as diffusive scatterers. This

translates into the pseudo-elastic incoherent structure factor

$$A(q) = p + (1-p)\, A_0(q) \tag{5.79}$$

The first five derivatives of $A(q)$, denoted by $A^{(n)}(q)$, were obtained by employing *Mathematica*® [181]:

$$\begin{aligned} A(0) &= 1 \\ A^{(1)}(0) &= 0 \\ A^{(2)}(0) &= -\frac{2\,(1-p)}{3}\,\left\langle \Delta\mathbf{r}^2 \right\rangle \\ A^{(3)}(0) &= 0 \\ A^{(4)}(0) &= \frac{1-p}{5}\,(m_x + m_y + m_z + 2\,m_{x,y} + 2\,m_{x,z} + 2\,m_{y,z}) \\ A^{(5)}(0) &= 0, \end{aligned} \tag{5.80, 5.81}$$

therein,

$$\left\langle \Delta\mathbf{r}^2 \right\rangle = \frac{1}{N} \sum_{j=1}^{N} \left\langle (\mathbf{r}_j - \langle \mathbf{r}_j \rangle)^2 \right\rangle \tag{5.82}$$

is the average fluctuation amplitude, related to the size of the confinement of the internal diffusive scatterer, such as the protein side chains. Moreover, the higher moments of the scattering coordinates are

$$m_x = \frac{2}{N} \sum_{j=1}^{N} \left(\left\langle x_j^4 \right\rangle + 3\,\left\langle x_j^2 \right\rangle^2 - 4\,\left\langle x_j^3 \right\rangle\,\left\langle x_j \right\rangle \right) \tag{5.83}$$

$$\begin{aligned} m_{x,y} = \frac{2}{N} \sum_{j=1}^{N} \Big(& 2\,\left\langle x_j\, y_j \right\rangle^2 - 2\,\left\langle y_j \right\rangle\,\left\langle x_j^2\, y_j \right\rangle \\ & + \left\langle x_j^2 \right\rangle\,\left\langle y_j^2 \right\rangle - 2\,\left\langle x_j \right\rangle\,\left\langle x_j\, y_j^2 \right\rangle + \left\langle x_j^2\, y_j^2 \right\rangle \Big) \ . \end{aligned} \tag{5.84}$$

We note that the expressions m_y, m_z and $m_{x,z}$, $m_{y,z}$ are analogously defined.

Taylor Coefficients Having obtained the n^{th}-derivative of the incoherent elastic structure factor $A^{(n)}(0)$, we proceed by calculating the Taylor coefficients in the truncated series (Eq. 5.75). For this end, we first calculate the derivatives for ξ at

$q = 0$, which are

$$\begin{aligned}
\xi(0) &= 1 && (5.85)\\
\xi^{(1)}(0) &= 0\\
\xi^{(2)}(0) &= -\frac{2\,D}{\Delta\omega}\sqrt{\frac{2}{\pi}} + \left[1 - F_\beta\left(0, \frac{\Gamma}{\Delta\omega}\right)\right] A^{(2)}(0)\\
\xi^{(3)}(0) &= 0\\
\xi^{(4)}(0) &= \left[1 - F_\beta\left(0, \frac{\Gamma}{\Delta\omega}\right)\right] A^{(4)}(0)\\
&\quad + \frac{12\,D^2}{\Delta\omega^2}\left[1 - \frac{\Delta\omega}{D}\,A^{(2)}(0)\left\{\sqrt{\frac{2}{\pi}} + F_\beta^{(1,0)}\left(0, \frac{\Gamma}{\Delta\omega}\right)\right\}\right] && (5.86)\\
\xi^{(5)}(0) &= 0, && (5.87)
\end{aligned}$$

where $F_\beta^{(1,0)}$ denotes the derivative of F_β (Eq. 5.70) in respect to the first argument. Using $\xi^{(n)}(0)$ we obtain the Taylor coefficients:

$$\begin{aligned}
a_0 &= -\frac{3}{2}\,\xi^{(2)}(0) && (5.88)\\
a_1 &= 0\\
a_2 &= \frac{1}{4}\left[3\,\xi^{(2)}(0)^2 - \xi^{(4)}(0)\right]\\
a_3 &= 0 && (5.89)
\end{aligned}$$

Finally, the general total mean-squared displacement $\left\langle u^2\right\rangle_q$ can be approximated as follows

$$\left\langle u^2\right\rangle_q = a_0 + \frac{a_2}{2}\,q^2 + \mathcal{O}(q^4). \tag{5.90}$$

Decomposition of Total Mean-Squared Displacement Using Eq. 5.90 the total mean-squared displacement simplifies to

$$\langle u^2\rangle := -3\lim_{q\to 0}\left\{\frac{\log\left[S\left(q, |\omega| < \Delta\omega\right)\right]}{q^2}\right\} = a_0. \tag{5.91}$$

by combining Eqs. 5.89, 5.87 and 5.81 the total mean-squared displacement can be decomposed into the following sum

$$\begin{aligned}
\left\langle u^2\right\rangle &= \left\langle u^2_{\text{vib}}\right\rangle + \left\langle u^2_{\text{sub}}\right\rangle + \left\langle u^2_{\text{diff}}\right\rangle && (5.92)\\
\left\langle u^2_{\text{sub}}\right\rangle &= (1-p)\,\chi\,\left\langle \Delta\mathbf{r}^2\right\rangle\\
\left\langle u^2_{\text{diff}}\right\rangle &= 3\sqrt{\frac{2}{\pi\,\Delta\omega^2}}\,D,
\end{aligned}$$

therein, $\chi = \left[1 - F_\beta\left(0, \frac{\Gamma}{\Delta\omega}\right)\right]$. Due to the energy resolution of the instrument the global diffusion of the protein can only be observed within a time window of width

$\tau = 2\pi/\Delta\omega$. During that time the protein has isotropically explored a space, which size is characterized by a mean-squared displacement of $\left\langle \Delta\mathbf{R}^2(\tau) \right\rangle = 6\,D\,\tau$. Hence, $\left\langle u_{\text{diff}}^2 \right\rangle = (2\,\pi)^{-3/2}\,\left\langle \Delta\mathbf{R}^2(\tau) \right\rangle$.

Fit Strategy Determining the limit Eq. 5.91 from a measured elastic intensity $S\,(q, |\omega| < \Delta\omega)$ is not feasible due to the experimental accuracy. Eq. 5.90 provides a better way to retrieve $\left\langle u^2 \right\rangle$ from the elastic yielding the polynomial Eq. 5.67.

Chapter 6

Results & Discussion

Contents

This chapter summarizes the key findings of the papers A-D, which are incorporated in subsequent publication-style chapters. This will unavoidably lead to some repetition caused by self-contained components that will overlap with parts of the other sections of this thesis. For each paper we briefly outline the content and put the key findings coherently into the context of this thesis.

6.1 Paper A. Protein Diffusion in Crowded Electrolyte Solutions

Paper A (see Chap. 7) investigates the apparent diffusion of the globular protein Bovine Serum Albumin (BSA) in crowded aqueous solution as a function of protein concentration and sodium chloride concentration by combining cold neutron backscattering and spin-echo spectroscopy. Additionally, employing SAXS we retrieve complementary information on the equilibrium structure. The aim of the study is to find an answer to the question: How concentrated does a protein solution has to be for crowding to impact the protein diffusion behavior?

By means of SAXS we find a qualitative change from an uncorrelated to a strongly correlated solution due to increased excluded-volume effects. With a more detailed analysis, we conclude that below a volume fraction of approximately 10 % crowding is induced by unscreened charges, whereas above that volume fraction crowding is dominated by the excluded-volume contribution.

In contrast to the static data, the diffusion coefficients as obtained with quasi-elastic measurements do not reveal a distinct value where crowding due to the

excluded-volume contribution sets in. Instead, we find a continuously declining apparent diffusion coefficient with increasing volume-fraction. Furthermore, the addition of sodium chloride has little or only a slight effect, although charge screening is assumed to change significantly the intermolecular interaction.

Anticipatory, we point out that paper B (see Chap. 8) gives the explanation for the latter observation. In this study we confirm the applicability of colloid diffusion models to globular protein self-diffusion. The theoretical functions for colloidal hard-spheres and charged hard-spheres are very similar in the short-time limit [115, 4, 33, 165, 162]. As consequence of the given measured accuracy, we cannot distinguish between these models. Moreover, the reduced diffusion coefficient for charged hard-spheres is virtually independent of the surface charge, implying that screening effects are almost not perceivable. Even though the formation of a counter-ion layer on the protein surface alters the hydrodynamic radius [169], such an expansion is not detectable within the instrumental accuracy. Finally, salt induced solvent viscosity changes (compare Sec. 5.1.2) are negligible for the investigated salt concentration range of $0 - 300\,\mathrm{mM}$.

6.2 Paper B. Protein Self-Diffusion in Crowded Solutions

Perez et al. [125] showed that the apparent diffusion coefficient of a protein measured with quasi-elastic neutron spectroscopy is in general larger than the translational diffusion coefficient due to a non-negligible contribution of the rotational diffusion. Following up paper A, we develop an analytic framework to extract the translational diffusion coefficient from the apparent diffusion. This enables a comparison of the translational diffusion with theoretical models. Consequently, the motivation of paper B (see Chap. 8) is to test the applicability of colloid models to protein diffusion in crowded solutions.

Employing cold neutron backscattering spectroscopy (see Sec. 5.3.1), we measure the short-time self-diffusion in bovine serum albumin solutions for volume fractions in the range $7\,\% \leq \phi \leq 30\,\%$ and compare it with existing short-time colloid models for diffusion [115, 4, 33, 165, 162]. Moreover, by means of SAXS, we determine the shape of the protein in solution using an ellipsoid. We demonstrate that within the entire volume fraction range, the experimental translational diffusion coefficient can be described by

$$D_t(\varphi) \approx D_t(0)\, f\left[\varphi \left(\frac{R_h}{R}\right)^3\right], \tag{6.1}$$

in which f is indistinguishable from the series expansions of the reduced short-time diffusion coefficient of hard-spheres [162] and charged hard-spheres [4] within the error bars. R is the radius of a sphere with the same volume as the bare protein, R_h is the hydrodynamic radius, retrieved from the ellipsoidal model, and $D_t(0)$ is the dilute-limit diffusion coefficient. In a nutshell, we show that effective hard-

spheres no matter whether charged or non-charged accurately describe the measured short-time self-diffusion of a globular protein. Since in the short-time limit hydrodynamic interactions prevail, our experimental study fundamentally validates the simulation results from Ando and Skolnick [7], who found that the effect of macromolecular crowding on protein diffusion can be explained solely with hydrodynamic interactions and excluded volume. Furthermore, the surprising finding that a relatively simple colloidal model reproduces the behavior of the non-spherical and non-homogeneously charged protein represents a reliable framework for future studies on internal dynamics of proteins in solution and under crowding conditions.

6.3 Paper C. Dynamics of Highly Concentrated Protein Solutions around the Denaturing Transition

After having investigated crowding effects and the volume-fraction dependence of the self-diffusion of a protein suspension, we focus our research effort on the temperature dependence of the diffusion coefficient and use it to extract the total mean-squared displacement of the internal motion. Using computer simulations Kudlay et al. [91] concluded that macromolecular crowding has an impact on the random coil to helix transition of polymers. Mittal [111] found employing Langevin dynamics simulations that for monodisperse repulsive crowders, protein stability and folding rate will increase with increasing packing rate. It is therefore important to develop a framework to experimentally quantify folding and particularly its inverse process denaturing in the situation of crowding. Paper C (see Chap. 9) is a combined quasi-elastic and fixed elastic window neutron backscattering study to investigate both the *global* and *internal* dynamics of a highly concentrated *bovine serum albumin* solution around the denaturing transitions. Using fixed elastic window neutron backscattering, we recorded the total mean-squared displacement $\langle u^2 \rangle$ for the temperature range $280\,K < T < 370\,K$ and using quasi-elastic backscattering we determined the corresponding apparent diffusion coefficient.

Along with the data we developed a novel framework to analyze the denaturing process of the protein. Knowing that the secondary structure *bovine serum albumin* is dominated by α-helices, we describe the temperature dependence of $\langle u^2 \rangle$ with a model inspired by the Zimm-Bragg Model [187]:

$$\langle u^2 \rangle = a\,T + b - \Delta u^2\,\Theta\left(\frac{T - T_0}{\Delta T}\right) \tag{6.2}$$

in which a, b, Δu^2, T_0 and ΔT characterize the denaturing and cross-linking process and Θ is the smeared-out step function

$$\Theta(x) = \frac{1}{1 + e^{-x}}\ , \tag{6.3}$$

measuring the population of the denatured and cross-linked proteins. Using the apparent diffusion coefficient D from the quasi-elastic spectra, we separate internal

and global dynamics by

$$\left\langle u_{\mathrm{int}}^2 \right\rangle = \left\langle u^2 \right\rangle - (2\,\pi)^{-3/2}\,6\,D\,\tau. \tag{6.4}$$

Thereby, we reveal a discontinuous change in the first derivative of the temperature dependence of $\left\langle u_{\mathrm{int}}^2 \right\rangle$ at the denaturing temperature that has not been discovered before. We speculate that this observation can be attributed to the higher conformational flexibility of the unfolded protein chains in the cross-linked network than in the native state. Importantly, the framework can also be applied to any system with both center-of-mass and internal dynamics, such as conventional polymer solutions.

6.4 Paper D. Charge-Induced Dynamic Density Inhomogeneities in Protein Solutions

As we will explain in paper A (see Chap. 7), the addition of the monovalent salt sodium chloride has little or only a slight effect on the diffusion of BSA. In contrast, a multivalent salt such as YCl_3 induces a quite different behaviour. Zhang et al. [185, 186] showed that highly positively charged metal ions such as Y^{3+} can induce a charge inversion of negatively charged proteins. In particular, they showed that if the ion-concentration approaches a distinct value c^*, which depends on the protein concentration, short-range attractions increasingly become dominant and finally describe the protein interaction. Furthermore, they showed that at c^* the surface charge of the protein is negligible.

Consequently, the specific binding effect of Y^{3+} on the protein surface is suitable for tuning the intermolecular forces to investigate the competition between long-range repulsion and short-range attraction on the diffusion of BSA below and near the critical salt concentration c^*.

In paper D (see Chap. 10) we report on a combined neutron spin-echo spectroscopy and small-angle X-ray scattering study investigating the short-time self-diffusion coefficient and the isothermal compressibility of a globular protein *bovine serum albumin* in aqueous (D_2O) solution at various concentrations of the trivalent salt YCl_3. We increase the salt concentration up to the critical concentration c^*, where the protein surface charge is close to zero [185]. The normalized isothermal compressibility reveals that upon addition of YCl_3 the solution changes from a repulsion dominated to a attraction dominated system. Synchronously, we observe a reduction of the short-time self-diffusion. We attribute this slowing down to an increased number of other proteins in the close proximity hindering the diffusion by hydrodynamic forces. We speculate that the attraction-dominated nature of the potential of mean force favors the formation of transient clusters [27, 99] having a lifetime shorter than the instrumental time resolution due to the high surface charge of the proteins. The more the system is dominated by attraction the longer the lifetime of the clusters. When approaching the critical salt concentration c^* the lifetime diverges, coinciding with the observation that slightly above c^* the BSA

solution becomes abruptly turbid and shows macroscopic static clusters. Due to the short lifetime of transient clusters, the proteins can be considered as independent and therefore the dynamical response of the system will be essentially determined by monomers. Importantly, Liu et al. [99] point out that transient clusters are strictly speaking not clusters, but rather can be conceived as fluctuating inhomogeneities in the particle density. To quantify this inhomogeneities, we generalize the model of effective hard-spheres developed in paper B (see Chap. 8) to the present case yielding

$$d_s\left(c_s,\varphi\right) = d_0\, f_{\mathrm{HS}}\left[\left(\frac{R_h}{R}\right)^3 \varphi_{\mathrm{local}}\left(c_s\right)\right], \tag{6.5}$$

in which f_{HS} is the theoretical reduced translational diffusion function of hard-spheres [115, 162] and d_0 the dilute limit translational diffusion coefficient and R is the radius of a sphere with the same volume as the bare protein volume. If no salt is present the proteins are highly charged and favor a homogeneous density distribution corresponding to a volume fraction φ, consequently $\varphi_{\mathrm{local}}(0) = \varphi$. With increasing salt concentration the density of the solution becomes more inhomogeneous expressed by an increase of the local density relative to φ:

$$\varphi_{\mathrm{local}}\left(c_s\right) = \xi\left(c_s\right)\,\varphi, \tag{6.6}$$

Therein, we introduce the local crowding factor $\xi\left(c_s\right)$. We find that the maximum local crowding factor corresponds to a decrease of 20 % of the nearest neighbor distance of the protein, corroborating the picture of dynamic local inhomogeneities rather than tightly bound clusters. Above the critical salt concentration c^* we observe the discontinuous onset of the formation of macroscopic clusters indicating an abrupt increase of the cluster lifetime.

Chapter 7

Paper A. *Protein Diffusion in Crowded Electrolyte Solutions*

Contents

Paper A. Protein Diffusion in Crowded Electrolyte Solutions

Biochimica et Biophysica Acta **1804** (2010) 68-75

Authors: F. Roosen-Runge[1], M. Hennig[1,2], T. Seydel[2], F. Zhang[1], M.W.A. Skoda[3], S. Zorn[1], R.M.J. Jacobs[4], M. Maccarini[2], P. Fouquet[2], and F. Schreiber[1]

[1]Institut für Angewandte Physik, Universität Tübingen,
D-72076 Tübingen, Germany
[2]Institut Laue-Langevin, F-38042 Grenoble, France
[3]ISIS, Rutherford Appleton Laboratory, Chilton, Didcot OX11 0QX, UK
[4]Department of Chemistry, Chemistry Research Laboratory, University of Oxford,
Oxford OX1 3TA, UK

Authors contribution: F. Roosen-Runge, M. Hennig, M.W.A. Skoda, S. Zorn, R.M.J. Jacobs, F. Zhang, T. Seydel and F. Schreiber designed research. The samples were prepared by F. Roosen-Runge and M. Hennig. The experiments were performed by F. Roosen-Runge, M. Hennig and T. Seydel. M. Maccarini and P. Fouquet provided technical assistance and performed data reduction. Data analysis was performed by F. Roosen-Runge and M. Hennig. The article was written by F. Roosen-Runge, M. Hennig, T. Seydel and F. Schreiber. All authors contributed to the discussion.

7.1 Abstract

We report on a combined cold neutron backscattering and spin-echo study of the short-range and long-range nanosecond diffusion of the model globular protein Bovine Serum Albumin (BSA) in aqueous solution as a function of protein concentration as well as NaCl salt concentration. Complementary small-angle X-ray scattering data are used to obtain information on the correlations of the proteins in solution. Particular emphasis is put on the effect of crowding, i.e. conditions under which the proteins cannot be considered as objects independent of each other. We thus address the question at which concentration this crowding starts to influence the static and in particular also the dynamical behaviour. We also briefly discuss qualitatively which charge effects, i.e. effects due to the interplay of charged molecules in an electrolyte solution, may be anticipated. Both the issue of crowding as well as that of charge effects are particularly relevant for proteins and their function under physiological conditions, where the protein volume fraction can be up to approximately 40 % and salt ions are ubiquitous. The interpretation of the data is put in the context of existing studies on related systems and of existing theoretical models.

7.2 Introduction

Proteins constitute the basis of the function of living cells. In addition to their structure, the dynamics of proteins is closely related to their biological function. Some proteins occur in cell membranes, whilst others - the so-called globular ones - occur freely in water inside and outside the cells [134]. It is the latter category that the present article is concerned with. These globular proteins cannot be understood without their aqueous environment, and the ensemble of proteins and water may be denoted a solution, suspension, or gel, depending on the physical – in particular viscoelastic – properties of the ensemble [163, 112, 73].

In a simplified picture, living cells operate through the motion of proteins embedded in a high-concentration ("crowded") aqueous solution of various macromolecules and salts [49]. Considerable debate therefore addresses the connection of protein function and protein motion in an aqueous environment as a function of environmental parameters such as charges and temperature. It can be assumed that protein function cannot be understood without taking into account protein motion in an aqueous environment and the interaction of proteins, ions, and water [11].

Neutron spectroscopy has since long been proven to be a useful tool to investigate protein dynamics [15]. Whilst most other spectroscopic techniques, such as dynamic light scattering, are restricted to $Q \approx 0$, neutrons probe motion as a function of length scale from interatomic to mesoscopic distances in the sample, on time scales from sub-picoseconds to approximately 200 nanoseconds.

Most of the early neutron spectroscopy work concerning protein dynamics has been performed on powders or hydrated powder samples (for a review, see e.g. [61]). Interestingly, the biologically highly relevant case of protein solutions

has rarely been studied, *inter alia* due to the difficulty of discriminating the contribution from the centre-of-mass diffusion of both protein and solvent molecules and also the problem of obtaining the required protein scattering volume whilst keeping the solvent scattering contribution low. Various studies indicate that protein dynamics in solution strongly depends on the external environment parameters, such as temperature, solution composition, concentration, ionic strength, and pH [131, 129, 100, 144, 43, 87, 105].

In addition to the issues related to solutions in general, the issue of crowding has to be observed. It is clear that with increasing protein concentration the protein-protein interaction becomes more relevant both for static and dynamic behaviour. However it is not at all obvious and also not well studied experimentally at which concentration the behaviour changes qualitatively. In other words: How concentrated does a protein solution have to be for crowding to impact the protein diffusion behaviour? Furthermore, crowding is expected to be influenced by salt effects, since proteins in solution are generally charged, and the screening of these charges by salt ions has a profound impact on the effective interactions [184, 185].

In the present article we report on our experiments on protein dynamics in crowded electrolyte solutions using high resolution quasi-elastic neutron scattering techniques, namely backscattering and spin-echo techniques. We discuss the results in the context of crowding and charge effects, i.e. effects due to the interplay of charged molecules in an electrolyte solution, on different length scales – i.e. on protein nearest neighbor distances and on intramolecular length scales – in the context of structural information obtained by applying small-angle x-ray scattering (SAXS) techniques.

This article is organized as follows. After a short review of some theoretical concepts of diffusion in Sec. 7.3, the experimental details and data analysis procedures are explained in Sec. 7.4. In Sec. 7.5, first the (static) SAXS data are presented, followed by backscattering and neutron spin echo (NSE) data. We attempt a comprehensive discussion in Sec. 7.6. A summary and conclusions are presented in Sec. 7.7.

7.3 Theory

For a general introduction into quasi-elastic neutron scattering we refer to the textbooks by M. Bée and G.L. Squires [13, 151]. Backscattering spectroscopy probes the incoherent scattering function S_{inc} and thus the ensemble-averaged motion of one single molecule, i.e., self-diffusion. In an idealized view, diffusion is referred to as Brownian motion of one particle experiencing no interactions except from stochastic forces due to solvent fluctuations which fulfill the fluctuation-dissipation theorem. This so-called free diffusion is described by the Langevin equation and yields a mean square displacement (MSD) linear in time:

$$W(t) = \left\langle \left| \mathbf{r}_1(0) - \mathbf{r}_1(t) \right|^2 \right\rangle = 6\, D_0\, t \tag{7.1}$$

hereby defining the diffusion coefficient D_0.

Since our experiments probe interacting particles (especially in crowded solutions), truly free diffusion is not seen. Nevertheless, in many experiments which probe only a certain time scale we obtain a MSD linear in time

$$W(t) = 6\, D_{\mathrm{app}}\, t \tag{7.2}$$

where the apparent diffusion coefficient D_{app} is defined analogously to D_0.

7.3.1 Smoluchowski Equation

The apparent diffusion can be treated according to a Langevin equation with additional interaction forces which operate rapidly when compared to the experimental time window. The aqueous medium causes a damping of motion, thus there exists a time scale on which the moments relax to zero. For BSA this so-called diffusive time scale equals

$$\tau_D \gg M\,\gamma \approx 2\,\mathrm{ps} \tag{7.3}$$

where $M = 66.43\,\mathrm{kDa}$ is the mass of the BSA molecule and the friction parameter γ can be estimated from the dilute diffusion coefficient $D_0 = 6.62 \cdot 10^{-11}\,\mathrm{m^2\,s^{-1}}$ [87] using the Einstein relation $D_0 = k_B\,T/\gamma$ at a given temperature ($T = 296\,\mathrm{K}$).

A generalized description of motion on the diffusive time scale can be derived using the Smoluchowski equation, which describes the relaxation of interacting particles in a solvent experiencing a potential in their equilibrium distribution. Bundling all position vectors $\mathbf{r}_l$ of the centers of mass of the molecules into one single configuration vector $\mathbf{r}$, the Smoluchowski equation describes the time evolution of the N particle distribution function $P(\mathbf{r}, t)$ by

$$\partial_t P(\mathbf{r}, t) = \nabla\, \mathbf{D}(\mathbf{r})\, \left[\beta\, [\nabla\, V(\mathbf{r})]\, P(\mathbf{r}, t) + \nabla\, P(\mathbf{r}, t)\right] \tag{7.4}$$

where the diffusion tensor $\mathbf{D}$ characterizes hydrodynamic interactions [40] and V is the total potential energy of all molecules. Diffusion coefficients are calculated by averaging over the probability density function P obtained from the Smoluchowski equation. This approach is applicable for our purposes, since the nanosecond time scale probed by neutron scattering is comparable to the diffusive time scale τ_D.

Due to the high protein concentration, which we investigate here, the molecules feel the presence of the surrounding molecules mediated by both hydrodynamic interactions and direct interactions. While the former interactions act quasi-instantaneously on the diffusive time scale, the latter are established on a longer time-scale which is referred to as interaction time and can be estimated as

$$\tau_I = \frac{a^2}{D_0} \approx 100\,\mathrm{ns} \tag{7.5}$$

where $a \approx 2.8\,\mathrm{nm}$ is the radius of one BSA molecule [40].

7.3.2 Self-Diffusion

The self-diffusion coefficient D_s, which in general depends on both time t and scattering vector $\mathbf{Q}$, is a measure of mobility of a single tracer molecule under the influence of intermolecular interactions and is linked to the incoherent intermediate scattering function by

$$I_{\text{inc}}(Q,t) = \langle \exp\{\mathrm{i}\,\mathbf{Q}\,(\mathbf{r}_1(0) - \mathbf{r}_1(t))\}\rangle = \exp\left\{-D_s(\mathbf{Q},t)\,Q^2\,t\right\} \tag{7.6}$$

where the angular brackets denote the averaging over the joint distribution $P(\mathbf{r},\mathbf{r}_0,t) = P(\mathbf{r},t|\mathbf{r}_0)\,P(\mathbf{r}_0)$. The conditional distribution $P(\mathbf{r},t|\mathbf{r}_0)$ is the solution of the Smoluchowski equation given that the molecules were initially in the configuration $\mathbf{r}_0$ and $P(\mathbf{r}_0)$ is the Boltzmann distribution for the potential function.

In the short-time limit $\tau \ll \tau_I$ the molecules diffuse a short distance on the order of their own size influenced only by the quasi-instantaneously acting hydrodynamic interactions. Direct interactions play a less important role, since the potential does not change on the corresponding length scale. Thus, short-time self-diffusion can be understood intuitively as relatively free diffusion on a length scale limited by the direct interactions, while the hydrodynamic interactions act via a change of the effective solvent viscosity. Expanding both sides of the equation 7.6 in time and neglecting higher order terms, i.e. in the short-time limit, the MSD reads

$$W(t) = \left\langle |\mathbf{r}_1(t) - \mathbf{r}_1(0)|^2 \right\rangle = 6\,D_s^s\,t. \tag{7.7}$$

Here the short-time self-diffusion coefficient D_s^s turns out to be independent from time and Q.

7.3.3 Collective Diffusion

Unlike self-diffusion, collective diffusion relates to the motion of many Brownian particles simultaneously and describes in the small Q limit the relaxation of the macroscopic density according to Fick's law [55]. Therefore, it is measured in a coherent experiment like dynamic light scattering or neutron spin echo spectroscopy. The time and Q dependent collective diffusion coefficient D_c can be expressed by means of the coherent intermediate scattering function as follows [40, 44]

$$S(\mathbf{Q})\,\exp\left\{-D_c(\mathbf{Q},t)\,Q^2\,t\right\} = \frac{1}{N}\sum_{i,j=1}^{N}\langle \exp\{\mathrm{i}\,\mathbf{Q}\,(\mathbf{r}_i(0) - \mathbf{r}_j(t))\}\rangle\,. \tag{7.8}$$

The importance of direct interactions is reflected in the appearance of the static structure factor $S(\mathbf{Q})$. For large wave vectors $\mathbf{Q}$ the collective diffusion coefficient converges to the self-diffusion coefficient, because all cross-terms (those with $i \neq j$) become equal to zero, due to the rapidly oscillating behaviour of $\exp\{i\mathbf{Q}\,(\mathbf{r}_i - \mathbf{r}_j)\}$ [100, 44, 170].

7.4 Experiments

7.4.1 Samples and Measurements

Serum albumin is the most abundant protein in the blood plasma with an important role as stabilisator of both pH value and osmotic pressure of the blood. Furthermore serum albumin acts as essential transport protein for a large variety of ligands, including fatty acids and metals [29]. The native concentration of serum albumin is typically 50 mg/ml, which corresponds to a volume fraction of 3.6 %. The high solubility and availability of bovine serum albumin (BSA) and its importance as multifunctional carrier make BSA a good model protein to study both collective and tracer diffusion in crowded solutions.

BSA was purchased from Sigma with an indicated purity of 99 %. The protein was dissolved in D_2O at the desired NaCl and protein concentrations. Measurements of the pH-value confirmed a constant pH in all samples of pH 6.93 ± 0.07. After preparation the protein solutions were left for several hours in the cold room to achieve complete solvation and equilibrium. Right before the measurement the solutions were filled into a cylindric thin-walled aluminum container (outer diameter 22 mm, gap width 0.23 mm) and sealed against vacuum.

Neutron backscattering spectroscopy data were collected at IN16 [59, 79] (BSA volume fractions $\phi = 12.9$ % and 27 % corresponding to concentrations of 200 mg/ml and 500 mg/ml, respectively) and IN10 [79] ($\phi = 27$ %) at the ILL, Grenoble, both using cold neutrons with a wavelength of 6.27 Å and unpolished Si(111)-monochromators with a resolution of 0.9 μeV FWHM. The Q-range was 0.43 - 1.93 $Å^{-1}$ / 0.5 - 1.96 $Å^{-1}$ with a dynamic range of $\pm 15\,\mu$eV / $\pm 10\,\mu$eV (IN16 / IN10).

Neutron spin echo scans were performed at IN11 [79, 109] (BSA volume fractions $\phi = 3.6$ % and 12.9 % corresponding to concentrations of 50 mg/ml and 200 mg/ml, respectively) at the ILL, Grenoble, using wavelengths of 8.5 and 10 Å for Q-vectors ranging from 0.04 to 0.2 $Å^{-1}$. Data sets were recorded for 280 K (both NSE and backscattering) and 325 K (only backscattering), respectively. In the Q range of up to 0.2 $Å^{-1}$ we were able to exploit the strong coherent small angle scattering signal of the samples with NSE. At higher Q values this is not possible anymore, the signal gets very weak and incoherent scattering becomes comparable in strength to coherent scattering or even dominant. We note that for the different experiments on NSE and backscattering spectrometers different cryostats have been used. Although the temperature sensors were calibrated, a systematic error in the absolute sample temperature of a few Kelvin may occur due to the distance between the temperature sensor on the tip of the stick holding the sample and the sample itself as well as due to thermal conductivity differences.

The SAXS measurements were performed at Daresbury, UK, employing procedures similar to those of Ref.[184].

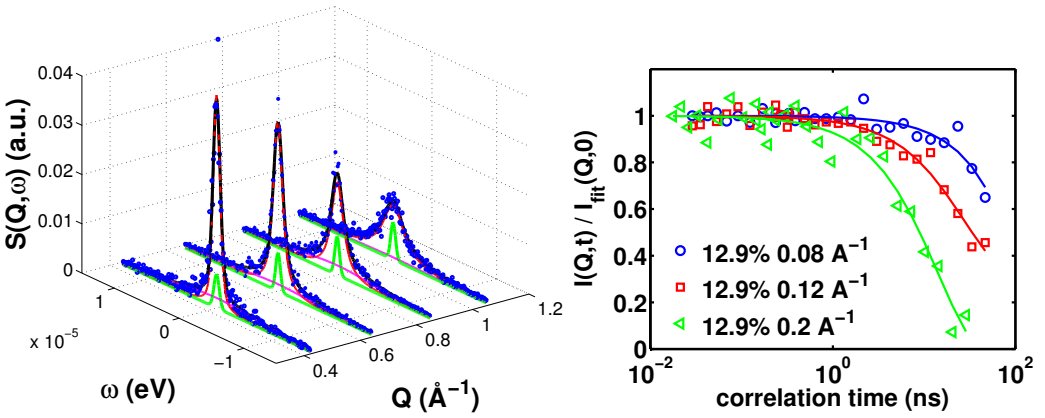

Figure 7.1: (a) Backscattering spectra recorded at IN16, ILL, at different Q vectors for a BSA volume fraction of 12.9 % without salt at $T = 280\,\mathrm{K}$, after normalization to the individual detector efficiencies. After the subtraction of the water background the data (blue symbols) can be fitted well by a model function (black line) consisting of two Lorentzians (red and magenta lines) convoluted with the Gaussian resolution function (green line). (b) Example correlation functions $I(Q,t)/I_{fit}(Q,0)$ derived from neutron spin echo (NSE) scans for a BSA volume fraction of 12.9 % without salt. The fits are single exponentials.

7.4.2 Data Analysis

Backscattering

After normalization of the backscattering data to the monitor spectrum, the spectra of pure D_2O were subtracted from the protein solution spectra. The bulk D_2O and the salt ions dissolved therein only contribute a constant signal, since their mobility is on picosecond time scales and therefore beyond the accessible dynamic window of a backscattering spectrometer. Therefore, we have neglected excluded-volume effects in the solvent subtraction. The instrumental resolution σ and the detector efficiency were determined detector-wise from the spectrum of vanadium measured in the sample geometry at $T = 280\,\mathrm{K}$ by a fit of a Gaussian and integration of the elastic line, respectively. This resolution was used as fixed parameter in the fits to the scattering function $S_{\mathrm{exp}}(Q,\omega)$ (Fig. 7.1). We used an approach with two Lorentzian line shapes (as used also in Refs.[125, 25]). The fit function can thus be written as

$$S_{\mathrm{fit}}(Q,\omega) = \mathcal{R}(\omega,\sigma) \otimes [A(Q)\,\mathcal{L}(\omega,\Gamma_1) + (1-A(Q))\,\mathcal{L}(\omega,\Gamma_2)] + B(Q) \quad (7.9)$$

$$= A(Q)\,\mathcal{V}_{\Gamma_1,\sigma}(\omega) + (1-A(Q))\,\mathcal{V}_{\Gamma_2,\sigma}(\omega) + B(Q) \quad (7.10)$$

where $\mathcal{R}$ is the Gaussian resolution function with width σ, $\mathcal{L}$ is a Lorentzian function with half width at half maximum (HWHM) Γ, and $\mathcal{V}$, is a Voigt function [8, 146, 167]. $B(Q)$ is the background and $A(Q)$ is the quasi-elastic incoherent structure factor (QISF). The half width at half maximum (HWHM) of the second Lorentzian was

fixed in our fits to $\Gamma_2 = 8\,\mu$eV, assuming that this broad Lorentzian accounts for fast motions near the cut off due to the constant Q-independent dynamic window of the spectrometer.

This model function can be interpreted as the combination of two dynamical processes, the centre-of-mass movement (diffusion in an unconfined medium) of the whole protein and other (faster) inter-domain and internal dynamics which are confined due to the protein topology:

$$S_{\text{fit}} = S_{\text{diff}} \otimes S_{\text{internal}} = \mathcal{L}\left(\omega, \Gamma_{\text{diff}}\right) \otimes \left[A(Q)\,\delta(\omega) + (1 - A(Q))\,\mathcal{L}\left(\omega, \Gamma_{\text{internal}}\right)\right] \quad (7.11)$$

In this interpretation the narrow Lorentzian corresponds to the global particle motion, whereas the broad Lorentzian consists of the convolution of both motions.

Error analysis: Different errors affect the experimental result. The counts I_k per energy channel k and detector exhibit a Poissonian distribution, thus normalization to the monitor spectrum yields for the k^{th} energy channel an error in intensity

$$\delta I_k = \Delta\left(\frac{N_k}{M_k}\right) = \frac{\sqrt{N_k}}{M_k} + \frac{N_k\sqrt{M_k}}{M_k^2} \quad (7.12)$$

where N_k corresponds to the detector counts and M_k to the monitor counts, respectively. The error of the experimental channel position due to a finite energy channel width ΔE can be approximated by the deviation of the mean energy of all counts in the k^{th} channel:

$$\delta\omega_k = \sqrt{\frac{\langle\delta E^2\rangle}{N_k}} = \frac{\Delta E}{2\sqrt{3N_k}} \quad (7.13)$$

where

$$\langle\delta E^2\rangle = \int_{-0.5\Delta E}^{0.5\Delta E} \mathrm{x}\frac{x^2}{\Delta E} = \frac{\Delta E^2}{12} \quad (7.14)$$

corresponds to the deviation of one count (assuming an uniform distribution in each channel). Further error propagation is treated according to Gaussian error propagation.

Neutron Spin Echo (NSE)

The neutron spin echo data were processed by the standard IGOR routines (including fits and error analysis) used at IN11, ILL. NSE spectroscopy measures the real part of the normalized intermediate scattering function $\Re[I(Q,t)]/I(Q,0)$. In our case the imaginary part of $I(Q,t)$ is negligible, so we measure, in fact, $I(Q,t)/I(Q,0)$[109]. The resolution correction in NSE is achieved by a simple division by the signal of an elastically scattering sample with the same sample geometry. We used graphite powder as the elastic sample.

The resolution corrected $I(Q,t)$ data were fitted accurately by simple exponen-

tial decay curves $\exp(-t/\tau)$, where τ is the decay time of the relaxation. The Fourier transform of an exponential decay is a Lorentzian function as observed in the backscattering spectra with a corresponding quasielastic broadening (HWHM) given by $\Gamma = \hbar/\tau$ [13].

SAXS

With SAXS we measure the total scattering intensity $I(q)$, which for a monodisperse system can be expressed as

$$I(q) = N\ (\Delta\rho)^2\ V^2\, P(q)\, S(q), \tag{7.15}$$

where $S(q)$ is the structure factor, containing information about the intermolecular interaction, and $P(q)$, the so-called form factor, characterizes the shape of the molecule. Furthermore, N is the number density of proteins and $\Delta\rho = \rho_P - \rho_s$ the electron density difference of the protein molecule and of the solvent, usually denoted scattering contrast. For an infinitely dilute solution the structure factor is unity. Hence, assuming a monodisperse system and a concentration independent form factor, we determined the form factor from a sufficiently dilute solution [184]. Finally, the total intensity data $I(q)$ were fitted using the structure factor

$$S(q) = 1 + 4\,\pi\,N \int_0^\infty [g(r) - 1]\, \frac{\sin(q\,r)}{q\,r}\, r^2\, dr \tag{7.16}$$

via the Ornstein-Zernicke equation for different effective particle interactions, including the static pair-correlation function $g(r)$.

7.5 Results

7.5.1 Crowded Aqueous Solution of BSA - Charge Effect and SAXS

It is useful to first characterize the correlations and static (or so-called direct) interactions of crowded solutions by means of SAXS before examining their impact on dynamical properties. In previous SAXS measurements the static interactions of BSA in aqueous solutions has been systematically examined [184]. Here we focus on the effects which are related to crowding behaviour.

The low Q regime corresponds directly to the structure factor. Figure 7.2(a),(b) displays two typical scattering profiles for different protein and salt concentrations. For all samples without salt a pronounced correlation peak is observed. The corresponding nearest neighbour distance $r_{\text{c-c}} = \frac{2\,\pi}{Q_{\text{corr}}}$ decreases upon increasing the concentration of BSA and is shown in Fig. 7.3. The line in the plot denotes the calculated nearest neighbour distance by simple geometrical consideration (see inset of figure 7.3) assuming a closest sphere packing of virtual spheres whose centers

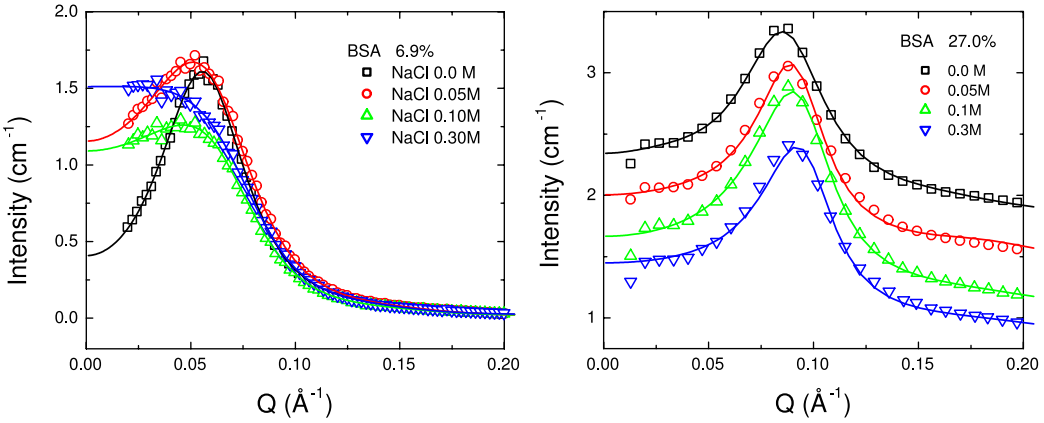

Figure 7.2: Intensity data from SAXS measurements at BSA concentrations of 100 mg/ml (a) and 500 mg/ml (b) corresponding to volume fractions $\phi = 6.9\,\%$ (a) and 27 % (b), respectively, for increasing NaCl concentrations. The dashed line indicates the shift of the maximum upon salt addition. For low salt concentrations both show an intense correlation peak. While for increasing NaCl concentration this correlation peak disappears for BSA solutions at $\phi = 6.9\,\%$, the profile for $\phi = 27\,\%$ remains nearly unchanged upon increasing the salt concentration.

correspond to the equilibrium positions of the molecules:

$$r_{\text{c-c}} \approx \left(\frac{\phi_{csp}}{\phi}\right)^{\frac{1}{3}} 2\ a \tag{7.17}$$

where $\phi_{\text{csp}} = \frac{\pi}{3\sqrt{(2)}} \approx 0.74$ corresponds to the volume fraction of the closest sphere packing, ϕ is the volume fraction of the molecules and $a \approx 2.8\,\text{nm}$ the effective radius of one molecule.

In Figure 7.2(a),(b) the salt dependence of the scattering profile is shown for two crowded protein solutions (volume fraction 6.9 % and 27 %, respectively). For the lower protein concentration the correlation peak disappears by addition of NaCl due to the salt screening effect. The interaction used for the fitting changes from a screened-Coulomb potential to an effective square-well potential. In contrast, for protein volume fractions above 13 % the correlation peak is conserved upon addition of salt, and salt screening causes only a slight shift. The conservation of the correlation peak also for higher salt concentrations implies the absence of aggregation in this highly concentrated protein solution and indicates a behaviour corresponding to hard spheres in a random sphere packing (but not crystallinity).

7.5.2 Global Motion of Single BSA Molecules in Solution: Backscattering

Figure 7.1(a) shows a backscattering spectrum and the fit by two Lorentzian functions convoluted with a Gaussian resolution function. The derived widths Γ_1 of the

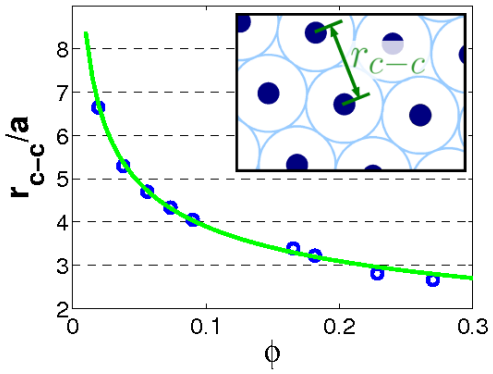

Figure 7.3: Centre-to-centre distance $r_{\text{c-c}}$ normalized to the effective radius $a = 2.8\,\text{nm}$ of BSA molecules in aqueous solution as a function of the BSA volume fraction ϕ obtained from SAXS data (circle symbols) and theoretical estimate according to equation 7.17 (line). By increasing the protein concentration the particles move closer together, as intuitively expected. The inset shows the geometrical consideration leading to equation 7.17: the equilibrium positions of the molecules (corresponding to the full spheres) are the centers of virtual spheres which establish a closest sphere packing.

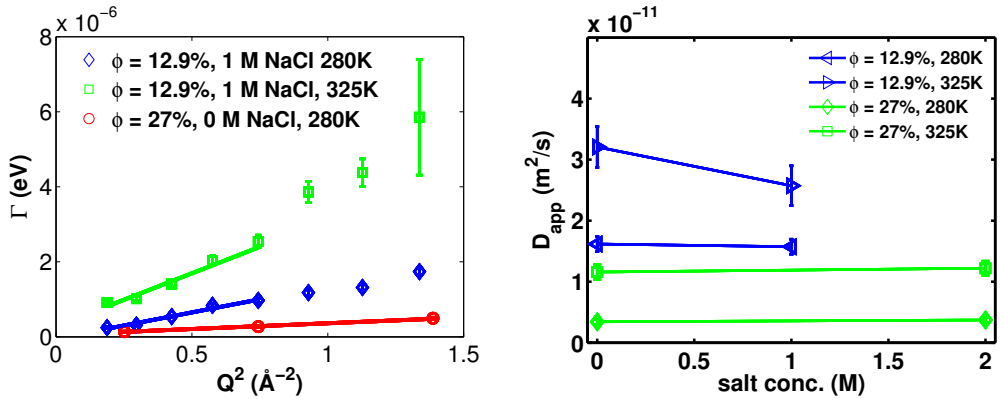

Figure 7.4: Backscattering: (a) Widths of the narrow Lorentzian versus Q^2 for different protein concentrations which are derived as described in Sect.7.4.2. The fit $\Gamma = D_{\text{app}}^{\text{inc}}\, Q^2$ defines the apparent diffusion coefficient derived from backscattering spectroscopy, the fit range being restricted to the region where $\Gamma \propto Q^2$ holds (see text). Data recorded on IN16 (square and diamond symbols) and IN10 (circle symbols). (b) Apparent diffusion constants versus NaCl concentration. While for different protein concentrations there are obvious differences in $D_{\text{app}}^{\text{inc}}$, the addition of salt appears to have little effect. (Corresponding data recorded on IN10 and IN16. The lines are guides to the eye.)

narrow Lorentzian function for our fits are shown in Fig. 7.4(a) with a Q^2 relationship for low Q according to simple diffusion. We note that for higher Q we see a sub-Q^2 behaviour (sometimes taken as evidence for "jump diffusion"), which has also been observed in previous studies on proteins in crowded solutions by neutron backscattering [25], whereas there are several studies by time-of-flight spectroscopy in a comparable Q-range which do not show this deviation [125, 64]. This discrepancy suggests that the deviation is caused by the finite energy window of the spectrometer and therefore an inappropriate fitting model, but also real effects including crowding could be considered [25]. Since our backscattering data do not provide further information on the nature of the deviation, we concentrate on the Q^2 regime. We derive the apparent diffusion coefficient by a fit to the low-Q regime: $\Gamma_1(Q) = D_{\mathrm{app}}^{\mathrm{inc}} Q^2$. For the samples with a BSA volume fraction $\phi = 12.9\,\%$ (measured at IN16) and $\phi = 27\,\%$ (IN10) we constrain the fit to $Q < 0.85\,\text{Å}^{-1}$ and $Q < 1.2\,\text{Å}^{-1}$, respectively (Figure 7.4(a)). The difference in the fit range accounts for the fact that the deviation from $\Gamma \propto Q^2$ occurs for lower protein concentration already at lower Q. We attribute this to the fact that at lower concentration (or higher temperature) the mobility becomes faster than detectable by the dynamic window of the spectrometer already at lower Q.

In Figure 7.4(b) the apparent diffusion coefficients are summarized. Two basic conclusions can be drawn: Firstly, increasing the BSA concentration, the apparent diffusion is clearly slowed down. Secondly, the addition of NaCl has little or no effect for solutions with BSA volume fraction of 27 %. For solutions with $\phi = 12.9\,\%$ there is a small decrease in diffusion upon addition of salt. We note that the choice of the width of the second, broad Lorentzian (see section 7.4.2) has a systematic influence on the fit result for the narrow Lorentzian. An increase of the width of the broad Lorentzian results in a nearly constant shift of the apparent diffusion constants. However, this influence has little effect on the observed salt- and concentration-dependent trends. We motivate the choice of the value of 8 μeV for the HWHM of the broad Lorentzian by the dynamic range covered by the backscattering spectrometer (see section 7.4.2).

7.5.3 Relaxation of Fluctuations of BSA Concentration in Solution: NSE

In Figure 7.1(b) three typical NSE spectra are depicted. The time window accessed by our experiment can be estimated from this figure (Fig. 7.1b)), i.e. approximately 30 ps to 50 ns. All data sets are fitted well by a single exponential decay $I(Q,t)/I(Q,0) \propto \exp(-t/\tau)$. The resulting decay times are summarized in Figure 7.5(a). Assuming $H(Q)/S(Q) = \text{const.}$ with the hydrodynamic function $H(Q)$ [44], the decay times τ can be related to a diffusion coefficient:

$$\frac{1}{\tau(Q)} = D_{\mathrm{app}}^{\mathrm{coh}} Q^2 \tag{7.18}$$

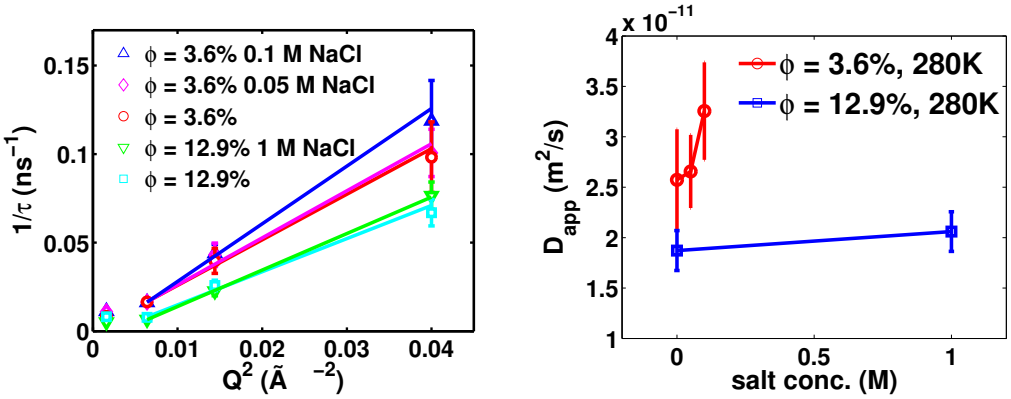

Figure 7.5: NSE: (a) Inverse decay times τ^{-1} for different experimental conditions. The linear fit $\tau^{-1} = D_{\text{app}}\, Q^2$ yields an apparent diffusion coefficient derived from NSE. (b) Apparent diffusion coefficients versus NaCl concentration. Decreasing protein concentration and increasing salt concentration enhance the diffusion. (The lines in (b) are guides to the eye. The sample temperature was always $T = 280\,\text{K}$.)

$D_{\text{app}}^{\text{coh}}$ is the apparent diffusion coefficient, corresponding to the relaxation of fluctuations of BSA density [100, 44, 69]. The corresponding Q^2 fits are shown as lines in Figure 7.5(a). For the fit, the lowest value in Q has been ignored (see discussion below).

The apparent diffusion coefficients are shown in Figure 7.5(b). Two trends can be observed: Firstly, the apparent diffusion is slowed down with increasing protein concentration. Secondly, the addition of salt appears to slightly increase the diffusion in this regime.

7.6 Discussion

As the starting point for the discussion of the data we consider the SAXS data presented in Sec. 7.5.1. These provide information on equilibrium properties such as (averaged) particle-particle distances and effective interactions. Whereas for a protein volume fraction $\phi = 6.9\,\%$ the addition of salt changes the SAXS pattern, at a protein volume fraction $\phi = 27\,\%$ salt has little impact, indicating that at such a high concentration the solution is already rather crowded.

Generally, one obvious effect of crowding is simply the excluded-volume effect, i.e., by increasing the protein concentration the particle-particle distance is decreased and thus the particle interactions are more important. We assume that for volume fractions above a certain value, spherical macromolecules whose interactions are dominated by strongly screened charges, i.e., close to the hard-sphere limit, organize in a pattern similar to random sphere packing. At this volume fraction the gap between two molecules drops below the diameter of one molecule, i.e. $r_{\text{c-c}} < 4\,a$, we obtain for the corresponding volume fraction $\phi \approx \frac{\phi_{\text{csp}}}{8} = 9.25\,\%$ from equation 7.17.This qualitative change in the correlation of molecules is reflected in

the appearance of a correlation peak in SAXS measurements at high concentrations of both protein ($\phi > 12\,\%$) and salt (above 0.5 M NaCl). For solutions without or with less salt, the correlation peak is observed already for very dilute solutions [184], indicating a long-range order of the time averaged position coordinates.

Concerning the change of dynamical behaviour of crowded solutions due to the excluded-volume effect, a strong dependence of the long-time self-diffusion is expected, again changing qualitatively at a volume fraction around 10 % and including features like jump-diffusion in the high-concentration regime. In contrast, the short-time self-diffusion is expected to change continuously over the entire concentration range. In this time regime direct interactions are not relevant and the impact on the particle motions increases continuously starting from very low concentrations, as it is only mediated by long-ranged and quasi-instantaneously acting hydrodynamic interactions.

Apart from this behaviour, which on a qualitative level is not surprising, the screened-Coulomb interaction has additional effects on the issue of crowding. By increasing the salt concentration the screening length is decreased. Hence, the length scale on which direct interactions become important, the so-called interaction length scale λ_I, is decreased. This interaction length scale λ_I corresponds to a shortened interaction time scale $\tau_I \approx \frac{\lambda_I^2}{D_s^s}$. Thus, crowding in terms of an increased (screened-) Coulomb interaction causes a qualitative change in the dynamic behaviour.

Our neutron backscattering data show a Q^2 relationship $\Gamma = D_{\mathrm{app}}^{\mathrm{inc}}\, Q^2$ for $Q \leq 1.2\,\text{Å}^{-1}$. Upon increasing the protein concentration we observe a trend to slower diffusion, whereas salt seems to have little or no effect. The neutron spin echo data show a Q^2 relationship $\frac{1}{\tau} = D_{\mathrm{app}}^{\mathrm{coh}}\, Q^2$. In contrast to backscattering data, we see an increase of diffusion upon addition of salt, whereas the dependence on protein concentration remains qualitatively the same, i.e., a decrease of apparent diffusion upon increasing protein concentration.

At this point, it is important to recall the similarities and the differences of backscattering and NSE, as well as the associated time and length scales. Generally, the neutron backscattering technique depends on incoherent scattering and thus studies self-diffusion. Since the interaction time $\tau \approx \frac{a^2}{D_0} \approx 100\,\mathrm{ns}$ (eq.7.5) is larger than our experimental time window, the derived apparent diffusion can be interpreted in terms of short-time self-diffusion. With this in mind, both observed trends are reasonable. Whilst a variation of the protein concentration has a strong impact mediated by hydrodynamic interactions, the addition of salt yields only a slight variation. The latter can be rationalized as increasing of the effective hydrodynamic radius due to the formation of the counter-ion layer [184, 169].

Neutron spin echo probes coherent scattering, thus in principle collective diffusion. The interaction time is close to the experimental time window. Effects related to charge interactions are therefore expected. In our data this effect is reflected in the screening effect of salt. Importantly, in the high Q limit (i.e., $Q \gg 2\,\pi\, r_{\text{c-c}}^{-1}$), neutron spin echo data can be interpreted effectively in terms of self-diffusion [100, 44, 170]. Since the nearest neighbour distances (see Fig.7.3) are around 15 nm ($\phi = 3.6\,\%$)

	ϕ	NaCl concentration	D (10^{-11}m^2/s) 280 K	325 K
NSE	3.6 %	0 M	2.57 ± 0.50	
		0.05 M	2.66 ± 0.36	
		0.1 M	3.26 ± 0.48	
	12.9 %	0 M	1.87 ± 0.20	
		1 M	2.06 ± 0.20	
Backscattering	12.9 %	0 M	1.77 ± 0.13	4.44 ± 0.37
		1 M	1.73 ± 0.13	4.00 ± 0.35
	27 %	0 M	0.422 ± 0.041	1.26 ± 0.12
		2 M	0.416 ± 0.040	1.33 ± 0.11

Table 7.1: Summary of apparent diffusion coefficients derived from our backscattering and neutron spin echo experiments on BSA solutions (see text).

and 10 nm ($\phi = 12.9\,\%$), this approximation is fulfilled relatively well for the three higher Q values.

Both experiments agree quite well, as summarized in table 7.1, evidencing a general slowing-down trend according to an excluded-volume interaction. The dilute limit for the self-diffusion coefficient has been measured by dynamic light scattering in H_2O [87]. The derived $D_0 \approx 6.62 \cdot 10^{-11}\,\mathrm{m}^2/\mathrm{s}$ agrees well with an extrapolation of our observed trend towards the low concentration limit.

The different trends upon salt addition in our results are caused by different time regimes – while backscattering is in the short-time limit, neutron spin echo probes time scales comparable to the interaction time.

7.7 Summary, Conclusions, and Outlook

We have presented a high-resolution cold neutron scattering study of the dynamics of the model protein BSA in crowded aqueous solution as a function of the protein concentration and added salts. We have thus investigated molecular diffusion on nanosecond time scales on length scales ranging from protein nearest neighbour distances down to intramolecular length scales. These dynamical data have been combined with small angle X-ray scattering data on the same system.

From SAXS data we find a qualitative change from an uncorrelated to a strongly correlated solution due to increased excluded-volume effects. We conclude that below a volume fraction of approximately 10 % crowding is induced by unscreened charges, whereas above that volume fraction crowding is dominated by the excluded-volume contribution. For weaker screening (i.e. less salt) this correlation is found already for lower protein concentrations.

For QENS data we find a continuously changing behaviour of the self-diffusion due to the excluded-volume effect. The addition of salt has little or no effect on the apparent diffusion coefficients, although charge screening is assumed to change both interaction time and coupling strength. In the protein concentration range covered

by our experiments, i.e. from approximately 4 % to 27 % volume fraction, our data are in agreement with a continuous decrease of the apparent diffusion constants with the protein concentration. In contrast to the static data, our dynamic data show no distinct value where crowding due to the excluded-volume contribution sets in.

Understanding the dynamics of crowded solutions is not only a necessity to interpret QENS data, because usually these involve higher protein concentrations to achieve adequate statistics. Crowding itself, caused by a variety of hydrodynamic and direct interactions, is an important feature of cellular environments and has to be studied in further detail. We thus wish to prepare the ground for future experiments using multivalent salts giving rise to more complex phenomena such as the reentrant condensation [185] and the future extension to other protein systems.

Acknowledgements

Felix Roosen-Runge and Marcus Hennig gratefully acknowledge financial support from the ILL through studentships. The authors benefited from discussions with E. Reister (Stuttgart) and H. Schober (ILL, Grenoble).

Chapter 8

Paper B. *Protein Self-Diffusion in Crowded Solutions*

Contents

Paper B. Protein Self-Diffusion in Crowded Solutions

Proceedings of the National Academy of Sciences (USA) **108** (2011) 29:11815-11820

Authors: F. Roosen-Runge[1], M. Hennig[1,2], F. Zhang[1], R.M.J. Jacobs[3], M. Sztucki[4], H. Schober[2], T. Seydel[2], and F. Schreiber[1]

[1]Institut für Angewandte Physik, Universität Tübingen,
D-72076 Tübingen, Germany
[2]Institut Laue-Langevin, F-38042 Grenoble, France
[3]Department of Chemistry, Chemistry Research Laboratory, University of Oxford,
Oxford OX1 3TA, UK
[4]European Synchrotron Radiation Facility, 38043 Grenoble Cedex 9, France

Authors contribution: F. Roosen-Runge, M. Hennig, H. Schober, M.W.A. Skoda, S. Zorn, R.M.J. Jacobs, F. Zhang, T. Seydel and F. Schreiber designed research. The samples were prepared by F. Roosen-Runge and M. Hennig. The experiments were performed by F. Roosen-Runge, M. Hennig and T. Seydel. M. Sztucki provided technical assistance and performed data reduction. Data analysis was performed by F. Roosen-Runge and M. Hennig. The article was written by F. Roosen-Runge, M. Hennig, F. Zhang, T. Seydel and F. Schreiber. All authors contributed to the discussion.

8.1 Abstract

Macromolecular crowding in biological media is an essential factor for cellular function. The interplay of intermolecular interactions at multiple time and length scales governs a fine-tuned system of reaction and transport processes, including particularly protein diffusion as a limiting or driving factor. Using quasi-elastic neutron backscattering, we probe the protein self-diffusion in crowded aqueous solutions of *bovine serum albumin* on nanosecond time and nanometer length scales employing the same protein as crowding agent. The measured diffusion coefficient $D(\varphi)$ strongly decreases with increasing protein volume fraction φ explored within $7\,\% \leq \varphi \leq 30\,\%$. With an ellipsoidal protein model and an analytical framework involving colloid diffusion theory, we separate the rotational $D_r(\varphi)$ and translational $D_t(\varphi)$ contributions to $D(\varphi)$. The resulting $D_t(\varphi)$ is described by short-time self-diffusion of effective spheres. Protein self-diffusion at biological volume fractions is found to be slowed down to 20 % of the dilute limit solely due to hydrodynamic interactions.

8.2 Introduction

The interior of biological cells is a medium with a macromolecular volume fraction of up to 40 %. This crowding crucially affects reaction kinetics and equilibria in the cell [49, 188]. Cellular function and structure thus cannot be understood without a systematic understanding of both phase behavior and transport processes in crowded media. Diffusion is the main transport process for systems at low Reynolds numbers, governing many dynamic processes in nature [133]. From the perspective of a single tracer molecule, all other molecules act as obstacles. *In-vivo* diffusion coefficients for globular proteins in living cells [7, 179, 9, 168] are strongly decreased compared to the *in-vitro* diffusion coefficient in dilute buffer solutions. Systematic measurements of the tracer diffusion of proteins dissolved in concentrated suspensions of crowding agents, i.e. other proteins or polymers, reveal a complex dependence of the slowing down on the combination of tracer molecule and crowding agent [174, 113, 42]. Furthermore, macromolecular crowding is found to induce subdiffusive behavior in several cases [12, 176], being suggested as a slower but more reliable diffusive search process inside the cell [67]. This anomalous diffusion process has been found also in theory and simulations [107, 143, 176, 67] suggesting a crossover from subdiffusive behavior at small times to diffusive behavior at larger times.

Proteins are macromolecules generally with a non-spherical shape and a non-homogeneous surface charge, showing specific interactions with ligands. Furthermore, proteins not only show global motions like translational and rotational diffusion but also internal and inter-domain motions. Therefore, proteins pose a challenge to colloid theory [130, 185]. In a recent simulation study T. Ando and J. Skolnick [7] revealed that using an equivalent-sphere model for macromolecules is a reasonable approximation to describe diffusion. Moreover, they demonstrated that interactions between the molecules, including both hydrodynamic interactions mediated by the

solvent and direct interactions due to hard-sphere and Coulomb potentials crucially affect diffusion in a crowded environment. Consequently, it is of fundamental interest to test the applicability of colloid models to protein diffusion in crowded solutions.

The dynamics of a colloidal suspension is characterized by different time scales, corresponding to different regimes of motion [115]. The solvent time scale τ_s is in general much shorter than the diffusive time scale of the dissolved particles $\tau_B \approx m/(6\pi\eta R)$ on which the motion changes from ballistic to diffusive motion. In this diffusive regime and for non-interacting particles with radius R and mass m in a solvent with viscosity η the well-known Stokes-Einstein diffusion constant $D_t(0) = k_B T/(6\pi\eta R)$ is recovered. In real systems and at finite concentrations, interparticle interactions give rise to additional relevant time scales. Hydrodynamic interactions arise on the time scale $\tau_H \approx R^2\rho/(\eta\,\varphi) \gg \tau_B$ with the solvent density ρ, and the colloidal volume fraction φ, affecting the so-called short-time diffusive regime $\tau_H \ll t \ll \tau_I$. The structural relaxation time $\tau_I \approx R^2/D_t(0)$ defines the onset of caging effects on the particle center-of-mass diffusion due to direct interparticle interactions. For $t \gg \tau_I$ long-time self-diffusion is observed, affected by both hydrodynamic and direct interactions. For the short-time and long-time regimes, series expansions have been derived for the self-diffusion of spherical colloids with and without charge [115, 4, 33, 165, 162].

In this study we report on extensive experimental data on protein self-diffusion in crowded aqueous solutions of *bovine serum albumin* (BSA) as determined from quasi-elastic neutron backscattering on nanosecond time and nanometer length scales. Thereby, we investigate the fundamental case where tracer particle and crowding agent are identical proteins. Quasi-elastic neutron scattering accesses both microscopic spatial and time correlations by measuring the van Hove scattering function $S(Q,\omega)$ [13].

Due to the large incoherent scattering length of hydrogen, neutron backscattering of biological samples directly probes self-correlations of the hydrogen atoms. Moreover, neutron scattering is the only non-invasive and non-destructive technique to access protein solution samples at high protein concentrations. In an incoherent measurement of a highly concentrated solution, all molecules can be conceived as unlabeled and simultaneously play the role of both tracer molecule and crowding agent.

Recent neutron scattering work studied protein dynamics in solutions, thereby mainly addressing the hydration and temperature dependence of internal motions [125, 152, 80, 19, 153, 121]. Few studies, however, investigated protein short-time diffusion [25, 69, 138, 154] or long-time diffusion [100, 44, 94].

Here, we present detailed results on the dependence of protein short-time self-diffusion on protein concentration. We obtain the translational diffusion coefficient $D_t(\varphi)$ at different protein volume fractions φ and discuss the results in comparison with colloidal suspension models, thereby testing the applicability of colloid approximations.

8.3 Protein Modeling

Proteins differ considerably from hard spheres for which theoretical predictions for colloidal diffusion are available. A sensible comparison of experiment and theoretical predictions requires a mapping of the protein on an effective sphere [82]. Simulations of proteins in a crowded environment showed that effects of the shape on the diffusion can be accounted for using effective spheres [7].

The simplest choice for an effective radius would be the radius of a sphere with the same volume as the bare protein volume calculated from the specific volume (see Methods), in our case $R \approx 2.68\,\mathrm{nm}$.

In the case of diffusion, however, the resulting effective radius has to be larger than R for the following reasons: First, the hydration shell surrounding the protein increases the size of the proteins. Second, the anisotropic shape of the protein described by the Perrin factors [128, 82] additionally increases the effective radius.

In order to determine the effect of the anisotropy and the hydration shell on the effective radius, we performed small-angle X-ray scattering (SAXS) on dilute aqueous BSA solutions, comprising the following samples: 0.15 M NaCl (1, 2, 5, 10 mg/ml BSA), 0.01 M HEPES buffer with 0.4 M NaCl (1, 2, 10 mg/ml BSA) and 0.15 M HEPES buffer (5, 10 mg/ml BSA). Fig. 8.1 shows an example data set of 5 mg/ml BSA in 0.15 M HEPES buffer. Using an oblate ellipsoid the form factor of all SAXS data was modeled (see Methods and Ref. [184]). Averaging the results, we finally obtain an oblate ellipsoid with polar semi-axis $a \approx 1.8 \pm 0.05\,\mathrm{nm}$ and equatorial semi-axis $b \approx 4.6 \pm 0.15\,\mathrm{nm}$. Note that the fit result includes the hydration shell since the higher mass density of hydration shell water causes a scattering contrast [158].

Based on this ellipsoidal protein model, we calculate the effective hydrodynamic radii for translational diffusion, $R_h = 3.62\,\mathrm{nm}$ which defines the translational diffusion coefficient in the dilute limit (see Methods). Note the good consistency of the effective radius R_h with the hydrodynamic radius $R_h^{\mathrm{DLS}} = (3.66 \pm 0.03)\,\mathrm{nm}$ calculated from results from dynamic light scattering [62].

For theoretical predictions, the volume fraction of the effective spheres is of central importance. This effective volume fraction is connected to the physical protein volume fraction φ by

$$\varphi_t = \varphi \left(\frac{R_h}{R} \right)^3 . \tag{8.1}$$

To compare the measured translational diffusion coefficient with the theoretical prediction of a colloid model we use the effective volume fraction

$$D_t^{\mathrm{theory}}(\varphi) = D_t(0)\, f\left(\varphi_t\right), \tag{8.2}$$

in which f is the theoretical reduced translational diffusion coefficient and $D_t(0)$ the dilute limit translational diffusion coefficient.

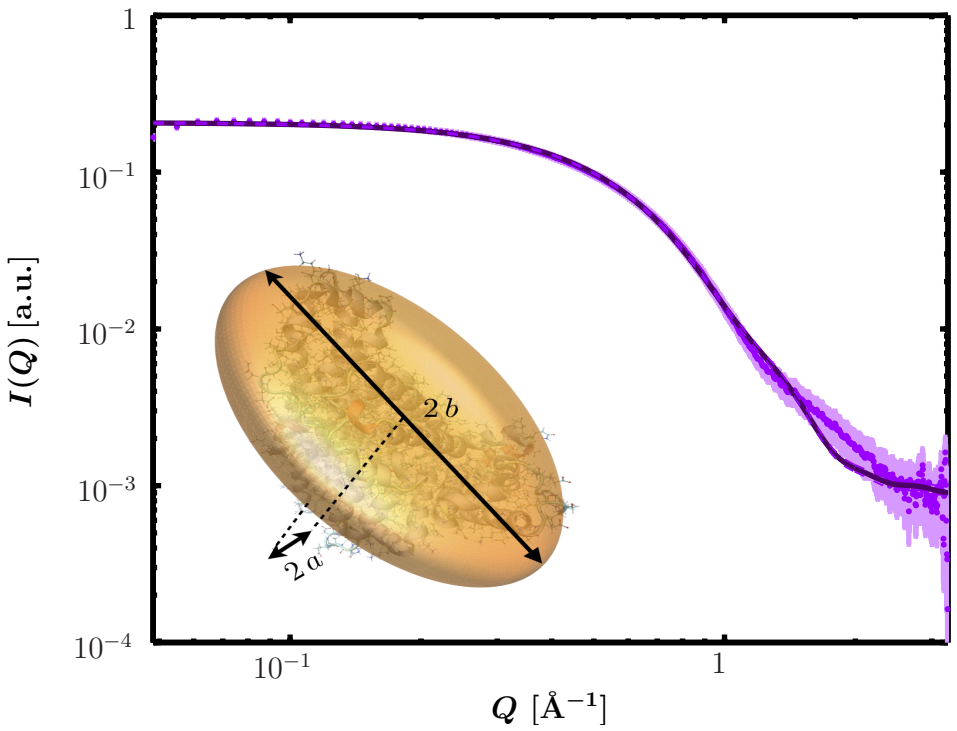

Figure 8.1: Small-angle X-ray scattering intensity for a dilute solution of BSA (5 mg/ml, room temperature) in 150 mM HEPES buffer after subtraction of background contributions. The data (circle) can be fitted with the form factor of an oblate ellipsoid (solid line). The deviation at higher Q is caused from the deviation of the protein shape from an ellipsoid at smaller length scales. The fitting of scattering data from several solutions with protein concentration below 10 mg/ml and varying concentration of HEPES buffer and NaCl is consistent with an oblate ellipsoid with polar semiaxis $a \approx 1.8 \pm 0.05$ nm and equatorial semiaxes $b \approx 4.6 \pm 0.15$ nm. This protein model of an oblate ellipsoid (inset lower left corner) is used as input for the further data analysis based on colloid theory.

8.4 Results

8.4.1 Quasielastic Spectra and Simple Diffusion Coefficient

We performed a series of quasielastic neutron backscattering measurements covering the full range of protein volume fraction φ from 5 to 30 % using the instruments IN10 and IN16 at the ILL. The inset of Fig. 8.2 depicts a typical spectrum $S(Q,\omega)$ recorded on IN16. All spectra can be fitted according to the model [125, 152, 25, 138]

$$S(Q,\omega) = \mathcal{R}(\omega) \otimes \mathcal{L}_\gamma(\omega) \otimes [\beta_1\,\delta(\omega) + \beta_2\,\mathcal{L}_\Gamma(\omega)] + B \tag{8.3}$$

Therein, $\mathcal{R}$ denotes the instrumental resolution function, $\beta_{1,2}$ are scalars, B is a flat background accounting for the water diffusion which is beyond the accessible dynamic range of both instruments, and $\delta(\omega)$ designates the Dirac function of the elastic scattering. The width of the two Lorentzians $\mathcal{L}_\gamma$ and $\mathcal{L}_\Gamma$ represent the time scales of two separated spectral components: while the broader width Γ accounts for fast internal and inter-domain motions within the protein, γ is attributed to the convolution of the translational and rotational diffusion of the entire protein [125, 152, 25, 138]. The widths γ as obtained from the fits (Eq. (8.3)) are plotted in Fig. 8.2. For $Q^2 < 1.5\,\text{Å}^{-2}$, a clear relationship $\gamma = D\,Q^2$ is observed, defining the diffusion coefficient D. This clear relationship is observed for all samples in the full volume fraction range and is consistent with simple diffusion on the accessible time and length scales. Superdiffusive jump-diffusion or subdiffusion due to crowding would cause a varying local slope corresponding to the changing diffusion coefficient for different time and length scales, i.e. with scattering vector Q. For $Q^2 > 1.5\,\text{Å}^{-2}$ the scattering signal from the proteins becomes weaker and considerably broadened with respect to the accessible energy range. These two factors can cause fitting artifacts, we neglected these data points for the fitting of the diffusion coefficient, although the Q^2 relationship seems conserved.

8.4.2 Separation of Translational and Rotational Diffusion

Fig. 8.3 shows the resulting diffusion coefficients $D(\varphi)$ (upper points). The extrapolation $D(\varphi \to 0)$ using a polynomial fit (upper blue line) reveals a higher dilute limit compared to the value in D_2O at $T = 280\,\text{K}$, $D_t(0) = (3.01 \pm 0.04)\,\text{Å}^2/\text{ns}$, calculated from dynamic light scattering results [62, 32]. This indicates a non-negligible contribution of the rotational diffusion to D. We thus have to separate the measured D into the translational and rotational contributions. Pérez et al. showed numerically that the rotational contribution causes an additional line broadening [125], assuming spherical particles in the dilute limit. Inspired by this analysis, we develop an analytical method to extract D_t from D also for high concentrations (see Appendix for a detailed derivation). The calculated scattering function $S_{\text{t+r}}(Q,\omega)$ for rotational and translational diffusion can be approximated by a single Lorentzian line shape with HWHM γ and amplitude α in the Q-range relevant for our experiment.

We recover $\gamma = D\,Q^2$ for this approximation in the measured Q-range, defining

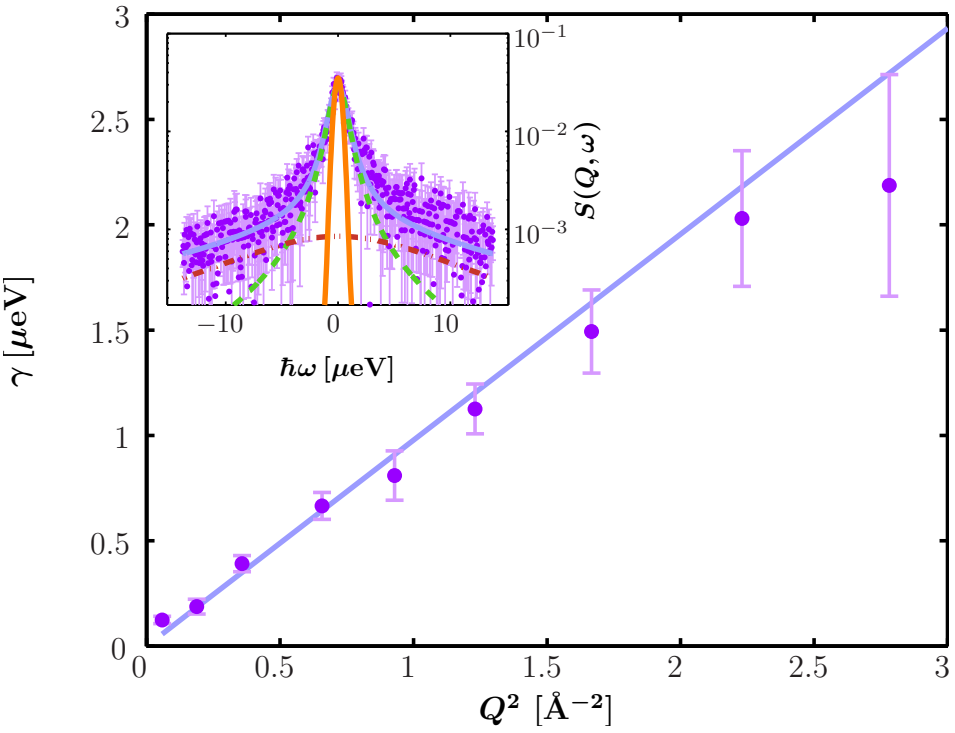

Figure 8.2: Inset: Example backscattering spectrum $S(Q,\omega)$ (symbols) recorded at IN16 for BSA in D_2O ($c = 500\,\mathrm{mg/ml}$, $\varphi = 28.5\,\%$, T = 300 K, individual detector at $Q = 0.81\text{Å}^{-1}$). The magenta solid line is the fit of the model from Eq. (8.3). The two Lorentzians in Eq. (8.3) are indicated by the dashed and dash-dotted lines. The orange solid line denotes the resolution function. Main figure: Fitted γ (symbols) versus Q^2 for the full Q-range of the example data. The fit of $\gamma = D\,Q^2$ (blue line) is consistent with simple diffusive behavior. For statistical reasons the fit range is restricted to $Q^2 < 1.5\,\text{Å}^{-2}$.

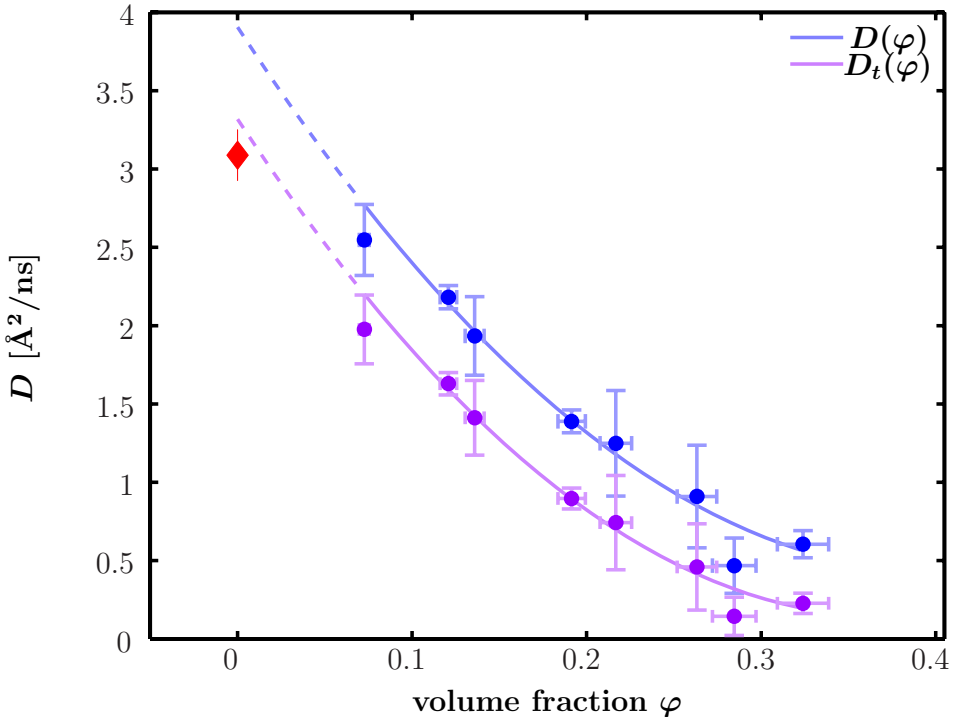

Figure 8.3: Measured diffusion coefficients D for BSA solutions in D_2O at $T = 280\,K$ (blue circles on upper curve) and translational diffusion coefficients D_t (purple circles on lower curve) computed from D using Eq. (8.4) and the theoretical rotational diffusion coefficient from Ref. [4]. The lines are polynomial fits. The dilute limit $D_t(0)$ (diamond symbol) is calculated from results of dynamic light scattering [62]. The non-coincidence of $D_t(0)$ and the fit to D indicates a significant rotational contribution. After separation of the rotational contribution, the translational diffusion coefficient D_t is in accordance with the dilute limit, supporting the validity of our approach.

the diffusion coefficient D [125]. By minimizing the $\mathbb{L}^2$-norm $\|S_{t+r}(Q,\cdot) - \alpha\,\mathcal{L}_\gamma(\cdot)\|^2$ we obtain

$$\sum_{l=0}^{\infty} B_l(Q)\,\frac{D_r\,l\,(l+1) + (D_t - D)\,Q^2}{\left[D_r\,l\,(l+1) + (D_t + D)\,Q^2\right]^2} = 0. \tag{8.4}$$

We assume that D_r can be approximated by the short-time rotational diffusion for charged spheres $D_r(\varphi) = D_r(0)\,(1 - 1.3\,\varphi^2)$ [4] with the dilute limit $D_r(0)$ from Eq. (8.9). Using Eq. (8.4), we evaluate $D_t(\varphi)$. Importantly, this extraction is robust, since other models for short-time rotational diffusion do not change $D_t(\varphi)$ significantly.

8.4.3 Protein Self-Diffusion in Crowded Media

The resulting reduced diffusion $D_t(\varphi)/D_t(0)$ is displayed for different temperatures in Fig. 8.4, showing a strong decrease of the translational diffusion coefficient due to

macromolecular crowding on nanosecond time scales. At volume fractions $\varphi \approx 25\%$ as present in living cells, the translational diffusion is decreased to 20 % of the dilute-limit value, implying a slowing down of diffusion-driven transport and diffusion-limited reactions. Interestingly, the reduced diffusion seems to obey a temperature-independent master-curve.

The experimental $D_t(\varphi)/D_t(0)$ agree almost perfectly with the normalized short-time self-diffusion coefficient predicted by colloid theory for charged [4] and non-charged hard spheres [162] (Fig. 8.4). Both predictions take into account only hydrodynamic interactions, which depend on the equilibrium structure of the solution and thus differ between charge-stabilized and hard-sphere suspensions [4]. Reconsidering the simplistic nature of the model system of effective hard spheres for the complex soft protein, this excellent agreement is not expected.

8.5 Discussion

8.5.1 Colloid Picture of Protein Self-Diffusion in Crowded Media

We identify the measured self-diffusion coefficient with short-time self-diffusion. This interpretation is consistent with theoretical expectations: the accessible time scales of the neutron spectrometer,

$$0.3\,\mathrm{ns} \leq \tau \leq 5\,\mathrm{ns}, \tag{8.5}$$

are in the short-time regime for self-diffusion of BSA in D_2O, since

$$100\,\mathrm{ps} \approx t_H \ll \tau \ll t_I = \frac{R^2}{D_t(0)} \approx 425\,\mathrm{ns}. \tag{8.6}$$

Short-time self-diffusion implies that the observed slow-down of the protein diffusion is mainly caused by hydrodynamic interactions.

8.5.2 Reduction Factor and Influence of Hydrodynamic Interactions

Experimental results on the *in-vivo* reduction factor of protein diffusion in a cellular medium compared to buffer solutions show a dependence on the protein size. The reported values corresponding to BSA-sized molecules range from 1/70 [179] to approximately 0.2 [9, 168]. Measurement in crowded *in-vitro* solutions of proteins obtained a reduction factor of approximately 0.08 for albumin tracers at 25 % volume fraction of the crowding agent [42] and a factor of 0.35 for BSA tracers at 13 % volume fraction of BSA [113]. All these results have been obtained using fluorescence-labeling techniques at the μs time scale and are generally rationalized by an effectively increased viscosity, hindrance due to obstacles and transient adsorption at larger obstacles [174]. The reduction factors found in the present study of 0.2 at 25 % and 0.4 at 13 % occur already at nanoseconds and are attributed solely to hy-

drodynamic interactions, i.e. an increased effective viscosity of the cellular medium, but not to hindrance due to obstacles. The obtained short-time self-diffusion values are of similar order of magnitude as the long-time values obtained from fluorescence-labeling techniques, implying an important and non-negligible role of hydrodynamics to the observed crowding effect. Protein dynamics and, in particular, protein diffusion in a crowded environment thus cannot be understood simply by excluded volume and confined motions, but has to include hydrodynamic interactions.

These experimental findings are in perfect accordance with recent results from simulations [7]. Ando and Skolnick found that the effect of macromolecular crowding on protein diffusion can be explained solely with hydrodynamic interactions and excluded volume, supporting the mentioned colloid picture of macromolecular crowding. Their findings for the reduced short-time self-diffusion coefficient fit to our data quantitatively.

For concentrated solutions of hemoglobin, the crowding effect on the diffusion has been also investigated with quasi-elastic neutron scattering using neutron spin-echo spectroscopy, obtaining a reduction factor around 0.2 at 22 % volume fraction [44]. Although the behavior seems qualitatively and quantitatively similar, the comparison to our data, however, fails for two reasons. First, the accessed time scales are around 50 ns and comparable to the colloidal interaction time scale, implying significant long-time effects of direct interactions on the diffusive motion. Second, neutron spin-echo is a coherent scattering technique, thus probing collective diffusion. In the short-time limit and at large Q, collective diffusion equals self-diffusion. This equality does not strictly hold for the case of long-time diffusion, disallowing a consideration of the measured diffusion as self-diffusion. Thus, while their data probe collective diffusion with long-time effects, our data corresponds undoubtedly to short-time self-diffusion.

8.5.3 Essential Role of Anisotropy in Protein Modeling

Proteins are non-spherical molecules. In order to account for this anisotropy, colloid models have to be refined. In our modeling approach, the protein is mapped on an oblate ellipsoid that incorporates the full anisotropy and governs the dilute limit rotational and translational diffusion coefficients of the protein through the Perrin factors. It is important to notice that rotational and translational diffusion are affected differently by anisotropy and that this difference in the effective radii matters. It should be noted that other macromolecular properties and processes could modify the diffusion but seems to be less important or cancel out in our system. Water-permeability of the protein core results in a larger $D_t(\varphi)/D_0$ [3]. The effect of a gradually changing hydration shell, the flexibility of the protein, the hydrophobicity and non-homogeneous charge distribution has not been systematically studied to our knowledge. Furthermore, in attractive systems below the solubility limit, oligomerization and transient clustering could decrease the diffusion coefficient. Crowding is known to induce compaction of protein structures [49, 155]. A decrease in the radius of gyration of smaller than 0.4 % has been found when comparing a globular

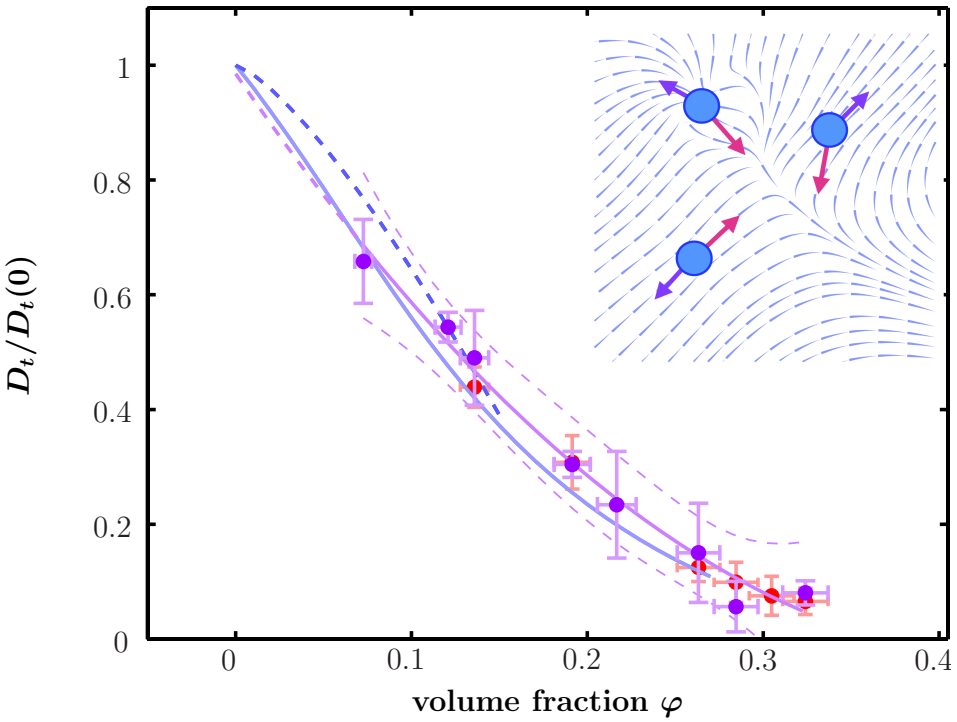

Figure 8.4: Normalized translational self-diffusion coefficients (Fig.8.3) $D_t/D_t(0)$ (circles) for two different temperatures (red and purple circles denote 280 and 300 K, respectively) after separation of the rotational contributions. The purple line superimposed on the data is a guide to the eye obtained from a polynomial fit indicating the temperature-independent master-curve. The upper and lower dashed purple lines indicate the upper and lower 96 % prediction bounds, respectively. The blue lines denotes the colloidal short-time self-diffusion for hard spheres (light blue, solid) and charged spheres (dark blue, dashed). The inset in the upper right corner illustrates the flow field (light blue stream line plot) generated by the movement of three spheres (velocities are denoted by blue arrows) and therefore experiencing a hydrodynamic forces (pink arrows).

protein structure in dilute and crowded ($\varphi = 0.25$) protein solutions [155]. The related change of R_h under crowding conditions is not discernible with our method within the experimental errors and thus does not affect our conclusions.

8.6 Conclusions

We studied the effect of crowding on the self-diffusion of BSA by means of quasi-elastic neutron backscattering. Our analysis confirms that crowding has a very substantial effect on the protein self-diffusion already at the nanoseconds time scale. Moreover, we reveal that the diffusion coefficient at biological volume fractions is strongly decreased compared to the dilute limit. This finding is described with very good accuracy in terms of colloidal short-time self-diffusion, outlining the important

role of hydrodynamic interactions on crowding behavior. We conclude that general features of protein diffusion can be understood in terms of existing colloidal hard sphere models if anisotropy is considered using reasonable protein modeling. The modeling approach used in this study is based on an experimentally established protein shape model without adjustable parameters, i.e. an oblate ellipsoid from the fitting of SAXS data. The analysis of the protein diffusion including the separation of rotational and translational contributions is performed for effective spheres with existing predictions from colloid theory. The success of this simple mapping of the complex protein on an effective sphere is promising for further investigations.

8.7 Materials

8.7.1 Sample Preparation

BSA was purchased from Sigma-Aldrich with an indicated purity of 99 % and used without further purification. The samples were prepared by dissolving BSA powder with mass m_{BSA} in the solvent with volume V_{solv}. For neutron scattering we used pure D_2O as solvent; for SAXS we used a H_2O-based solution with 150 mM HEPES buffer as solvent. Correcting for the protein volume, we obtain the volume fraction occupied by the bare proteins

$$\varphi = \frac{\vartheta\, m_{\mathrm{BSA}}}{V_{\mathrm{solv}} + m_{\mathrm{BSA}}\, \vartheta} \tag{8.7}$$

where $\vartheta = 0.735\,\mathrm{ml/g}$ is the specific volume of BSA [96]. The prepared φ cover a range of 7-30 %. After complete dissolution and equilibration the solutions were filled in double-walled aluminum cylinders (23 mm outer diameter, 0.3 mm gap), which were sealed against vacuum and kept at $T = 280$, 300, and 325 K, respectively, for the measurements. The pH values of the samples were checked to be neutral over the full concentration range. No precise data on oligomerization are available for high volume fractions. However, the samples show no visible aggregation or precipitation on time scales of months; monomeric aqueous BSA solutions are charge-stabilized and have been shown to be thermodynamically stable [78, 184].

8.7.2 Quasielastic Neutron Backscattering

We used the backscattering spectrometers IN10 and IN16 at the Institute Laue-Langevin in Grenoble, France, in the standard configuration with unpolished Si(111)-monochromator and analyzer crystals, which set the selected neutron wavelength to 6.27 Å and achieve an energy resolution of approximately 0.9 μeV (gaussian FWHM). The energy range accessible by Doppler-shifting the incident wavelength on both instruments defines the accessible time scales $\tau = 2\pi\hbar/E$, the Q-ranges set

the probed length scales $l = 2\pi/Q$:

$$0.3\,\text{ns} \leq \tau \leq 5\,\text{ns}$$

$$0.32\,\text{nm} \leq l \leq 1.2\,\text{nm} \qquad \text{(IN10)}$$

and $$0.33\,\text{nm} \leq l \leq 3.3\,\text{nm} \qquad \text{(IN16)}$$

The raw data were normalized to the incident neutron flux and relative detector efficiency. The scattering signal of an empty cylinder was subtracted to correct for background contributions. Water background was not removed but included in the data fitting as flat background.

8.7.3 Small-Angle X-ray Scattering (SAXS)

The SAXS data were measured at ID02 at the ESRF, Grenoble, France. For a detailed description of the data treatment we refer to Ref. [184, 185]. In general, SAXS measures the product of structure factor $S(Q)$ and form factor $P(Q)$, $I(Q) \propto P(Q)\,S(Q)$. Due to the low protein concentration of 5 mg/ml and strong charge-screening of the added buffer, protein-protein interactions can be neglected, i.e. $S(Q) \equiv 1$. The data can be simply fitted by the formula $I(Q) = n\Delta\rho^2 P(Q)$ with the number density n, the scattering contrast $\Delta\rho^2$ and the form factor $P(Q)$ on an oblate ellipsoid.

8.7.4 Perrin Factors for Ellipsoids of Revolution and Effective Hydrodynamic Radii

For an ellipsoid of revolution with polar semiaxis a and equatorial semiaxes b, the Perrin factors specify the translational and rotational diffusion coefficient in the dilute limit:

$$D_t(0) = \frac{k_B\,T}{6\,\pi\,\eta\,a}\,A(p) \tag{8.8}$$

$$D_r(0) = \frac{k_B\,T}{8\,\pi\,\eta\,a^3}\,B(p) \tag{8.9}$$

where $p = b/a$ is the ellipsoid aspect ratio. Moreover, we can extract the effective hydrodynamic radius $R_h = a\,A(p)^{-1}$. $A(p)$ and $B(p)$ result from the angular average of translational and rotational friction factors [128]:

$$A(p) = \frac{1}{\sqrt{|1-p^2|}} \begin{cases} \arctan\left(\sqrt{p^2-1}\right) & \text{(oblate: } p > 1\text{)} \\ \ln\left(\frac{1+\sqrt{1-p^2}}{p}\right) & \text{(prolate: } p < 1\text{)} \end{cases}$$

$$B(p) = \frac{1 + 3\,p^2\,A(p)}{2\,p^2\,(1+p^2)}.$$

For the present case of an oblate ellipsoid with $a = 1.8\,\mathrm{nm}$ and $b = 4.6\,\mathrm{nm}$, we obtain $p = 2.56$ and thus $A(p)^{-1} = 2.01$ and $B(p)^{-1/3} = 2.09$.

8.8 Implicit Relation Between Rotational, Translational and Fitted Diffusion Coefficient

The scattering function of a particle performing rotational and translational diffusion reads [125]

$$S_{\mathrm{t+r}}(Q,\omega) = \frac{1}{\pi}\sum_{l=0}^{\infty} B_l(Q)\,\frac{\Gamma_l(Q)}{\omega^2+\Gamma_l(Q)} \tag{8.10}$$

$$\text{with}\quad B_l(Q) = \int_0^{\infty} \mathrm{d}r\,\rho(r)\,(2\,l+1)\,j_l^2(Q\,r) \tag{8.11}$$

$$\text{and}\quad \Gamma_l(Q) = D_r\,l\,(l+1) + D_t\,Q^2, \tag{8.12}$$

where D_r and D_t denote the rotational and translational diffusion coefficients, respectively. The rotational dynamic structure factors are entirely determined by the radial density distribution of the hydrogen atoms in the molecule, $\rho(r)$. $j_l(x)$ is the lth-order spherical Bessel function of first kind.

It was found [125, 152] and reproduced in our study that a single Lorentzian line shape with HWHM γ and amplitude α approximates the calculated scattering function $S_{\mathrm{t+r}}(Q,\omega)$ for rotational and translational diffusion inside error bars in the Q-range relevant for our experiment. The minimization of the $\mathbb{L}^2$-norm

$$\|S_{\mathrm{t+r}}(Q,\cdot) - \alpha\,\mathcal{L}_\gamma(\cdot)\|^2 = \int \left[S(Q,\omega) - \alpha\,\mathcal{L}_\gamma(\omega)\right]^2\,\mathrm{d}\omega \tag{8.13}$$

reduces to two non-linear equations:

$$\alpha = 2\,\gamma(Q)\sum_{l=0}^{\infty}\frac{B_l(Q)}{\Gamma_l(Q)+\gamma(Q)} \tag{8.14}$$

$$0 = \sum_{l=0}^{\infty} B_l(Q)\,\frac{\gamma(Q)-\Gamma_l(Q)}{2\,\gamma(Q)\,(\Gamma_l(Q)+\gamma(Q))^2} \tag{8.15}$$

Inserting Eq. (8.12) and the Q-dependent diffusion coefficient $d(Q) = \gamma(Q)/Q^2$ into Eq. (8.15), an implicit relation of the three involved diffusion coefficients $d(Q)$, D_r and D_t is derived:

$$0 = \sum_{l=0}^{\infty} B_l(Q)\,\frac{D_r\,l\,(l+1) + (D_t - d(Q))\,Q^2}{\left[D_r\,l\,(l+1) + (D_t + d(Q))\,Q^2\right]^2}\ . \tag{8.16}$$

For given D_t and D_r, which are Q-independent, the Q-dependence of $d(Q)$ can be discussed. For $Q = 0$, we obtain $B_l = \delta_{l,0}$ which renders the implicit Eqs. [8.14,

8.15] explicitly solvable yielding $\gamma = D_t\, Q^2$ and $\alpha = 1$, i.e. $d(0) = D_t$. For finite Q, $d(Q)$ monotonously increases with Q and converges rapidly to a constant value. By the limit

$$D = \lim_{Q\to\infty} d(Q), \tag{8.17}$$

we define the observable diffusion coefficient D. The rapid convergence of $d(Q)$ restates the simple diffusive relation $\gamma(Q) = D\, Q^2$ as observed in the accessible Q-range, as found already numerically [125, 152]. Rotational diffusion thus acts as an additional contribution not distinguishable from translational diffusion without careful modeling and approximations.

Inserting $d(Q) = D$ into Eq. (8.16) finally returns the implicit relation Eq. (8.4) connecting the three diffusion coefficients D, D_r and D_t. For a given pair of two diffusion coefficients, the third can thus be calculated by solving Eq. (8.4). This is performed numerically for a truncated sum. The truncation is dependent on the Q range and generally valid since $B_l(Q)$ rapidly decays to zero at finite Q for increasing l [125]. For our Q range, we use $n_{\max} = 250$.

8.9 Acknowledgments

We are grateful to the ILL and ESRF for the allocation of beamtime. Moreover, F. Roosen-Runge and M. Hennig acknowledge financial support from the ILL, through studentship grants. The authors benefitted from discussions with E. Reister (Stuttgart, Germany), G. Zaccai, D. Bicout, E. Kats (ILL, Grenoble, France), and G. Nägele (FZ Jülich, Germany).

Chapter 9

Paper C. *Dynamics of Highly Concentrated Protein Solutions around the Denaturing Transition*

Contents

Paper C. Dynamics of Highly Concentrated Protein Solutions around the Denaturing Transition

In preparation for Physical Review Letters

Authors: M. Hennig[1,2], F. Roosen-Runge[1], F. Zhang[1], S. Zorn[1], M.W.A. Skoda[3], R.M.J. Jacobs[4], T. Seydel[2], and F. Schreiber[1]

[1]Institut für Angewandte Physik, Universität Tübingen,
D-72076 Tübingen, Germany
[2]Institut Laue-Langevin, F-38042 Grenoble, France
[3]ISIS, Rutherford Appleton Laboratory, Chilton, Didcot OX11 0QX, UK
[4]Department of Chemistry, Chemistry Research Laboratory, University of Oxford,
Oxford OX1 3TA, UK

Authors contribution: M. Hennig, F. Roosen-Runge, M.W.A. Skoda, S. Zorn, R.M.J. Jacobs, F. Zhang, T. Seydel, and F. Schreiber designed research. The samples were prepared by M. Hennig. The experiments were performed by M. Hennig and T. Seydel. Data analysis was performed by M. Hennig and F. Roosen-Runge. The article was written by M. Hennig, F. Roosen-Runge, T. Seydel, and F. Schreiber. All authors contributed to the discussion.

9.1 Abstract

Using both quasi-elastic and fixed-window neutron spectroscopy, we study the dynamics of highly concentrated aqueous protein solutions of *bovine serum albumin* around the denaturing transition. For the temperature range $280\,\mathrm{K} < T < 370\,\mathrm{K}$, the total mean-squared displacement $\langle u^2 \rangle$ is recorded. Below and above the denaturing, we observe that $\langle u^2 \rangle$ increases monotonically with T, but at the denaturing transition it decreases strongly. This observation can be rationalized and quantitatively modeled as a transition from a liquid protein solution to a gel-like state. Atomic vibrations, molecular subunit diffusion and, most importantly, diffusion of the entire protein determine $\langle u^2 \rangle$. The latter is strongly hindered due to entanglement and cross-linking of the chains and causes the pronounced decrease of $\langle u^2 \rangle$. Using information from the full quasi-elastic signal, we separate the diffusion contribution from $\langle u^2 \rangle$ and reveal the transition temperature. For the analysis of this separation, we introduced a general concept which is applicable to other systems exhibiting both center-of-mass and internal dynamics.

9.2 Introduction

Crucial to the physical understanding of soft and biological matter is the obvious, but in general insufficiently understood, link between the microscopic properties and the functionality of the system. Microscopic properties, such as dynamics have been intensely addressed by, *inter alia*, neutron spectroscopy techniques [57, 61, 45, 100]. Neutron spectroscopy allows both the picosecond subunit diffusion and the nanosecond translational and rotational diffusion of globular proteins to be probed [15, 13]. A significant amount of work on protein dynamics has been carried out on powder or hydrated powder samples (for a review, see e.g. [61]), which simplifies the analysis, since some degrees of freedom including the center-of-mass motion do not contribute. Solutions of proteins [15, 28, 54, 152, 125, 50, 138] are obviously more complex, but closer to physiological conditions. Importantly, in many situations in biology, proteins are found at rather high concentrations, known as macromolecular crowding, up to and above 30 % in volume. This implies that, in contrast to dilute aqueous solutions with effectively independent proteins, the interactions between the dissolved proteins are important and give rise to qualitatively different effects.

At elevated temperatures proteins denature. The denaturing transition itself is an important key to the physical behavior of the protein. The issue of denaturing of a protein in a crowded environment was previously addressed by simulation [91], concluding that crowding can enhance the structural stability, but experimentally the effects arising upon denaturing of crowded proteins with their intrinsic complex charge distribution are not clear. Only few experimental results on the dynamics of protein suspensions around denaturation are available [140, 65], but a systematic understanding and a theoretical framework have not been achieved yet. In this Letter, we report on a detailed neutron spectroscopy study of the denaturing transition of bovine serum albumin (BSA) in crowded aqueous (D_2O) solutions and a newly

developed framework to quantitatively investigate the *hindered* dynamics of the proteins upon entanglement and cross-linking and to analyze the different contributions to the mean-squared displacement $\langle u^2 \rangle$ around the denaturing transition. Importantly, our novel framework is not restricted to the study of denaturing of proteins, but can be applied to any system with both center-of-mass and internal dynamics, e.g. also conventional polymer solutions.

9.3 Experimental and Methods

For all neutron measurements the samples were prepared by dissolving BSA (Sigma-Aldrich product code A3059, 99 % purity) with mass m in D_2O with volume V to obtain the protein concentration $c = m/V$. After complete dissolution and equilibration, the solutions were contained in double-walled aluminum cylinders with 23 mm outer diameter and 0.3 mm gap which were sealed against vacuum. Due to the complete filling and sealing of these sample holders, the neutron scattering experiments were performed at constant sample volume while the pressure changes with sample temperature. We used the neutron backscattering spectrometers IN10 and IN16 at the ILL in Grenoble in the standard configuration with unpolished Si(111)-monochromator and analyzer crystals, which set the selected neutron wavelength to 6.27 Å and achieve an energy resolution of approximately $\hbar\,\Delta\omega = 0.9\,\mu$eV (gaussian FWHM). The Q-ranges set the probed length scales to 3.2 Å $\leq l \leq$ 12 Å (IN10) and 3.3 Å $\leq l \leq$ 33 Å (IN16), respectively, with $l = 2\pi/Q$. The data were normalized to the incident neutron flux. Using Paalman-Pings coefficients [122] the empty cylinder signal was subtracted. Subsequently, all data were scaled by the inverse detector efficiency obtained from the elastic intensity of vanadium. Due to the large incoherent scattering cross-section of the proteins, our data reflect the single particle correlation function of the protein hydrogen atoms. For the quasi-elastic data, we assume that vibrational and diffusive modes are uncoupled and obtain [46, 39, 125, 13]

$$\begin{aligned} S(Q,\omega) &= \exp\left(-\frac{1}{3}\langle u^2_{\text{vib}}\rangle Q^2\right) \mathcal{L}(\omega,\gamma) \\ &\quad \otimes \{A(Q)\,\delta(\omega) + [1 - A(Q)]\,\mathcal{L}_\beta(\omega,\Gamma)\} \end{aligned} \tag{9.1}$$

$A(Q)$ is the incoherent elastic structure factor and $\langle u^2_{\text{vib}} \rangle$ denotes the so-called mean-squared displacement of vibrations. The Lorentzian function $\mathcal{L}(\omega,\gamma)$ models the convolution of translational and rotational diffusion of the entire protein [125]. Using a single phenomenological parameter $0 \leq \beta \leq 1$, the Kohlrausch-Williams-Watts (KWW) function $\mathcal{L}_\beta(\omega,\Gamma)$ [178] describes a broad range of internal relaxation times. Finally, $\delta(\omega)$ designates the Dirac function of the elastic scattering. The experimental quasi-elastic scattering function reads

$$S_{\text{exp}}(Q,\omega) = \mathcal{R}_{\Delta\omega}(\omega) \otimes S(Q,\omega) + B \tag{9.2}$$

with the instrumental resolution function $\mathcal{R}_{\Delta\omega}(\omega)$ and a flat background B accounting for both the water diffusion and the phonon contribution which exceed the accessible dynamic range of the instrument. The measured fixed-window scattering is linked to the quasi-elastic signal by

$$S\left(Q, |\omega| < \Delta\omega\right) = \int_{-\infty}^{\infty} \mathrm{d}\omega\, \mathcal{R}_{\Delta\omega}(\omega)\, S(Q,\omega). \tag{9.3}$$

The total mean-squared displacement is

$$\langle u^2 \rangle := -3 \lim_{Q\to 0} \left\{ \frac{\log\left[S\left(Q, |\omega| < \Delta\omega\right)\right]}{Q^2} \right\}, \tag{9.4}$$

consisting of three contributions from atomic vibrations $\langle u^2_{\mathrm{vib}} \rangle$, molecular subunit diffusion $\langle u^2_{\mathrm{sub}} \rangle$ and, most importantly, diffusion of the entire protein $\langle u^2_{\mathrm{diff}} \rangle$ (see supplementary material Eq. 9.36):

$$\langle u^2 \rangle = \langle u^2_{\mathrm{vib}} \rangle + \langle u^2_{\mathrm{sub}} \rangle + \langle u^2_{\mathrm{diff}} \rangle \tag{9.5}$$

$$\langle u^2_{\mathrm{sub}} \rangle = (1-p)\,\chi\, \langle \Delta\mathbf{r}^2 \rangle \tag{9.6}$$

$$\langle u^2_{\mathrm{diff}} \rangle = (2\,\pi)^{-3/2}\, 6\, D\, \tau, \tag{9.7}$$

with $\chi = 1 - \sqrt{2/\pi}\, \int_0^\infty \exp\left(-\xi^2/2 - |y\,\xi|^\beta\right)\, d\xi$, where $y = \frac{\Gamma}{\Delta\omega}$ (see supplementary material Eq. 9.37). For our data $\chi \approx 1$, since for high resolution instruments we can safely assume that $\Gamma \gg \Delta\omega$. A fraction p of protons has a correlation time far beyond the accessible time window, such that they have a very narrow energy signal and, therefore, can be considered as immobile. The internal diffusive modes are confined on the given time scale to an average length of $\langle \Delta\mathbf{r}^2 \rangle^{1/2}$. The mean-squared displacement due to the translational and rotational diffusion of the entire protein is $6\,D\,\tau$, where $\tau = 2\,\pi/\Delta\omega$ is the maximum observation time of the instrument.

9.4 Results and Discussion

Fig. 9.1(A) shows $\langle u^2 \rangle$ for a full temperature scan through the denaturation transition for an aqueous BSA solution with $c = 500\,\mathrm{mg/ml}$ corresponding to a volume fraction of 27%. $\langle u^2 \rangle$ was extracted from the data by a quadratic fit to $\log\left[S\left(Q, |\omega| < \Delta\omega\right)\right]$ versus Q^2 (see Sec. 9.7.1) using the entire Q-range of IN10, as shown for one example data set in the inset. Starting at $T = 280\,\mathrm{K}$, $\langle u^2 \rangle$ increases linearly with temperature up to 325 K. A steep decrease is observed in the temperature range of denaturing, namely $331\,\mathrm{K} < T < 354\,\mathrm{K}$, consistent with structural changes observed by small-angle x-ray scattering [51]. Upon further heating, $\langle u^2 \rangle$ starts to increase again with temperature. $\langle u^2 \rangle$ is significantly larger than the typical observed vibrational amplitude of only $10^{-2}\,\mathrm{Å}^2$, suggesting that protein diffusive modes are present in addition to atomic vibrations confirming the validity of Eq. 9.5. We rationalize the data depicted in Fig. 9.1(A), remembering that below

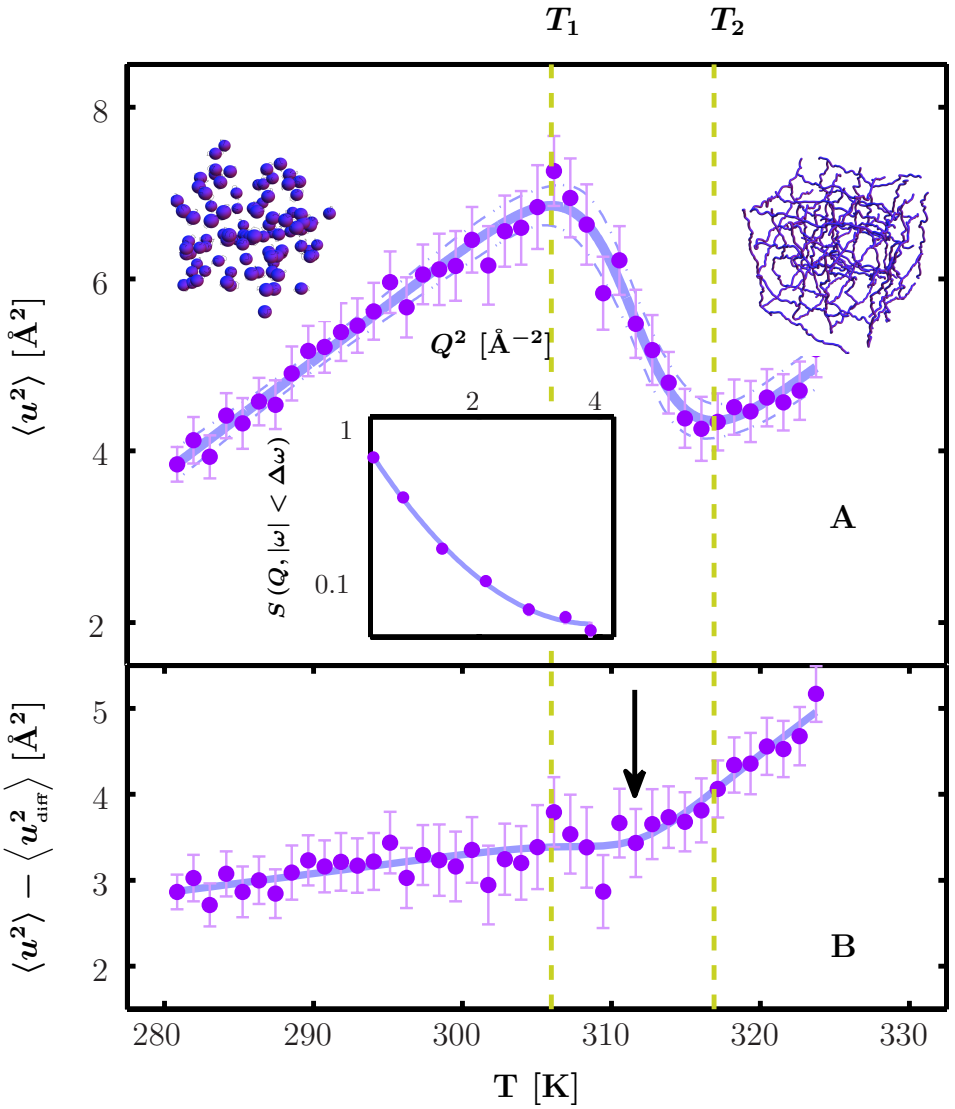

Figure 9.1: (A) Total mean-squared displacement $\langle u^2 \rangle$ (circles) of an aqueous BSA (500 mg/ml) solution versus temperature T. The solution was heated at $7.4 \cdot 10^{-2}$ K/min. Using Eq. 9.8 we describe the data (solid line superimposed on the data) and determine the denaturing interval $T_1 < T < T_2$ (dotted vertical lines).The upper images illustrate a colloidal suspension of native proteins (left) and the cross-linked network of denatured proteins (right). Inset: Measured elastic intensity $S(Q, |\omega| < \Delta\omega)$ versus Q^2 (circles) for the same sample at $T = 290$ K recorded at IN10. As described in Sec. 9.7.1 a quadratic fit (solid line) was used to determine $\langle u^2 \rangle$. (B) $\langle u^2 \rangle - \langle u^2_{\text{diff}} \rangle$ (circles). The transition regime is denoted by the two vertical dashed lines. At $T_0 = (T_1 + T_2)/2$ a transition occurs, characterized by a kink in the curve (arrow).

the denaturation temperature, proteins occur in their native state, which for most globular proteins is a solution of charge-stabilized monomers [78, 184]. The protein dynamics in this region consists of global translational and rotational diffusion, internal and confined diffusive motion of side chains and protein domains and vibrational modes. Upon increasing the temperature, the proteins enter the denaturation regime ($T_1 < T < T_2$). We rationalize this transition in two steps. First, the proteins unfold and extend, which can be understood as similarly to a helix to random coil transition, initially proposed in the seminal paper by Zimm and Bragg [187]. Second, the unfolded protein chains entangle and potentially cross-link partly. This entanglement and cross-linking process can be seen as in between chemical gelation and polymer vulcanization [22, 18]. The entanglement significantly reduces translational and rotational diffusion. While a quantitative theory of the amplitude (Δu^2 in the model described below) of the effect is not available at present, we can qualitatively use the analogy to existing theories for the cross-linking of polymers (vulcanization) [37]. The segment dynamics is then reduced typically by (some power of) the inverse number of entanglement points, N_e, and it appears plausible that a similar mechanism is at work also for concentrated protein solutions. Thus, raising the temperature above the denaturation regime, a gel-like state is observed which can be understood rather in terms of the dynamics of a cross-linked network than in terms of the dynamics of separated molecules. In the spirit of the above, we model the dynamics of the transition by

$$\left\langle u^2 \right\rangle = (a_1\, T + b_1)\,[1 - \Theta\,(T^*)] + (a_2\, T + b_2)\,\Theta\,(T^*) \tag{9.8}$$

where $T^* = (T - T_0)/\Delta T$ with the transition width ΔT and the denaturing temperature T_0. The indices 1 and 2 denote the liquid state of native proteins and gel-like state of denatured proteins, respectively, and $\Theta(x)$ is a smeared-out step function,

$$\Theta(x) = (1 + \exp(-x))^{-1} \tag{9.9}$$

with the functional characteristics of the helix melting models by Zimm and Bragg [187]. For the case $a_1 = a_2$, which is approximately fulfilled here, the temperatures $T_{1,2}$ of the turning points of $\left\langle u^2 \right\rangle$, defining the denaturing interval, are

$$T_{1,2} \;=\; T_0 \pm \Delta T\, \ln\left[z + \sqrt{z\,(z-2)} - 1\right] \tag{9.10}$$

where $\Delta u^2 = b_1 - b_2$ and $z = \frac{\Delta u^2}{2\,a\,\Delta T}$. T_1 can be interpreted as the temperature where unfolding of the proteins starts and T_2, where the entanglement and cross-linking of the chains is completed. $\Delta u^2/\Delta T$ is a measure of how rapidly $\left\langle u^2 \right\rangle$ decreases. The width ΔT of the transition in a simple model depends on the inverse number of participating units of the helix, but of course for a real protein this is more complex. The reduction Δu^2 of the dynamics is due to entanglement. Although we observe that the slopes a_i are nearly the same below and above denaturing, we point out that in the general case, a_i probably depends on the protein concentration. Note,

when the gel-like state is cooled back from 370 K down to 280 K, the curve for $T < T_2$ of $\langle u^2 \rangle$ (see Fig. 9.4) is well below the heating curve in Fig. 9.1(A), which shows the irreversibility of the denaturing process and corroborates the assumption that translational and rotational diffusion are significantly hindered by entanglement and cross-links. Hence, upon cooling the cross-linked network of denatured proteins persists.

In order to unveil the temperature dependence of $\langle u^2 \rangle - \langle u^2_{\text{diff}} \rangle$, namely the cumulative mean-squared displacement originating only from vibrational and subunit-diffusive modes, we use the apparent diffusion coefficient D (see supplementary material Table 9.1) extracted from quasi-elastic spectra to calculate the corresponding contribution to $\langle u^2 \rangle$ by Eq. 9.7. Fig. 9.2 shows a typical spectrum recorded on IN16. The width γ as obtained from the fits to Eq. 9.2 are plotted in the left-hand inset of Fig. 9.2. We observe a clear relationship $\gamma = D\,Q^2$ defining the apparent diffusion coefficient D. Considering that not only the translational but also the rotational diffusion contributes to D [125, 50], we can interpret D as a measure for the global diffusive dynamics of the protein. The right-hand inset in Fig. 9.2 depicts the temperature dependence of the mean-squared displacement $\langle u^2_{\text{diff}} \rangle$ calculated from Eq. 9.7 using the energy resolution $\hbar\,\Delta\omega = 0.9\,\mu$eV. Below the transition regime, indicated by the two vertical lines, we observe a linear relation $\langle u^2_{\text{diff}} \rangle = a\,T + b$. Inspired by de Gennes' scaling law for the diffusion of a polymer in a cross-linked network [37], we assume a negligible global diffusion coefficient D for $T > T_2$. Indeed, near and above the denaturing temperature, fitting according to Eq. 9.2 yields diffusion coefficients D dropping close to zero. Therefore, we describe the full temperature dependence by

$$\langle u^2_{\text{diff}} \rangle = (a\,T + b)\;[1 - \Theta\,(T^*)] \tag{9.11}$$

where $\Theta\,(T^*)$ is the same smeared-out step function used for the fit of $\langle u^2 \rangle$ as shown in Fig. 9.1(A). Fig. 9.1(B) depicts the temperature dependence of the mean-squared displacement $\langle u^2 \rangle - \langle u^2_{\text{diff}} \rangle$. We observe a change of the dynamics at a temperature $T_0 = 343$ K characterizing the transition from a liquid protein solution to a gel-like state. The inverse slopes of $\langle u^2 \rangle - \langle u^2_{\text{diff}} \rangle$ versus T, occasionally discussed in the literature as a phenomenological force constant [182], are $k_1 = (a_1 - a)^{-1} = 4.1 \cdot 10^{-2}$ N/m and $k_2 = a_2^{-1} = 0.7 \cdot 10^{-2}$ N/m, for $T < T_1$ and $T > T_2$, respectively. We note that the physical significance of the force constant is limited in the present case, but it is stated for reasons of comparability.

We speculate that the difference in k_1 and k_2 can be attributed to the higher conformational flexibility of the unfolded protein chains in the cross-linked network. In the native state the proteins are stiffer due to hydrogen bonds and surface charge both of which are mainly responsible for the stable three-dimensional structure.

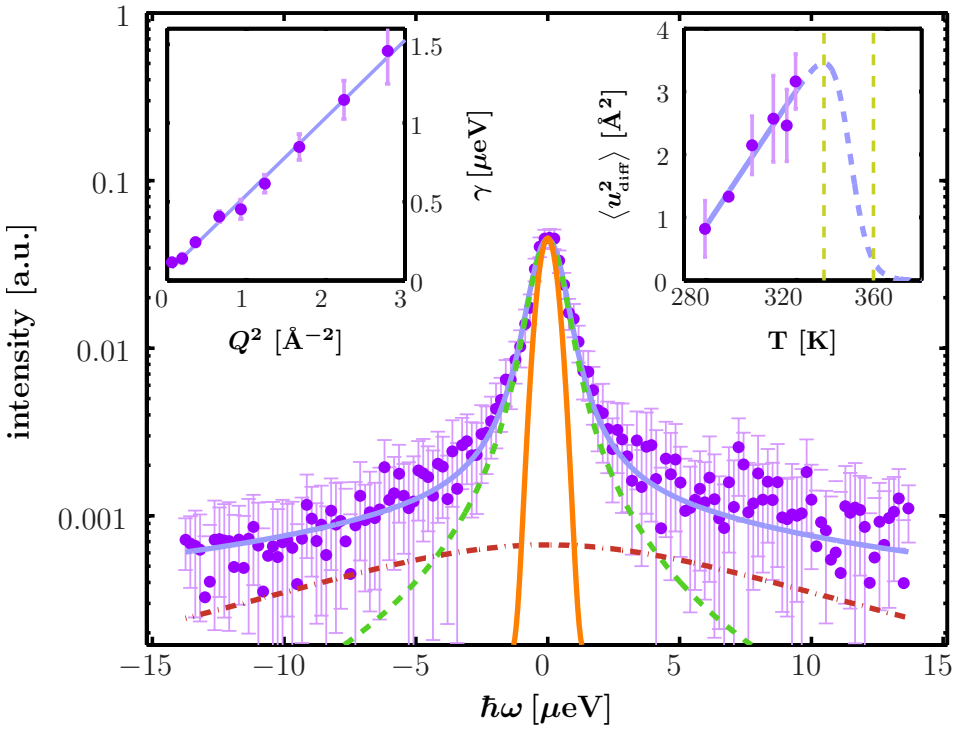

Figure 9.2: Example spectrum $S(Q,\omega)$ (symbols) recorded at IN16 for BSA in D_2O (protein concentration 500 mg/ml corresponding to a volume fraction $\phi = 27\,\%$, T = 301 K, individual detector tube at $Q = 0.6\,\text{Å}^{-1}$). The blue solid line superimposed on the data indicates the fit of the model from Eq. 9.2 with $\beta = 1$, hence the KKW function turns into to Lorentzian $\mathcal{L}(\omega,\Gamma)$. The Lorentzians in Eq. 9.2 are indicated by the dashed $[\mathcal{R}(\omega) \otimes \mathcal{L}(\omega,\gamma)]$ and dash-dotted $[\mathcal{R}(\omega) \otimes \mathcal{L}(\omega,\gamma+\Gamma)]$ lines, respectively. The orange solid line denotes a Gaussian model of the resolution function $\mathcal{R}(\omega)$. The scattering signal decreases with Q, resulting in larger error bars on the fitted γ. Inset left: γ (symbols) fitted to the signal from grouped detectors versus Q^2. Inset right: Temperature dependence of $\langle u^2 \rangle$ due to global diffusion as calculated from Eq. 9.7 (symbols). The solid line is a linear fit for $T \leq 320\,\text{K}$, namely $\langle u^2 \rangle = a\,T + b$. For temperatures beyond 320 K we assume that the diffusion is hindered by entanglement of the proteins and, hence, nearly zero. Therefore, we postulate $\langle u^2 \rangle = (a\,T + b)\,[1 - \Theta(T^*)]$. The transition regime is denoted by the two vertical dashed lines.

9.5 Conclusions

In summary, we investigated the dynamics of crowded BSA protein solutions around the denaturing transition. We have identified denaturing in the fixed-window data. We have developed a novel physical framework for the unfolding and entanglement allowing $\langle u^2 \rangle (T)$ to be understood. Using both the quasi-elastic and fixed-window scattering data, the measured $\langle u^2 \rangle$ can be decomposed into the vibrational, subunit diffusive, and global diffusive contributions. The characteristic transition temperatures defining the denaturation range become observable. The driving force for the drop in $\langle u^2 \rangle$ in the denaturing regime can be rationalized by the significant slowdown of the global diffusion, accounting for both translational and rotational diffusion. This slowdown is induced by structural change and entanglement as well as cross-linking of the proteins. The experimental and analytical framework which we have introduced will allow to accurately test computer models [91].

9.6 Acknowledgments

The authors gratefully acknowledge the allocation of beamtime at the ILL. The authors benefitted from discussions with G. Zaccai and H. Schober.

Supplementary Material for Paper C.

Dynamics of Highly Concentrated Protein Solutions around the Denaturing Transition

Submitted to Physical Review Letters

Authors: M. Hennig[1,2], F. Roosen-Runge[1], F. Zhang[1], S. Zorn[1], M.W.A. Skoda[3], R.M.J. Jacobs[4], T. Seydel[2], and F. Schreiber[1]

[1]Institut für Angewandte Physik, Universität Tübingen,
D-72076 Tübingen, Germany
[2]Institut Laue-Langevin, F-38042 Grenoble, France
[3]ISIS, Rutherford Appleton Laboratory, Chilton, Didcot OX11 0QX, UK
[4]Department of Chemistry, Chemistry Research Laboratory, University of Oxford,
Oxford OX1 3TA, UK

Authors contribution: M. Hennig, F. Roosen-Runge and R.M.J. Jacobs designed research. The samples were prepared by M. Hennig. The experiments were performed by M. Hennig under the supervision of T. Seydel. Data analysis was performed by M. Hennig and F. Roosen-Runge. The article was written by M. Hennig under the supervision of F. Schreiber and T. Seydel. All authors contributed to the discussion.

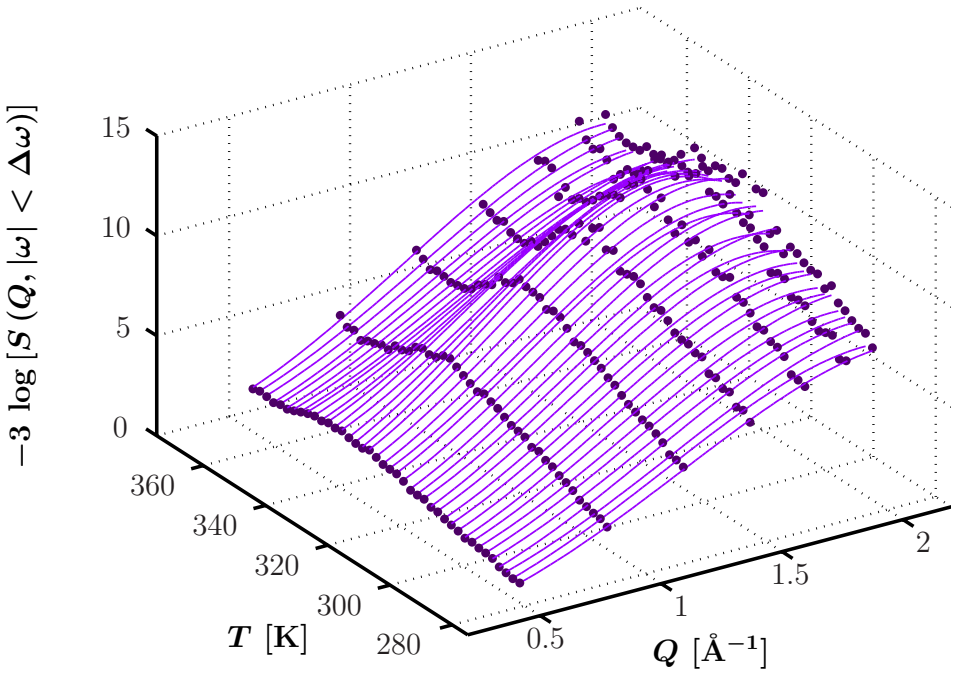

Figure 9.3: Raw data (dark purple solid circles) for the elastic intensity $S\left(Q,|\omega|<\Delta\omega\right)$ of a 500 mg/ml BSA aqueous (D_2O) solution upon heating from 280 to 370 K with $7.4\cdot10^{-2}$ K/min. The data was recorded at IN10. Fits of the polynomial Eq. 9.12 to the data at fixed temperatures are superimposed as purple solid lines.

9.7 Supplementary Material

Here we provide supplementary material for the fitting procedure and the analytical framework quoted in the main text. Furthermore, we briefly discuss the temperature dependence of $\langle u^2\rangle$ upon cooling of a denatured protein solution and provide a table of the apparent diffusion coefficient used to determine the mean-squared displacement of the internal dynamics $\langle u^2_{\text{vib}}\rangle + \langle u^2_{\text{sub}}\rangle$.

9.7.1 Data Fitting

Bringing forward the result of the analysis from the next section, we summarize the fitting procedure to determine the total mean-squared displacement $\langle u^2\rangle$ from the measured elastic intensity $S\left(Q,|\omega|<\Delta\omega\right)$ of a protein in solution. We fit $-3\ \log\left[S\left(Q,|\omega|<\Delta\omega\right)\right]$ with the following polynomial

$$P\left(Q\right) = b + \langle u^2\rangle\ Q^2 + c\,Q^4 \tag{9.12}$$

therein, b accounts for both the background and the arbitrary scaling of the experimental elastic line, c originated from higher spatial correlations as described in detail in the next section. In Fig. 9.3 we display raw data for $-3\ \log\left[S\left(Q,|\omega|<\Delta\omega\right)\right]$ of

a 500 mg/ml BSA aqueous (D_2O) solution upon heating from 280 to 370 K with $7.4 \cdot 10^{-2}$ K/min. At each temperature we fit the polynomial Eq. 9.12 to determine the total mean-squared displacement as shown in Fig. 9.1.

9.7.2 Analysis of the Elastic Intensity

In this section, we derive a formula describing the elastic line intensity in terms of vibrational, global and internal diffusive modes for small Q values. Assuming the independence of diffusive and vibrational modes, as well as the harmonicity of the latter, we can write the quasi-elastic scattering function of a protein solution as [46, 39, 125, 86, 140]:

$$S(Q,\omega) = \exp\left(-\frac{1}{3}\left\langle u_{\text{vib}}^2\right\rangle Q^2\right) \mathcal{L}(\omega,\gamma) \otimes \left\{A\left(Q\right)\, \delta(\omega) + \left[1 - A\left(Q\right)\right]\, \mathcal{L}_\beta(\omega,\Gamma)\right\}, \tag{9.13}$$

where $\mathcal{L}(\omega,\gamma)$ is a Lorentzian function with a width $\gamma = D\,Q^2$, accounting for translational and rotational diffusion [125]. A diversity of amplitudes and correlation times renders the characterization of internal diffusive modes (expression in the curly brackets) an intricate task. Using a Kohlrausch-Williams-Watts function [178],

$$\mathcal{L}_\beta(\omega,\Gamma) = \int_{-\infty}^{\infty} \frac{dt}{2\,\pi} e^{-\mathrm{i}\,\omega\,t}\, \exp\left(-|t\,\Gamma|^\beta\right), \tag{9.14}$$

we can describe a broad range of correlation times with a single phenomenological parameter $0 \leq \beta \leq 1$. $A\left(Q\right)$ is the elastic incoherent structure factor, which is related to the average accessible space of internal diffusive scatterers, such as side chains or molecular subunits. Γ and β are assumed to be nearly constant for $Q < 2\,\text{Å}^{-2}$ [86, 171]. For an instrument with resolution function $\mathcal{R}_{\Delta\omega}$ the elastic line intensity reads

$$S\left(Q, |\omega| < \Delta\omega\right) = \mathcal{R}_{\Delta\omega}(\omega) \otimes S(Q,\omega)|_{\omega=0} = \int \mathcal{R}_{\Delta\omega}(\omega)\, S(Q,\omega)\, d\omega. \tag{9.15}$$

Assuming a Gaussian resolution function $\mathcal{R}_{\Delta\omega}(\omega) = \exp\left(-\frac{\omega^2}{2\Delta\omega^2}\right)$, the integral Eq. 9.15 using the model function Eq. 9.13 yields

$$S\left(Q, |\omega| < \Delta\omega\right) = \exp\left(-\frac{1}{3}\left\langle u_{\text{vib}}^2\right\rangle Q^2\right) \left\{A(Q)\, F_1\left(\frac{\gamma}{\Delta\omega}, 0\right) + \left[1 - A(Q)\right]\, F_\beta\left(\frac{\gamma}{\Delta\omega}, \frac{\Gamma}{\Delta\omega}\right)\right\}, \tag{9.16}$$

where F_β is the integral expression

$$F_\beta(x,y) = \sqrt{\frac{2}{\pi}}\, \exp\left(\frac{x^2}{2}\right) \int_0^\infty \exp\left[-\frac{1}{2}\left(\xi + x\right)^2 - |y\,\xi|^\beta\right] d\xi \tag{9.17}$$

We define the Q-dependent total mean-squared displacement $\langle u^2 \rangle_Q$ by

$$\exp\left[-\frac{Q^2}{3}\,\langle u^2\rangle_Q\right] := S\left(Q, |\omega| < \Delta\omega\right). \tag{9.18}$$

Note that the explicit Q-dependence is denoted by a subindex Q to distinguish it from the later introduced Q-independent total mean-squared displacement $\langle u^2 \rangle$. Using Eq. 9.18 and 9.16, we obtain

$$\langle u^2\rangle_Q = \langle u^2_{\mathrm{vib}}\rangle - \frac{3}{Q^2}\,\log\xi(Q), \tag{9.19}$$

where

$$\xi(Q) = A(Q)\,F_1\left(\frac{\gamma}{\Delta\omega}, 0\right) + [1 - A(Q)]\;F_\beta\left(\frac{\gamma}{\Delta\omega}, \frac{\Gamma}{\Delta\omega}\right). \tag{9.20}$$

We approximate Eq. 9.19 up to 4^{th} order using a Taylor expansion around $Q = 0$:

$$\langle u^2\rangle_Q = \sum_{n=0}^{3} \langle u^2\rangle_0^{(n)}\;\frac{Q^n}{n!} + \mathcal{O}(Q^4), \tag{9.21}$$

therein, we use the following notation

$$\langle u^2\rangle_0^{(n)} = \lim_{Q\to 0}\frac{\partial^n}{\partial Q^n}\,\langle u^2\rangle_Q. \tag{9.22}$$

Next we determine the Taylor-coefficients in Eq. 9.21. As we will show later in this section, we can assume that the incoherent elastic structure factor has the following properties $A(0) = 1$, $A^{(1)}(0) = 0$, $A^{(3)}(0) = 0$ and $A^{(5)}(0) = 0$, where $A^{(n)}$ denotes the n^{th}-derivative of A in respect to Q. With these assumptions, we get the following derivatives for ξ at $Q = 0$

$$\begin{aligned}
\xi(0) &= 1 \\
\xi^{(1)}(0) &= 0 \\
\xi^{(2)}(0) &= -\frac{2\,D}{\Delta\omega}\sqrt{\frac{2}{\pi}} + \left[1 - F_\beta\left(0, \frac{\Gamma}{\Delta\omega}\right)\right]\,A^{(2)}(0) \\
\xi^{(3)}(0) &= 0 \\
\xi^{(4)}(0) &= \left[1 - F_\beta\left(0, \frac{\Gamma}{\Delta\omega}\right)\right]\,A^{(4)}(0) + \frac{12\,D^2}{\Delta\omega^2}\left[1 - \frac{\Delta\omega}{D}\,A^{(2)}(0)\left\{\sqrt{\frac{2}{\pi}} + F_\beta^{(1,0)}\left(0, \frac{\Gamma}{\Delta\omega}\right)\right\}\right] \\
\xi^{(5)}(0) &= 0,
\end{aligned} \tag{9.23}$$

where $F_\beta^{(1,0)}$ denotes the derivative of F_β (Eq. 9.17) in respect to the first argument. Using $\xi^{(n)}(0)$ we calculate the coefficients of the Taylor expansion (Eq. 9.21):

$$\begin{aligned} \langle u^2 \rangle_0 &= -\frac{3}{2}\,\xi^{(2)}(0) \\ \langle u^2 \rangle_0^{(1)} &= 0 \\ \langle u^2 \rangle_0^{(2)} &= \frac{1}{4}\left[3\,\xi^{(2)}(0)^2 - \xi^{(4)}(0)\right] \\ \langle u^2 \rangle_0^{(3)} &= 0 \end{aligned} \tag{9.24}$$

We derive expressions for the n$^{\text{th}}$ derivatives of the incohrent structure factor at zero denoted by $A^{(n)}(0)$. According to M.Bee [14] the general incoherent structure factor $B(\mathbf{Q})$ for a localized diffusive scatterer reads

$$B(\mathbf{Q}) = \frac{1}{N}\sum_{j=1}^{N} \left|\left\langle e^{\mathrm{i}\,\mathbf{Q}\,\mathbf{r}_j}\right\rangle\right|^2. \tag{9.25}$$

where $\mathbf{r}_j = (x_j, y_j, z_j)^T$. In a protein solution the proteins have no preferential orientation. Consequently, we can assume that the orientations are nearly equally distributed. Therefore, we have to average the general elastic incoherent structure factor $A(Q)$ over all possible orientations to obtain the solution incoherent structure factor $A(Q)$ in Eq. 9.13,

$$A_0(Q) = \frac{1}{4\,\pi}\int_0^{2\,\pi}\int_0^{\pi} B(\mathbf{Q})\sin\theta\,d\theta\,d\varphi. \tag{9.26}$$

with $\mathbf{Q} = Q\,[\cos(\varphi)\,\sin(\theta), \sin(\varphi)\,\sin(\theta), \cos(\theta)]^T$. Correlation times much longer than the instrumental time window correspond to a very narrow signal in ω which is indistinguishable from the elastic peak. Therefore, we consider a fraction p of scatters as immobile, the remaining fraction $1-p$ as diffusive scatters [86, 140]. Which translates into the following pseudo elastic incoherent structure factor

$$A(Q) = p + (1-p)\,A_0(Q) \tag{9.27}$$

To obtain $A^{(n)}(0)$ we employ Eq. 9.26 and calculate the corresponding integrals and obtain:

$$\begin{aligned} A(0) &= p + (1-p)\, B(\mathbf{0}) \qquad (9.28)\\ A^{(1)}(0) &= 0 \\ A^{(2)}(0) &= \frac{1-p}{3}\left\{ B_{\mathbf{0}}^{(2,0,0)} + B_{\mathbf{0}}^{(0,2,0)} + B_{\mathbf{0}}^{(0,0,2)} \right\} \\ A^{(3)}(0) &= 0 \\ A^{(4)}(0) &= \frac{1-p}{5}\left\{ B_{\mathbf{0}}^{(4,0,0)} + B_{\mathbf{0}}^{(0,4,0)} + B_{\mathbf{0}}^{(0,0,4)} + 2\, B_{\mathbf{0}}^{(2,2,0)} + 2\, B_{\mathbf{0}}^{(2,0,2)} + 2\, B_{\mathbf{0}}^{(0,2,2)} \right\} \\ A^{(5)}(0) &= 0, \end{aligned}$$

using the notation

$$B_{\mathbf{0}}^{(n1,n2,n3)} = \left(\frac{\partial}{\partial Q_1}\right)^{n_1} \left(\frac{\partial}{\partial Q_2}\right)^{n_2} \left(\frac{\partial}{\partial Q_3}\right)^{n_3} B(\mathbf{Q})\Big|_{\mathbf{Q}=\mathbf{0}}. \qquad (9.29)$$

Using the generalized product derivation rule we get

$$B_{\mathbf{0}}^{(n_1,n_2,n_3)} = \frac{1}{N} \sum_{j=1}^{N} \sum_{k_1,k_2,k_3=0}^{n_1,n_2,n_3} \prod_{l=1}^{3} \binom{n_l}{k_l} (-1)^{k_l}\, \mathrm{i}^{n_l} \left\langle x_j^{n_1-k_1}\, y_j^{n_2-k_2}\, z_j^{n_3-k_3} \right\rangle \left\langle x_j^{k_1}\, y_j^{k_2}\, z_j^{k_3} \right\rangle \qquad (9.30)$$

Evidently, $B_{\mathbf{0}} = 1$. With Eq. 9.30 we arrive at

$$\begin{aligned} A^{(2)}(0) &= -\frac{2\,(1-p)}{3} \left\langle \Delta\mathbf{r}^2 \right\rangle \qquad (9.31)\\ A^{(4)}(0) &= \frac{1-p}{5}\left(m_x + m_y + m_z + 2\, m_{x,y} + 2\, m_{x,z} + 2\, m_{y,z}\right) \end{aligned}$$

where $\left\langle \Delta\mathbf{r}^2 \right\rangle = \frac{1}{N} \sum_{j=1}^{N} \left\langle \left(\mathbf{r}_j - \langle \mathbf{r}_j \rangle\right)^2 \right\rangle$ is an average fluctuation length, related to the size of the confinement of the diffusive scatterer. Furthermore,

$$\begin{aligned} m_x &= \tfrac{2}{N} \sum_{j=1}^{N} \left(\left\langle x_j^4 \right\rangle + 3 \left\langle x_j^2 \right\rangle^2 - 4 \left\langle x_j^3 \right\rangle \langle x_j \rangle \right) \qquad (9.32)\\ m_{x,y} &= \tfrac{2}{N} \sum_{j=1}^{N} \Big(2\, \langle x_j\, y_j \rangle^2 - 2\, \langle y_j \rangle \left\langle x_j^2\, y_j \right\rangle \\ &\quad + \left\langle x_j^2 \right\rangle \left\langle y_j^2 \right\rangle - 2\, \langle x_j \rangle \left\langle x_j\, y_j^2 \right\rangle + \left\langle x_j^2\, y_j^2 \right\rangle \Big)\ . \qquad (9.33) \end{aligned}$$

The expressions m_y, m_z and $m_{x,z}$, $m_{y,z}$ are analogously defined. Finally, $\left\langle u^2 \right\rangle_Q$ can be approximated as follows

$$\left\langle u^2 \right\rangle_Q = \left\langle u^2 \right\rangle_0 + \frac{1}{2} \left\langle u^2 \right\rangle_0^{(2)} Q^2 + \mathcal{O}(Q^4) \qquad (9.34)$$

This approximation is crucial to determine $\langle u^2 \rangle_0$ from the experimental elastic line data. The linear coefficient of a 2$^{\text{nd}}$-order polynomial fit to $-3 \log [S(Q, |\omega| < \Delta\omega)]$ versus Q^2 corresponds to $\langle u^2 \rangle_0$.

$$-3 \log [S(Q, |\omega| < \Delta\omega)] = x \left(\langle u^2 \rangle_0 + \langle u^2 \rangle_0^{(2)} \frac{x}{2} \right) + b \tag{9.35}$$

where $x = Q^2$ and b originates from the arbitrary scaling of the experimental elastic line. For the sake of a simpler notation we will use $\langle u^2 \rangle := \langle u^2 \rangle_0$. $\langle u^2 \rangle$ is the total mean-squared displacement for small Q-values and by using Eq. 9.24 and 9.31 can be decomposed in the following way

$$\langle u^2 \rangle = \langle u^2_{\text{vib}} \rangle + \langle u^2_{\text{sub}} \rangle + \langle u^2_{\text{diff}} \rangle \tag{9.36}$$

$$\langle u^2_{\text{sub}} \rangle = (1-p)\, \chi\, \langle \Delta \mathbf{r}^2 \rangle \tag{9.37}$$

$$\langle u^2_{\text{diff}} \rangle = 3 \sqrt{\frac{2}{\pi\, \Delta\omega^2}}\, D. \tag{9.38}$$

therein, $\chi = \left[1 - F_\beta \left(0, \frac{\Gamma}{\Delta\omega}\right)\right]$. Due to the energy resolution of the instrument the global diffusion of the protein can only be observed within a time window of width $\tau = 2\pi/\Delta\omega$. During that time the protein has isotropically explored a space which size is characterized by a mean-squared displacement of $\langle \Delta \mathbf{R}^2(\tau) \rangle = 6\, D\, \tau$. Hence, $\langle u^2_{\text{diff}} \rangle = (2\,\pi)^{-3/2}\, \langle \Delta \mathbf{R}^2(\tau) \rangle$.

9.7.3 Cooling of a denatured protein solution

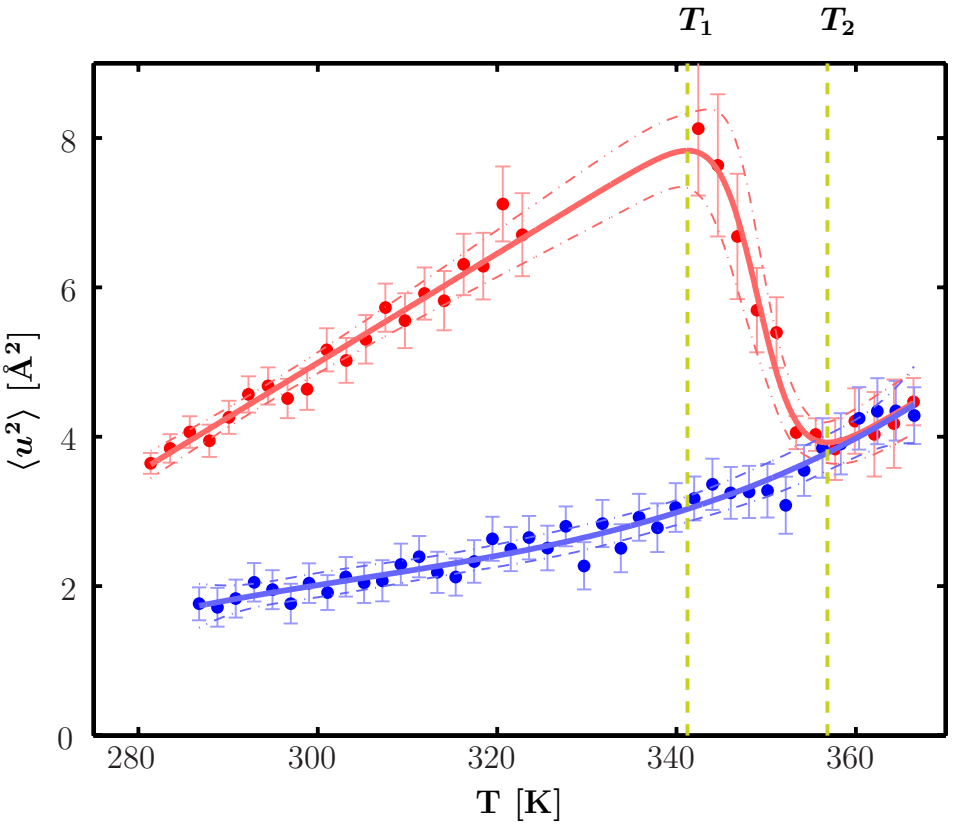

Figure 9.4: Total mean-squared displacement $\langle u^2 \rangle$ for a 500 mg/ml BSA aqueous solution with 1 M NaCl upon heating from 280 to 370 K with $8.4 \cdot 10^{-2}$ K/min (red solid line) and cooling back to 280 K with $12.4 \cdot 10^{-2}$ K/min (blue solid line). The dashed dotted lines denotes the 95% confidence intervals of the corresponding fits. The transition regime is denoted by the red dashed lines. Note that for the heating process between 324 and 342 K no data was recorded due to an unexpected neutron beam stop during the temperature ramp.

Fig. 9.4 shows $\langle u^2 \rangle$ for a 500 mg/ml BSA aqueous solution with 1 M NaCl for two different processes: heating from 280 to 370 K (red solid line) and cooling from 370 back to 280 K. During the heating process we encountered an unexpected loss of the neutron beam between the temperatures 324 and 342 K, hence no data was recorded. Upon heating $\langle u^2 \rangle$ displays the behavior described in the main paper. Cooling reveals the irreversibility of the denaturing process, since for $T < T_2$ the curve progression of $\langle u^2 \rangle$ is evidently different from the heating curve. Note that at T_1 there is a weak kink indicating a change in the flexibility of the cross-linked network. For cooling we observe a significantly lower $\langle u^2 \rangle$ which we attribute to the hindered global motion of the proteins due to entanglement and cross-linking. We assume that upon cooling the cross-linked network remains and that the denatured proteins are not 'disentangled'.

9.7.4 Temperature Dependent Apparent Diffusion Coefficient

T[K]	279	290	300	310	316	319
D [Å^2/ns]	0.47	0.76	1.23	1.47	1.41	1.81
ΔD [Å^2/ns]	±0.26	±0.01	±0.27	±0.39	±0.33	±0.25

Table 9.1: Temperature dependence of apparent diffusion coefficient for a 500 mg/ml BSA aqueous (D_2O) solution measured at IN10 and IN16.

Chapter 10

Paper D. *Charge-Induced Dynamic Density Inhomogeneities in Protein Solutions*

Contents

Paper D. Charge-Induced Dynamic Density Inhomogeneities in Protein Solutions

In preparation for Soft Matter

Authors: M. Hennig[1,2], F. Roosen-Runge[1], F. Zhang[1], P. Falus[2], S. Zorn[1], M.W.A. Skoda[3], R.M.J. Jacobs[4], H. Schober[2], T. Seydel[2], and F. Schreiber[1]

[1]Institut für Angewandte Physik, Universität Tübingen, D-72076 Tübingen, Germany
[2]Institut Laue-Langevin, F-38042 Grenoble, France

[3]ISIS, Rutherford Appleton Laboratory, Chilton, Didcot OX11 0QX, UK

[4]Department of Chemistry, Chemistry Research Laboratory, University of Oxford, Oxford OX1 3TA, UK

Authors contribution: M. Hennig, H. Schober, F. Roosen-Runge, M.W.A. Skoda, S. Zorn, R.M.J. Jacobs, F. Zhang, T. Seydel and F. Schreiber designed research. The samples were prepared by M. Hennig. The experiments were performed by M. Hennig and T. Seydel. P. Falus provided technical assistance and performed data reduction. Data analysis was performed by M. Hennig and F. Roosen-Runge. The article was written by M. Hennig, H. Schober, F. Zhang, F. Roosen-Runge, and T. Seydel. All authors contributed to the discussion.

10.1 Abstract

We investigate the structure and the dynamics of solutions of the globular protein *bovine serum albumin* near the transition from a homogeneous to a cluster-dominated phase using small-angle X-ray scattering and neutron spin-echo spectroscopy. To this end, we tune the repulsive part of the protein interactions by charge-control using the trivalent salt YCl_3. We observe the emergence of dynamic density inhomogeneities with the charge approaching zero. By analyzing the short-time self-diffusion of the protein, we introduce an observable quantifying the charge-induced inhomogeneities due to the cluster formation.

10.2 Introduction

The competition between long-range repulsion and short-range attraction characterizes the interaction of charged proteins in solution and gives rise to a rich phase behavior [75, 147, 142, 98, 132, 124, 27, 99]. This balance of repulsive and attractive interaction is crucial to understand the crystallization of proteins [161, 63]. A balance in favor of attraction can cause protein aggregation, which is believed to be a trigger of fiber formation [172] and neurodegenerative diseases such as Parkinson's disease [93, 139].

In addition to their biological role, proteins are of fundamental interest in the context of soft matter science since they form highly monodisperse colloidal suspensions [78, 184]. Proteins, however, differ in one important aspect from many simple colloid systems: The distribution of charges on the surface of a protein is in general inhomogeneous [102, 130]. This inhomogeneous surface charge distribution can be assumed to have a fundamental biological relevance in controlling for instance aggregation phenomena and biological activity such as docking processes. Characteristic of proteins in their native environment is the aqueous solvent containing salt ions, which can affect the competition between repulsion and attraction by both screening as well as ion condensation [185]. The nature of the interaction between the proteins crucially determines the equilibrium structure of the solution. While repulsive interactions prefer a low local particle density, attractive interactions lead to inhomogeneity in the particle density and can cause the formation of equilibrium clusters [75, 147, 98, 132, 27, 99].

Using small-angle scattering Stradner et al. [157] provided experimental evidence for the existence of so-called equilibrium clusters in lysozyme solutions by observing a low-q peak that they associated with the formation of clusters. The first dynamic measurement on equilibrium clusters using spin-echo spectroscopy was conducted by Porcar et al. [132]. They investigated the short-time self-diffusion of lysozyme clusters depending on the protein concentration and found that the size of the clusters increased with rising volume fraction. Using small-angle X-ray scattering and spin-echo spectroscopy Cardinaux et al. [27] characterized the structure and the dynamics of a salt-free lysozyme solution undergoing a transition from a monomer to transient cluster-dominated system with increasing volume fraction. Additionally,

employing molecular and brownian dynamics simulation they confirm the existence of transient clusters and verify their experimental results. Combining dynamic and static scattering techniques Liu et al. [99] concluded in a recent study that there is no direct connection between cluster formation in a solution and the existence of the cluster peak. They point out that experimental evidence for the existence of clusters has to rely on the dynamical behavior of the system and they attribute the correlation peak to the density structure at the intermediate range.

Inspired by this previous work, we endeavor to tune the parameters determining the competition between repulsion and attraction, such as the surface charge of the protein. Thus, we aim to control the equilibrium structure of a protein solution and favor the generation of equilibrium clusters as proposed by Liu et al. [99].

In this context, Zhang et al. [185, 186] showed that highly positively charged metal ions such as Y^{3+} can induce a charge inversion of negatively charged proteins. Thereby, the proteins undergo a condensation phase between two critical ion-concentrations denoted by c^* and c^{**}. Using small-angle X-ray scattering they showed that when the ion-concentration c approaches c^* short-range attractions increasingly become dominant and finally describe the protein interaction in the condensed phase, $c^* < c < c^{**}$, causing molecular aggregates. For $c > c^{**}$ the surface charge becomes positive and the protein aggregates redissolve. Consequently, the specific binding effect of Y^{3+} on the protein surface is suitable for tuning the intermolecular forces. In this paper we report on a combined neutron spin-echo spectroscopy and small-angle X-ray scattering study investigating the short-time self-diffusion coefficient and the isothermal compressibility of the globular protein *bovine serum albumin* in aqueous (D_2O) solutions at various concentrations of the trivalent salt YCl_3. We increase the salt concentration up to the critical concentration c^* [185] where the protein surface charge is close to zero. Thereby, we gradually compensate the repulsive part of the protein interaction and, hence, favor cluster formation. Finally, from the dynamical data we introduce a local crowding factor quantifying the salt-induced increase of the local volume fraction within the protein clusters.

10.3 Experimental

10.3.1 Sample Preparation

For all measurements we purchased lyophilized *Bovine Serum Albumin* (BSA) powder with a purity of 99 % and anhydrous YCl_3 powder with a purity of 99.99 % from the Sigma-Aldrich® company (product codes: A3059 and 451363, respectively) and stored the samples in a cold room at a temperature of 8°C. Weeks prior to the experiment we prepared all sample solutions by dissolving 200 mg of BSA in 1 ml D_2O containing YCl_3 in the range of 0 to 18 mM and filled it into clean glass vials, which we sealed with paraffin stripes. The volume fraction φ of BSA corresponding to the concentration 200 mg/ml is 13.6 % [137]. Additionally, we prepared a very dilute salt-free solution sample with 2 mg BSA per 1 ml D_2O. For several hours we homog-

enized the sample solutions with a laboratory shaker until the BSA was completely dissolved. After 3 weeks of equilibration the solutions showed no visible traces of aggregates or precipitates. Using pH-indicator stripes we determined the pD values of the 200 mg/ml BSA solutions. For the salt-free solution and the highest salt concentration we measured pD 6.7 ± 0.5 and pD 5.5 ± 0.5, respectively. All samples were prepared at a room temperature of 297 K.

10.3.2 Small-Angle X-Ray Scattering

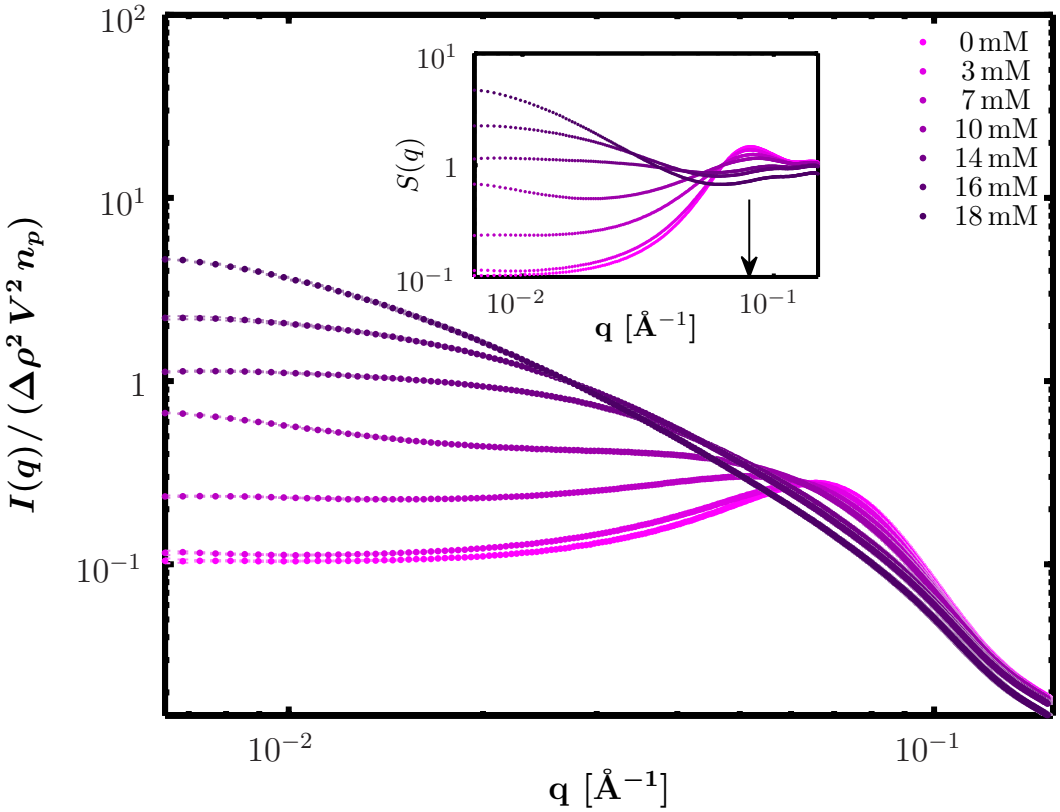

Figure 10.1: Normalized SAXS scattering intensity $I(q)/(\Delta\rho^2 V^2 n_p)$ of BSA 200 mg/ml aqueous (D_2O) solutions at room temperature of 297 K containing different concentrations of YCl_3 (see legend). The data were recored at the ESRF beamline ID02. Inset: corresponding structure factor $S(q)$ calculated from Eq. 10.1 by estimating the form factor $P(q)$ from a BSA 2 mg/ml aqueous (D_2O) solution sample. Note the pronounced protein-protein correlation peak $q_m \approx 0.08$ Å^{-1} (indicated by the arrow) is only discernible for salt concentrations $c_s < 7$ mM. For higher salt concentrations the correlation peak disappears, indicating that the Coulomb repulsion between the protein in solution becomes very weak.

We carried out the small-angle X-ray scattering (SAXS) experiments at the ID02 beamline at the European Synchrotron Radiation Facility (ESRF, Grenoble, France). The X-ray beam with a cross section of 0.2×0.4 mm^2 (vertical and hor-

izontal, respectively) had an energy of 16.062 keV corresponding to a wavelength $\lambda = 0.77\,\text{Å}$. The SAXS detector was located 2 m from the sample, yielding an accessible q-range from $2 \cdot 10^{-3}\,\text{Å}^{-1}$ to $5 \cdot 10^{-1}\,\text{Å}^{-1}$ setting the probed length scales $l = 2\pi/q$ to $12.6\,\text{Å} \leq l \leq 3.1 \cdot 10^3\,\text{Å}$. For each measurement approximately $100\,\mu$l of protein solution was filled into a Teflon® tube and part of it was pushed into an adjacent quartz capillary tube with an inner diameter of 1.9 mm using a syringe pump controlled by a step-motor. To avoid beam damage of the protein solution the SAXS counting time per illuminated spot on the sample was 0.05 s – 0.3 s and the spot was exchanged after each exposure. After each measurement the capillary tube was cleaned with deionized water containing a detergent. Additionally, we measured water as background in exactly the same way as the protein solutions. Employing the standard online reduction tool *SAXS utilities*, we reduced the raw data by correcting for transmission, detector sensitivity and capillary thickness [117]. From the resulting scattering intensity we subtracted the water background taking the protein volume fraction into account and calculated the absolute intensity using water as calibration standard [120].

With SAXS we measure the differential scattering cross-section $\mathrm{d}\Sigma(q)/\mathrm{d}\Omega$, which for a monodisperse solution of dissolved proteins factorizes as follows

$$\frac{\mathrm{d}\Sigma(q)}{\mathrm{d}\Omega} = \Delta\rho^2\, V^2\, n_p\, P(q)\, S(q). \tag{10.1}$$

Therein, n_p is the number density of the scattering particles, each having a volume V. The scattering vector $q = 4\,\pi/\lambda\,\sin(\theta/2)$ depends on the scattering angle θ and the wavelength λ of the X-rays. The contrast relative to the featureless solvent background is expressed by the average excess scattering length density $\Delta\rho = \rho - \rho_s$ with ρ and ρ_s being the average scattering length density of the particle and the solvent, respectively. The form factor $P(q)$ is the Fourier transform of the particle shape:

$$P(q) = \left\langle |f(\mathbf{q})|^2 \right\rangle_\Omega \tag{10.2}$$

$$f(\mathbf{q}) = \frac{1}{V} \int_V \exp\left[i\,\mathbf{q}\,\mathbf{r}\right]\,\mathrm{d}^3\mathbf{r}, \tag{10.3}$$

in which the angular brackets denote the average over all orientations of $\mathbf{q} = q\,\mathbf{e}_\Omega$ with $\mathbf{e}_\Omega$ being the unit vector pointing into the solid angle Ω. Thereby, we assume that in solution the protein orientation is equally distributed. In non-diluted system, where interactions are present, the scattering intensity is additionally modulated by the interparticle structure factor,

$$S(\mathbf{q}) = \left\langle \frac{1}{N} \sum_{j,k=1}^{N} \exp\left[i\,\mathbf{q}\;(\mathbf{r}_j - \mathbf{r}_k)\right] \right\rangle, \tag{10.4}$$

where $\mathbf{r}_j$ are the position vector of the j^{th} particle. The angular brackets denote

the ensemble average using the equilibrium conformational density distribution of the system. If the system is isotropic the particle structure $S(q)$ factor simplifies to

$$S(q) = \langle S(\mathbf{q}) \rangle_\Omega = 1 + 4\,\pi\,n_p \int_0^\infty [g(r) - 1]\,\frac{\sin(q\,r)}{q\,r}\,r^2\,\mathrm{d}r. \tag{10.5}$$

Therein, the pair-correlation $g(r)$ function describes the spatial arrangement set by the interparticle interactions. For very dilute sample ($n_p \approx 0$) we have $S(q) = 1$, consequently the q-dependence of the scattering intensity in Eq. 10.1 originates only from the form factor.

Since the X-rays illuminate a small constant volume within the much larger sample volume, we can classify the observed system as an open NVT–system with constant V and T and where the number of particles N can fluctuate. This allows the following interpretation of the structure factor in the $q \to 0$ limit:

$$\lim_{q\to 0} S(q) = \frac{\chi_\mathrm{T}}{\chi_\mathrm{T}^\mathrm{ideal}} = 1 - 2\,n_p\,B_w \tag{10.6}$$

$$B_w = -\frac{1}{2}\int \left[e^{-\beta\,w(r)} - 1\right]\,\mathrm{d}^3\mathbf{r}, \tag{10.7}$$

in which $\beta = (k_B\,T)^{-1}$, with T being the system temperature and k_B the Boltzmann constant. $\chi_\mathrm{T}^\mathrm{ideal}$ and χ_T are the isothermal compressibility of the proteins in solution and an ideal gas [116], respectively. The effective potential between two proteins separated by a distance r ensemble-averaged over the remaining proteins in solution is described by the potential of mean force, reading [116]

$$w(r) = -k_B\,T\,\log\left[g(r)\right]. \tag{10.8}$$

Note, that the integral in Eq. 10.7 shares similarities with the second virial coefficient. Thus, analogously to the second virial coefficient, B_w characterizes the nature of the potential of mean force, in other words: $B_w < 0$ and $B_w > 0$ indicate that attraction and repulsion are dominating, respectively. Consequently, $S(q \to 0) < 1$ indicates that the protein solution is controlled by repulsion, while $S(q \to 0) > 1$ is a sign that attraction prevails.

10.3.3 Neutron Spin-Echo Spectroscopy

The neutron spin-echo experiments were performed at the Institut Laue-Langevin (ILL, Grenoble, France) using the IN15 spectrometer at incident wavelengths 8, 10 and 16 Å for momentum transfers q ranging from 0.023 to 0.23 $\mathrm{Å}^{-1}$ allowing to observe the length scale range 27.3 Å $\leq l \leq$ 273 Å. In this configuration the instrument covers a Fourier time range from 0.35 ns $\leq \tau \leq$ 207 ns. Prior to the experiment, we dispersed the solutions into thin quartz cuvettes with a thickness of 1 mm. The measured raw data were reduced by applying standard IGOR routines. Using neutron spin-echo scattering we probe the intermediate scattering function of

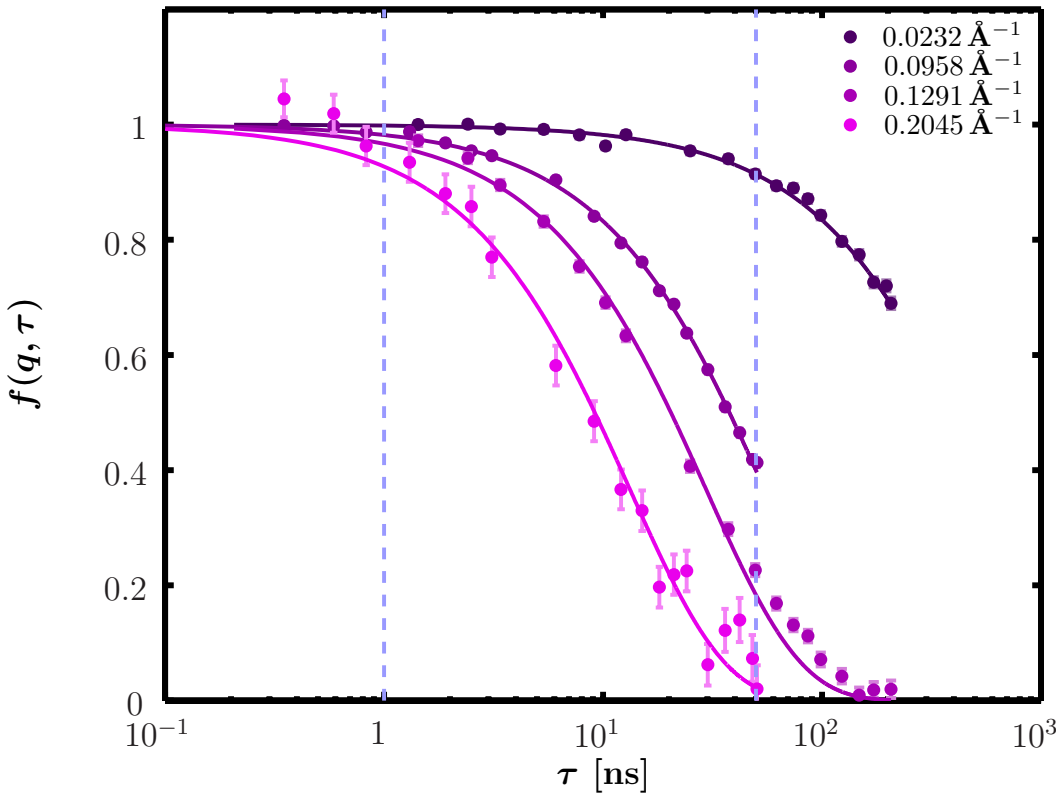

Figure 10.2: Normalized dynamic structure factor of a 200 mg/ml BSA aqueous (D_2O) solution with 10 mM YCl_3 at room temperature (circles) for different momentum transfers q. The data were recored at the IN15 spectrometer at the ILL. The solid lines superimposed to the data are fits with a single exponential within the short-time regime indicated by the two vertical dashed blue lines.

the protein solution, reading

$$S(q,\tau) = \frac{1}{N} \sum_{i,j} \langle \exp\left[-i\,\mathbf{q}\,\{\mathbf{r}_i(0) - \mathbf{r}_j(\tau)\}\right] \rangle \,, \tag{10.9}$$

in which $\mathbf{r}_i(\tau)$ is the coordinate vector of the i^{th} atom in a molecule at Fourier time τ. For q-values larger than the particle-particle correlation peak position q_m of the structure factor $S(q)$, Holmqvist and Nägele [74] showed that the normalized dynamic structure factor can be written as follows:

$$f(q,\tau) = \frac{S(q,\tau)}{S(q)} \approx \exp\left\{-q^2\,\frac{D_s(q)}{d_s}\,W(\tau)\right\}. \tag{10.10}$$

Therein, $W(\tau)$ is the mean-squared displacement of the diffusing particle, $D_s(q)$ is the short-time diffusion function and d_s is the short-time self-diffusion coefficient.

In the following, we will discuss the time-scale behavior for $W(\tau)$ and, thereby, elucidate the meaning of d_s. Subsequently, we will briefly explain the asymptotic be-

havior of $D_s(q)$ for $q \gg q_m$. In a very dilute solution the slope of $W(\tau)$ coincides with the dilute-limit diffusion coefficient d_0 in the diffusive regime $\tau \gg \tau_b \approx m/(6\,\pi\,\eta R_h)$. Therein, m is the mass of the diffusing particle with hydrodynamic radius R_h, η is the viscosity of the solvent and d_0 is given by the well-known Stokes-Einstein diffusion constant $d_0 = k_B\,T/(6\,\pi\,\eta\,R_h)$. By contrast, for a non-dilute solution, different slopes of $W(\tau)$ are caused by the time-scale dependent diffusive behaviour of the particles [115, 40]. Hydrodynamic interactions arise on the time scale

$$\tau_h \approx \frac{R_h^2\,\rho}{\eta\,\varphi}, \tag{10.11}$$

with the solvent density ρ and the particle volume fraction φ, affecting the so-called short-time diffusive regime $\tau_h \ll t \ll \tau_i$. The structural relaxation time

$$\tau_i \approx \frac{R_h^2}{d_0} \tag{10.12}$$

defines the onset of caging effects on the particle center-of-mass diffusion due to direct interparticle interactions. On this time sale $W(\tau)$ yields the short-time self-diffusion coefficient by

$$W(\tau)/\tau = d_s. \tag{10.13}$$

Short-time self-diffusion is mainly affected by hydrodynamic interactions and the equilibrium structure of the solvent. For $t \gg \tau_I$ long-time self-diffusion is observed,

$$W(\tau)/\tau = d_l, \tag{10.14}$$

affected by both hydrodynamic and direct interactions [40]. In Eq. 10.10 the short-time diffusion function is

$$D_s(q) = d_0\,\frac{H(q)}{S(q)}. \tag{10.15}$$

Therein, $H(q)$ is the hydrodynamics function, reflecting the influence of of hydrodynamic interactions. The hydrodynamic function can be decomposed as follows [40]:

$$H(q) = \frac{d_S}{d_0} + H_d(q) \tag{10.16}$$

for $q \gg q_m$ the distinct part $H_d(q)$ vanishes, in other words

$$D_s(q) \approx d_s. \tag{10.17}$$

10.4 Results and Discussion

We commence this section by reviewing the critical salt concentration, which induces a surface charge of BSA close to zero. Then we present the SAXS results and

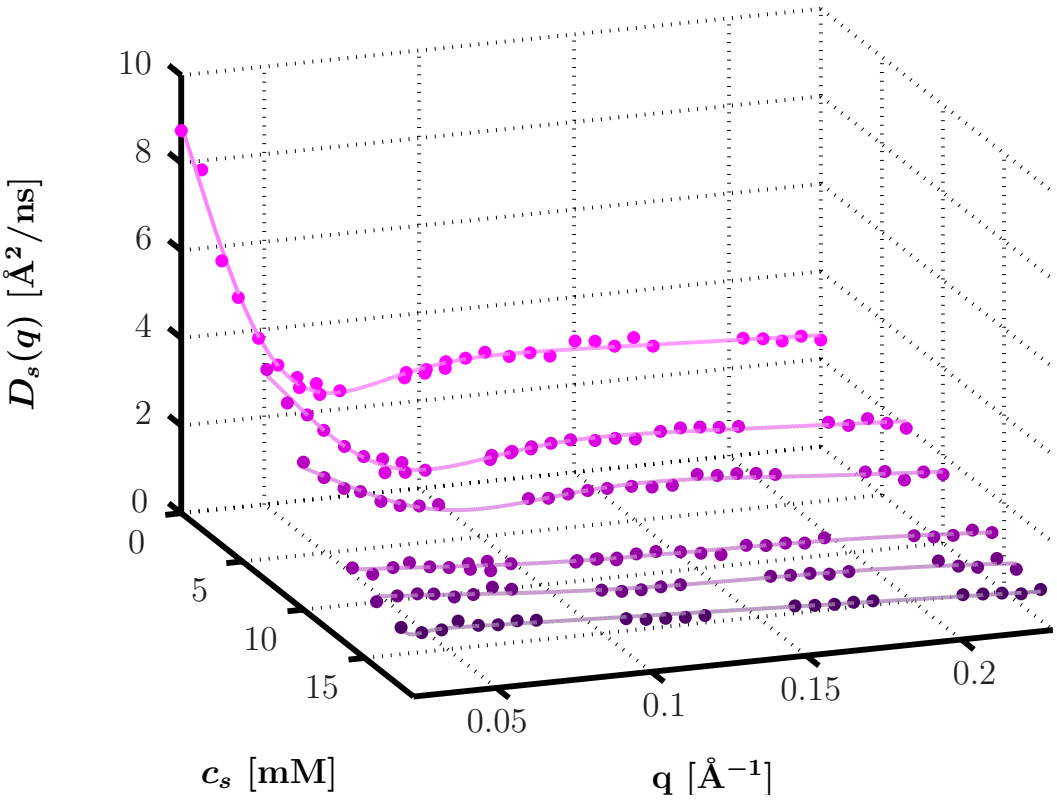

Figure 10.3: Short-time diffusion function Eq. 10.15 for a 200 mg/ml BSA aqueous (D_2O) solution at room temperature for various YCl_3 concentrations (circles). The solid lines superimposed on the data are guides to the eye. For $q \gg q_m$ the diffusion function $D_s(q)$ converges to the short-time self-diffusion coefficient d_s.

discuss them in context with the critical salt concentration. Thereby, we quantify the nature of the potential of mean force between the proteins in solution at different concentrations of the trivalent salt YCl_3. In the subsequent section we comment on the results from the dynamic response of the samples as measured with neutron spin-echo spectroscopy and will give evidence for the existence of dynamic density inhomogeneities. Finally, we combine the results from the static and dynamic scattering by introducing a local crowding parameter quantifying the protein density inhomogeneities induced by the addition of YCl_3.

10.4.1 Critical Salt Concentration

Fig. 10.4 displays a photograph of a series of BSA 200 mg/ml BSA aqueous (D_2O) solutions at room temperature with YCl_3 concentrations around the critical salt concentration c^*. The onset of the formation of macroscopic clusters is evidenced by the abruptly increased turbidity of the solution (to the right of the vertical line). This defines the critical salt concentration, which we determined by eye to be $c^* = (19 \pm 0.5)$ mM. According to findings by Zhang et al. [185, 186] increas-

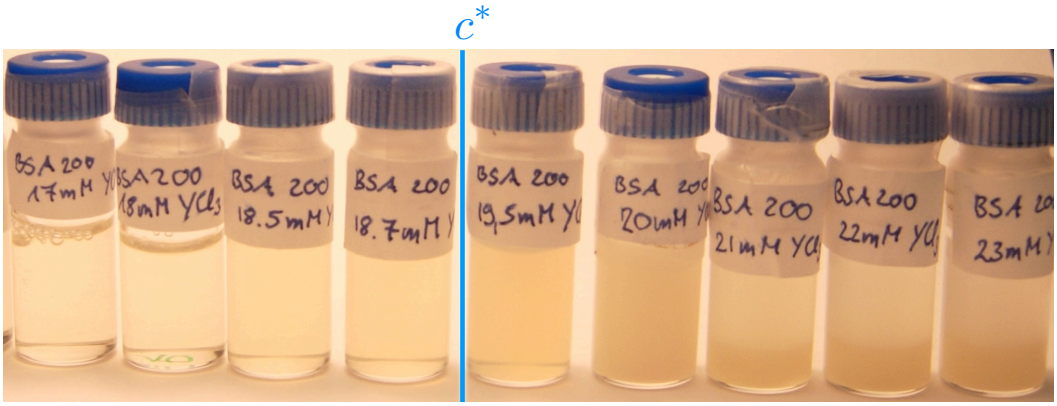

Figure 10.4: Photograph of glass vials containing 200 mg/ml BSA aqueous (D_2O) solutions at room temperature with YCl_3 concentrations (see labels on vials). The vertical blue line indicates the critical salt concentration $c^* = (19 \pm 0.5)$ mM in the present case ($c_p = 200$ mg/ml). Below c^* the solution is homogeneous and above c^* abruptly becomes turbid and shows visible aggregates (to the right of the vertical line).

ing the salt concentration up to a distinctive concentration $c^* = 19$ mM induces a charge inversion of the initially highly negatively charged BSA molecules [21]. Most importantly, they found experimental evidence that BSA possess specific binding sites for the Y^{3+}-ions, which are gradually occupied with increasing salt concentration. Therefore, the bound ions alter the surface charge. Furthermore, by employing Fourier transform infrared spectroscopy and circular dichronism, they showed that the secondary structure of BSA in the presence of Y^{3+}-ions is conserved.

10.4.2 SAXS Data

Fig. 10.1 shows the normalized SAXS scattering intensity of BSA 200 mg/ml aqueous (D_2O) solutions at room temperature of 297 K with different YCl_3 concentrations c_s. The inset to the figure contains the corresponding structure factor calculated from Eq. 10.1 by using the dilute BSA solution sample (2 mg/ml) as approximation for the form factor $P(q)$. For $c_s < 7$ mM we observe a pronounced protein-protein correlation peak q_m at approximately 0.08 Å^{-1}, corresponding to a nearest neighbor distance $d = 2\pi/q_m = 78.6$ Å. For higher salt concentrations the correlation peak disappears, indicating that the Coulomb repulsion between the protein in solution becomes very weak. Investigating the structure factor at q approaching zero allows to characterize the nature of the intermolecular potential of mean force Eq. 10.8. To this end, we employ a 2$^{\text{nd}}$-order fit polynomial extrapolation of the scattering intensity to $q = 0$ over the region $0.006\,\text{Å}^{-1} \leq q \leq 0.01\,\text{Å}^{-1}$ to obtain the normalized isothermal compressibility, which is depicted in Fig. 10.5. We observe a dramatic increase of $\chi_T/\chi_T^{\text{ideal}}$ when c_s approaches the critical concentration c^*, indicated by the green vertical line. When crossing c^* we observe a transition from a clear homogeneous phase with no appreciable light scattering to a phase containing

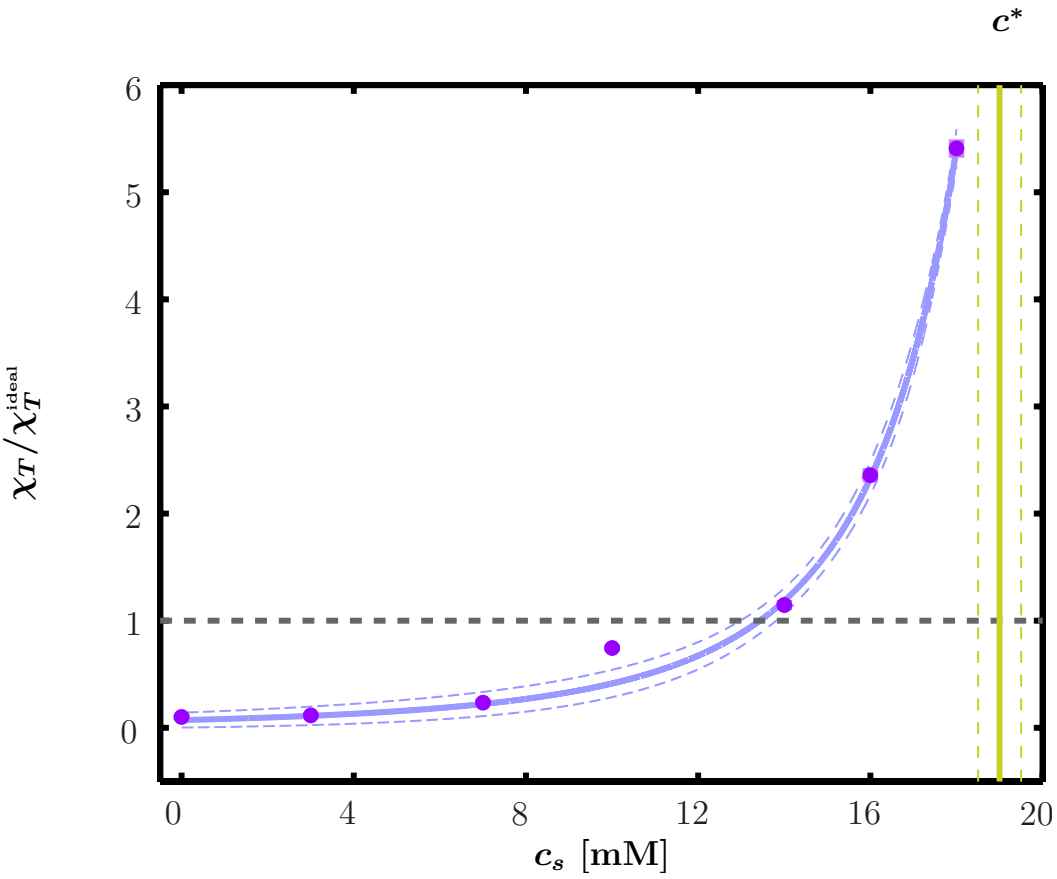

Figure 10.5: Dependence of the normalized isothermal compressibility $\chi_T/\chi_T^{\text{ideal}}$ on the YCl_3 concentrations c_s (purple circles). The blue line denotes a fit with the scaling law Eq. 10.18. Thereby, we skipped the data point at the salt concentrations $c_s = 10\,\text{mM}$, since it appears to be an outlier. The dashed blue line denotes the 95 % confidence interval of the fit. For $\chi_T/\chi_T^{\text{ideal}} < 1$ the interaction is repulsive and for $\chi_T/\chi_T^{\text{ideal}} > 1$ the interaction is attractive (the boundary $\chi_T/\chi_T^{\text{ideal}} = 1$ is indicated by a gray dashed line).

visible macroscopic clusters. Motivated by this observation, we tentatively model the behavior of $\chi_T\left(c_s\right)/\chi_T^{\text{ideal}}$ near the critical point with the general form of a phase transition [156]:

$$\chi_T\left(c_s\right) = \chi_T(0)\left(\frac{c_s^c - c_s}{c_s^c}\right)^{-\gamma}. \tag{10.18}$$

A fit to the data yields the critical-point exponent $\gamma = 3.5 \pm 1.4$, the proportionality factor $\chi_T(0)/\chi_T^{\text{ideal}} = (1.2 \pm 4.2)\,10^{-2}$ and the critical point $c_s^c = (25.3 \pm 3.7)\,\text{mM}$. Notably, a comparison of the calculated critical point $c_s^c = (25.3 \pm 3.7)\,\text{mM}$ with Fig. 10.4 shows that c_s^c within the error bars coincides with a salt concentration regime, in which the protein solution is separated into two phases.

The normalized isothermal compressibility quantifies the competition between

repulsion and attraction of the potential of mean force between two proteins in solution. This becomes evident, when we decompose Eq. 10.7 into an attractive and repulsive contribution:

$$\begin{aligned} B_w &= B_{w>0} + B_{w<0} \\ B_{w>0} &= -\frac{1}{2}\int_{w(r)>0}\left[e^{-\beta\, w(r)} - 1\right] \mathrm{d}^3\mathbf{r} \\ B_{w<0} &= -\frac{1}{2}\int_{w(r)<0}\left[e^{-\beta\, w(r)} - 1\right] \mathrm{d}^3\mathbf{r}. \end{aligned} \tag{10.19}$$

$B_{w>0}$ quantifies the strength of the repulsion and is always positive. Conversely, $B_{w<0}$ accounts for the contribution of attraction to the potential of mean force and is always negative. Hence, the balance between repulsion and attraction crucially determines the sign of B_w and, thereby, whether $\chi_T/\chi_T^{\mathrm{ideal}}$ is below or above unity. For salt concentrations $c_s < 14\,\mathrm{mM}$, the isothermal compressibility of the system is $\chi_T/\chi_T^{\mathrm{ideal}} < 1$, which indicates that the intermolecular mean force is repulsive. In a salt-free solution BSA is highly negatively charged [21] and therefore the long-range Coulomb repulsion dominates the interaction. Due to their short range, attractive interactions play a less important role. The effects of the addition of YCl_3 are twofold: In D_2O the salt dissociates into Y^{3+} and Cl^-. A fraction of the salt ions remain in the solution and screen the protein surface charge. Thereby, they reduce the range of the repulsion. The other fraction of the Y^{3+}-ions occupy specific binding sites on the protein surface and therefore lower the net surface charge [185, 175]. Consequently, the surface net charge is approaching zero and therefore the repulsive part of the potential is weakened. Synchronously, the short-range attraction gradually becomes stronger. This coincides with the observation $\chi_T/\chi_T^{\mathrm{ideal}} > 1$ for salt concentrations $c_s \geq 14\,\mathrm{mM}$. In an attraction dominated system, the formation of equilibrium clusters is favored and causes fluctuations in the local particle density, which evidently will affect the dynamical response of the system [132, 27, 99].

10.4.3 Spin-Echo Data

Fig. 10.2 shows the normalized dynamic structure factor $f(q,\tau)$ of a $200\,\mathrm{mg/ml}$ BSA aqueous (D_2O) solution with $10\,\mathrm{mM}$ YCl_3 at room temperature for different momentum transfers q. With the hydrodynamic radius $R_h = 3.66\,\mathrm{nm}$ of BSA calculated from results from dynamic light scattering [62] and $T = 297\,\mathrm{K}$, we determine the short-time regime for self-diffusion of BSA in D_2O from Eq. 10.11 and Eq. 10.12 yielding $\tau_h \approx 89\,\mathrm{ps} \ll \tau \ll \tau_i \approx 255\,\mathrm{ns}$. For $1\,\mathrm{ns} \leq \tau \leq 50\,\mathrm{ns}$ (indicated by the two vertical dashed blue lines) there is no departure of $f(q,\tau)$ from a single exponential for fixed q, indicating that we are indeed in the short-time limit. From the fit we retrieve the short-time diffusion function $D_s(q)$, which is illustrated in Fig. 10.3. In accordance with the SAXS data $D_s(q)$ has a pronounced minimum for $q \approx q_m = 0.08\,\mathrm{Å}^{-1}$, which is disappearing for higher salt concentrations. For $q > q_m$ we observe a convergence to a constant value. Consequently, by averaging

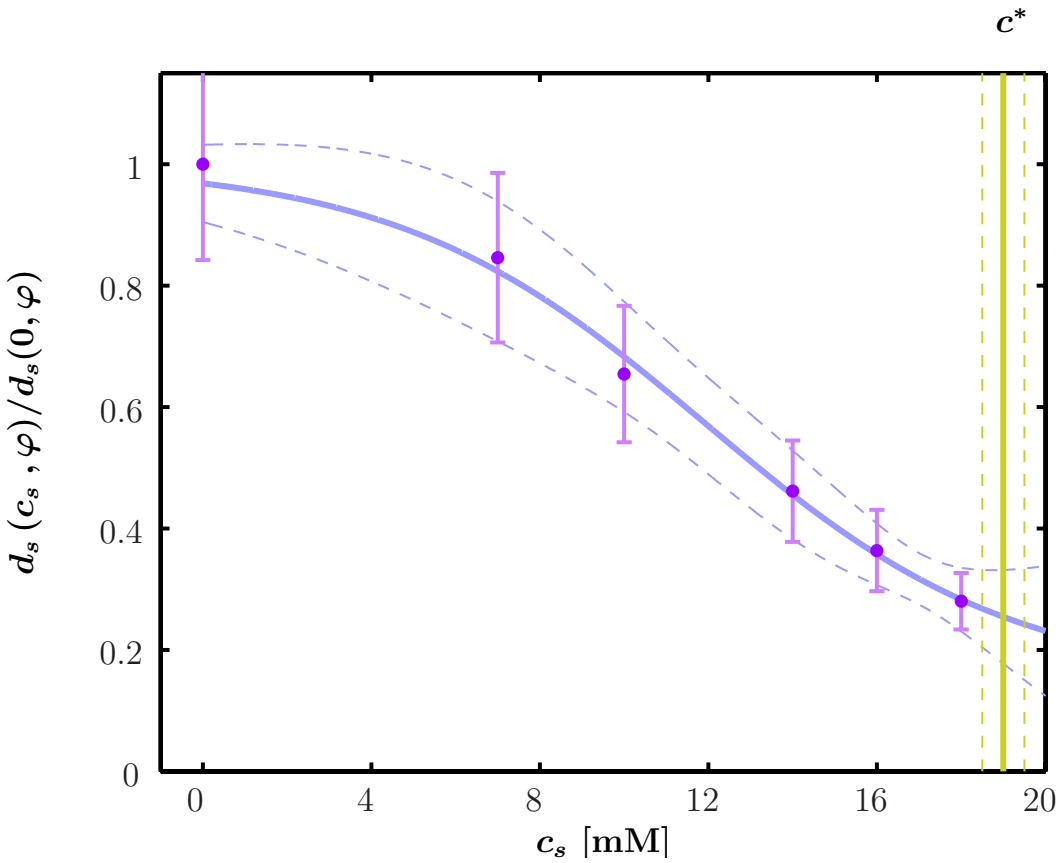

Figure 10.6: Short-time self-diffusion coefficient d_s extracted from the short-time diffusion function $D_s(q)$ for a 200 mg/ml BSA aqueous (D_2O) solution at room temperature for various YCl_3 concentrations (purple circles). The solid line superimposed to the data is the phenomenological model function Eq. X. The vertical solid line indicates the salt concentration causing a nearly zero charge of the protein.

$D_s(q)$ for $q > 0.15\,\text{Å}^{-1}$ we determine the asymptotic behavior of $D_s(q)$ giving the short-time self-diffusion coefficient d_s. Fig. 10.6 depicts the normalized short-time self-diffusion coefficient $d_s\,(c_s, \varphi)\,/d_s(0, \varphi)$ depending on the YCl_3 concentration c_s. We recognize that with increasing salt concentrations the diffusion of the protein significantly slows down. At a salt concentration $c_s \approx c^*/2$ the decrease is maximal and when c_s approaches the critical concentration c^* the slope of d_s becomes smaller. Using the phenomenological two-state transition model:

$$\frac{d_s\,(c_s, \varphi)}{d_s(0, \varphi)} = p + (1 - p)\,\Theta\left[\frac{c_s - c_s^0}{\Delta c}\right] \tag{10.20}$$

with the smooth step function $\Theta(x) = 1/[1 + \exp(x)]$, we can adequately describe the short-time self-diffusion coefficient and obtain the following fit parameters: $p = 0.15 \pm 0.19$, $c_s^0 = (11.9 \pm 2.1)\,\text{mM}$ and $\Delta c_s = (3.6 \pm 1.6)\,\text{mM}$. Remarkably, we observe that $c_s^0 \approx c^*/2$ within the error bars.

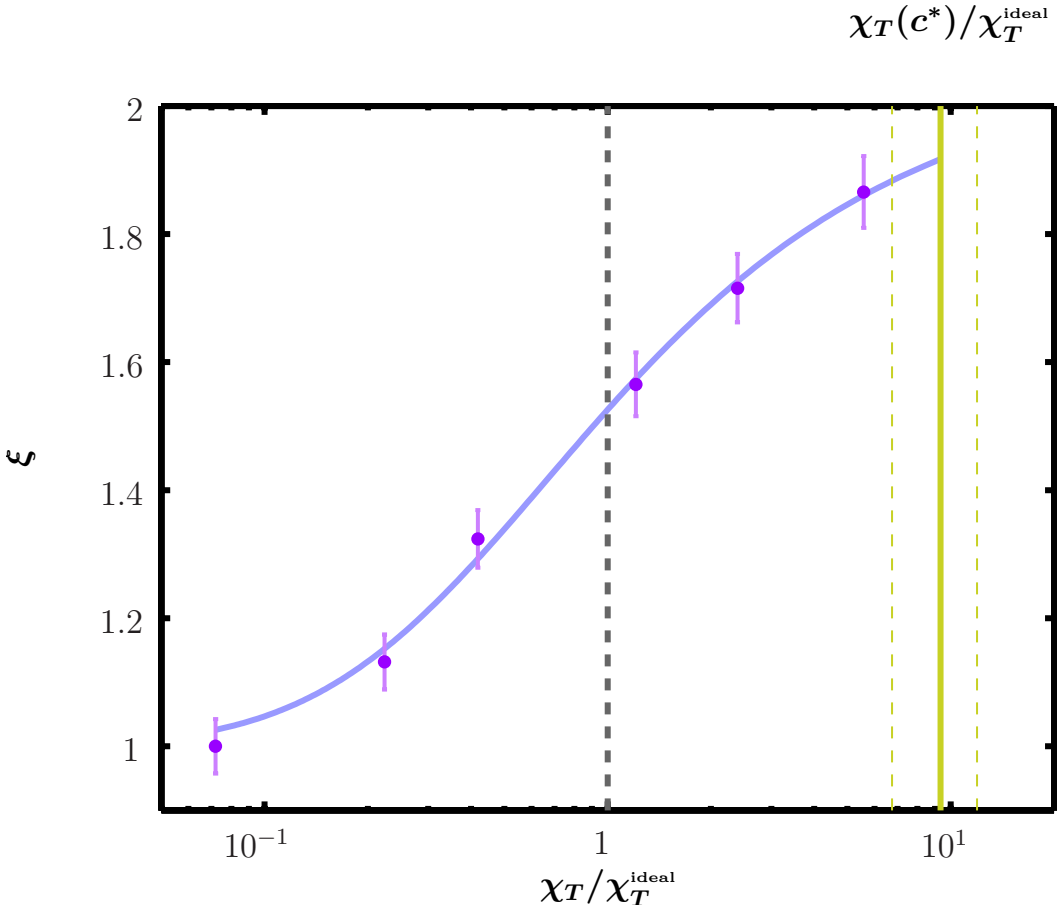

Figure 10.7: Dependence of the local crowding factor, calculated from Eqs. 10.21 and 10.22, on the normalized isothermal compressibility (purple circles). The green vertical line denotes the normalized isothermal compressibility of a protein solution with a salt concentration $c_s = c^*$. Note that $\chi_T/\chi_T^{\text{ideal}} > 1$ and $\chi_T/\chi_T^{\text{ideal}} < 1$ indicate an attractive and repulsive system, respectively.

We speculate that with the increasing attraction-dominated nature of the potential of mean force the formation of transient clusters [27, 99] is favored, which for low salt concentrations have a lifetime shorter than the instrumental time resolution due to a the high surface charge of the proteins. With the salt-induced attenuation of the Coulomb repulsion the lifetime of the cluster increases and finally rapidly diverges in the vicinity of the critical salt concentration c^*. This coincides with our observations that slightly above c^* the BSA solution becomes turbid and shows macroscopic static clusters (see Fig. 10.4). Due to the short lifetime of transient clusters, the proteins can be considered as independent and therefore the dynamical response of the system will be essentially determined by monomers. Importantly, Liu et al. [99] point out that transient clusters are strictly speaking not clusters, but rather can be conceived as fluctuating inhomogeneities in the particle density.

The short-time self-diffusion coefficient is sensitive for changes in the equilibrium

structure of the solution and therefore unambiguously can confirm the existence of dynamic density homogeneities [99]. This is for the following reason: Self-diffusion measures the diffusion of a single molecule – the so-called tracer molecule – in the solvent surrounded by the other molecules for a very short time, such that the tracer molecule moves a distance comparable with its own molecular diameter. Its diffusion is mainly determined by the hydrodynamic interactions with the surrounding molecules [116, 162, 115]. This motivates to introduce a local volume fraction φ_{local}, which crucially determines the short-self diffusion coefficient. In previous work [137] we found that the short-time self-diffusion coefficient d_s of globular proteins in salt-free solution can be accurately described by effective colloidal hard spheres. Generalizing our model to the present case of local volume fractions yields

$$d_s\left(c_s,\varphi\right) = d_0\, f_{\text{HS}}\left[\left(\frac{R_h}{R}\right)^3 \varphi_{\text{local}}\left(c_s\right)\right] \tag{10.21}$$

in which f_{HS} is the theoretical reduced translational diffusion function of hard-spheres [115, 162] and d_0 the dilute limit translational diffusion coefficient and $R \approx 2.68$ is the radius of a sphere with the same volume as the bare protein volume [137]. If no salt is present the proteins are charged and have the smallest local density $\varphi_{\text{local}}(0) = \varphi$. With increasing salt concentration the local density increases relative to φ by

$$\varphi_{\text{local}}\left(c_s\right) = \xi\left(c_s\right)\,\varphi, \tag{10.22}$$

thereby, introducing the local crowding factor $\xi\left(c_s\right)$.

Fig. 10.7 contains the local crowding factor ξ calculated from Eq. 10.21 and Eq. 10.22 depending on the normalized isothermal compressibility. We observe, an increase of the particle density inhomogeneities, when the system evolves from a repulsion- ($\chi_T/\chi_T^{\text{ideal}} < 1$) to a attraction-dominated ($\chi_T/\chi_T^{\text{ideal}} > 1$) solution. $\xi > 1$ quantifies the formation of local inhomogeneities in solution, while $\xi = 1$ corresponds to a homogenous solution. When the attraction is maximal, the initial volume fraction is increased by a factor $\xi = 1.9$, causing a decrease of the nearest neighbor distance [138] by a factor $\xi^{1/3} \approx 1.2$. This moderate change of the nearest neighbor distance indicates that the clusters are not tightly bound, but rather can be considered as unattached assemblies of proteins, which is consistent with a picture of dynamic local inhomogeneities.

10.5 Conclusions

In conclusion, we observe the formation of local inhomogeneities in solution of BSA by progressively suppressing the charge stabilization through the addition of a multivalent salt. In order to quantify these inhomogeneities, we have described the response of the short-time self-diffusion of a protein to the local inhomogeneities by a generalized a model of effective spheres introduced in earlier work [137]. Thereby, we present a local crowding factor quantifying the local inhomogeneities in the so-

lution.

Moreover, from the knowledge of the reentrance effect discovered for globular proteins for the first time by Zhang et al. [185], we can further conclude that weakening the Coulomb repulsion between by the addition of a multivalent salt gradually increases the life time of local inhomogeneities. We have found that the maximum local crowding factor corresponds to a decrease of 20 % of the nearest neighbor distance of the protein, corroborating the picture of dynamic local inhomogeneities rather than tightly bound clusters. Above the critical salt concentration c^* we observe the discontinuous onset of the formation of macroscopic clusters indicating an abrupt increase of the cluster lifetime.

The experimental data and the analysis we have shown, proves that in absence of a cluster peak in the structure factor, the dynamical response of the system can unambiguously reveal the existence of dynamic local inhomogeneities.

10.6 Acknowledgement

We are grateful to the ILL and ESRF for the allocation of beamtime. Moreover, M. Hennig and F. Roosen-Runge acknowledge financial support from the ILL, through studentship grants.

Chapter 11

Summary & Conclusion

The aim of the present thesis was to study the dynamics of a model globular proteins, namely *bovine serum albumin*, in highly concentrated electrolyte solution as a function of several parameters such as the protein concentration, the ionic strength of the solution, the valence of the ions, and the temperature around the protein denaturing point. This work was inspired by the simplified picture that living cells operate through the motion of proteins embedded in a "crowded" aqueous solution of various macromolecules and salts [49]. Therefore the motivation arose from the pursuit to understand proteins under biologically relevant conditions by exploiting knowledge and methods established in soft matter macromolecules research.

In the following three paragraphs, we will consecutively discuss the findings of our investigation on the effects of crowding, temperature related to protein thermal denaturation, as well as ion strength and valence on the dynamics of the globular protein BSA in aqueous solution. Thereby, we will briefly describe the steps that took us through the research process, review the results and draw a conclusion. At the end of each paragraph, we will discuss future perspectives on the basis of both our results and recent findings by other authors.

Crowding Molecular crowding is an essential feature of the living cell, affecting reaction kinetics and equilibria in the cell [49, 188]. Cellular function thus cannot be understood without a systematic understanding of transport processes in crowded media. Therefore, we studied the protein self-diffusion in crowded aqueous solutions of BSA as determined from quasi-elastic neutron backscattering on nanosecond time and nanometer length scales. In order to mimic the "crowded" cellular environment, we investigated the protein volume fraction range $7\,\% \leq \varphi \leq 30\,\%$ and the fundamental case where tracer particle and crowding agent are identical proteins. We observed a significant slow down of the self-diffusion with increasing volume fraction. Moreover, we revealed that the diffusion coefficient at biological volume fractions between 20 and 30 % [49] is strongly decreased compared to the dilute limit. We showed that mapping the proteins on effective hard spheres with an identical dilute-limit hydrodynamic radius allows describing the observed volume fraction dependence of the diffusion with very good accuracy in terms of colloidal short-time self-diffusion, outlining the important role of hydrodynamic interactions on crowding behavior. This modeling approach was based on an experimentally established protein shape model without adjustable parameters, i.e. an oblate ellipsoid from the fitting of SAXS data. We conclude that general features of protein diffusion can be under-

stood in terms of existing colloidal hard sphere models if anisotropy is considered using reasonable protein modeling.

The success of this simple mapping of the complex protein on an effective sphere is promising for further investigations. Assuming that globular proteins share common physical properties, it is crucial to validate our findings for other globular proteins than BSA. Moreover, in a recent publication Ando and Skolnick [7] showed by computer simulations that the size of crowding agents has an effect on self-diffusion. This study inspires to systematically investigate the size and shape dependence of crowders on diffusion to better understand how the molecular shape heterogeneity in the cytoplasm influences transport-driven processes.

Thermal Denaturing At elevated temperatures proteins denature and form random coils, thereby they lose their biological function. Consequently, denaturing defines an upper temperature limit for the existence of live. Furthermore, it is assumed that denaturing is also a key for understanding protein folding. In a simulation study Kudlay et al. [91] provided evidence that crowding can enhance structural stability and therefore effect denaturing. Using both quasi-elastic and fixed-window neutron spectroscopy, we studied the dynamics of highly concentrated aqueous protein solutions of BSA around the denaturing transition. Within the temperature range $280\,\mathrm{K} < T < 370\,\mathrm{K}$, we recorded the total mean-squared displacement $\langle u^2 \rangle$. Outside of the denaturing regime, we observed that $\langle u^2 \rangle$ increases monotonically with T, but at the denaturing transition it decreases strongly. We rationalize this observation as a transition from a liquid protein solution to a gel-like state in which the proteins form a cross-linked network. In order to quantify and understand this observation, we developed a novel physical framework for the unfolding and entanglement allowing to analytically describe $\langle u^2 \rangle (T)$. The combination of the quasi-elastic and fixed-window scattering data enabled us to decompose $\langle u^2 \rangle$ into the vibrational, subunit diffusive, and global diffusive contributions. The characteristic transition temperatures defining the denaturation range became observable. We rationalize that structural change and entanglement as well as cross-linking of the proteins significantly slow down the diffusion and, hence, explain the drop in $\langle u^2 \rangle$ in the denaturing regime.

Recently, Stagg et al. [155] showed that crowding can significantly shift the denaturing temperature of globular proteins by increasing their compactness. This observation inspires to quantify and understand the entropic contribution of crowding to unfolding. To this end our novel analysis can be enhanced by incorporating a transition model similar to that by Zimm and Bragg [187] allowing to measure the entropic penalty of unfolding.

Salt Effects The cytoplasm contains ions, which change the ionic strength of the aqueous solution. Furthermore, it was found that multivalent ions can adsorb onto the surface of globular proteins and change the net surface charge [185].

To study the effects of the presence of salt ions on the mobility of BSA we

conducted two studies.

In the *first* study, using cold neutron backscattering we investigated the short-time diffusion of BSA in crowded aqueous solution, inter alia as function of the ionic strength using the monovalent salt NaCl. We observed that the addition of salt has little or no effect on the diffusion, although charge screening is assumed to change the coupling strength. We conclude that within the measured accuracy the short-time scale diffusion coefficient is not affected by the ionic-strength. This observation is in accordance with predictions from colloid theory for the following reason: the theoretical functions for colloidal hard-spheres and charged hard-spheres are very similar in the short-time limit [115, 4, 33, 165, 162]. Consequently, we can predict that charge screening is not discernible within the given experimental accuracy.

The *second* study looked into the effect of a multivalent ion that can adsorb onto the surface of the protein and change its net charge. We combined spin-echo spectroscopy and small-angle X-ray scattering to investigate the dynamics and structure of solutions of BSA near the transition from a homogeneous to a cluster-dominated phase. To this end, we tuned the repulsive part of the protein interactions by charge-control using the trivalent salt YCl_3. We observe a substantial decrease of the short-time self-diffusion coefficient with increasing the salt concentration up a distinct value c^* at which the proteins visibly aggregate [185]. We attribute this slow down of the diffusion to the formation of local inhomogeneities in the solution of proteins. In order to quantify these inhomogeneities, we described the response of the short-time self-diffusion of a protein to the local inhomogeneities by generalizing the model of effective hard spheres, which we have briefly explained in the first paragraph. Thereby, we introduced a local crowding factor quantifying the local inhomogeneities. We found that the maximum local crowding factor corresponds to a decrease of 20 % of the nearest neighbor distance of the protein, corroborating the picture of dynamic local inhomogeneities rather than tightly bound clusters. Above the critical salt concentration c^* we observe the discontinuous onset of the formation of macroscopic clusters indicating an abrupt increase of the cluster lifetime. From the knowledge of the reentrance effect discovered for globular proteins for the first time by Zhang et al. [185], we can conclude that weakening the Coulomb repulsion by the addition of a multivalent salt, which adsorb to the protein surface and change the net charge, significantly changes the mobility of the protein due to the formation of local inhomogeneities.

This seems to be a remarkable mechanism to control or disturb transport-related processes and inspires further research on small organic ions that can bind to the surface. This balance of repulsive and attractive interaction is crucial to understand the crystallization of proteins [161, 63]. A balance in favor of attraction can cause protein aggregation, which is believed to be a trigger of fiber formation [172] and neurodegenerative diseases such as Parkinson's disease [93, 139].

Acknowledgments

FORMOST, I would like to express my deepest appreciation to my thesis advisors Prof. Dr. Frank SCHREIBER from the University of Tübingen, Prof. Dr. Helmut SCHOBER and Dr. Tilo SEYDEL from the ILL for their continuous support of my Ph.D. study and research. Their guidance helped me in all the time of research and writing of this thesis. Without their assistance and inspiration this thesis would not have been possible.

Throughout the three years of my thesis work, important guidance came from Dr. Tilo SEYDEL. I truly benefited from his considerable expertise in neutron scattering and his assistance. He helped me to carry out and prepare the various neutron scattering experiments at the ILL, which constitute the fundament of this thesis.

I would like to express my sincere gratitude to Dr. Fajun ZHANG, who helped me to understand the technique of small-angle scattering and the physics behind the remarkable reentrance behavior of globular proteins he discovered shortly before I started my Ph.D. work.

While employing several neutron spectrometers at the ILL and the SAXS ID02 beam line at the ESRF for conducting my research, I benefited from the assistance and advises from those people, who devote their valuable time besides their own research efforts to support users carrying out their experiments. At the IN16 and IN10 neutron backscattering spectrometers, Dr. Bernhard FRICK and Dr. Tilo SEYDEL provided excellent support for setting up the instruments, carrying out the measurements, and analyzing the data.

My sincere gratitude to Dr. Peter FALUS, Dr. Macro MACCARINI and Dr. Peter FOUQUET, who assisted me to collect an essential part of my data at the IN15 and IN11 neutron spin-echo spectrometers. Moreover, I particularly thank Dr. Peter FALUS to have sacrificed valuable time to explain me the mystery of neutron spin-echo spectroscopy.

It is a pleasure to thank Dr. Theyencheri NARAYANAN and Dr. Michael SZTUCKI for their support at the ID02 beam line and their fruitful discussions concerning the data analysis.

During my Ph.D. thesis time office colleagues and team member contributed to my thesis with productive discussion about, *inter alia*, physics. I am grateful to Felix ROOSEN-RUNGE, who joined the project as a Diploma student and over the time became a Ph.D. student. He helped me with designing and conducting nearly all experiments. With his thoughtful and profound comments, he was a continuous source of inspiration and his persistency to tackle and scrutinize complex problems helped us to develop new data analysis and insights throughout the project. Furthermore, I am thankful to Fabio ZANINI who joined likewise as a Diploma student, with helping me to carry out experiments at the Oak Ridge National Lab and the ILL. His admirable attitude to try to get to the bottom of problems gave

me many insights and inspiration. Finally, without Elena Jordan's remarkable long working hours in the laboratory and at the ID02 my work would miss the complementary X-ray data, she helped me to record at the ID02 beamline.

I am thankful to Prof. Dr. Judith Peters who was so kind to serve as a third referee for this thesis and who helped me with her remarks to further improve this work.

Within the Tübingen - Oxford collaboration, I would like to acknowledge Dr. Maximilian W. A. Skoda, Dr. Stefan Zorn and Dr. Robert M. J. Jacobs. Furthermore, I am thankful to Dr. Alexander Gerlach to have organized yearly Klausurtagung in Oberjoch, which was always an important event to exchange ideas with the other group members. Many thanks to the team of the machine shop at the University of Tübingen to produce the aluminum sample cylinders which were an essential part to carry out the numerous experiments at the ILL.

Last but not least, I am deeply thankful to my wife Dan who gave me the support and the encouragement I needed throughout the period of Ph.D. research.

I am grateful to the ILL and ESRF for the allocation of beamtime. The work was financed by the ILL through the Ph.D. studentship grant scheme.

Appendix A

Appendix

A.1 Paalman-Pings Coefficients

Eliminating the sample container signal $I_{\mathrm{C}}^{\mathrm{C}}$ from the measured intensity signal $I_{\mathrm{SC}}^{\mathrm{SC}}$ of the sample requires an absorption calculation based on the theory of Paalman and Pings [122]. They showed that self-shielding and absorption of neutrons traveling through the sample and the sample container has to be considered when subtracting the sample container from the sample signal. For the sample container correction they derived the following equation:

$$I^{\mathrm{S}} = \frac{1}{A_{\mathrm{SC}}^{\mathrm{S}}} \left(I_{\mathrm{SC}}^{\mathrm{SC}} - \frac{A_{\mathrm{SC}}^{\mathrm{C}}}{A_{\mathrm{C}}^{\mathrm{C}}} I_{\mathrm{C}}^{\mathrm{C}} \right), \tag{A.1}$$

in which I^{S} is the scattering intensity from the sample, if there were no absorption or self-shielding effects. $A_{\mathrm{SC}}^{\mathrm{S}}$, $A_{\mathrm{SC}}^{\mathrm{C}}$ and $A_{\mathrm{C}}^{\mathrm{C}}$ are the $\mathbf{q}$ depended so-called Paalman-Pings coefficients. For convenience, we introduce the following expressions:

$$\begin{aligned} \alpha_{\mathrm{SC}} &= \frac{1}{A_{\mathrm{SC}}^{\mathrm{S}}} \\ \beta_{\mathrm{SC}} &= \frac{1}{A_{\mathrm{SC}}^{\mathrm{S}}} \frac{A_{\mathrm{SC}}^{\mathrm{C}}}{A_{\mathrm{C}}^{\mathrm{C}}} , \end{aligned} \tag{A.2}$$

to which we will refer to as Paalman-Pings coefficients in Sec. 5.4. Note that the upper index in Eq. A.1 denotes the volume effecting the absorption-based loss of intensity and the lower index indicates which material is contained by the volume. Depending whether the index S is at the upper or lower position, S denotes the sample volume or the sample solution, respectively. Analogously, C denotes either the can volume or the can material. Fig. A.1 illustrates the path of a neutron beam traveling through the sample container filled with a sample solution. On their path neutrons of the beam can be either scattered or absorbed, causing an attenuation of the neutron beam intensity. The Paalman-Pings coefficients measure the attenuation of the neutron beam intensity that is accumulated along the path $\boldsymbol{\gamma}$ of a neutron with initial wavevector $\mathbf{k}$ scattered in the volume V (which either denotes the sample volume S or the volume C of the sample container):

$$A_{\Sigma}^{\mathrm{V}}(\mathbf{q}) = \frac{1}{V} \int_{V} \exp\left[- \int_{\boldsymbol{\gamma}(\mathbf{x})} \Sigma(\mathbf{x}') \, \mathrm{d}s(\mathbf{x}') \right] \mathrm{d}^3\mathbf{x}. \tag{A.3}$$

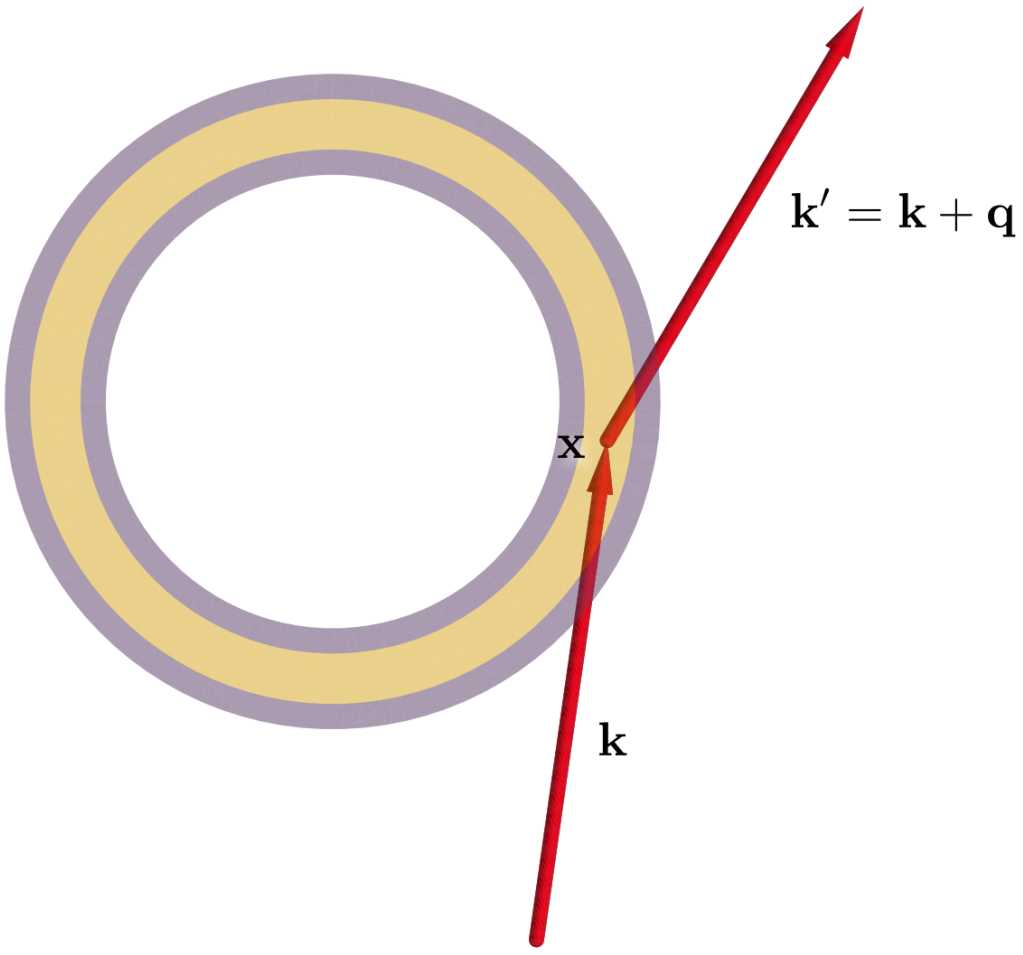

Figure A.1: A neutron beam illustrated by a red arrow with the initial wavevector $\mathbf{k}$ is scattered at the position $\mathbf{x}$ in the sample container volume and therefore changes its wavevector to $\mathbf{k}' = \mathbf{k}+\mathbf{q}$. Therein, $\mathbf{q}$ denotes the momentum transfer vector. The sample container walls (gray) and the sample solution (yellow) have the different attenuation coefficients Σ_C and Σ_S (yellow), respectively.

Attenuation Coefficient		
Sample	density [g/cm^3]	Σ [cm^{-1}]
Vanadium foil	6.11	1.673
Aluminum sample container	2.7	0.147
Aqueous (D_2O) BSA (200mg/ml)	0.174	0.708
Pure D_2O	1.1056	0.649

Table A.1: Linear attenuation coefficient of different samples at room temperature for neutrons with wavelength $\lambda = 6.4\,\text{Å}$.

Therein, $\Sigma(\mathbf{x})$ is the linear attenuation coefficient at position $\mathbf{x}$ and $\mathrm{d}s(\mathbf{x})$ denotes the infinitesimal line element of the line integral. If the lower index of the Paalman-Pings coefficient A in Eq. A.3 is $\Sigma = \text{SC}$ then the attenuation coefficient is $\Sigma(\mathbf{x}) = \Sigma_S\,\Omega_S(\mathbf{x}) + \Sigma_C\,\Omega_C(\mathbf{x})$, whilst a lower index $\Sigma = \text{S}$ implies that $\Sigma(\mathbf{x}) = \Sigma_S\,\Omega_S(\mathbf{x})$ (an analog consideration holds for $\Sigma = \text{C}$). Therein, the function $\Omega_V(\mathbf{x})$ is unity for $\mathbf{x} \in V$ otherwise zero. A neutron with initial wavevector $\mathbf{k}$ scattered at position $\mathbf{x}$ and thereby changing its wavevector to $\mathbf{k}' = \mathbf{q} + \mathbf{k}$ travels along the path

$$\boldsymbol{\gamma}(\mathbf{x}) = \begin{cases} \mathbf{x} + t\,\mathbf{k}/k & \text{if } t \leq 0 \\ \mathbf{x} + t\,\mathbf{k}'/k' & \text{if } t > 0 \end{cases} \tag{A.4}$$

with $t \in [-\infty, \infty]$. The attenuation coefficient is calculated from both the neutron scattering and absorption cross-section:

$$\Sigma = \rho\,(\sigma_{\text{coh}} + \sigma_{\text{inc}} + \sigma_{abs})\,. \tag{A.5}$$

Therein, ρ is the number density of the scattering particles. Values for the cross-section of various chemical elements can be found in Ref. [1]. Table A.1 shows some exemplary attenuation coefficients, relevant for this thesis.

A.2 Correction of the specific volume measured by Densitometry

In the following we want to elaborate the influence of a hydration shell of water molecules, sticking to the protein surface, on the apparent specific volume ϑ, measured by densitometry. This will allow us to obtain the specific volume of the non-hydrated protein, denoted by ϑ_p. Within the framework of densitometry the

apparent specific volume of a protein is determined by

$$\vartheta = \frac{1}{\rho_{\text{buff}}} \left(1 - \frac{\rho_{\text{sol}} - \rho_{\text{buff}}}{c}\right) \tag{A.6}$$

where c is the mass concentration of the proteins in the buffer solution with density ρ_{buff}. Finally, ρ_{sol} denotes the density of the protein solution. In a simple picture we have N_p proteins each with a volume V_p and a mass m_p, surrounded by n water molecules occupying a volume V_{sp}. In the bulk water in which these hydrated proteins are submerged we have N_s water molecules each with volume V_s. We have to distinguish between water molecules in solution and those which are sticking to the proteins surface since they occupying different volumes. Using all these variables, the solvent density reads

$$\rho_{\text{sol}} = \frac{N_p\, m_p + (N_s + n\, N_p)\; m_s}{N_p\, V_p + (N_s\, V_s + n\, N_p\, V_{sp})} \tag{A.7}$$

The buffer density is simply $\rho_{\text{buff}} = m_s/V_s$. Substitute these expressions into equation A.6 yields

$$\vartheta = \frac{V_p}{m_p} + \frac{n\;(V_{sp} - V_s)}{m_p} \tag{A.8}$$

By introducing the hydration level $\eta = n\, m_s/m_p$, the bulk water density $\rho_{\text{bulk}} = m_s/V_s$ and the density of the hydration shell water $\rho_{\text{hydr}} = m_s/V_{sp}$ as well as the proteins dry specific volume $\vartheta_p = V_p/m_p\; \vartheta$, we obtain finally the relation

$$\vartheta_p = \vartheta + \eta \left(\frac{1}{\rho_{\text{bulk}}} - \frac{1}{\rho_{\text{hydr}}}\right) \tag{A.9}$$

Using densitometry, Lee and Timasheff [96] determined the apparent specific volume $\vartheta = 0.735\,\text{ml/g}$ for the native structure of BSA in solution. Taking the average of published values, we assume the protein hydration level $\eta = 0.4 g/g$ [92, 44, 135] and a density of protein-bound water which is 13% higher than bulk water [127, 106, 158]. We thus obtain the specific volume $\vartheta_p = 0.7795\,\text{ml/g}$ which is in agreement with $(0.7763 \pm 0.0067)\,\text{ml/g}$ computed from the amino acid sequence of BSA following reference [126].

A.3 Volume Fraction Calculation

A globular protein can be seen in a simple model as compact solid particle with a layer of water molecules sticking to its surface. Even if the macromolecule is somehow porous or permeable to the solvent, the fluid inside it is trapped, moves along with it, and belongs to the hydrodynamic particle. With this simple notion of a protein we will try derive with a formula for the volume fraction. In the following we use the variables which we introduced in the previous section without further explanation. Accounting for the volume of the protein, the number density of the protein with hydration shell is

$$c_n = \frac{N_p}{N_p V_p + N_s V_s + n N_p V_{sp}} \tag{A.10}$$

During the preparation of a protein solution, we put a mass of $N_p \cdot m_p$ of proteins together with a total volume $(N_s + n \cdot N_p)\, V_s$ of water, where $(N_s + n \cdot N_p)$ is the total number of water molecules. Thereby, we introduce the quantity c, which is not precisely a concentration but merely a preparative: detail.

$$c = \frac{N_p m_p}{(N_s + n N_p)\, V_s}. \tag{A.11}$$

Expressing N_p in dependence of c and substituting into equation A.10 yields

$$c_n = \frac{c}{m_p \left(1 + c \left[\frac{V_p}{m_p} + \frac{n}{m_p} (V_{sp} - V_s)\right]\right)} \tag{A.12}$$

When introducing $\vartheta_p = V_p/m_p$, $\eta = n \cdot m_s/m_p$ and the densities $\rho_{\text{bulk}} = m_s/V_s$ as well as $\rho_{\text{hydr}} = m_s/V_{sp}$ becomes

$$c_n = \frac{c}{m_p \left(1 + c \left[\vartheta_p + \eta \left(\frac{1}{\rho_{\text{hydr}}} - \frac{1}{\rho_{\text{bulk}}}\right)\right]\right)} \tag{A.13}$$

The volume of a single hydrated protein reads

$$V = m_p \vartheta_p + \frac{\eta \cdot m_p}{\rho_{\text{hydr}}} \tag{A.14}$$

Eventually, combining equations A.13, A.14 and A.9, the resulting volume fraction $\phi = c_n \cdot V$ of proteins in the solution depends on the dissolved protein and hydration shell sizes as follows

$$\phi = \frac{c \left(\vartheta + \frac{\eta}{\rho_{\text{bulk}}}\right)}{1 + c \cdot \vartheta} \tag{A.15}$$

As expected, the denominator accounts for the volume contribution of the protein to the total solution volume. The hydration shell increases the apparent specific volume with a term $\frac{\eta}{\rho_{\text{bulk}}}$. We note that the volume effect of the increased water density in the hydration shell is included in the apparent specific volume ϑ itself

List of Figures

List of Tables

List of Symbols

$\mathbb{Z}^3$	Three-dimensional integer lattice
$\dagger$	Adjoint
$\top$	Transposition
tr	Trace of square matrix
diag	Diagonal matrix
∇	Nabla as column vector
$\delta(.)$	Dirac delta function
$\mathcal{L}(.)$	Lorentzian function
$\mathcal{O}(.)$	Big O notation for residual in Taylor series
$\otimes$	Convolution in respect to ω
$\|.\|$	Vector norm
$\|.\|$	Modulus of complex number
k_B	Boltzmann constant
$\hbar$	Planck constant
τ	Fourier time
t	Time
T	Temperature
χ_T	Isothermal compressibility
χ_T^{ideal}	Isothermal compressibility of an ideal gas
β	$\beta = k_B\,T$
η	Dynamical viscosity
N	Number of particles
φ	Volume fraction of particles
$\hat{H}_0$	Free neutron Hamiltonian
$\hat{H}$	Hamiltonian of sample
$\hat{b}$	Scattering length operator
$\hat{S}$	Smoluchowski operator
U	Total potential of N-particle system
m	Mass of neutron
$\mathbf{k}$	Wavevector of incoming neutron
$\mathbf{k}'$	Wavevector of scattered neutron
$\mathbf{q}, \mathbf{Q}$	Momentum transfer vector of neutron
E	Energy of incoming neutron
E'	Energy of scattered neutron
ω	Angular frequency corresponding to energy change of neutron
λ	Wavelength of neutron
$\hat{\mathbf{R}}(t)$	Heisenberg operator of the position operator

Bibliography

[1] Neutron scattering lengths and cross sections of the elements and their isotopes. *Neutron News*, 3(3):29–37, 1992. (Cited on pages 26, 187 and 203.)

[2] *MATLAB: Version 2010b*. The MathWorks Inc., Natick, Massachusetts, 2010. (Cited on page 81.)

[3] G. Abade, B. Cichocki, and M. Ekiel-Jezewska. Short-time dynamics of permeable particles in concentrated suspensions. *J. Chem. Phys.*, 132(014503), 2010. (Cited on page 135.)

[4] J. B. Adolfo and G. Nägele. Short-time transport properties in dense suspensions: From neutral to charge-stabilized colloidal spheres. *J. Chem. Phys.*, 128(10):104903, 2008. (Cited on pages 102, 128, 133, 134, 181 and 198.)

[5] B. Alefeld, M. Birr, and A. Heidemann. Ein neues hochauflösendes Neutronenkristallspektrometer und seine Anwendung. *Naturwissenschaften*, 56: 410–412, 1969. (Cited on page 66.)

[6] J. Als-Nielsen and D. McMorrow. *Elements of Modern X-ray Physics*. John Wiley & Sons, Ltd, 2001. (Cited on pages 33 and 65.)

[7] T. Ando and J. Skolnick. Crowding and hydrodynamic interactions likely dominate in vivo macromolecular motion. *Proc. Natl. Acad. Sci. U.S.A.*, 107 (43):18457–18462, 2010. (Cited on pages 4, 8, 103, 127, 129, 135 and 180.)

[8] B. Armstrong. Spectrum line profiles: the voigt function. *J. Quant. Spectrosc. Radiat. Transfer*, 7:61–88, 1967. (Cited on pages 88 and 114.)

[9] M. Arrio-Dupont, G. Foucault, and M. Vacher. Translational Diffusion of Globular Proteins in the Cytoplasm of Cultured Muscle Cells. *Biophys. J.*, 78:901–907, 2000. (Cited on pages 127 and 134.)

[10] N. W. Ashcroft and N. D. Mermin. *Solid State Physics*. Holt, Rinehart and Winston, New York, 1976. (Cited on page 66.)

[11] P. Ball. Water as an active constituent in cell biology. *Chem. Rev.*, 108:74–108, 2008. (Cited on pages 2, 14 and 109.)

[12] D. S. Banks and C. Fradin. Anomalous Diffusion of Proteins Due to Molecular Crowding. *Biophys. J.*, 89:2960–2971, 2005. (Cited on page 127.)

[13] M. Bée. *Quasielastic neutron scattering*. Taylor & Francis, London, UK, 1988. (Cited on pages 32, 86, 110, 116, 128, 143 and 144.)

[14] M. Bée. A physical insight into the elastic incoherent structure factor. *Physica B*, 182(4):323 – 336, 1992. (Cited on pages 88, 96 and 155.)

[15] M. Bée. Localized and long-range diffusion in condensed matter: state of the art of qens studies and future prospects. *Chem. Phys.*, 292(2-3):121–141, 2003. (Cited on pages 14, 109 and 143.)

[16] M. C. Bellissent-Funel, J. Teixeira, and L. Bosio. Structure of high density amorphous water. II. Neutron scattering study. *J. Chem. Phys.*, 87(4):2231–2235, 1987. (Cited on page 61.)

[17] L. Belloni. Electrostatic interactions in colloidal solutions: Comparison between primitive and one-component models. *J. Chem. Phys.*, 85(1):519–526, 1986. (Cited on page 40.)

[18] P. L. San Biagio, D. Bulone, A. Emanuele, and M. U. Palma. Self-assembly of biopolymeric structures below the threshold of random cross-link percolation. *Biophys. J.*, 70:494–499, 1996. (Cited on page 147.)

[19] R. Biehl, B. Hoffmann, M. Monkenbusch, P. Falus, S. Préost, R. Merkel, and D. Richter. Direct observation of correlated interdomain motion in alcohol dehydrogenase. *Phys. Rev. Lett.*, 101(13):138102, 2008. (Cited on page 128.)

[20] R. Biehl, M. Monkenbusch, and D. Richter. Exploring internal protein dynamics by neutron spin echo spectroscopy. *Soft Matter*, 7(4):1299—1307, 2011. (Cited on pages 1 and 13.)

[21] U. Böhme and U. Scheler. Effective charge of bovine serum albumin determined by electrophoresis NMR. *Chem. Phys. Lett.*, 435:342 – 345, 2007. (Cited on pages 60, 171 and 173.)

[22] C. Le Bon, T. Nicolai, and D. Durand. Kinetics of aggregation and gelation of globular proteins after heat-induced denaturation. *Macromolecules*, 32(19):6120–6127, 1999. (Cited on page 147.)

[23] W Bras. Sample environments and techniques combined with Small Angle X-ray Scattering. *Adv. Colloid Interface Sci.*, 75(1):1–43, 1998. (Cited on page 79.)

[24] R. Brown. A brief account of microscopical observations made in the months of june, july and august, 1827, on the particles contained in the pollen of plants; and on the general existence of active molecules in organic and inorganic bodies. *Phil. Mag.*, 4:161–173, 1828. (Cited on page 44.)

[25] S. Busch, W. Doster, S. Longeville, V. Sakai, and T. Unruh. Microscopic protein diffusion at high concentration. *MRS Bull.*, 2006. (Cited on pages 114, 119, 128 and 131.)

[26] E. Buxbaum. *Fundamentals of Protein Structure and Function*. Springer Science+Business Media, Inc., New York, 2007. (Cited on pages 1 and 13.)

[27] F. Cardinaux, E. Zaccarelli, A. Stradner, S. Bucciarelli, B. Farago, S. U. Egelhaaf, F. Sciortino, and P. Schurtenberger. Cluster-Driven Dynamical Arrest in Concentrated Lysozyme Solutions. *J. Phys. Chem. B*, 2011. doi: 10.1021/jp112180p. URL http://pubs.acs.org/doi/abs/10.1021/jp112180p. (Cited on pages 6, 104, 163, 173 and 175.)

[28] C. Caronna, F. Natali, and A. Cupane. Incoherent elastic and quasi-elastic neutron scattering investigation of hemoglobin dynamics. *Biophys. Chem.*, 116(3):219 – 225, 2005. (Cited on page 143.)

[29] D. C. Carter and J. X. Ho. Structure of serum albumin. *Adv. Chem. Ser.*, 45: 153–176, 1994. (Cited on pages 2, 13, 58 and 113.)

[30] J. Chadwick. The existence of a neutron. *Proc. R. Soc. London, Ser. A*, 136 (830):692–708, 1932. (Cited on page 20.)

[31] H.S. Chan and K. A. Dill. Origins of structure in globular proteins. *Proc. Natl. Acad. Sci. U.S.A.*, 87:6388–6392, 1990. (Cited on pages 1 and 13.)

[32] C. H. Cho, J. Urquidi, S. Singh, and G. W. Robinson. Thermal offset viscosities of liquid H_2O, D_2O, and T_2O. *J. Phys. Chem. B*, 103(11):1991–1994, 1999. (Cited on pages 61 and 131.)

[33] B. Cichocki, M. L. Ekiel-Jezewska, and E. Wajnryb. Lubrication corrections for three-particle contribution to short-time self-diffusion coefficients in colloidal dispersions. *J. Chem. Phys.*, 111(7):3265–3273, 1999. (Cited on pages 102, 128 and 181.)

[34] C. Cohen-Tannoudji, B. Diu, and F. Laloë. *Quantummechanik*, volume 1. Walter de Gruyter, 1999. (Cited on page 20.)

[35] The UniProt Consortium. Ongoing and future developments at the Universal Protein Resource. *Nucleic Acids Res.*, 39(suppl 1):D214–D219, 2011. (Cited on pages 58 and 203.)

[36] C. G. Darwin. The theory of X-ray reflexion. Part II. *Phil. Mag.*, 27(160): 675–690, 1914. (Cited on page 70.)

[37] P. G. de Gennes. *Scaling concepts in polymer physics*. Cornell University, 1979. (Cited on pages 147 and 148.)

[38] J. García de la Torre, M. Huertas, and B. Carrasco. Calculation of hydrodynamic properties of globular proteins from their atomic-level structure. *Biophys. J.*, 78:719 – 730, 2000. (Cited on page 45.)

[39] S. Dellerue, A. Petrescu, J. Smith, and M. C. Bellissent-Funel. Radially softening diffusive motions in a globular protein. *Biophys. J.*, 2001. (Cited on pages 85, 88, 144 and 153.)

[40] J. K. G. Dhont. *An Introduction to Dynamics of Collloids*. Elsevier Science, 1996. (Cited on pages 18, 37, 50, 111, 112 and 169.)

[41] P. A. M. Dirac. *The principles of quantum mechanics*. Oxford UK: Oxford University Press, 4 edition, 1982. (Cited on page 21.)

[42] J. A. Dix and A. S. Verkman. Crowding Effects on Diffusion in Solutions and Cells. *Annu. Rev. Biophys.*, 37:247–263, 2008. (Cited on pages 127 and 134.)

[43] R. Dorshow and D. Nicoli. The effect of hydrodynamics on the diffusivity of charged macromolecules: Application to BSA. *J. Chem. Phys.*, 75(12): 5853–5856, 1981. (Cited on page 110.)

[44] W. Doster and S. Longeville. Microscopic diffusion and hydrodynamic interactions of hemoglobin in red blood cells. *Biophys. J.*, 93(4):1360 – 1368, 2007. (Cited on pages 51, 60, 112, 119, 120, 121, 128, 135 and 188.)

[45] W. Doster, S. Cusack, and W. Petry. Dynamical transition of myoglobin revealed by inelastic neutron scattering. *Nature*, 337:754 – 756, 1989. (Cited on page 143.)

[46] W. Doster, S. Busch, A. M. Gaspar, and H. Scheer. Dynamical transition of protein-hydration water. *Phys. Rev. Lett.*, 104(9):098101, 2010. (Cited on pages 85, 88, 144 and 153.)

[47] B. Eckert. A Conformational Unfolding Reaction Activates Phage fd for the Infection of Escherichia coli. *J. Mol. Biol.*, 373:452–461, 2007. (Cited on pages 1 and 13.)

[48] A. Einstein. Über die von der molekularkinetischen Theorie der Wärme geforderte Bewegung von in ruhenden Flüssigkeiten suspendierten Teilchen. *Ann. Phys.*, 17(549-560), 1905. (Cited on pages 44 and 45.)

[49] R. J. Ellis. Macromolecular crowding: an important but neglected aspect of the intracellular environment. *Curr. Opin. Struct. Biol.*, 11(1):114–119, 2001. (Cited on pages 2, 14, 109, 127, 135 and 179.)

[50] F. Roosen-Runge et al., 2011. unpublished. (Cited on pages 143 and 148.)

[51] F. Zhang et al., 2011. unpublished. (Cited on page 145.)

[52] B. Farago. Recent neutron spin-echo developments at the ILL (IN11 and IN15). *Physica B*, 267-268(1):270–276, 1999. (Cited on pages 76 and 204.)

[53] B. U. Felderhof and R. B. Jones. Orientational relaxation in a colloidal suspension of spheres. *Phys. Rev. E*, 48(2):1084–1090, 1993. (Cited on page 56.)

[54] P. Fenimore, H. Frauenfelder, B. McMahon, and R. Young. Bulk-solvent and hydration-shell fluctuations, similar to alpha-and beta-fluctuations in glasses, control protein motions and functions. *Proc. Natl. Acad. Sci. U.S.A.*, 101(40): 14408–14413, 2004. (Cited on page 143.)

[55] A. Fick. Über Diffusion. *Ann. Phys.*, 170(1):59–86, 1855. (Cited on pages 44, 50 and 112.)

[56] J. Figge, T. H. Rossing, and V. Fencl. The role of serum proteins in acid-base equilibria. *J. Lab. Clin. Med.*, 117(6):453–467, 1991. (Cited on page 58.)

[57] J. Fitter, T. Gutberlet, and J. Katsaras. *Neutron scattering in biology: techniques and applications.* Springer, Berlin Heidelberg, 2006. (Cited on page 143.)

[58] B. Frick. Neutron Backscattering spectroscopy. In F. Hippert, E. Geissler, J. L. Hodeau, E. Lelièvre-Berna, and J. R. Regnard, editors, *Neutron and X-ray Spectroscopy*, pages 483–525. Springer, 2006. (Cited on page 66.)

[59] B. Frick and M. Gonzalez. Five years operation of the second generation backscattering spectrometer IN16–a retrospective, recent developments and plans. *Physica B*, 301:8–19, 2001. (Cited on pages 67, 71, 113 and 203.)

[60] B. Frick, E. Mamontov, L. van Eijck, and T. Seydel. Recent backscattering instrument developments at the ILL and SNS. *Z. Phys. Chem.*, 224:33–60, 2010. (Cited on page 66.)

[61] F. Gabel, D. Bicout, U. Lehnert, M. Tehei, M. Weik, and G. Zaccai. Protein dynamics studied by neutron scattering. *Q. Rev. Biophys.*, 35(04):327–367, 2003. (Cited on pages 109 and 143.)

[62] A. K. Gaigalas, J. B. Hubbard, M. McCurley, and S. Woo. Diffusion of bovine serum albumin in aqueous solutions. *J. Phys. Chem.*, 96(5):2355–2359, 1992. (Cited on pages 129, 131, 133, 173 and 198.)

[63] O. Galkin and P. G. Vekilov. Control of protein crystal nucleation around the metastable liquid–liquid phase boundary. *Proc. Natl. Acad. Sci. U.S.A.*, 97 (12):6277–6281, 2000. (Cited on pages 163 and 181.)

[64] A. Gaspar, M. Appavou, S. Busch, T. Unruh, and W. Doster. Dynamics of well-folded and natively disordered proteins in solution: a time-of-flight neutron scattering study. *Eur. Biophys. J.*, 37(5):573–582, 2008. (Cited on page 119.)

[65] G. Gibrat, F. Assairi, Y. Blouquit, C. Craescu, and M. Bellissentfunel. Biophysical study of thermal denaturation of apo-calmodulin: Dynamics of native and unfolded states. *Biophys. J.*, 95(11):5247–5256, 2008. (Cited on page 143.)

[66] D. S. Goodsell. *The Machinery of Life*. Springer Science + Business Media, New York, 2009. (Cited on pages 1 and 13.)

[67] G. Guigas and M. Weiss. Sampling the Cell with Anomalous Diffusion-The Discovery of Slowness. *Biophys. J.*, 94(1):90–94, 2008. (Cited on page 127.)

[68] H.C. Hamaker. The London—van der Waals attraction between spherical particles. *Physica IV*, (10):1058–1072, 1937. (Cited on pages 42 and 43.)

[69] W. Häussler. Neutron spin echo studies on ferritin: free-particle diffusion and interacting solutions. *Eur. Biophys. J.*, 37(5):563–571, 2008. (Cited on pages 120 and 128.)

[70] W. M. Haynes, editor. *"Properties of saturated liquid D_2O," in CRC Handbook of Chemistry and Physics*. CRC Press/Taylor and Francis, Boca Raton, FL, 91st edition (internet version 2011) edition, 2011. (Cited on page 60.)

[71] J. Hayter and J. Penfold. An analytic structure factor for macroion solutions. *Mol. Phys.*, 42(1):109–118, 1981. (Cited on pages 36 and 192.)

[72] M. Hennig, B. Frick, and T. Seydel. Optimum velocity of a phase space transformer for cold neutron backscattering spectroscopy. *J. Appl. Crystallogr.*, 44: 467–472, 2011. (Cited on pages 72 and 73.)

[73] T. Hianik, S. Poniková, J. Bágel'ová, and M. Antalík. Specific volume and compressibility of human serum albumin-polyanion complexes. *Bioorg. Med. Chem. Lett.*, 16:274–279, 2006. (Cited on page 109.)

[74] P. Holmqvist and G. Nägele. Long-time dynamics of concentrated charge-stabilized colloids. *Phys. Rev. Lett.*, 104(5):058301, 2010. (Cited on page 168.)

[75] B. Hribar. Clustering of Macroions in Solutions of Highly Asymmetric Electrolytes. *Biophys. J.*, 78(2):694–698, 2000. (Cited on page 163.)

[76] J. Hubbard and J. F. Douglas. Hydrodynamic friction of arbitrarily shaped Brownian particles. *Phys. Rev. E*, 47(5):2983–2986, 1993. (Cited on page 45.)

[77] W. Humphrey, A. Dalke, and K. Schulten. VMD - Visual Molecular Dynamics. *J. Molec. Graphics*, 14:33–38, 1996. (Cited on pages 27, 59, 87, 191, 193 and 195.)

[78] A. Hunter and G. Carta. Effects of bovine serum albumin heterogeneity on frontal analysis with anion-exchange media. *J. Chromatogr. A*, 937:13 – 19, 2001. (Cited on pages 60, 137, 147 and 163.)

[79] ILL, editor. *The ILL YellowBook*. ILL, Grenoble, 2008. URL `http://www.ill.eu/instruments-support/instruments-groups/yellowbook/`. (Cited on pages 67, 76, 113, 203 and 204.)

[80] M. Jasnin, M. Moulin, M. Haertlein, G. Zaccai, and M. Tehei. In vivo measurement of internal and global macromolecular motions in escherichia coli. *Biophys. J.*, 95(2):857 – 864, 2008. (Cited on page 128.)

[81] H. Jenkins and Y. Marcus. Viscosity B-coefficients of ions in solution. *Chem. Rev.*, 95:2695–2724, 1995. (Cited on page 61.)

[82] B. Jennings and K. Parslow. Particle size measurement: the equivalent spherical diameter. *Proc. R. Soc. London, Ser. A*, 419(1856):137–149, 1988. (Cited on page 129.)

[83] R. Jones. Rotational diffusion of a tracer colloid particle I. Short time orientational correlations. *Physica A*, 150:339–356, jan 1988. (Cited on page 56.)

[84] K. Nakamura and Particle Data Group. The review of particle physics. *J. Phys. G: Nucl. Part. Phys.*, 37(7A):075021, 2010. URL `http://pdg.lbl.gov`. (Cited on pages 22 and 203.)

[85] M. Kamal and S. S. Malik. Neutron incoherent elastic scattering study of the temperature dependence of the Debye-Waller exponent in vanadium. *Phys. Rev. B*, 18(4):1609–1617, 1978. (Cited on page 62.)

[86] M. Kataoka, M. Ferrand, A. Goupil-Lamy, H. Kamikuboa, J. Yunokia, T. Okaa, and J. C. Smith. Dynamical and structural modifications of staphylococcal nuclease on C-terminal truncation. *Physica B*, 266:20–26, 1999. (Cited on pages 85, 88, 96, 153 and 155.)

[87] K. H. Keller, E. R. Canales, and S. Yum. Tracer and mutual diffusion coefficients of proteins. *J. Phys. Chem.*, 75(3):379–387, 1971. (Cited on pages 110, 111 and 122.)

[88] R. C. G Killean. An investigation of the Debye-Waller factor and Debye temperature of aluminium using nearest neighbour central force pair interactions. *J. Phys. F: Met. Phys.*, 4:1908–1915, 1974. (Cited on page 64.)

[89] M. Kleman and O. D. Lavrentovich. *Soft Matter Physics*. Springer-Verlag New York, Inc., 2003. (Cited on pages 37 and 42.)

[90] S. H. Koenig. Brownian motion of an ellipsoid. A correction to Perrin's results. *Biopolymers*, 14(11):2421–2423, 1975. (Cited on pages 44 and 55.)

[91] A. Kudlay, M. S. Cheung, and D. Thirumalai. Crowding effects on the structural transitions in a flexible helical homopolymer. *Phys. Rev. Lett.*, 102 (118101), 2009. (Cited on pages 5, 103, 143, 150 and 180.)

[92] I. Kuntz Jr and W. Kauzmann. Hydration of proteins and polypeptides. *Adv. Protein Chem.*, 28:239 – 345, 1974. (Cited on pages 60 and 188.)

[93] P. T. Lansbury and H. A. Lashuel. A century-old debate on protein aggregation and neurodegeneration enters the clinic. *Nature*, 443(7113):774–779, 2006. (Cited on pages 163 and 181.)

[94] C. Le Coeur. Microscopic protein diffusion at high concentration by neutron spin-echo spectroscopy. *Chem. Phys.*, 345:298–304, 2008. (Cited on page 128.)

[95] J. L. Lebowitz and J. K. Percus. Mean Spherical Model for Lattice Gases with Extended Hard Cores and Continuum Fluids. *Phys. Rev.*, 144(251), 1966. (Cited on page 36.)

[96] J. Lee and S. Timasheff. Partial specific volumes and interactions with solvent components of proteins in guanidine hydrochloride. *Biochemistry*, 13:257 – 265, 1974. (Cited on pages 60, 137 and 188.)

[97] C. Leggio, L. Galantini, and N. V. Pavel. About the albumin structure in solution: cigar Expanded form versus heart Normal shape. *Phys. Chem. Chem. Phys.*, 10(45):6741, 2008. (Cited on page 58.)

[98] Y. Liu, E. Fratini, P. Baglioni, W. Chen, and S. Chen. Effective Long-Range Attraction between Protein Molecules in Solutions Studied by Small Angle Neutron Scattering. *Phys. Rev. Lett.*, 95:118102, jan 2005. (Cited on pages 43 and 163.)

[99] Y. Liu, L. Porcar, J. Chen, W. Chen, P. Falus, A. Faraone, E. Fratini, K. Hong, and P. Baglioni. Lysozyme Protein Solution with an Intermediate Range Order Structure. *J. Phys. Chem. B*, 2011. doi: doi:10.1021/jp109333c. (Cited on pages 6, 7, 104, 105, 163, 164, 173, 175 and 176.)

[100] S. Longeville, W. Doster, and G. Kali. Myoglobin in crowded solutions: structure and diffusion. *Chem. Phys.*, 292(2-3):413 – 424, 2003. (Cited on pages 51, 110, 112, 120, 121, 128 and 143.)

[101] S. W. Lovesey. *Theory of Neutron Scattering from Condensed Matter*, volume 1 and 2. Oxford University Press, 2004. (Cited on pages 22 and 25.)

[102] H. Löwen, E. Allahyarov, and C. N. Likos. Charged colloids, polyelectrolytes and biomolecules viewed as strongly coupled Coulomb systems. *J. Phys. A: Math. Gen.*, 36:5827–5834, 2003. (Cited on page 163.)

[103] H. Maier-Leibnitz and T. Springer. Ein Interferometer für langsame Neutronen. *Z. Phys. A-Hadron Nucl.*, 167:386–402, 1962. (Cited on page 66.)

[104] V. Makarov, B. Pettitt, and M. Feig. Solvation and hydration of proteins and nucleic acids: a theoretical view of simulation and experiment. *Acc. Chem. Res*, 35:376 – 384, 2002. (Cited on page 60.)

[105] N. Meechai, A. Jamieson, and J. Blackwell. Translational Diffusion Coefficients of Bovine Serum Albumin in Aqueous Solution at High Ionic Strength. *J. Colloid Interface Sci.*, 218:167–175, 1999. (Cited on page 110.)

[106] F. Merzel and J. C. Smith. Is the first hydration shell of lysozyme of higher density than bulk water? *Proc. Natl. Acad. Sci. U.S.A.*, 99(8):5378–5383, 2002. (Cited on page 188.)

[107] R. Metzler and J. Klafter. The random walk's guide to anomalous diffusion: a fractional dynamics approach. *Phys. Rep.*, 339(1):1–77, 2000. (Cited on page 127.)

[108] F. Mezei. Neutron spin echo: A new concept in polarized thermal neutron techniques. *Z. Phys.*, 255(2):146–160, 1972. (Cited on page 75.)

[109] F. Mezei, editor. *Neutron Spin Echo , Lecture Notes in Physics*, volume 128. Springer, Berlin, 1980. (Cited on pages 113 and 115.)

[110] F. Mezei, C. Pappas, and T. Gutberlet. *Neutron spin echo spectroscopy: basics, trends, and applications*. Springer, 2003. (Cited on page 75.)

[111] J. Mittal. Dependence of Protein Folding Stability and Dynamics on the Density and Composition of Macromolecular Crowders. *Biophys. J.*, 98(2): 315–320, 2010. (Cited on pages 5 and 103.)

[112] K. Monkos. Viscosity of bovine serum albumin aqueous solutions as a function of temperature and concentration. *Int. J. Biol. Macromol.*, 18(1-2):61–68, 1996. (Cited on page 109.)

[113] N. Muramatsu. Tracer diffusion of globular proteins in concentrated protein solutions. *Proc. Natl. Acad. Sci. U.S.A.*, 85:2984–2988, 1988. (Cited on pages 127 and 134.)

[114] LR Murphy and A Wallqvist. Simplified amino acid alphabets for protein fold recognition and implications for folding. *Protein Eng.*, 13(3):149–152, 2000. (Cited on pages 1 and 13.)

[115] G. Nägele. On the dynamics and structure of charge-stabilized suspensions. *Phys. Rep.*, 272(5-6):215–372, 1996. (Cited on pages 7, 102, 105, 128, 169, 176 and 181.)

[116] G. Nägele. *The Physics of Colloidal Soft Matter*. Lecture Notes 14. Institute of Fandamental Technological Research, Polish Academy of Sciences Publishing, Warsaw, 2004. URL `http://hera.physik.uni-konstanz.de/igk/news/workshops/Naegele.pdf`. (Cited on pages 37, 43, 167 and 176.)

[117] T. Narayanan. Synchrotron Small-Angle X-Ray Scattering Studies of Colloidal Suspensions. In M. Gomez, A. Nogales, M. C. Garcia-Gutierrez, and T. A.

Ezquerra, editors, *Applications of Synchrotron Light to Scattering and Diffraction in Materials and Life Sciences*, volume 776 of *Lecture Notes in Physics*, pages 133–156. Springer Berlin / Heidelberg, 2009. (Cited on page 166.)

[118] P. Nelson. *Biological Physics*. W. H. Freeman and Company, New York, 2004. (Cited on pages 2 and 13.)

[119] S. Nir. Van der Waals interactions between surfaces of biological interest. *Prog. Surf. Sci.*, 8(1):1–58, 1977. (Cited on pages 42 and 43.)

[120] D. Orthaber, A. Bergmann, and O. Glatter. SAXS experiments on absolute scale with Kratky systems using water as a secondary standard. *J. Appl. Crystallogr.*, 33:218–225, 2000. (Cited on pages 84 and 166.)

[121] M. G. Ortore, F. Spinozzi, P. Mariani, A. Paciaroni, L. R. S. Barbosa, H. Amenitsch, M. Steinhart, J. Ollivier, and D. Russo. Combining structure and dynamics: non-denaturing high-pressure effect on lysozyme in solution. *J. R. Soc. Interface*, 6, 2009. doi: doi:10.1098/rsif.2009.0163.focus. (Cited on page 128.)

[122] H. Paalman and C. Pings. Numerical evaluation of x-ray absorption factors for cylindrical samples and annular sample cells. *J. Appl. Phys.*, 33(8):2635–2639, 1962. (Cited on pages 144 and 185.)

[123] E. Paci and M. Karplus. Unfolding proteins by external forces and temperature: The importance of topology and energetics. *Proc. Natl. Acad. Sci. U.S.A.*, 97(12):6521–6526, 2000. (Cited on pages 1 and 13.)

[124] W. Pan, P. G. Vekilov, and V. Lubchenko. Origin of Anomalous Mesoscopic Phases in Protein Solutions. *J. Phys. Chem. B*, 114(22):7620–7630, 2010. (Cited on page 163.)

[125] J. Perez, J. Zanotti, and D. Durand. Evolution of the internal dynamics of two globular proteins from dry powder to solution. *Biophys. J.*, 77(1):454–469, 1999. (Cited on pages 4, 85, 88, 90, 91, 102, 114, 119, 128, 131, 133, 139, 140, 143, 144, 148 and 153.)

[126] S. J. Perkins. Protein volumes and hydration effects. the calculations of partial specific volumes, neutron scattering matchpoints and 280-nm absorption coefficients for proteins and glycoproteins from amino acid sequences. *Eur. J. Biochem.*, 157(1):169, 1986. (Cited on page 188.)

[127] S. J. Perkins. X-ray and neutron scattering analyses of hydration shells: a molecular interpretation based on sequence predictions and modelling fits. *Biophys. Chem.*, 93(2-3):129–139, 2001. (Cited on page 188.)

[128] F. Perrin. Mouvement brownien d'un ellipsoide-I. Dispersion diélectrique pour des molécules ellipsoidales. *Le Journal de Physique*, 10:497–511, 1934. (Cited on pages 44, 55, 129 and 138.)

[129] G. Phillies, G. Benedek, and N. Mazer. Diffusion in protein solutions at high concentrations: A study by quasielastic light scattering spectroscopy. *J. Chem. Phys.*, 65(5):1883–1892, 1976. (Cited on page 110.)

[130] R. Piazza. Protein interactions and association: an open challenge for colloid science. *Curr. Opin. Colloid Interface Sci.*, 8(6):515 – 522, 2004. (Cited on pages 127 and 163.)

[131] M. Placidi and S. Cannistraro. A dynamic light scattering study on mutual diffusion coefficient of bsa in concentrated aqueous solutions. *Europhys. Lett.*, 43(4):476–481, 1998. (Cited on page 110.)

[132] L. Porcar, P. Falus, W. Chen, A. Faraone, E. Fratini, K. Hong, P. Baglioni, and Y. Liu. Formation of the Dynamic Clusters in Concentrated Lysozyme Protein Solutions. *J. Phys. Chem. Lett.*, 1(1):126–129, 2010. (Cited on pages 163 and 173.)

[133] E. M. Purcell. Life at low Reynolds number. *Am. J. Phys.*, 45:3–11, 1977. (Cited on pages 2, 13, 37 and 127.)

[134] P. Lindgård. Reflections on the protein-folding problem. *J. Phys. Condens. Matter*, 15(18):S1779, 2003. (Cited on page 109.)

[135] H. N. Ritland, P. Kaesberg, and W. W. Beeman. An x-ray investigation of the shapes and hydrations of several protein molecules in solution. *J. Chem. Phys.*, 18(9):1237–1242, 1950. (Cited on pages 60 and 188.)

[136] W. C. Röntgen. Über eine neue Art von Strahlen. *Ann. Phys.*, 300(1):1–11, 1898. (Cited on page 33.)

[137] F. Roosen-Runge, M. Hennig, F. Zhang, R. M. J. Jacobs, M. Sztucki, H. Schober, T. Seydel, and F. Schreiber. Protein Self-Diffusion in Crowded Solutions. Unpublished. (Cited on pages 60, 164 and 176.)

[138] F. Roosen-Runge, M. Hennig, T. Seydel, F. Zhang, M. W. A. Skoda, S. Zorn, R. M. J. Jacobs, M. Maccarini, P. Fouquet, and F. Schreiber. Protein diffusion in crowded electrolyte solutions. *BBA-Proteins Proteom*, 1804(1):68–75, 2010. (Cited on pages 128, 131, 143 and 176.)

[139] C. A. Ross and M. A. Poirier. Protein aggregation and neurodegenerative disease. *Nature Medicine*, 10(7):S10–S17, 2004. (Cited on pages 163 and 181.)

[140] D. Russo, J. Pérez, J. Zanotti, and M. Desmadril. Dynamic transition associated with the thermal denaturation of a small beta protein. *Biophys. J.*, 83 (5):2792–2800, 2002. (Cited on pages 85, 88, 96, 143, 153 and 155.)

[141] V. G. Sakai and A. Arbe. Quasielastic neutron scattering in soft matter. *Curr. Opin. Colloid Interface Sci.*, 14:381–390, 2009. (Cited on page 66.)

[142] R. Sanchez and P. Bartlett. Equilibrium cluster formation and gelation. *J. Phys. Condens. Matter*, 17(45):S3551, 2005. (Cited on page 163.)

[143] M. J. Saxton. Anomalous diffusion due to obstacles: a Monte Carlo study. *Biophys. J.*, 66:394–401, 1994. (Cited on page 127.)

[144] G. Scatchard, A. Batchelder, and A. Brown. Preparation and properties of serum and plasma proteins. vi. osmotic equilibria in solutions of serum albumin and sodium chloride. *J. Am. Chem. Soc*, 68(11):2320–2329, 1946. (Cited on pages 40, 60 and 110.)

[145] P. Schleger, G. Ehlers, A. Kollmar, B. Alefeld, J. F. Barthelemy, H. Casalta, B. Farago, P. Giraud, C. Hayes, C. Lartigue, F. Mezei, and D. Richter. The sub-neV resolution NSE spectrometer IN15 at the Institute Laue–Langevin. *Physica B*, 266(1-2):49–55, 1999. (Cited on pages 76 and 204.)

[146] F. Schreier and D. Kohlert. Optimized implementations of rational approximations—a case study on the Voigt and complex error function. *Comput. Phys. Commun.*, 179(7):457–465, 2008. (Cited on pages 88 and 114.)

[147] F. Sciortino, S. Mossa, and E. Zaccarelli. Equilibrium cluster phases and low-density arrested disordered states: the role of short-range attraction and long-range repulsion. *Phys. Rev. Lett.*, 93(5):055701, 2004. (Cited on page 163.)

[148] V. F. Sears. Neutron scattering lengths and cross sections. *Neutron News*, 3 (3):26–28, 1992. (Cited on page 23.)

[149] V. F. Sears. Bragg Reflection in Mosaic Crystals. II. Neutron Monochromator Properties. *Acta Crystallogr., Sect. A: Found. Crystallogr.*, A53:46–54, 1997. (Cited on page 71.)

[150] M. V. Smoluchowski. Über Brownsche Molekularbewegung unter Einwirkung äusserer Kräfte und deren Zusammenhang mit der verallgemeinerten Diffusionsgleichung. *Ann. Phys.*, 353(24):1103–1112, 1916. (Cited on page 47.)

[151] G. L. Squires. *Introduction to the theory of thermal neutron scattering*. Dover Publications, Inc., 1996. (Cited on pages 22, 31 and 110.)

[152] A. M. Stadler, I. Digel, G. M. Artmann, J. P. Embs, G. Zaccai, and G. Büldt. Hemoglobin dynamics in red blood cells: Correlation to body temperature. *Biophys. J.*, 95(11):5449–5461, 2008. (Cited on pages 128, 131, 139, 140 and 143.)

[153] A. M. Stadler, I. Digel, J. P. Embs, T. Unruh, and M. Tehei. From Powder to Solution: Hydration Dependence of Human Hemoglobin Dynamics Correlated to Body Temperature. *Biophys. J.*, 96:5073–5081, 2009. (Cited on page 128.)

[154] A. M. Stadler, L. van Eijck, F. Demmel, and G. Artmann. Macromolecular dynamics in red blood cells investigated using neutron spectroscopy. *J. R. Soc. Interface*, 8(57):590–600, 2011. (Cited on page 128.)

[155] L. Stagg, S. Q. Zhang, M. S. Cheung, and P. Wittung-Stafshede. Molecular crowding enhances native structure and stability of α/β protein flavodoxin. *Proc. Natl. Acad. Sci. U.S.A.*, 104(48):18976–18981, 2007. (Cited on pages 8, 135, 136 and 180.)

[156] H. E. Stanley. *Introduction to Phase Transitions and Critical Phenomena*. Oxford University Press, Inc., 1987. (Cited on page 172.)

[157] A. Stradner, H. Sedgwick, and F. Cardinaux. Equilibrium cluster formation in concentrated protein solutions and colloids. *Nature*, 432:492–495, 2004. (Cited on pages 43 and 163.)

[158] D. I. Svergun, S. Richard, M. H. J. Koch, Z. Sayers, S. Kuprin, and G. Zaccai. Protein hydration in solution: experimental observation by x-ray and neutron scattering. *Proc. Natl. Acad. Sci. U.S.A.*, 95(5):2267, 1998. (Cited on pages 129 and 188.)

[159] C. Tanford, S. A. Swanson, and W. S. Shore. Hydrogen ion equilibria of Bovine Serum Albumin. *J. Am. Chem. Soc.*, 77(24):6414–6421, 1955. (Cited on pages 40 and 60.)

[160] J. Teixeira, M. C. Bellissent-Funel, and A. J. Dianoux. Experimental determination of the nature of diffusive motions of water molecules at low temperatures. *Phys. Rev. A*, 31(3):1913–1917, 1985. (Cited on page 61.)

[161] P. R. ten Wolde and D. Frenkel. Enhancement of Protein Crystal Nucleation by Critical Density Fluctuations. *Science*, 277(5334):1975–1978, 1997. (Cited on pages 163 and 181.)

[162] M. Tokuyama and I. Oppenheim. Dynamics of hard-sphere suspensions. *Phys. Rev. E*, 50(1):16–19, 1994. (Cited on pages 7, 102, 105, 128, 134, 176 and 181.)

[163] J. Trevors and G. Pollack. Hypothesis: the origin of life in a hydrogel environment. *Prog. Biophys. Mol. Biol.*, 89(1):1–8, 2005. (Cited on page 109.)

[164] G. A. Truskey, F. Yuan, and D. F. Katz. *Transport Phenomena in Biological Systems*. Pearson Education, Inc, 2004. (Cited on pages 2 and 13.)

[165] A. van Blaaderen, J. Peetermans, G. Maret, and J. K. G. Dhont. Long-time self-diffusion of spherical colloidal particles measured with fluorescence recovery after photobleaching. *J. Chem. Phys.*, 96:4591–4603, 1992. (Cited on pages 102, 128 and 181.)

[166] L. van Hove. Correlations in Space and Time and Born Approximation Scattering in Systems of Interacting Particles. *Phys. Rev.*, 95(1):249–262, 1954. (Cited on page 29.)

[167] J. Végh. Alternative form for the pseudo-voigt peak shape. *Rev. Sci. Instrum.*, 76(5):056107, 2005. (Cited on pages 88 and 114.)

[168] A. S. Verkman. Solute and macromolecule diffusion in cellular aqueous compartments. *Trends Biochem. Sci*, 27(1):27–33, 2002. (Cited on pages 127 and 134.)

[169] E. J. W. Verwey and J. T. G. Overbeek. *Theory of the Stability of Lyophobic Colloids*. Amsterdam: Elsevier, 1948. (Cited on pages 42, 102 and 121.)

[170] G. Vineyard. Scattering of slow neutrons by a liquid. *Phys. Rev.*, 110(5): 999–1010, 1958. (Cited on pages 51, 112 and 121.)

[171] F. Volino and A. J. Dianoux. Neutron incoherent scattering law for diffusion in a potential of spherical symmetry: general formalism and application to diffusion inside a sphere. *Mol. Phys.*, 41(2):271–279, 1980. (Cited on pages 88 and 153.)

[172] F. Vollrath and D. P. Knight. Liquid crystalline spinning of spider silk. *Nature*, 410(6828):541–548, 2001. (Cited on pages 163 and 181.)

[173] W. L. Bragg. The Diffraction of Short Electromagnetic Waves by a Crystal. *Proc. Cambridge Philos. Soc.*, 17:43–57, 1913. (Cited on page 66.)

[174] Y. Wang, C. Li, and G. Pielak. Effects of Proteins on Protein Diffusion. *J. Am. Chem. Soc.*, 132(27):9392–9397, 2010. (Cited on pages 127 and 134.)

[175] S. Weggler, M. Ziller, F. Zhang, F. Schreiber, O. Kohlbacher, and A. Hildebrandt. Monte Carlo simulation of multivalent metal ion-protein binding. Unpublished, 2011. (Cited on pages 27, 29, 58, 59, 87, 173, 191, 193 and 195.)

[176] M. Weiss, M. Elsner, and F. Kartberg. Anomalous Subdiffusion Is a Measure for Cytoplasmic Crowding in Living Cells. *Biophys. J.*, 87:3518–3524, 2004. (Cited on page 127.)

[177] M. K. Wilkinson. Early history of neutron scattering at oak ridge. *Physica*, 137B:3–16, 1986. (Cited on page 21.)

[178] G. Williams and D. C. Watts. Non-symmetrical dielectric relaxation behaviour arising from a simple empirical decay function. *Trans. Faraday Soc.*, 66:80–85, 1970. (Cited on pages 88, 144 and 153.)

[179] J. W. Wojcieszyn and R. A. Schlegel. Diffusion of injected macromolecules within the cytoplasm of living cells. *Proc. Natl. Acad. Sci. U.S.A.*, 78(7): 4407–4410, 1981. (Cited on pages 127 and 134.)

[180] Wolfram Alpha LLC. Wolfram|Alpha, (access May 4, 2011). URL http://www.wolframalpha.com/input/?i=neutron. (Cited on pages 22 and 203.)

[181] Wolfram Research, Inc. *Mathematica Edition: Version 8.0*. Wolfram Research, Inc., Champaign, Illinois, 2010. (Cited on page 97.)

[182] G. Zaccai. How Soft Is a Protein? A Protein Dynamics Force Constant Measured by Neutron Scattering. *Science*, 288(5471):1604–1607, 2000. (Cited on page 148.)

[183] W. H. Zachariasen. *Theory of X-Ray Diffraction in Crystals*. Dover Publications, Inc., 1945. (Cited on page 70.)

[184] F. Zhang, M. W. A. Skoda, R. M. J. Jacobs, R. A. Martin, C. M. Martin, and F. Schreiber. Protein Interactions Studied by SAXS: Effect of Ionic Strength and Protein Concentration for BSA in Aqueous Solutions. *J. Phys. Chem. B*, 111(1):251–259, 2007. (Cited on pages 60, 110, 113, 116, 121, 129, 137, 138, 147 and 163.)

[185] F. Zhang, M. W. A. Skoda, R. M. J. Jacobs, S. Zorn, R. A. Martin, C. M. Martin, G. F. Clark, S. Weggler, A. Hildebrandt, O. Kohlbacher, and F. Schreiber. Reentrant Condensation of Proteins in Solution Induced by Multivalent Counterions. *Phys. Rev. Lett.*, 101(14):148101, 2008. (Cited on pages 6, 104, 110, 123, 127, 138, 163, 164, 170, 173, 177, 180 and 181.)

[186] F. Zhang, S. Weggler, M. Ziller, L. Laneselli, B. S. Heck, A. Hildebrandt, O. Kohlbacher, M. W. A. Skoda, R. M. J. Jacobs, and F. Schreiber. On the universality of protein reentrant condensation in solution induced by multivalent metal ions. *Proteins Struct. Funct. Bioinf.*, 78(16):3450–3457, 2010. URL http://onlinelibrary.wiley.com/doi/10.1002/prot.22852/full. (Cited on pages 104, 164 and 170.)

[187] B. Zimm and J. Bragg. Theory of the phase transition between helix and random coil in polypeptide chains. *J. Chem. Phys.*, 31(2):526–535, 1959. (Cited on pages 5, 8, 103, 147 and 180.)

[188] S. B. Zimmerman and A. P. Minton. Macromolecular Crowding: Biochemical, Biophysical, and Physiological Consequences. *Annu. Rev. Biophys. Biomol. Struct.*, 22(1):27–65, 1993. (Cited on pages 127 and 179.)